Chevron-shaped protrusions for turbulent drag reduction

Experimental investigation into the drag performance and flow mechanics

J. Carrasco Grau

Delft University of Technology

TU Delft
DIMPLE

Chevron-shaped protrusions for turbulent drag reduction

Experimental investigation into the drag performance and flow mechanics

Master of Science Thesis

by

J. Carrasco Grau

in partial fulfilment of the requirements for the degree of

Master of Science

in Aerospace Engineering

at the Delft University of Technology

To be defended on Friday, August 5, 2022, at 13:00

Student number:	5361540	
Thesis committee:	Dr. D. Ragni,	Delft University of Technology
	Dr. ir. F. F. J. Schrijer,	Delft University of Technology
	Dr. ir. W. J. Baars,	Delft University of Technology
	Drs. ir. O. W. G. van Campenhout,	Dimple Aerospace B.V.

TU Delft DIMPLE

Delft University of Technology

Faculty of Aerospace Engineering
Department of Aerodynamics, Wind Energy, Flight Performance and Propulsion

The undersigned hereby certify that they have read and recommend to the Faculty of Aerospace Engineering for acceptance the thesis entitled **Chevron-shaped protrusions for turbulent drag reduction: Experimental investigation into the drag performance and flow mechanics** by **J. (Julio) Carrasco Grau** in partial fulfilment of the requirements for the degree of **Master of Science** in **Aerospace Engineering**.

Dated: August 5, 2022

Chair of supervisory committee and external reader:

Dr. D. (Daniele) Ragni

Supervisors:

Dr. ir. F. F. J. (Ferry) Schrijer

Dr. ir. W. J. (Woutijn) Baars

Drs. ir. O. W. G. (Olaf) van Campenhout

Preface

With this Master thesis report, I conclude my Master of Science program at the Delft University of Technology. The journey began almost two years ago during a very uncertain time for the world: the COVID-19 pandemic. In the summer of 2020, shortly before the start of my first academic year in Delft, the pandemic seemed to be fading away, and the hopes for 'normal times' were rising. So I moved to Delft, excited and intrigued for what was about to come. However, a new wave marked the return of restrictions, making the 'normal times' look very distant. The result was an academic year with not a single in-person lecture and uncountable hours online working with 'virtual' fellow students on assignments. Considering the circumstances, I am pleased to conclude this chapter of my life by presenting my thesis in person at TU Delft in front of my friends and family.

I want to thank my daily supervisor Olaf van Campenhout for giving me the opportunity to experience TU Delft offline. His unique energy and enthusiasm have motivated me throughout the entire Master thesis phase, and his support and feedback have been crucial to the project.

I also want to thank Ferry Schrijer and Woutijn Baars for their guidance and patience. Their input during our 14 progress meetings has shaped this work. But their support was not limited to the meetings: their office doors and email inboxes were always open for questions, and they did not hesitate to visit the M-tunnel during the experimental campaigns for a quick chat or to debug a faulty PTU.

I am also very grateful for the support I have received from Daniele Ragni. His proficiency with PIV setups and hands-on approach were paramount for the success of my 'thin sheet' PIV campaign. His tips on PIV post-processing and server access for this matter were also appreciated. Thus, I am happy to have him leading the supervisory committee for this thesis.

Working at Dimple Aerospace B.V. during my Master thesis has made this phase of my studies very special. Due to their remarkable work ethic, it has been very inspiring to work with Michiel van Nesselrooij and Friso Hartog. They have always been very approachable and have provided advice and support in several instances. A special mention goes to Friso H. for sharing his experimental data for this thesis and to Niels Verdegaal for his help with the measurements. The entire Dimple team, including all my fellow students, are exceptional. A vivid memory to exemplify their commitment and support was our 'peeling party' when everyone took an evening off to help with the manufacturing of the test plates. It has been a lot of fun to work with all of them.

I also would like to thank Mr Lawrence Sirovich for taking the time for a call with us. It was exceptional to share my findings with the researcher who inspired this experimental study and receive his feedback.

Furthermore, I want to express my gratitude to everyone that has supported this research: Willfried van der Lee for providing aerospace-graded vinyl foil, Alberto Rius Vidales for his advice on the PIV setup, Giulia Zoppini for her help in the LSL, and many more.

Finally, I want to thank my family, especially my parents, for their unconditional support and patience during this and every other phase of my life.

J. Carrasco Grau
Delft, August 2022

Abstract

In the last decades, the prevailing belief that smooth surfaces offer the lowest drag has been challenged often. Scholars have, for example, introduced rough and modified surfaces to reduce turbulent skin friction. One of the technologies proposed in the literature is an array of chevron-shaped protrusions; however, there is no academic consensus on the drag performance of this technique. Furthermore, although the theoretical working mechanism has been documented well, there is no experimental evidence in the literature to support the hypothesis around this mechanism.

In this study, the experiments from the literature are replicated, and new array configurations are tested to characterise the effect of individual parameters on the drag performance. The test plates are manufactured by applying vinyl protrusions of roughly 100 μm in thickness to an aluminium base plate. This thickness corresponds to $5\delta_\nu - 6\delta_\nu$ for the design Reynolds number of $Re_\tau = 1270$. Direct force measurements are performed in the M-tunnel at a Reynolds number range of approximately $630 < Re_\tau < 1850$ to determine the drag performance. Furthermore, the coherent structures are characterised by means of 2D-2C PIV of a wall-parallel plane at a minimum distance of $17\delta_\nu$ from the wall.

The drag reduction reported in the literature could not be replicated, and the balance measurement results offer relevant insights into the drag performance of chevron-shaped protrusions. The results consistently show that the added roughness due to the presence of the protrusions is not the only parameter that determines the drag performance, confirming a meaningful interaction between the protrusions and the flow. Moreover, the results are found to be highly sensitive to the randomisation of the array. No substantial effect of the protrusions on the coherent structures close to the wall has been observed. In particular, no evidence has been observed that supports the working mechanism as proposed in the literature.

An analysis of possible causes to explain the discordance between this study and the literature is performed. Based on this analysis and the results from the aforementioned parametric study, an improved design is proposed, and recommendations for future research are postulated. This technology has inherent benefits for real-world implementations as it can easily be (retro)fitted to aircraft by means of a foil. Further research into this flow control technique is thereby deemed relevant due to the combination of the large drag reduction reported in the literature, the advantages in practical applications, and the novel opportunities for additional investigations.

Contents

List of Figures

List of Tables

Nomenclature

Acronyms and Abbreviations

2D	Two-dimensional
2D-2C	Two-dimensional, two-component
BL	Boundary layer
CAD	Computer-aided design
CAN	Climate Action Network
CNC	Computer Numerical Control
CO2	Carbon dioxide
DASML	Delft Aerospace Structures and Materials Laboratory
DEMO	Dienst Elektronische en Mechanische Ontwikkeling
DNS	Direct numerical simulation
DR	Drag reduction
DSLR	Digital single-lens reflex
FOV	Field of view
GOP	Generalised optimal perturbations
HWA	Hot-wire anemometry
IATA	International Air Transport Association
IBL	Internal boundary layer
ICSA	International Coalition for Sustainable Aviation
IEL	Internal equilibrium layer
LSL	Low-speed laboratory
LW	Length × width
LWH	Length × width × height
NRMSD	Normalised root-mean-square deviation
PDF	Portable document format
PIV	Particle image velocimetry
PTU	Programmable timing unit
RMSD	Root-mean-square deviation
RMSE	Root-mean-square error
STR	Smooth to rough
TEU	Twenty-foot equivalent unit
TP	Test plate
TS	Tollmien–Schlichting
TU Delft	Delft University of Technology
ULCV	Ultra-large container vessels
UV	Ultraviolet
VLSM	Very Large Scale Motion
VU	Viscous unit length (δ_ν)

Greek Symbols

α	(Protrusion) apex angle
β	Adaptive constant in the logarithmic velocity law
δ	Boundary layer thickness
δ^*	Displacement thickness
δ_e	Thickness of the internal equilibrium layer
δ_i	Thickness of the internal boundary layer
δ_ν	Viscous unit length or wall unit

ϵ_u Relative uncertainty of the instantaneous velocity field u (equivalent for v and w)

ϵ_x Uncertainty of a quantity x

$\epsilon_{\Delta x_{px}}$ Correlation factor based on the uncertainty of modern digital cameras

$\epsilon_{\bar{u}}$ Uncertainty of the mean velocity field $\bar{u}$ (equivalent for $\bar{v}$ and $\bar{w}$)

$\epsilon_{\sigma(u)}$ Uncertainty of the standard deviation in the velocity field $\bar{u}$ (equivalent for $\sigma(v)$ and $\sigma(w)$)

$\epsilon_{\sigma^2(u)}$ Uncertainty of the standard deviation in the velocity field $\bar{u}$ (equivalent for $\sigma^2(v)$ and $\sigma^2(w)$)

η Wall normal distance normalised with boundary layer thickness

κ Von Kármán constant

μ Dynamic viscosity

ν Kinematic viscosity

$\phi_{\tau\tau}$ Power spectral density of the fluctuating wall stress

Π Coles' parameter

π Arbitrarily small distance

ρ Density

$\sigma(u)$ Standard deviation of u (equivalent for $\sigma(v)$ and $\sigma(w)$)

$\sigma^2(u)$ Variance of u (equivalent for $\sigma^2(v)$ and $\sigma^2(w)$)

σ_x Standard deviation of a quantity x

τ Shear stress

τ_w Wall shear stress

θ Momentum thickness

ξ Pressure gradient parameter

Non-Greek Symbols

ΔC_D Wall drag difference with respect to the reference smooth plate

Δt Time between frames of an image pair

ΔV Change in velocity

$\overline{\Delta x_{px}}$ Average pixel displacement

$\overline{u}, \overline{v}, \overline{w}$ Mean velocity in streamwise, wall-normal, and spanwise directions

A Streamwise separation between protrusion rows

a Streamwise separation between protrusion rows (in literature)

$A_{\text{protrusion}}$ Area of a protrusion element (from top view)

$A_{\text{test plate}}$ Area of a test plate exposed to the flow

B Protrusion streamwise length

b Protrusion streamwise length (in literature)

C Protrusion spanwise width

c Protrusion spanwise width (in literature)

C_f Friction coefficient

c_f Local friction coefficient

D Spanwise separation between protrusion elements in a rows

d Spanwise separation between protrusion elements in a rows (in literature)

d^+ Streamwise length of the near-wall streaks in viscous units

E Offset between rows in a protrusion array

e Offset between rows in a protrusion array (in literature)

F Protrusion height

f Focal length

f	Protrusion height (in literature)
f_s	PIV sampling frequency
H	Shape factor
h	Pipe diameter or channel height
H^+	Protrusion height expressed in viscous units (in literature)
L	Protrusion streamwise length (in literature)
l^+	Spanwise spacing of the near-wall streaks in viscous units
M	Scale or magnification factor
N	Number of samples
N_{elements}	Number of protrusion elements in an array
p_e	free-stream pressure
R_{uu}	Normalised two-point correlation coefficient
Re	Reynolds number
Re_1	Reynolds number per metre
Re_τ	Friction Reynolds number
Re_h	Reynolds number based on centerline velocity in a channel flow
Re_x	Reynolds number evaluated at x
Re_θ	Momentum thickness Reynolds number
Re_{U_b}	Reynolds number based on the bulk velocity U_b
S_x	Streamwise separation between protrusion rows (in literature)
S_z	Spanwise separation between protrusion elements in a rows (in literature)
T	Chevron leg thickness
t	Chevron leg thickness (in literature)
T^+	Non-dimensional frequency
T^+	Non-dimensional time scale
T_s	Time between two image pairs
u, v, w	Velocity in streamwise, wall-normal, and spanwise directions
u', v', w'	Velocity fluctuation in streamwise, wall-normal, and spanwise directions
U_∞	Free stream velocity
u_τ	Friction velocity
U_b	Bulk velocity
U_{cl}	Centerline velocity
W	Protrusion spanwise width (in literature)
x, y, z	Coordinates in streamwise, wall-normal, and spanwise directions
y_f	Thickness of the oil film

Superscripts

$+$	Expressed in wall or viscous units

Subscripts

air	Denotes a quantity evaluated for air
oil	Denotes a quantity evaluated for oil
w	Denotes a quantity evaluated at the wall

I

Introduction and theoretical background

1

Introduction

Observing current designs found on aircraft and other means of transportation, it is natural to conclude that smooth surfaces are optimal in terms of drag and fuel efficiency. However, this widespread belief has been proven wrong. In the case of laminar flow, Fransson et al. (2006) have been able to delay the transition to the turbulent regime by using surface bumps, with the consequent reduction in drag. More recently, Rius Vidales and Kotsonis (2021) experimentally delayed transition using forward-facing steps with a small step height. Moreover, in the case of turbulent flow, the use of riblets by Walsh (1982), omnidirectional roughness by Tani (1988), and chevron-shaped protrusions by Sirovich and Karlsson (1997) have successfully reduced friction drag. In all cases, the roughness or geometrical modification to the surface introduces disturbances to the flow, which either stabilise the flow (in the case of laminar) or interact with the structures present in the flow to reduce energy dissipation (in the case of turbulent). Although the results look promising, only some researchers have succeeded in replicating them (Choi, 2006). A good example of a controversial technique in terms of drag reduction performance is chevron-shaped protrusions, with studies showing varying results ranging from a 30% drag reduction all the way up to a 6% drag increase. This technique also presents some important research gaps: the hypothesis for the working mechanism has not been experimentally confirmed, and no systematic study on the relation between the relevant design parameters and the drag performance of the technique has been published. All in all, more investigation is required to understand this flow control technique.

Although the use of disturbances to reduce drag might sound counter-intuitive and even artificial, it is a technique that, in many cases, has been inspired by nature. A well-known example of biomimetics is riblets, which closely resemble shark skin denticles (Tian et al., 2022). Chevron-shaped protrusions can also be found in nature; as pointed out by Sagong et al. (2008), the sailfish has protrusion elements on its skin which might act as the protrusions tested by Sirovich and Karlsson (1997). An illustration of the sailfish and its skin protrusions is presented in figure 1.1.

(a) Sailfish

(b) Detail of the sailfish skin showing the protrusion pattern

Figure 1.1: The sailfish as 'bio-inspiration' for chevron-shaped protrusions, modified from Sagong et al. (2008)

The study of passive flow control techniques for reducing drag is of high societal interest. Aviation is responsible for approximately 2% of the global CO2 emissions, which translates into a 5% contribution to global warming when non-CO2 effects are taken into account, partially due to the special conditions at which aircraft operate (CAN & ICSA, 2018). Furthermore, aviation is one of the fastest-growing industries, with an expected increase of 8 billion passengers between 2021 and 2050, as illustrated in figure 1.2.

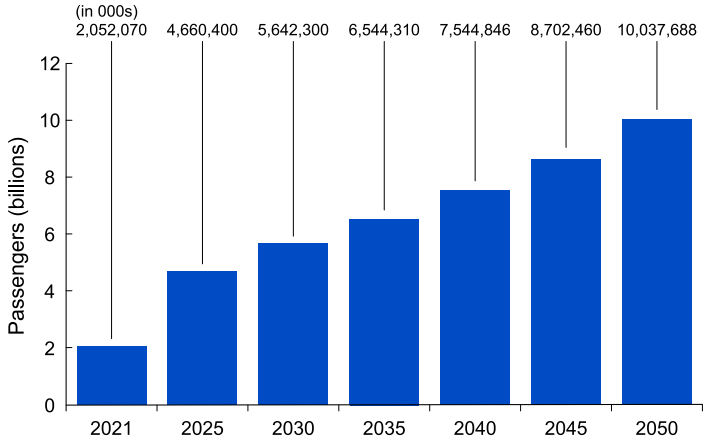

Figure 1.2: Forecasted evolution of air transport passenger traffic, from Mikosz (2021)

With drag force being the main aerodynamic contributor to aircraft emissions and considering that skin friction drag accounts for 50% of the total subsonic aircraft drag (Gad-el-Hak, 2000), a passive flow control technique to reduce skin friction drag on an aircraft, such as chevron-shaped protrusions, has the potential to improve its fuel efficiency and overall environmental footprint substantially (Tameike et al., 2021). This Master thesis will focus on the technique of chevron-shaped protrusions for reducing turbulent skin friction.

Chevron-shaped protrusions

A protrusion is an element of defined geometry that disturbs the flow and is roughly as high as the viscous sublayer. The chevron-shaped protrusions were introduced by Sirovich and Karlsson (1997), who presented the drag reduction capability of a flat surface covered by an array of these elements. A sketch of the array geometry used by Sirovich and Karlsson (1997) can be seen in figure 1.3.

Figure 1.3: Example for an array of chevron-shaped protrusions, geometry based on Sirovich and Karlsson (1997)

The theoretical working mechanism for this passive flow control device is well documented in literature: when arranged in a particular manner, the protrusions create disturbances in the flow that interact with the coherent structures and inhibit the formation of low-speed streaks, interrupting the near-wall cycle. Consequently, no undesired mixing occurs (bursts, ejection, and sweep events), and the skin friction is reduced. The geometry of the protrusion array plays a central role in determining its performance; the simple arrangement between protrusion rows can transform this skin friction reduction technique (random shift between rows) into a mixing enhancement device (aligned rows). Despite the importance of geometry on the drag reduction performance, no systematic study on the relation between these has been published to this date. Furthermore, no experimental flow visualisation has been performed for chevron-shaped protrusions, leaving the hypothesised working mechanism unconfirmed. A detailed

review of the current state of research on chevron-shaped protrusions for skin friction reduction can be found in section 3. Note that, sometimes in this thesis report, 'chevron-shaped protrusions' are referred to as 'protrusions' for brevity.

1.1. Research objective of the Master thesis

The promising drag reduction potential, the discrepancy between results in prior studies, the unknown effect of many design parameters, and the fact that the working mechanism has not been experimentally confirmed provide a unique opportunity for novel scientific research with a high industrial and societal impact. Hence, the overarching research objective of this Master thesis is defined as follows:

To experimentally investigate the turbulent drag reduction potential of chevron-shaped protrusions on a flat plate.

This main objective is further split into four sub-objectives, which detail the specific areas that will be explored:

1. **To reproduce the designs found in literature and to verify the corresponding results** by producing test plates with the reported protrusion geometries and measuring their drag in a wind tunnel.
2. **To explore the design parameter space for protrusions** by performing a large parametric study that includes design variations of the individual design parameters and by correlating these variations to the wind tunnel results.
3. **To test the working mechanism hypothesis presented by Sirovich and Karlsson (1997)** by performing quantitative flow visualisation (PIV).
4. **To define a design with improved drag performance or overall characteristics** by combining the previous findings.

1.2. Research questions of the Master thesis

The following research questions have been formulated to address each sub-objective and collectively reach the main research objective.

1. **Can the results found in the literature be reproduced?**
   (a) How can the reported designs/ experimental setup be replicated in the available experimental facilities? Is there missing information for which assumptions have to be made?
   (b) What is the difference in drag force measured between the various configurations and the reference smooth flat plate? And, in particular, can the reported drag reduction be reproduced?
   (c) How can differences between the performed measurements and the reported results be explained?
2. **How do the individual parameters of the protrusion array affect its performance?**
   (a) What granularity of the design parameter space can feasibly be tested?
   (b) How do changes in the individual design parameters affect the drag force difference with respect to a smooth reference plate and, in particular, the achieved drag reduction?
   (c) Can an outer envelope of drag-reducing designs be defined? Does this envelope change with Reynolds number?
3. **Do the flow characteristics and coherent structures in the flow support the working mechanism hypothesis presented by Sirovich and Karlsson (1997)?**

(a) Can low-speed streaks be visualised over the smooth reference test plate with the available experimental setup?

(b) Can the low-speed streaks be removed or be evidently weakened with a protrusion design that was shown to reduce skin friction?

(c) Can the low-speed streaks be evidently enhanced with an aligned protrusion design that was shown to increase skin friction?

(d) Do the turbulence statistics support the working mechanism hypothesis?

4. **To what extent can a design with improved drag performance or overall characteristics be defined?**

(a) What problems identified during the campaign can be addressed to lead to an improved design?

(b) What aspects, next to drag performance, can be improved in the array design?

1.3. Report overview

The structure of this report has been chosen with two objectives in mind: to guide the reader through the performed investigation in a natural manner and to effectively address the proposed research questions. On a high level, this report is structured in four parts, followed by an appendix (V).

First, the topic is introduced and the required theoretical background is provided in part I. This part includes an explanation of the boundary layer theory in chapter 2, followed by a literature review on chevron-shaped protrusions for skin friction reduction in chapter 3.

Next, the design and production of chevron-shaped protrusions are presented in part II. The rationale for the selected designs is included in chapter 4, followed by an explanation of the test plate design, manufacturing, and validation in chapter 5.

Part III provides an elaborate explanation of the wind tunnel experiments. This part starts with a description of the experimental apparatus in chapter 6 before presenting the direct force measurements in chapter 7, and the detailed flow investigation in chapter 8.

Finally, part IV closes this report with a discussion, conclusion, and some recommendations. In chapter 9 the outcomes of the previous discussions are briefly summarised, an improved array design is proposed, and some practical considerations for real-world applications of chevron-shaped protrusions are outlined. Last, chapter 10 concludes this thesis by addressing the research questions and giving recommendations for future research.

2

Boundary layer theory

This chapter is dedicated to providing the necessary theoretical background to understand and discuss the working mechanisms of skin friction reduction techniques and analyses presented in the following chapters. In section 2.1, a general overview of boundary layer theory is given, focusing primarily on definitions and parameters used to describe the boundary layer. In the subsequent section, 2.2, the structures present in a turbulent boundary layer flow are discussed. Special attention is given hereby to low-speed streaks due to their relevance to the working mechanism of the protrusions subject of this thesis report.

2.1. Theoretical overview: boundary layer theory

The boundary layer theory presented in this section, including the equations, is based on White (2006) unless otherwise indicated.

2.1.1. State of the boundary layer

While the introduction has stated that this report will focus on reducing turbulent skin friction drag, it is relevant to understand the differences in the state of the boundary layer in a laminar and a turbulent flow. Figure 2.1 shows the velocity profile in the boundary layer region for different states of a laminar to turbulent transition.

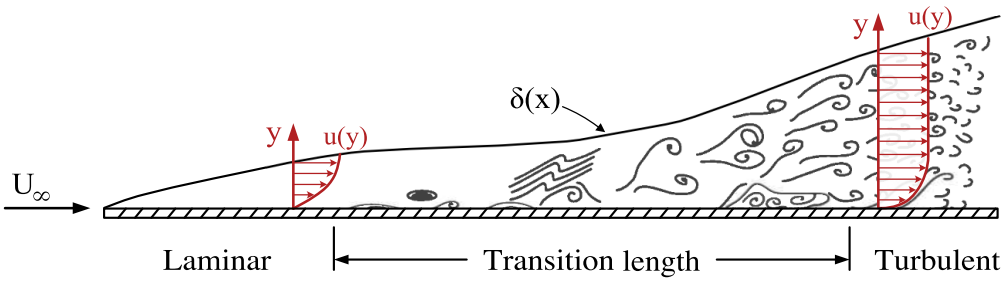

Figure 2.1: Boundary layer transition from laminar to turbulent flow, adapted from White (2006)

A common characteristic of the velocity profile, regardless of the boundary layer state, is that the velocity reaches zero at the wall, known as the no-slip condition imposed in viscous flows. As the distance from the wall increases, the velocity increases too until it eventually reaches the free-stream value. In a laminar flow, the boundary layer is made of separate layers that can be considered independent from each other and are dominated by the flow's free-stream direction. On the contrary, in the case of a turbulent flow, there are interactions between the layers in the form of mass and momentum mixing; this mixing, in which high energy flow is transported to regions of low energy flow in the proximity of the wall and vice versa, is responsible for the higher energy losses due to skin friction in a turbulent flow.

When comparing the velocity profiles corresponding to these two states (i.e. laminar and turbulent), it can be seen that the turbulent state has a 'fuller' velocity profile with a higher velocity gradient ($\frac{\partial u}{\partial y}$) near the wall. Considering this and looking at the equation for skin friction (equation 2.1), it can be concluded that the skin friction is higher in the turbulent state.

$$\tau_w = \mu \left(\frac{\partial u}{\partial y} \right)_{y=0}. \tag{2.1}$$

The Reynolds number (equation 2.2, where x is the distance from the leading edge, in the case of a flat plate) is usually used to characterise the state of the boundary layer. The Reynolds number at which laminar flow transitions to turbulent flow is called the critical Reynolds number (Re_{crit}).

$$Re_x = \frac{\rho U_\infty x}{\mu} = \frac{U_\infty x}{\nu}. \tag{2.2}$$

The discussion will centre around turbulent boundary layers in the following sections of this chapter.

2.1.2. Properties of the boundary layer

This section introduces several parameters used to analyse the boundary layer, namely the boundary layer thickness, the displacement thickness, the momentum thickness, and the shape factor.

Boundary layer thickness

The boundary layer thickness (δ) is the physical thickness of the boundary layer. In the case of pipe flow or channel flow, the boundary layer thickness is defined as half the diameter h or half the channel height h:

$$\delta = \frac{h}{2}. \tag{2.3}$$

In aerodynamics, however, it is common to define the boundary layer thickness as the distance from the wall at which the fluid velocity reaches 99% of the free-stream velocity:

$$\delta = \delta_{99\%} = y|_{\frac{u}{U_\infty}=99\%}. \tag{2.4}$$

With the so-called power-law, the boundary layer thickness can be approximated for turbulent flow over a flat plate with a zero pressure gradient:

$$\frac{\delta}{x} \approx \frac{0.16}{Re_x^{1/7}}, \tag{2.5}$$

where Re_x is the Reynolds number based on the distance from the leading edge, as defined in equation 2.2.

Displacement thickness

The displacement thickness (δ^*) is a measure of the distance by which a streamline (or particle) outside the shear area will deflect due to the presence of the boundary layer. The displacement thickness does only depend on the x coordinate and is defined as the integrated velocity deficit of the boundary layer:

$$\delta^* = \int_0^{\lim Y \to \infty} \left(1 - \frac{u}{U_\infty} \right) dy. \tag{2.6}$$

Momentum thickness

The momentum thickness (θ) is defined as the integrated momentum loss in the boundary layer and depends only on x. It can be interpreted as the thickness that a fluid layer in the free stream should

have in order to carry the momentum required to compensate for the momentum loss in the boundary layer.

$$\theta = \int_0^{\lim Y \to \infty} \frac{u}{U_\infty}\left(1 - \frac{u}{U_\infty}\right) dy. \tag{2.7}$$

Similarly to the power-law for the boundary layer thickness, the momentum thickness for turbulent flow over a flat plate with a zero pressure gradient can be approximated as:

$$\frac{\theta}{x} \approx \frac{0.016}{Re_x^{1/7}}. \tag{2.8}$$

Shape factor

The shape factor H is defined as the ratio of displacement thickness to momentum thickness. As suggested by its name, this factor is characteristic of the shape of the velocity profile over the boundary layer. Typical values for the shape factor in a laminar boundary layer are $H = 2.59$ (a so-called Blasius boundary layer) and in a turbulent boundary layer $H = 1.2 - 1.4$.

$$H = \frac{\delta^*}{\theta}. \tag{2.9}$$

2.1.3. Dimensionless scales of the boundary layer

In order to compare boundary layer profiles under different flow conditions, it is necessary to use dimensionless scales. The value used for the non-dimensionalisation depends on the region of interest. Close to the wall, an 'inner scaling' is performed; it is common to use an 'outer scaling' farther away.

Since friction forces dominate in the inner region, the 'inner scaling' uses the friction velocity u_τ:

$$u_\tau = \sqrt{\frac{\tau_w}{\rho}}, \tag{2.10}$$

where τ_w is the shear stress at the wall as defined in equation 2.1. With the friction velocity, the non-dimensional flow velocity (u^+) and wall distance (y^+) can be defined:

$$u^+ = \frac{u}{u_\tau}, \tag{2.11}$$

$$y^+ = \frac{y u_\tau}{\nu}, \tag{2.12}$$

Note that the superscript '+' denotes a parameter expressed in viscous or wall units. The definition of a wall unit, also called viscous unit length (δ_v), is given by the following equation:

$$\delta_v = \frac{\nu}{u_\tau}. \tag{2.13}$$

Using the friction velocity and the boundary layer thickness, a friction Reynolds number (Re_τ) can be defined:

$$Re_\tau = \frac{u_\tau \delta}{\nu}. \tag{2.14}$$

The 'outer scaling' uses the free-stream velocity to scale velocities and the boundary layer thickness to scale lengths. An example of the latter is given in the following equation:

$$\eta = \frac{y}{\delta}. \tag{2.15}$$

2.1.4. Regions of the boundary layer

The first distinction that is made when considering the regions of the boundary layer has been implicitly introduced in the previous section when presenting the two types of scaling: the outer layer (where outer scaling is used) and the inner layer (where inner scaling is used). The outer layer comprises the region farther away from the wall. In this region, free-stream conditions are found, and the turbulent forces dominate over the viscous forces. The mathematical model that describes the flow in the outer layer is called the 'defect law', which is given by:

$$\frac{U_\infty - \bar{u}}{u_\tau} = g(\eta, \xi), \tag{2.16}$$

where $\bar{u}$ is the mean velocity and ξ is the pressure gradient parameter, which is defined as:

$$\xi = \frac{\delta}{\tau_w} \frac{\mathrm{d}p_e}{\mathrm{d}x}. \tag{2.17}$$

The inner layer is the region closer to the wall, where the viscous forces dominate over the turbulent (or inertial) forces. This layer can be subdivided into three regions: the viscous sublayer, the buffer layer, and the overlap layer. In the viscous sublayer, the viscous forces dominate the momentum transport, and the flow is nearly two-dimensional since the vertical velocity component is strongly damped. Further, the velocity profile is linear in this region ($u^+ = y^+$). As the distance from the wall increases, the momentum transport by viscous forces is gradually replaced by transport by inertial forces. The buffer layer connects the viscous and the overlap layer; hence this region does not have a linear or logarithmic velocity profile but rather a transition between the two. Finally, the overlap layer is a region of logarithmic velocity profile. This last region of the inner layer 'overlaps' the outer layer, hence its name. The three regions can be summarised in the following manner:

$0 \leq y^+ \leq 5$	Viscous sublayer	$u^+ = y^+$
$5 \leq y^+ \leq 30$	Buffer layer	
$30 \leq y^+ \leq 350$	Overlap layer	$u^+ = \frac{1}{\kappa} \ln y^+ + \beta$

where κ is the von Kármán constant, and β is an adaptive constant in the logarithmic velocity law. Usual values of these two variables are: $\kappa = 0.40 - 0.41$ and $\beta = 5.0 - 5.5$. The inner layer with its three regions is mathematically described by Spalding's law of the wall, which is valid up to $y^+ \approx 350$:

$$y^+ = u^+ + e^{-\kappa\beta}\left[e^{\kappa u^+} - 1 - \kappa u^+ - \frac{(\kappa u^+)^2}{2} - \frac{(\kappa u^+)^3}{6}\right], \tag{2.18}$$

Figure 2.2 shows a graphical representation of Spalding's law of the wall and summarises the regions of a boundary layer with their corresponding mathematical models.

The outer layer and the overlap region can be mathematically represented by Coles' law of the wall. Coles (1956) observed that the deviation in the velocity profiles from the logarithmic velocity profile was shaped as a wake from the viewpoint of the free stream. This observation led to the formulation of the wake function $f(\eta)$, which can be added to the logarithmic law to describe the overlap region and the outer layer:

$$u^+ \approx \frac{1}{\kappa} \ln y^+ + \beta + \frac{2\Pi}{\kappa} f(\eta), \tag{2.19}$$

where Π is the Coles' wake parameter. White (2006) recommends to use this expression to compute u^+ only for $y^+ > 30$. For lower values of y^+, Spalding's law of the wall is preferred (equation 2.18).

2.1.5. Definition of skin friction drag

The shear stress has been previously introduced in a simplified manner for illustrative purposes (see equation 2.1). This section aims at giving a more comprehensive overview of that matter. In a two-dimensional unsteady turbulent flow, the total shear stress is defined as:

$$\tau = -\rho\overline{u'v'} + \mu\frac{du}{dy}. \tag{2.20}$$

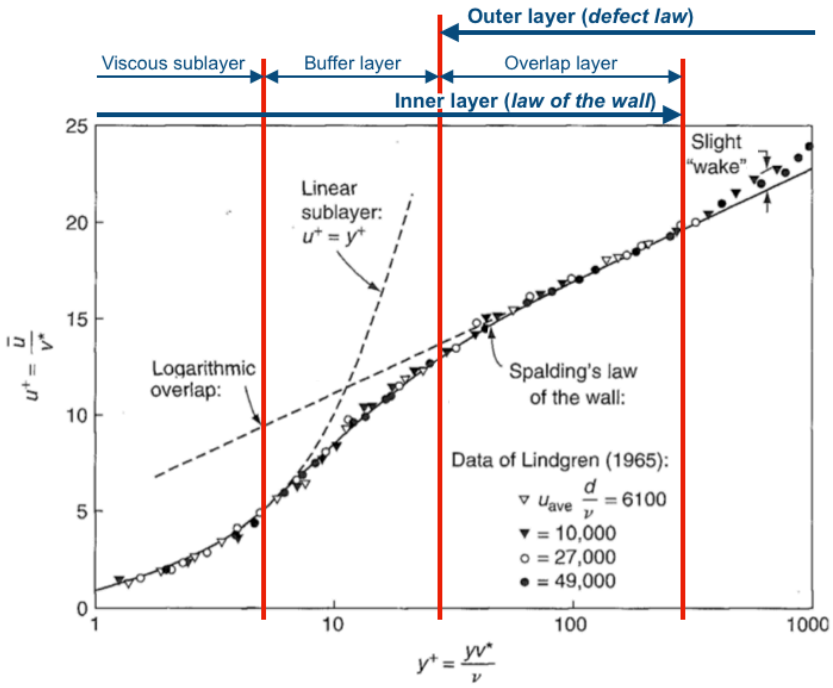

Figure 2.2: Spalding's law of the wall and regions of the boundary layer, adapted from White (2006)

In this definition, two components can be distinguished, namely the Reynolds shear stress ($-\rho\overline{u'v'}$) and the viscous stress ($\mu\frac{du}{dy}$).

A non-slip condition is imposed at the wall in viscous flows, meaning that the fluid velocity and the turbulent fluctuations u' and v' are zero at the wall. Combining this information with the previous equation yields the following expression for the wall shear stress:

$$\tau_w = \mu\left(\frac{\partial u}{\partial y}\right)_{y=0}. \qquad \text{(2.1 revisited)}$$

The wall shear stress can be expressed as a dimensionless quantity by dividing it by the free-stream dynamic pressure. The result is the skin friction coefficient C_f:

$$C_f = \frac{\tau_w}{\frac{1}{2}\rho U_\infty^2}. \qquad (2.21)$$

For the case of a turbulent flow over a flat plate, the power-law gives an expression to approximate the skin friction coefficient:

$$C_f = \frac{0.027}{Re_x^{1/7}}. \qquad (2.22)$$

The friction is indirectly affected by the Reynolds shear stress. In the first instance, a high Reynolds shear stress indicates a higher turbulence level in the flow, thus higher mixing. Moreover, higher mixing leads to a 'fuller' velocity profile or, in other words, a larger velocity gradient at the wall, increasing friction.

The power-law equations presented in this section will be used for approximations and other calculations in the following chapter. If other models or experimental data have been used, it is indicated in the respective chapter.

2.2. Coherent structures in wall-bounded flows

The prevailing idea of turbulence as a stochastic phenomenon of random velocity fluctuations over a certain mean flow changed some decades ago with the observation that quasi-periodic, large-scale vortex motions dominate the transport properties of turbulent shear flows (Gad-el-Hak, 2000). In an almost humorist tone, Hussain (1986) states that 'coherent structures are the embodiment of our desire to find order in apparent disorder', clearly referring to the large uncertainty around the nature of turbulent flow that exists in the scientific community up to this day. The reality is that no general agreement has been reached on the exact definition of coherent structures. Robinson (1991) defines a coherent motion as a 'three-dimensional region of the flow over which at least one fundamental flow variable (e.g. velocity component, density, or temperature) exhibits significant correlation with itself or with another variable over a range of space or time that is significantly larger than the smallest local scales of the flow'. This definition has been chosen by the author because of its general character; for other (more restrictive) definitions, please refer to: Hussain (1986), Fiedler (1987), or Blackwelder (1988).

In this section, coherent structures in free-shear flows will not be discussed. The discussion is restricted to the coherent structures found in wall-bounded turbulent flows. Note that many different viewpoints on this matter are presented in the literature, and some are even contradictory. In the following subsections, some coherent structures deemed relevant for the mechanism of chevron-shaped protrusions and for the later discussion will be explained.

2.2.1. The near-wall cycle

Figure 2.3 shows the 'bursting process' according to Smith (1984). As described in Nieuwstadt et al. (2016), the near-wall cycle starts with the perturbation of a 'low-speed streak' (figure 2.3a). Next, the perturbations grow due to the effect of a Kelvin-Helmholtz instability (figure 2.3b) and, in this process, the vortex sheets around the low-speed streaks roll up into hairpin vortices (figure 2.3c). Finally, the hairpin vortices are stretched until these become unstable and collapse in the form of a burst (figure 2.3d). This short description of the bursting process is an example of a complex phenomenon that can be decomposed into a sequence of defined steps and states using coherent structures. Now, the individual structures will be discussed more in detail following a review by Dennis (2015).

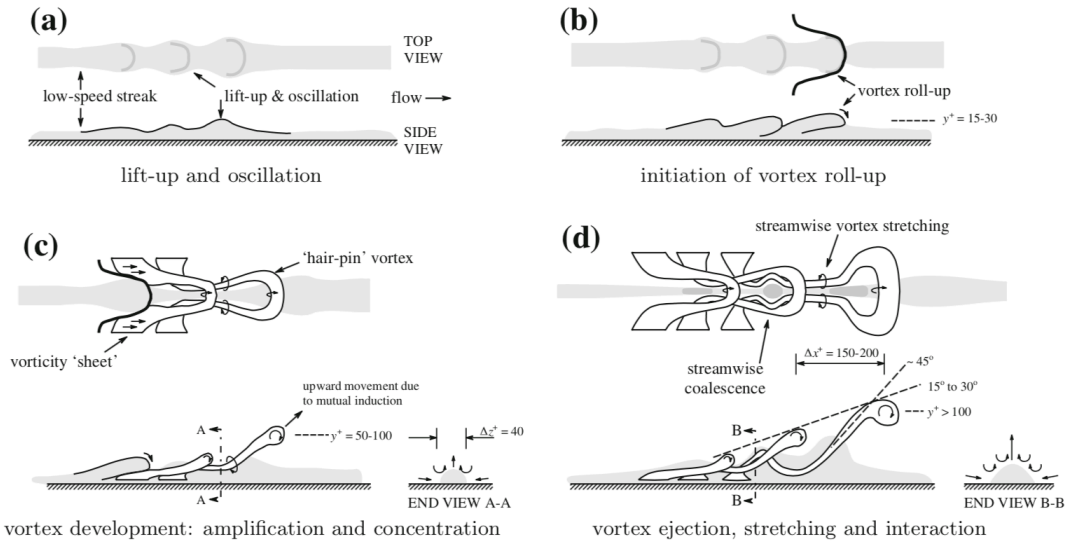

Figure 2.3: Schematic representation of the bursting process, from Nieuwstadt et al. (2016)

Low-speed streaks

One of the earliest observed coherent structures in turbulent flows were low-speed streaks, also known as near-wall streaks (Chernyshenko and Baig, 2005). These are defined as streaks of low-velocity elongated in the streamwise direction and which extend into the logarithmic region (Lagraa et al., 2004). Low-speed streaks are present everywhere in the near-wall region of turbulent flows, as shown in fig-

ure 2.4(a). Although many authors attribute this discovery to Kline et al. (1967), Gad-el-Hak (2000) pointed out that some years earlier, the first visualisations of low-speed streaks by Francis Hama at the University of Maryland were published by Corrsin (1957).

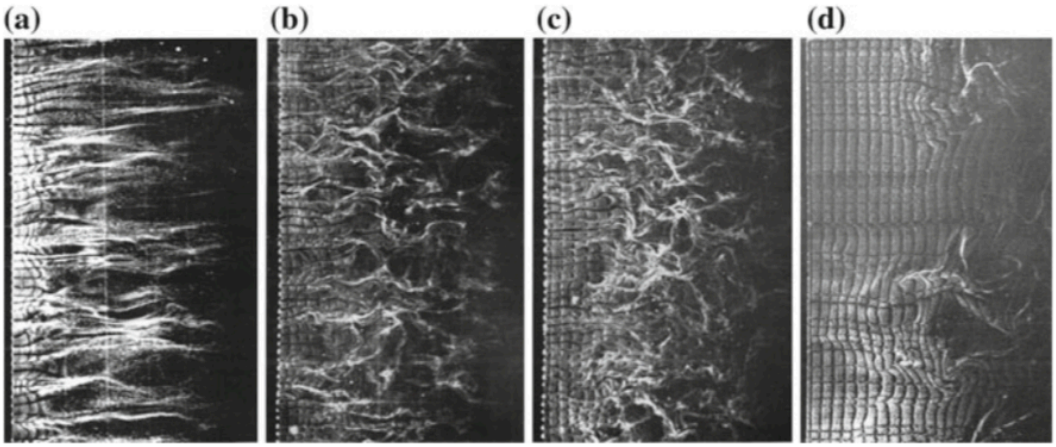

Figure 2.4: Flow visualisation in a turbulent boundary layer using hydrogen bubbles generated from a thin wire parallel to the wall following distances: (a) $y^+ = 2.7$, (b) $y^+ = 38$, (c) $y^+ = 101$, and (d) $y^+ = 407$, from Nieuwstadt et al. (2016)

No academic consensus exists on the formation of low-speed streaks. One possible explanation is that the low-speed streaks are produced due to the quasi-streamwise and spanwise vortices present in the near-wall. These vortices are also responsible for bringing the streaks away from the wall, as will be discussed later. Further 'conceptual frameworks of streak formation' can be found in Chernyshenko and Baig (2005). Regardless of their formation, there is general agreement that low-speed streaks play an essential role in the formation of turbulence; in their absence, a large decrease in turbulence intensity has been observed numerically (Chernyshenko and Baig, 2005).

These regions of low-speed fluid that are oriented in streamwise direction can extend over $1000\delta_v$ with a (spanwise) spacing (l^+) of $100\delta_v$. As explained by Chernyshenko and Baig (2005), these measures correspond to the low-speed streaks directly at the wall; with increasing distance to the wall, the spacing also increases. However, with increasing distance, the streaky structures also become less distinguishable. The researchers compare the spacing versus wall distance obtained from their generalised optimal perturbations (GOP), which is an analytical method to study the streak separation, with results from direct numerical simulations by Hu and Sandham (2001) and with experimental data from Smith and Metzler (1983) at different Reynolds numbers. The results for this comparison are shown in figure 2.5. Note that the spacing from the numerical simulations is obtained from the autocorrelation function, as will be explained in section 2.2.3. The spacing from the experimental data is obtained by measuring the spacing in a series of photographs and is expressed as the mean and the most probable spacing (Chernyshenko and Baig, 2005).

The range of wall distances shown in figure 2.5a has to be clarified to avoid confusion. Low-speed streaks are, as stated earlier, a near wall feature. Spacing values are given for large values of y^+ because the GOP analysis is limited to streaky structures; hence, it is possible to determine their spacing further away from the wall. In the case of DNS and the experimental data, it is not practicable to determine the spacing far from the wall because other structures with shorter longitudinal scales interfere. For this reason, experimental data is only presented in the detailed view shown in 2.5b. A workaround to still obtain the spacing at higher wall distances from the wall from DNS data is to filter out the structures with short longitudinal scales, leaving only the ones with large scales (Chernyshenko and Baig, 2005). As seen in the figure, there is some spread in the spacing values; Chernyshenko and Baig (2005) explain that to their knowledge, no theory can accurately predict the spacing of the near-wall streaks as a function of the wall distance.

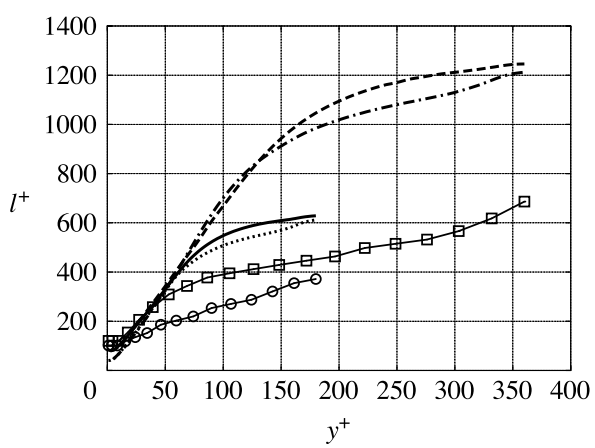

(a) Spacing in the region $0 \leq y^+ \leq 400$; only GOP and DNS data

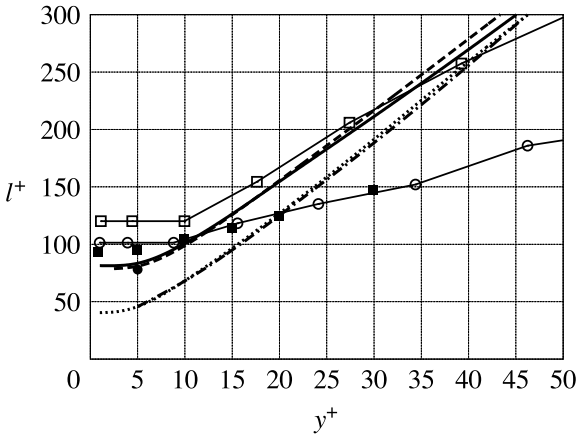

(b) Detailed view of the $0 \leq y^+ \leq 50$ region; GOP, DNS, and experimental data

Figure 2.5: Near-wall streak spacing as a function of wall distance; GOP results: '–' and '· · ·' for $Re = 180$ with different initial conditions, '– – –' and '– · –·' for $Re = 360$ with different initial conditions; Hu and Sandham (2001): white circle for $Re = 180$ and white square for $Re = 360$; Smith and Metzler (1983) at $Re_\theta = 2030$: black square indicates the mean and black circle indicated the most probable value; Re based on channel width and maximal velocity; modified from Chernyshenko and Baig (2005)

Burst, ejection, and sweep events

A related characteristic to the low-speed streak is that of a turbulent *burst*. When a low-speed streak lifts from the wall, it oscillates in the buffer layer and eventually breaks up in the region $10 \leq y^+ \leq 30$; this last event is known as a turbulent burst. The process leading to a burst, namely the rise of the streak away from the wall into the buffer layer, is known as *ejection*. Low-speed fluid from the region near the wall is transported into higher layers in an ejection. In other words, low momentum flow from the wall region is released in higher layers. Consequently, high-speed fluid is transported from higher layers into the wall vicinity in a process known as *sweep*. Both ejections and sweeps have a major contribution to the Reynolds stress, thus being crucial for generating and maintaining turbulence (Dennis, 2015).

Horseshoe/ hairpin and packets

As anticipated in the initial description of the near-wall cycle, horseshoe vortices form as the effect of the vortex sheets around the low-speed streaks rolling up as the low momentum flow is transported into higher layers. This upward movement elongates and pulls the head of the horseshoe vortex further downstream. The vorticity induced by the legs of the horseshoe vortex leads to a higher momentum transfer from low to higher layers, moving the head of the vortex even higher. This cycle continues until the legs detach from the wall and the horseshoe vortex breaks down.

The first description of a horseshoe vortex for wall-bounded turbulence was given by Theodorsen (1955) and is shown in figure 2.6a. Roughly 30 years later, Head and Bandyopadhyay (1981) were the first ones to find the structure of horseshoe vortices experimentally. In their experiments, they also found a dependence of the scales of the vortices on the Reynolds number, which led to the following categorisation of vortices: 'loops' for very low Reynolds numbers, 'horseshoes' for low to medium Reynolds numbers, and 'hairpins' for medium to high Reynolds numbers (figure 2.6b).

Hairpins usually do not exist alone, but in so-called 'packets' as discovered by Adrian et al. (2000). A hairpin packet is a group of hairpins aligned streamwise along an axis inclined away from the wall surface with a 10° to 20° angle. Hairpins usually appear in packets because the legs of an initial hairpin induce momentum transfer at the wall, leading to the creation of a second hairpin upstream of the first one, and so on.

Quasi-streamwise and spanwise vortices

Quasi-streamwise vortices appear in counter-rotating pairs in the wall region between $7 \leq y^+ \leq 70$ and are slightly inclined away from the wall (3° to 7°); this tilt gives these vortices their name. Experiments

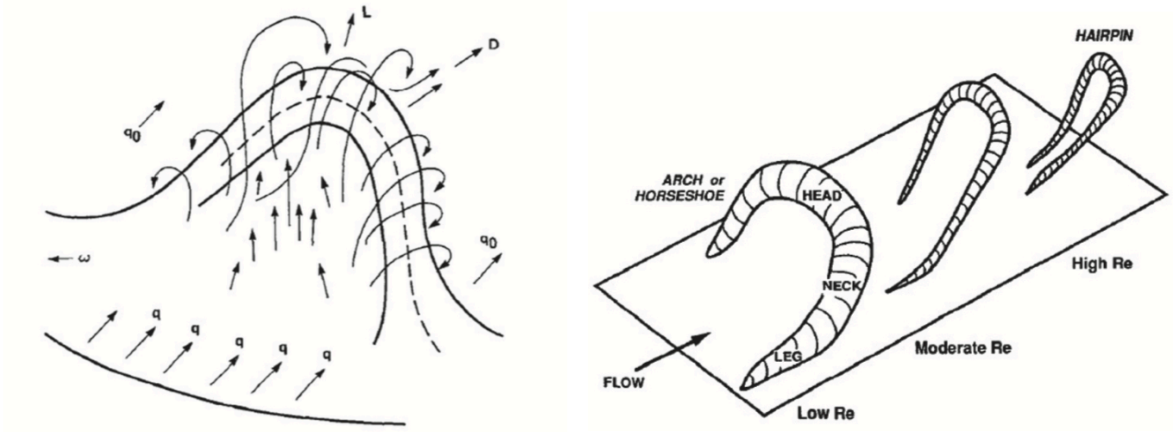

(a) by Theodorsen (1955)

(b) by Head and Bandyopadhyay (1981)

Figure 2.6: Schematic representation of the geometry of a horseshoe/ hairpin vortex

have shown that the most energetic vortices are confined in the region between $14 \leq y^+ \leq 25$. The quasi-streamwise vortices can be seen as the trail left by the hairpin packets. However, as discussed by Dennis (2015), some authors argue that the quasi-streamwise vortices are responsible for the burst, ejection and sweep events that lead to the hairpins in the first place. Although the cause-and-effect relation between quasi-streamwise vortices and the burst, ejection and sweep events is still a matter of discussion, there is general agreement on the important contribution of quasi-streamwise vortices to the Reynolds stress and, hence, to the generation of turbulence.

While quasi-streamwise vortices can be found in the wall region of the boundary layer, spanwise vortices are present in the outer region. These vortices have a streamwise scale of the order of the boundary layer thickness δ.

2.2.2. Very large scale motions

The Very Large Scale Motions (VLSM) are one of the latest discovered coherent structures. These motions are found at a distance from the wall in the overlap layer and lower wake region of the turbulent boundary layer and can extend over a long distance (20δ). Hutchins and Marusic (2007) define VLSM as a 'regime of very long meandering positive and negative streamwise velocity fluctuations', which is illustrated in figure 2.7. The VLSMs have been found to influence the near-wall motions: Ganapathisubramani et al. (2012) showed that the small-scale amplitude increases near the wall and decreases further away from the wall with increasing large-scale amplitude. A frequency modulation effect was also found, although only in the wall's proximity ($y^+ < 100$).

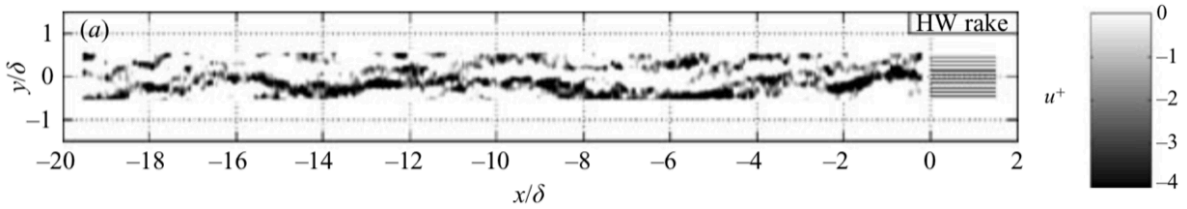

Figure 2.7: VLSM: Example rake signal at $\eta = 0.15$, for $Re_\tau = 14380$, from Hutchins and Marusic (2007). The flow is from left to right. Notice that 'y' denotes the spanwise coordinate in this figure (and not the wall-normal coordinate, as in the rest of this report)

2.2.3. Two-point statistics for low-speed streak analysis

Using two-point statistics to characterise the structures in the flow is a usual technique employed by many researchers (e.g. Lagraa et al., 2004; Hutchins and Marusic, 2007; Hutchins et al., 2011; Sillero et al., 2014). An example of its application has implicitly been presented when discussing the low-speed streaks: the spacing l^+ from direct numerical simulations in figure 2.5 has been derived from an

autocorrelation analysis of the flow for a wall-parallel plane close to the wall.

Lagraa et al. (2004) uses two-point correlations to characterise the low-speed streaks from wall shear stress measurements and velocity measurements employing laser Doppler anemometry. Hutchins et al. (2011) applies two-point statistics to shear-stress data from hot film sensors and velocity data from a hot-wire probe to identify a three-dimensional conditional structure in a turbulent boundary layer. Furthermore, this technique has also been applied to analyse DNS data by, for example, Sillero et al. (2014). These examples show the versatility of two-point statistics: they are actively applied for various purposes using data from different sources.

In this Master thesis, two-point statistics will be applied to instantaneous PIV measurements of the streamwise velocity in a wall-parallel plane (see section 8.2) to characterise the coherent structures present in the flow and, in particular, the low-speed streak spacing. Hutchins and Marusic (2007) make similar use of two-point statistics. In their study, the researchers analyse PIV data of a wall-normal x-y plane to find evidence of VLSM. Please note that 'y' is the spanwise coordinate used by the researchers and corresponds to the 'z' coordinate in this Master thesis. Amongst others, the authors look into the two-point correlation of the velocity fluctuations, which is defined for an x-z velocity plane as:

$$R_{uu}(\Delta x, \Delta z) = \frac{\overline{u(x,z)u(x+\Delta x, z+\Delta z)}}{\overline{u^2}} \tag{2.23}$$

The 2D correlation map corresponding to this two-point correlation is shown in figure 2.8. In this figure, positive contours are represented by solid lines and negative contours are represented by dashed lines.

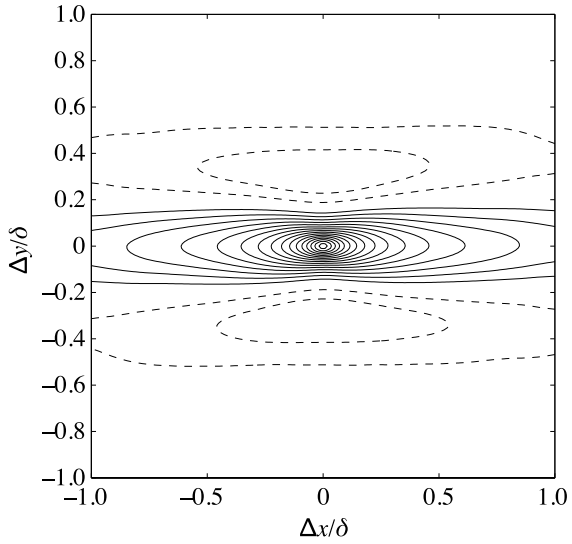

Figure 2.8: Two-point correlation map of the streamwise velocity fluctuation $R_{u,u}$ obtained from PIV data at $\eta = 0.087$; contour levels from $R_{u,u} = -0.12$ to $R_{u,u} = 0.96$ in increments of 0.06; '–' indicates positive values and '––' indicates negative values; from Hutchins and Marusic (2007);

As shown in figure 2.8, an area of positive correlation with a maximum at $\Delta y/\delta = \Delta x/\delta = 0$ is flanked by two regions of negative correlation, indicating that there is some structure in the flow. In the analysis of coherent structures, the spacing between the structures is defined as twice the displacement $\Delta y/\delta$ at which the minimum correlation is achieved (Chernyshenko and Baig, 2005).

In the same paper by Hutchins and Marusic (2007), two-point correlations are performed for hot-wire rake data, yielding the streamwise and spanwise correlations, as shown in 2.9.

In the spanwise two-point correlation plot (figure 2.9(b)), the two valleys of the correlation are clearly visible. The distance between these corresponds to the spanwise spacing between the structures (peak-

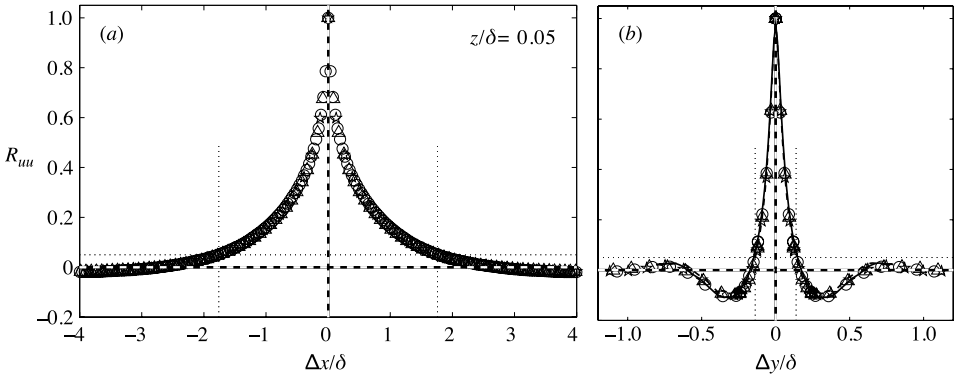

Figure 2.9: Streamwise (a) and spanwise (b) two-point correlations of the streamwise velocity fluctuation R_{uu} obtained from hot-wire rake experiments at $\eta = 0.05$; different markers and lines correspond to different Reynolds numbers; from Hutchins and Marusic (2007)

to-peak distance). Observing the streamwise correlation (figure 2.9(a)), it is clear that the peak-to-peak distance is unsuitable for characterising the streamwise length of the structures since no clear valleys are visible. The missing regions of negative correlation are already an indication of the higher level of disorder (or lower periodicity) in the streamwise direction compared to the spanwise direction. Instead of the peak-to-peak distance, the integral length scale is used for the streamwise length. In this Master thesis, the integral length scale is interpreted in terms of the 0.1 crossing; this means that the streamwise length of the structures is given by the distance between the points where the correlation crosses $R_{uu} = 0.1$. Other interpretations of the integral length scale exist (e.g. Bewley et al., 2012).

The streamwise and spanwise correlations shown in figure 2.9 can also be obtained from figure 2.8 by taking a cut at $\Delta y/\delta = 0$ and $\Delta x/\delta = 0$, respectively. This approach is the one that will be used in this Master thesis. As a last remark, note that an outer scaling has been used in the example discussed here; in applying this technique later in this report, an inner scaling will be used.

3

Chevron-shaped protrusions for skin friction reduction

This chapter provides some background information on the publications available on chevron-shaped protrusions. Note that chevron-shaped protrusions are the final technique to achieve a specific flow manipulation discussed later. In searching for this final technique, the researchers explored many options. While these techniques do not always involve protrusions, they will be addressed in this chapter since they contribute to understanding the intended flow manipulation and set the context for the final technique.

This chapter is structured as follows: first, a brief historical overview will be given (section 3.1). Next, the early work on the principles that would later lead to the development of protrusions will be discussed (section 3.2). Based on these theoretical principles, a series of devices were invented to manipulate the flow, which will be briefly mentioned (section 3.3). The performance and further modifications to the final device (i.e. chevron-shaped protrusions) are examined (section 3.4), followed by a discussion on practical implementations (section 3.5) and some final remarks (section 3.6).

3.1. Historical overview

Some years before protrusions were invented, researchers were already looking into the underlying phenomena targeted by the technique. One of the first publications is the one by Sirovich et al. (1990), in which the researchers studied plane waves and structures in turbulent channel flows. They found obliquely propagating waves of low energy content that were thought to trigger more energetic events such as bursting or sweeping. The existence of these waves was confirmed by Sirovich et al. (1991), and the first attempt to use this discovery for drag reduction was reported by Handler et al. (1993). In the latter, a forcing was introduced to interact with the propagating modes (i.e. the obliquely travelling waves) and to examine the effect of said forcing on the flow. The researchers found a considerable drag reduction. This observation was confirmed by Murakami et al. (1992).

Once the principle had been explored, many inventions appeared trying to exploit the working mechanism to obtain a drag reduction in an experimental setup (Sirovich et al., 1993; Sirovich and Levich, 1993; Sirovich et al., 1994, 1997, 1998a,b,c). Although many apparatuses were proposed, one passive technique involving an array of chevron-shaped protrusions was the most successful one, judging by the fact that it has been the subject of most publications, including the last patent filed.

The inventors of the protrusion array presented their findings in an article in the magazine Nature in which a sustained 10% drag reduction was reported for a protrusion array in a channel flow (Sirovich and Karlsson, 1997).

Bechert (1999) looked into several passive flow control techniques to reduce skin friction, amongst

others the protrusions proposed by Sirovich and Karlsson (1997). In his oil-channel experiments, direct force measurements were performed with surfaces with protrusions, but no skin friction reduction was found.

Later studies, such as Du and Karniadakis (2000) and Du et al. (2002), also looked into the possibilities of suppressing the transverse travelling waves in order to reduce turbulence. In their computational experiments, the researchers considered two techniques: arrays of electro-magnetic tiles in an application in salt water to produce travelling waves and the introduction of spanwise oscillations. In both cases, large drag reductions were reported, although the near-wall structures in both cases looked different: in the case of travelling waves, no wall streaks were present, while these streaks were evident in the case of spanwise oscillations. One possible reason for this different observation is that both techniques triggered a different mechanism: the direct inhibition of rolls and the enhancement of obliquely travelling modes, respectively. Even though this study did not look directly into the technique of protrusions, it does confirm that the underlying mechanisms described in early publications are effective (Handler et al., 1993).

Monti et al. (2001) acknowledged the potential of chevron-shaped protrusions and studied their application in turbulent boundary layers of external flows. Note that this is the first time a channel flow was not used. In several experiments, the researchers confirmed the behaviour described by Sirovich and Karlsson (1997) and reported a drag reduction of up to 30%. However, the protrusions outside of a channel flow presented some problems that made the protrusions only effective over a limited range of Reynolds numbers.

Inspired by the skin structure of sailfish, which is similar to the protrusion arrays proposed by Sirovich and Karlsson (1997), Sagong et al. (2008) performed an experimental study on protrusions of different sizes and arrangements. However, the researchers concluded that no drag reduction was found.

Tugluk and Tarman (2016) performed a numerical study (DNS) on the flow in a circular cylindrical pipe with a Reynolds number based on the bulk velocity (U_b) of $Re_{U_b} = 4900$ to which phase randomisation was applied. With this randomisation, the researchers expected to obstruct the wave-like structures in the wall, impeding the energy transfer between these and the rolls (i.e. low-speed streaks) and, ultimately, reduce drag. The researchers found similar flow characteristics as reported by Handler et al. (1993) and claimed a maximum drag reduction of around 20% using phase randomisation. This value is lower than the 52% maximal drag reduction originally reported by Handler et al. (1993) and more in line with experimental results.

Many publications cite Sirovich and Karlsson (1997), Monti et al. (2001) or Sagong et al. (2008) that do not deal with the technique presented in the mentioned papers, but rather other related skin friction manipulation techniques. Some of the most recent papers look into special developments of riblets (Zhang et al., 2020), surface modifications inspired by other fish species (Zhou et al., 2021), or methods to enhance cooling (Al Zahrani et al., 2020).

3.2. Skin friction reduction working mechanism - Early work

Sirovich et al. (1990) studied the plane waves and structures in a turbulent channel flow using direct simulations and the method of empirical eigenfunctions. Due to computational limitations, Direct Numerical Simulations (DNS) were very constrained at that time. The friction Reynolds number for the simulation was $Re_\tau = 80$, which is very low compared to the friction Reynolds number chosen for later experiments ($750 < Re_\tau < 2000$, Sirovich and Karlsson, 1997) or the one for modern DNS simulations of turbulent boundary layers ($Re_\tau = 360$, Wang et al., 2021). A more extreme example for the current capability of DNS is the simulation of a turbulent channel flow by Lee and Moser (2015) at $Re_\tau = 5200$. Sirovich et al. (1990) acknowledged that the plane channel flow in their simulation had a 'continuous but not fully developed' (Sirovich et al., 1990) turbulence. Furthermore, the spatial resolution of the flow was sacrificed in favour of the temporal resolution, which enabled the observation of the flow at small time increments. Even though the results of this study are not completely representative of a fully developed turbulent channel flow, these lay the foundation for the technology of chevron-shaped protrusions.

Starting from the observation previously described in the literature that secondary instabilities to the Tollmien-Schlichting (TS) waves travel at an angle to the streamwise direction and cause disturbances in the flow, the researchers set to demonstrate that these plane wave modes can be found in turbulent flows and have a crucial role in turbulent wall-bounded flows. For the flow analysis, the authors used the Karhunen-Loève procedure to generate empirical eigenfunctions. This method is also known as proper orthogonal decomposition; descriptions of its use in fluid flows can be found in the literature; some recommendations for this topic are the books by Lumley (1970) and Sirovich et al. (1989). The authors used this method to analyse the plane wave modes and the bursting structures in the presented flow case. They found a set of obliquely propagating plane waves with a relatively low energy content, which they thought could trigger more energetic bursting or sweeping events, hence having an important effect on the local production of turbulence and skin friction drag (Sirovich et al., 1990).

In a following article, Sirovich et al. (1991) focused explicitly on the propagating structures in wall-bounded turbulent flow and performed a similar analysis as the one presented previously to two different flows to test if some universal features could be identified. A larger domain, a finer grid, and a higher Reynolds number ($Re_\tau = 125$) were chosen for the new simulation. Despite the improvements, the simulation is still not comparable to modern DNS of turbulent boundary layers, as discussed previously. In the paper, the researchers found that the roll size corresponding to the most energetic mode had a size of roughly $100\delta_v$, which is in agreement with the low-speed streak spacing introduced in section 2.2.1. From the energy content of the eigenfunctions, the authors also concluded that the most energetic propagating structures move at approximately 70° from the downstream direction, followed by the second most energetic structures at approximately 60°. The modes of these structures seemed to be in resonance with the low-speed streak structures. The only aspect that remained unclear in the paper was why the location of maximal turbulence production (where burst and sweeps are thought to originate) was fixed at $y^+ \approx 14$, while the propagating waves that were thought to trigger these events travel away from $y^+ \approx 14$ with increasing Reynolds number. The authors hypothesise that at higher Reynolds numbers, other mechanisms could start to play a role and conclude that the results presented in the paper could be used to reduce the Reynolds stress or enhance mixing.

Handler et al. (1993) is the first paper co-authored by Sirovich that looked into drag reduction in a turbulent channel flow. This theoretical paper introduced a forcing derived from the randomisation of selected Fourier modes on a plane turbulent flow. The researchers' objective was to identify the temporal and spatial scales relevant for turbulence production and understand how the perturbation of these scales affects turbulence and, ultimately, drag. For this purpose, the authors concentrated on two wave-number bands: first, a subset of the largest length scales and second, the intermediate and smallest wavelengths. Large drag reductions were reported for the former, while a drag increase was found for the latter.

The objective of the introduction of a forcing was to interfere and produce incoherence in the propagating modes, which were found in earlier papers (Sirovich et al., 1990) and were thought to trigger burst and sweep events (Sirovich et al., 1991). For one of the simulated cases, a drag reduction of up to 52% was achieved. While these results can not be interpreted as the values of real drag reductions that could be obtained in a fully developed turbulent flow at typical application Reynolds numbers, they prove the authors' hypothesis and open the door for flow control techniques that target the same modes. In an experimental setup, the proposed forcing could be implemented as acoustic excitation or vibrating ribbons as explained by Handler et al. (1993).

All in all, Handler et al. (1993) show that 'significant drag reductions without affecting the small scale structure of the turbulence' can be obtained. As for the working mechanism that leads to this result, the authors speculate that the coherence of turbulence-producing structures near the wall is destroyed by the introduction of phase randomisation, hindering the mechanism of bursts and sweeps.

Murakami et al. (1992) confirmed the findings presented by Handler et al. (1993) and the underlying theory (Sirovich et al., 1990, 1991). In their research, the authors also performed numerical simulations, with a resolution of 64 elements in each spatial direction and at the low Reynolds number of $Re = 20 - 30$ (note: the reference for the Reynolds number computation is not mentioned in the paper). As discussed previously, the resolution and the Reynolds number are not comparable to the ones in

modern DNS. The research's focus was not on reducing drag but on understanding the effect of small-scale disturbances that preserved energy, enstrophy and helicity spectra on the energy cascade and the coherence of the turbulence. The paper built on a previous publication of some of their authors in which coherence in turbulent flows was discussed extensively; for more information on the topic, please refer to Levich et al. (1991) or the more recent revised version Levich (2009). Murakami et al. (1992) found that the introduction of workless perturbations of certain modes can destroy the coherence in the flow and affect the turbulence decay and hence the energy decay in the flow. One of the possible perturbations is the introduction of random disturbances to the propagating modes, which leads to a reduction in skin friction, as reported by Handler et al. (1993).

3.3. Devices for controlling turbulence

For the method and apparatus for controlling turbulence based on the findings in the previously presented papers, several patents were filed over the years with Orlev Scientific Computing Ltd as the owner of the technology (Sirovich et al., 1993; Sirovich and Levich, 1993; Sirovich et al., 1994, 1997, 1998a,b,c). Many of them have very similar content with only slight differences in wording or aggregated claims. For this reason, not all patents will be reviewed in this document; instead, the primary inventions and claims will be presented.

In the first patent available (Sirovich et al., 1993), the authors present the first concept to modify and manage turbulent flow through the modification of trigger modes. As explained previously, these trigger modes propagate at a certain angle from the free-stream velocity vector: the most energetic ones at an angle of 65°. The largest share of energy from the propagating modes is contained in the range from 50° to 80°. These modes are comparable to the roll modes' wavelength, which carry the energy in the flow. In the nomenclature used in Sirovich et al. (1993) and found in later publications, the main triggering modes are called long-wavelength modes; since these are the modes with the longest wavelengths, all others are called shorter wavelength modes. The counter-rotating roll pair attached to the wall that is targeted by the described invention is shown in figure 3.1(a); note that these roll pairs correspond to the low-speed streaks that were introduced in a previous chapter (see section 2.2.1). The low-speed streaks are also shown in figure 3.1(b) in a plan view of the flow field, together with the herringbone pattern formed by the undulations of the wall that will be discussed later, as well as the directions of the propagating mode, which are also indicated.

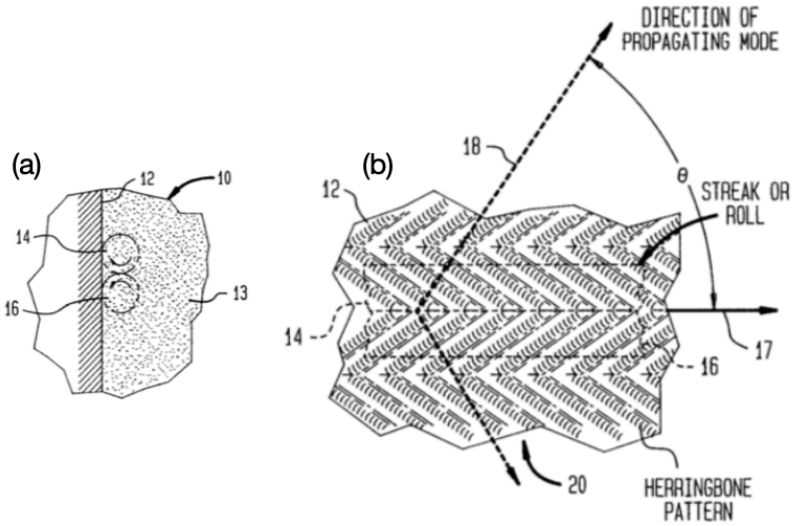

Figure 3.1: Wall cross-section perpendicular to the flow showing a pair of counter-rotating rolls (a) and plan view of the flow field showing a pair of rolls, the direction of propagation of the obliquely travelling waves and the herringbone pattern of the undulations (b), from Sirovich et al. (1993)

In Sirovich et al. (1993), the inventors proposed several passive and active methods to manipulate the flow as indicated previously. Some of these methods are:

- shape modifications (passive),
- flush-mounted wall transducers (active),
- variations in the magnetic or electromagnetic field (active),
- externally mounted sound generator (active),

The list of methods to manipulate the flow was extended in a later patent (Sirovich et al., 1997). The following techniques were added:

- small wires (passive)
- combination of disturbances (active and passive)
- chevron-shaped protrusions (passive), and
- airfoil-shaped protrusions (passive).

For their relevance to this Master thesis, the last two methods will be discussed in more detail.

Chevron-shaped protrusions. These protrusions may be distributed in a linear strip perpendicular to the flow direction or an array of strips (also perpendicular to the flow direction). According to the inventors, using protrusions without combining these with other sources of disturbances is somewhat less effective but can be appropriate in some cases. An observation about this patent (Sirovich et al., 1997) is that the inventors already present the chevron-shaped protrusions as a means of reducing drag. However, they claim to obtain drag reductions with the presented (regular) array arrangement, while they report later that the regular arrangement leads to drag increase and that drag reductions can only be achieved with a randomise array arrangement in Sirovich and Karlsson (1997).

The height of the protrusions is between $12\delta_\nu$ and $15\delta_\nu$, or $\approx$ 0.5 mm for the conditions described in the patent. The nominal angle of the protrusions is 45°. Figure 3.2(b) shows a possible arrangement for the protrusions.

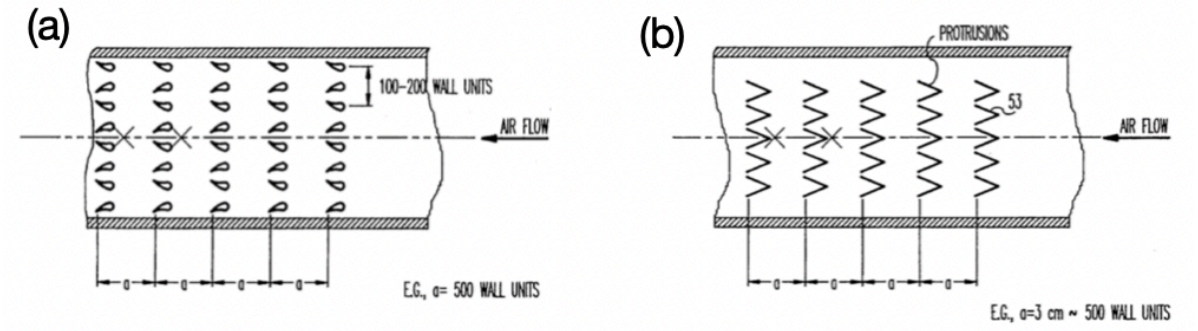

Figure 3.2: Plan view of a wind tunnel test section with an array of airfoil-shaped protrusions (a) and an array of delta-shaped protrusions (b), from Sirovich et al. (1997)

Airfoil-shaped protrusions. These protrusions can be arranged in the same manner as the chevron-shaped ones, namely as a single strip or as an array. As shown in figure 3.2(a), the airfoils are mounted in counter-lifting pairs so that the tip vortices of a pair produce a pair of counter-rotating rolls. In order to produce roll pairs similar to the natural ones, the airfoil pairs should be mounted at a distance of $100\delta_\nu$ to $200\delta_\nu$.

The protrusions as discussed in Sirovich and Karlsson (1997) appear in Sirovich et al. (1998b) (and some months earlier in the European patent Sirovich et al., 1998c). In this patent, the inventors aim to provide a simplified means of introducing a disturbance into the flow that uses a passive mechanism and does not require combining two methods. The mechanism proposed had a fundamental differ-

ence from the previous ones: while the mechanism discussed so far targeted the so-called triggering modes, which were thought to interact with the roll modes and avoid bursting and sweep events, the new mechanism creates a disturbance that either enhances or inhibits directly the creation of rolls and, hence, the turbulence in the flow. The two options, namely enhancement and inhibition, correspond to the two applications of this method: drag reduction and drag increase (i.e. increased mixing); the following discussion will focus on the former.

A wall portion containing the protrusions proposed in the invention is shown in figure 3.3 along with a cross-sectional view of the same wall taken along the line labelled as *6*. In this figure, the dimension a stands for the pitch of the protrusions in the flow direction and is in the range of $200\delta_\nu - 400\delta_\nu$. b indicates the length of the protrusion in flow direction, which is approximately $150\delta_\nu - 250\delta_\nu$. The width of the protrusion elements or their length perpendicular to the flow is given by c. d indicates the pitch of the elements in the direction perpendicular to the flow, which typically ranges between $200\delta_\nu - 300\delta_\nu$. The offset in the alignment between the protrusion elements of one row and the next one is denoted by e, an offset $e = 0$ corresponds to two rows aligned in the flow direction. The height of the protrusions is given by f and ranges between $5\delta_\nu - 15\delta_\nu$. The apex of the protrusions points toward the flow, and the apex angle (α) is in the range 20°– 90°. The typical design ranges just mentioned are summarised in table 3.1. This table also contains the values in mm for six different designs that the researchers tested; design 2 (D2) resulted in drag reductions, while designs 3 to 7 (D3 – D7) yielded a drag increase. Design 2 was tested with a constant offset e and with a random offset; in this last scenario, the value indicated in table 3.1 indicates the average offset. Although figure 3.3 shows the sides of the protrusions as straight lines (i.e. the legs of the 'vees'), the inventors indicate that these can also be curved in a concave or convex manner. Besides randomising the offset between rows (e), the height of the protrusions (f), the 'vee'-shapes of the pattern and the position of the protrusion elements in a row (i.e. the position of an element relative to the row centerline elements) can be randomised. As a final remark on the geometry, the inventors noted that modifications in the scales indicated may be required, for example, in the case of a growing turbulent boundary layer; for these scenarios 'scale sizes change slowing as the 1/10 power of the streamwise distance' (Sirovich et al., 1998b).

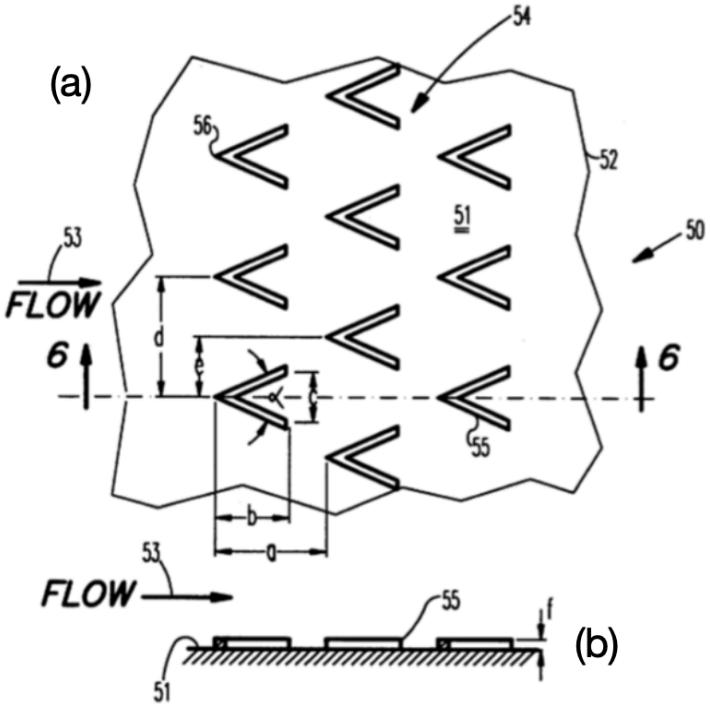

Figure 3.3: Protrusion pattern for flow modification according to the patent, from Sirovich et al. (1998b)

The designs in table 3.1 were tested in a channel flow in a close-return low-speed facility. The channel was 8.5 m long, 750 mm wide and 55 mm high. The settling chamber placed upstream of the channel

Dimension	D2	D3	D4	D5	D6	D7	Design range
			[mm]				$[\delta_\nu]$ or [°]
a	13.9	36.5	31.3	10	10.1	18.3	200 – 400 $[\delta_\nu]$
b	10	15	10	15	7.3	7.3	150 – 250 $[\delta_\nu]$
c	9.1	12.5	7.7	12.5	6.6	6.6	–
d	13.5	19.7	10.5	19.7	9.8	9.8	200 – 300 $[\delta_\nu]$
e	6.75	0	0	0	0	0	–
f	0.25	0.25	0.25	0.25	0.25	0.25	5 – 15 $[\delta_\nu]$
α	–	–	–	–	–	–	20 – 90 [°]

Table 3.1: Dimensions of the protrusions for different designs D2 – D7 and typical design range, adapted from Sirovich et al. (1998b)

had a length of 1.5 m. The protrusion elements were only applied to the channel floor; the walls and the ceiling were kept smooth. The researchers performed the experiments at a centerline velocity of 6 – 10 m/s, corresponding to a Reynolds number of 10800 – 18000. For reference, a wall unit $\delta_\nu = 50$ μm at 7 m/s. The test results for design 2 (D2) with a random offset are shown in table 3.2 for several velocities. The drag reduction obtained with the previously mentioned configuration and design ranged from 6.5% to 13.5%, which is comparable with the results reported in Sirovich and Karlsson (1997).

U_∞ [m/s]	Drag change [%]
5.86	-9.95
7.03	-13.5
8.39	-8.1
9.48	-6.7
10.05	-6.5

Table 3.2: Drag change with design 2 (D2) and random offset for the protrusions, adapted from Sirovich et al. (1998b)

As mentioned previously, this same method can be used to increase drag (i.e. enhance mixing) when the offset is chosen to be 0 ($e = 0$). The results for two drag-increasing designs (D3 and D4) are shown in table 3.3 for three different velocities. The obtained drag increase ranges from 41.2% to 47%, showing that this method can be very effective for mixing.

U_∞ [m/s]	6	7	8	
Drag change [%]	42.5	45	47	D3
	41.2	42.7	43.5	D4

Table 3.3: Drag change with design 3 and 4 (D3 and D4) for three free-stream velocities, adapted from Sirovich et al. (1998b)

According to the inventors, the results for both drag reduction and enhanced mixing could be greatly improved by applying the protrusion pattern to the remaining surfaces of the channel (i.e. wall and ceiling), resulting in more than double the reported drag change (see table 3.2 and 3.3).

According to the inventors, the same flow modification can be obtained by cavities instead of protrusions. In this case, all dimensions indicated above are applied to the cavities, where the protrusions' height corresponds to the cavity's depth. The inventors mention that protrusions are the preferred method; however, no measurement results or one-to-one comparison between protrusions and cavities is provided. Such data was also not found in other publications and is a research gap that will be addressed in this Master thesis.

3.4. Skin friction reduction performance

The first publication that details the drag performance of the protrusions is the one by Sirovich and Karlsson (1997) in Nature. In this paper, the authors report the results of a wind tunnel test campaign

involving the use of protrusion elements. The experimental facility was a channel 56.3 mm high, 750 mm wide and 8.5 m long. A plan view of this channel can be seen in figure 3.4a. The initial black area represents the settling chamber, followed by a rough surface to force transition (squared area). The hatched area is the test section covered with flow manipulators, and the black dots on top show the pressure tabs' location. The black dot marked as **B** indicates the position of the hot wire probe for wall-normal and transverse velocity measurements. The flow in this channel was in the fully developed turbulent regime with a Reynolds number range based on the centerline velocity of $15000 < Re_h < 40000$ (equation 3.1). Using the friction velocity and the boundary layer thickness as introduced in section 2.1, the friction Reynolds number for the experiments is $750 < Re_\tau < 2000$.

$$Re_h = \frac{U_\infty h}{\nu} \tag{3.1}$$

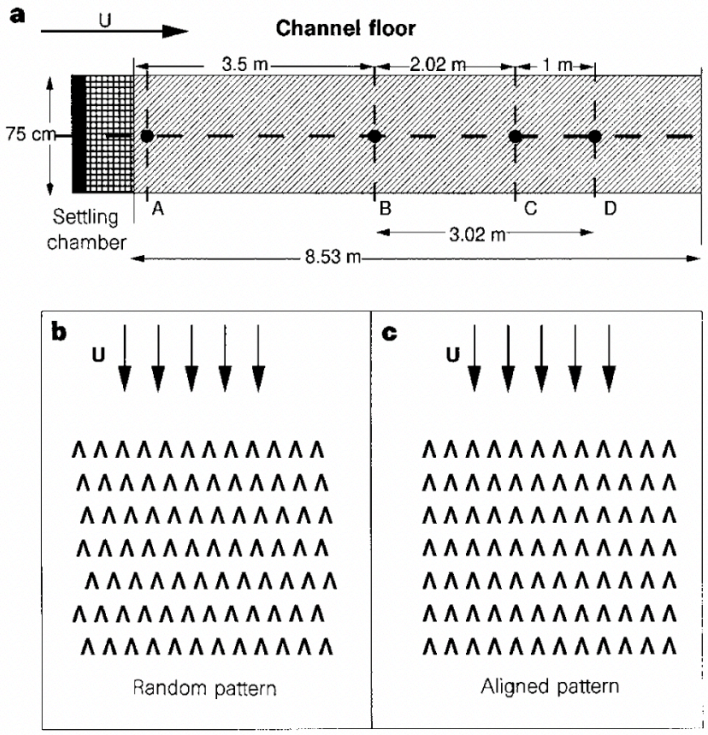

Figure 3.4: Plan view of the channel used for the experiments (a), random protrusion pattern (b), and aligned protrusion pattern (c), from Sirovich and Karlsson (1997)

The authors (Sirovich and Karlsson, 1997) explain the origin of skin friction in the flow: the low-speed streaks (in the paper called rolls) appear in counter-rotating pairs close to the wall. Their role can be interpreted as an inverse cascade; namely, they take small-scale turbulence and bring it to larger scales. Through a series of bursts and sweep events discussed in section 2.2.1, the rolls separate from the wall leading to mixing in the flow (i.e. slow-moving flow from the inner region is transported away from the wall and fast-moving flow from the outer region is transported to the inner region). This event is relatively infrequent and only occurs 20% of the time; however, it accounts for 80% of the skin friction of the wall (Sirovich et al., 1998b). One way to avoid this event is to maintain the coherence of the rolls by restraining their movement, as done with riblets. Another way is to introduce disturbances into the flow to excite specific propagating modes according to Sirovich et al. (1990), Sirovich et al. (1991), and Handler et al. (1993). The authors choose the latter for their experiments.

Sirovich and Karlsson (1997) performed experiments with three configurations: a smooth wall that serves as a baseline when speaking about drag increase and reduction, a wall with a random protrusion pattern (figure 3.4b), and a wall with an aligned protrusion pattern (figure 3.4c). In all cases, the protrusions had a width (in transverse direction) of $200\delta_\nu$, a period of $260\delta_\nu$ inside a row, a period

between rows of $300\delta_v$, and a height of $5\delta_v - 6\delta_v$. According to the researchers, the random protrusion pattern was chosen to have the largest possible effect on the rolls to prevent their formation or destroy them. The geometry definition that the researchers provide is not comprehensive and leaves dimensions such as the apex angle, the length of the protrusions (in the streamwise direction), or the chevron leg thickness undefined. Although the missing dimensions can be estimated from other publications, the missing values are problematic for replicating the results presented by Sirovich and Karlsson (1997).

The results for the measurements by Sirovich and Karlsson (1997) are displayed in figure 3.5 in terms of skin friction coefficient versus Reynolds number Re_h. The results are based on the pressure drop between the locations **B** and **D**. A power law has been fitted to each set of measurements. With respect to the smooth wall, the results for the randomly shifted protrusion pattern present an approximately 10% drag reduction; in one of the three independent experimental runs with a random protrusion pattern ('+', '*', and '×'), this reduction is even larger reaching 12.5%. The researchers explain these results with the delayed time until final energy loss through dissipation due to the inhibition of rolls. The opposite effect is achieved when the protrusion pattern is aligned: in this case, the rolls are enhanced (i.e. more energy is added to the roll modes), and the skin friction increases notably; for the experiments, the measured increase amounts to 20% with respect to the smooth wall.

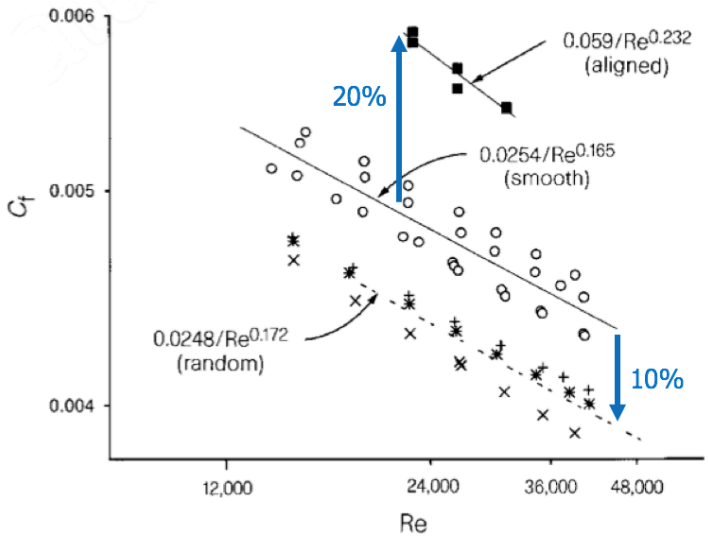

Figure 3.5: Friction coefficient C_f against Reynolds number for a smooth channel floor, a random protrusion pattern, and an aligned pattern, adapted from Sirovich and Karlsson (1997)

The Reynolds number regime of the experiments was compared to the one in the publication by Schoppa and Hussain (1998) to increase the confidence in the results reported by Sirovich and Karlsson (1997). Schoppa and Hussain (1998) is a known example of an allegedly large drag reduction that was found to be limited to very low Reynolds numbers. The experiments by Sirovich and Karlsson (1997) were performed at $15000 < Re_h < 40000$ while Schoppa and Hussain (1998) performed theirs at $3600 < Re_h < 6400$. Hence, the tests with the protrusions were performed at considerably higher Reynolds numbers (×4 - ×6). Also the friction Reynolds number in the experiments with protrusions ($750 < Re_\tau < 2000$) were considerably larger than in the simulations of large-scale streamwise vortices ($Re_\tau = 104$, from Canton et al. (2016)). This check is not a conclusive comparison to show that the results by Sirovich and Karlsson (1997) are universally applicable to high Reynolds numbers but rather an initial assessment to be sure that the measured effect is not limited to low Reynolds numbers. This check is also considered relevant because the simulations provided in the papers that lay the theoretical foundation for this technology use a very low Reynolds number.

Although Sirovich and Karlsson (1997) are very confident in their results and the drag reduction potential of the protrusion pattern, they acknowledge that many configurations remain to be studied, such as patterns with different apex angles or protrusion heights. Only one study was found where a parametric study was performed (Sagong et al., 2008); however, none of the studies reviewed presents the drag reduction potential for different geometrical choices systematically. A possible reason for this knowledge

gap might be the difficulty in manufacturing the required large number of configurations; this research gap will be addressed in this Master thesis.

Some years later, Monti et al. (2001) acknowledged the potential of the 3D V shapes technology (i.e. chevron-shaped protrusions) and performed some tests closer to the industrial application of the method. For this purpose, the experiments were conducted in an equilibrium turbulent boundary layer with a slightly favourable pressure gradient. The researchers planned five test series using the protrusion technology:

- shear stress measurements at several streamwise positions without manipulators as a baseline for later comparison between smooth boundaries and protrusions, the shear stresses were deduced from measured velocity profiles;
- shear stress measurement at several streamwise positions with protrusion elements installed;
- shear stress measurements from the velocity profiles at the inlet and outlet of the test section with protrusion elements installed in reverse direction (i.e. the apex of the protrusions pointing downstream);
- rough turbulent power spectra at selected positions with and without protrusions; and
- velocity profiles in conditions of flow reattachment (Monti et al., 2001).

The protrusion elements used by the researchers were very similar to the ones used by Sirovich and Karlsson (1997). A sketch of these elements and their arrangement is shown in figure 3.6b, and the exact dimensions used for the experiments can be seen in figure 3.4. The column 'Dimension in patent nomenclature' references the parameter names used in the patents to allow for easy comparison. Please note that the dimension 'a' in the table (i.e. inner axis direction x) does not correspond to the parameter 'a' in figure 3.6b (i.e. distance from the wall to the apex of the first protrusion). For the dimensions of the protrusions, the researchers assumed a statistically steady boundary layer with a friction coefficient $c_f = 0.0020 - 0.0025$, corresponding to 10 m/s asymptotic velocity. The test plate was manufactured by electroerosion of three aluminium alloy plates of 0.3×0.3 m, which were connected to form the final plate of 0.9×0.3 m (see figure 3.6a). The aluminium plates were used as a mould for the epoxy resin to manufacture longer models.

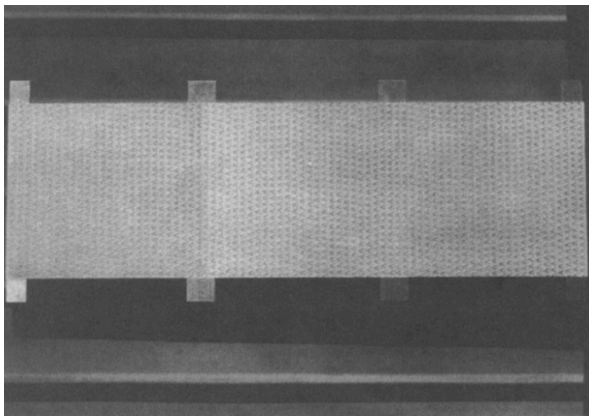

(a) Aluminium test plate used for wind tunnel testing

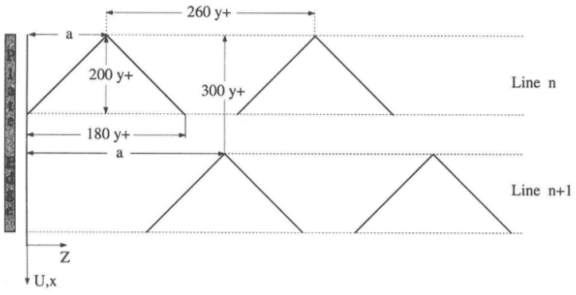

(b) Dimensions of the protrusion element array

Figure 3.6: Test plate and protrusion element arrangement, from Monti et al. (2001)

While the distance between protrusions in one row was chosen to be constant, there is a shift between the individual rows in the z-direction. This shift was chosen according to a Gaussian distribution; the corresponding probability density function is shown in figure 3.7.

The original test facility chosen by Monti et al. (2001) for the wind tunnel experiments with a test section dimension of 0.3 m width, 0.1 m height and 1.5 m length was found to be too small, and a new one had to be built. The new test section had the same width (0.3 m) but was higher (0.4 m) and longer (6 m).

Dimension	Dimension in patent* nomenclature	Size in wall units [δ_ν]	Size in [mm] or [°]
Transverse direction z	d	260	12.73 [mm]
Inter axis direction x	a	300	11.03 [mm]
Thickness	f	5	0.21 [mm]
V Triangle base	c	180	7.64 [mm]
V Triangle high	b	200	8.48 [mm]
Apex angle	α	–	60 [°]

Table 3.4: Design parameters of the protrusion elements; * nomenclature from (Sirovich et al., 1998b); adapted from Monti et al. (2001)

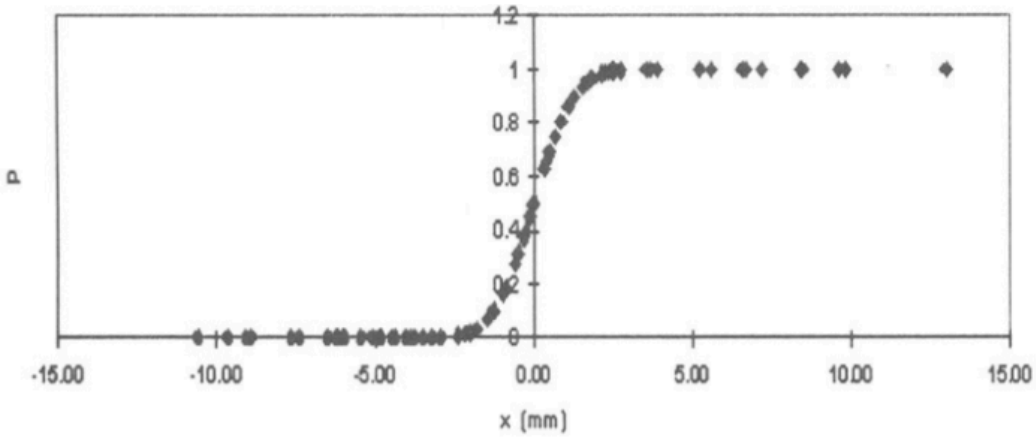

Figure 3.7: Probability density function of the shift in protrusion rows, from Monti et al. (2001)

The researchers hypothesised that the protrusion elements require a long test section to have a notable effect. The longitudinal pressure gradient was measured utilising pressure tabs located along the test section and the velocity using a total pressure probe and wall pressure tabs. The longitudinal pressure gradient was found to be negative, which can be explained by the effect of buoyancy (Glauert, 1933). An element was inserted into the wind tunnel to produce a strong local contraction followed by a flow deceleration for the measurements under a strong adverse pressure gradient.

For the evaluation of the skin friction, Monti et al. (2001) chose the von Kármán integral equation because they suspected that the law of the wall might be unreliable for a wall with protrusion elements. Errors introduced by this method (e.g. flow convergence) were considered unproblematic because the baseline measurements with the smooth surface were performed in the same manner. The authors mention that a skin friction balance was not used due to 'technical reasons' (Monti et al., 2001).

The results obtained by Monti et al. (2001) are shown in figure 3.8. In this figure, the authors plotted the skin friction coefficient versus the momentum thickness Reynolds number, which is defined as:

$$Re_\theta = \frac{U_\infty \theta}{\nu} \tag{3.2}$$

In the same figure, it can be seen that a large drag reduction is obtained over a certain range of Reynolds numbers. The integration distance has an important effect on the obtained result, as shown in figure 3.9. The researchers claimed that the most critical difference to the channel flow studied in earlier publications (e.g. Sirovich and Karlsson, 1997) is the relation between the streamwise length and the Reynolds number at which a skin friction reduction is obtained. Their hypothesis for this observation was that the boundary layer thickness develops in boundary layer flow, as opposed to the streamwise constant properties of a fully developed channel flow.

As introduced previously, one of the tests planned by the researchers consisted in inverting the direction of the protrusion elements (i.e. the apex of the element point downstream); the results of this

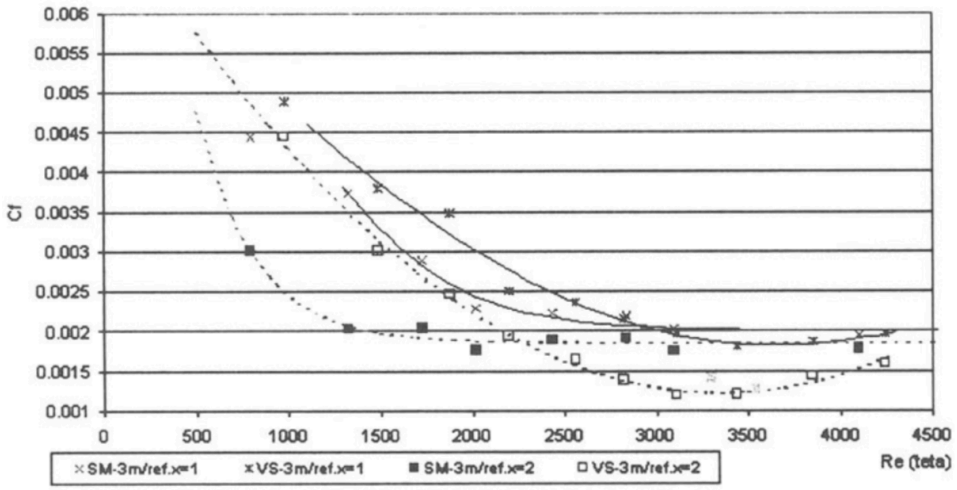

Figure 3.8: Skin friction coefficient c_f versus momentum thickness Reynolds number Re_θ at $x = 3$ m from the inlet for a test plate with protrusions (VS) and a smooth one (SM) from the von Kármán equation integrated over a distance of 1 m and 2 m, from Monti et al. (2001)

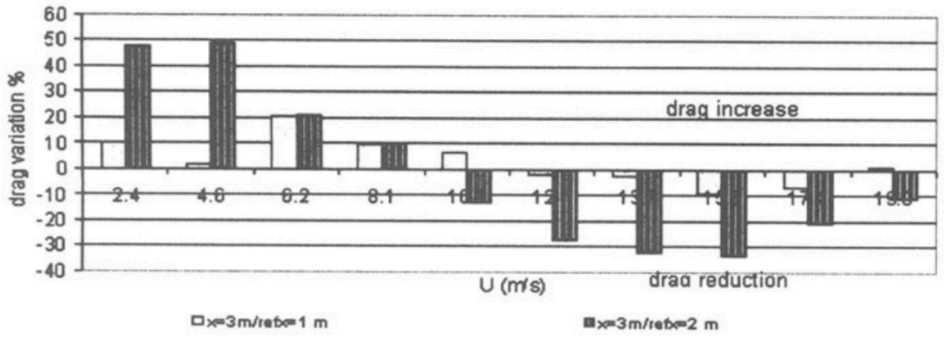

Figure 3.9: Drag change between the smooth plate and the plate with protrusion elements at a distance $x = 3$ m from the inlet for the two integration distances 1 m and 2 m, from Monti et al. (2001)

experiment are shown in figure 3.10. The drag increase obtained from this test serves as proof for the researchers to conclude that the effect observed from the protrusion elements is not a mere roughness effect (Monti et al., 2001).

A further test with an adverse pressure gradient was attempted by Monti et al. (2001); however, the walls had a substantial effect, and thus, the test was not possible without a redesigned wind tunnel with a much wider test section. Nevertheless, the researchers found the preliminary result that protrusion elements moderately anticipate separation based on the initial test. While this result agrees with their expectation, the authors stress that this is not a definite answer.

All in all, the authors concluded that the theoretical principles on which the protrusions are based are correct, although some doubt on the validity of the methodology used by Sirovich and Karlsson (1997) remains. Furthermore, they reaffirm the difference between the application in a duct and a turbulent boundary layer flow. In their view, the dependence of the mechanism of turbulent energy exchange by protrusions on some external parameter has to be determined in order to be incorporated into the design of protrusions in turbulent boundary layer conditions (Monti et al., 2001).

Some years later, Sagong et al. (2008) observed that the sailfish had delta-shaped protrusions on the skin of similar shape and dimensions as the protrusions proposed by Sirovich and Karlsson (1997). A fundamental difference between the sailfish protrusions and those proposed in the literature is the orientation: the protrusions on the sailfish are pointing downstream, i.e. opposite to the ones by Sirovich and Karlsson (1997). Please note that one of the test series by Monti et al. (2001) also involved pro-

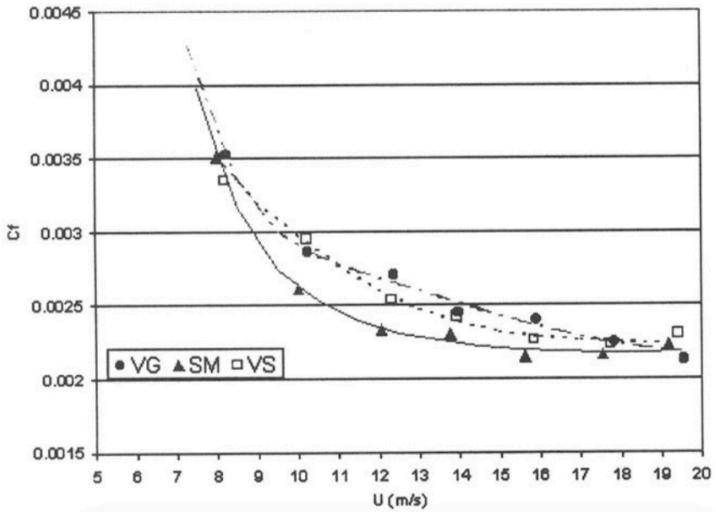

Figure 3.10: Skin friction coefficient c_f versus centerline velocity U from the von Kármán equation integrated between x = 1 m and x = 5 m for a smooth plate (SM), a plate with protrusion elements (VS) and a plate with protrusion elements oriented in reverse direction (VG); from Monti et al. (2001)

trusions with opposite orientation; as mentioned earlier, no drag reduction was found for this configuration by Monti et al. (2001). Due to the similarity between the geometry found in nature and the one investigated by several researchers, Sagong et al. (2008) decided to explore the sailfish protrusions through an experimental campaign and DNS.

The protrusion-like skin structure of the sailfish is shown in figure 1.1. In their experiments, Sagong et al. (2008) chose initially a spanwise width of $W = 1.8$ mm, a streamwise length of $L = 4.7$ mm and a protrusion height of the order of 0.1 mm. The ratio W/L was fixed at 0.383 and the angle α at 53° (please note that α does not refer to the apex angle in this context but to the dimension shown in figure 3.11). The protrusions were arranged in three different configurations: parallel, staggered, and random. A total of 170 configurations were tested, where width (W), height (H), streamwise spacing (S_x), spanwise spacing (S_z) and the protrusion arrangement were varied. The experimental facility had a 2 m long test section with a wind tunnel entrance size of 0.3 × 0.4 m (slightly larger in the exit to achieve a zero pressure gradient). The dimension of the test plates was 598 × 298 mm. No information about their material or manufacturing technique is provided. The measurements were carried out at a free-stream velocity between 15 – 30 m/s, corresponding to a momentum thickness Reynolds number of $Re_\theta = 4400 - 8300$. For comparison, the Re_θ at which skin friction reduction was achieved in the study by Monti et al. (2001) was $Re_\theta = 2000 - 4500$ (see figure 3.8). The drag force was measured by a direct balance measurement system validated with known smooth and riblet surfaces. A drag increase or a negligible drag reduction was found for all considered cases. The authors considered that this might be the result of an inaccurate representation of the sailfish skin; i.e. the sailfish protrusions are blended into the skin and have no sharp edges as opposed to the ones used for the experimental and numerical simulations; however, these were not replicated due to manufacturing limitations.

In a second experimental campaign, Sagong et al. (2008) tested the protrusions with the orientations proposed by Sirovich and Karlsson (1997). For this purpose, the researchers use the geometries indicated in Sirovich and Karlsson (1997) and Sirovich et al. (1998b), a summary of these dimensions is shown in figure 3.12. For the only dimension that was not provided, namely the thickness of the 'vee'-leg, the authors tested three sizes: $t^+ = 20$, 30, and 40.

In all experiments, the drag was increased or negligibly decreased. Numerical simulations confirmed these results and showed that for the staggered and random protrusion arrangements, skin friction was indeed reduced due to the interaction of the generated vortex pairs (3% reduction for the staggered arrangement). However, in these cases, the increased form drag due to the presence of the protrusions led to a net drag increase of 5%. In the case of parallel protrusions, the skin friction is increased by 3%.

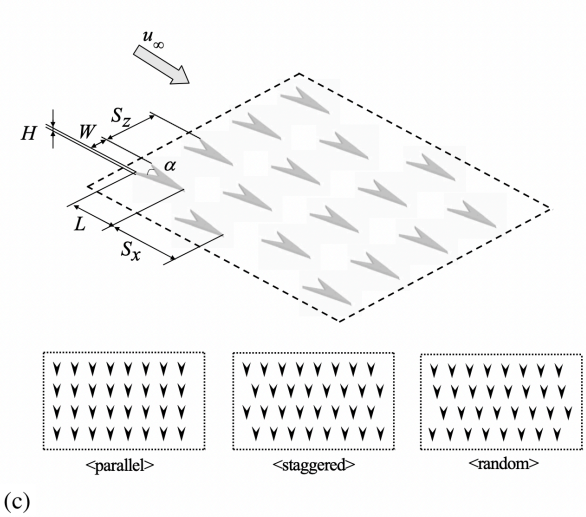

Figure 3.11: Schematic of the sailing fish protrusion pattern, from Sagong et al. (2008)

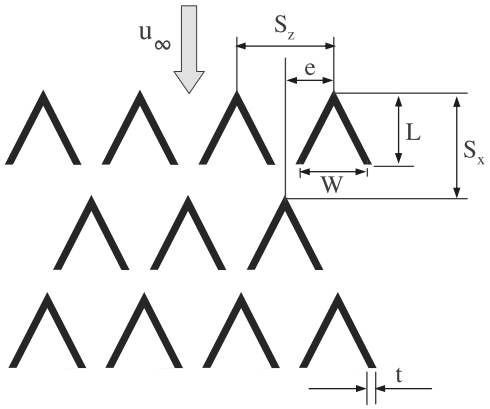

	Sirovich and Karlsson	Sirovich et *al.*
W^+	200	182
L^+	-	200
H^+	5 ~ 6	5
S_z^+	260	270
S_x^+	300	278
e^+	130	135

Figure 3.12: Schematic of a chevron-shaped protrusion pattern with the dimensions used by Sirovich and Karlsson (1997) (left values) and Sirovich et al. (1998b) (right values)], modified from Sagong et al. (2008)

These low values are attributed to the weak stream vortices due to the low height of the protrusions (i.e. $5\delta_v$). The left column in figure 3.13 shows the vortex pairs generated by the protrusions, which rotate opposite to the ones generated in the case of sailfish protrusions (opposite orientation); this rotation leads to an increased skin friction in the middle and a reduced one in the sides of the elements (right column in figure 3.13).

The drag reduction values obtained with chevron-shaped protrusions in the different studies which have been reviewed are summarised in table 3.5. This table also contains information such as the type of study and flow, the test range reported in the respective source, and a comment on the technique used to determine the drag reduction, if available.

3.5. Practical implementation

Besides the previously described experimental test, no other applications were found in the literature. Furthermore, no industrial application of this technology was attempted, or at least no industrial attempt was documented and published, despite the promising results reported in some papers and patents.

This section will discuss the practical aspects of the protrusion technology that must be considered when implementing this technique. A limiting factor for protrusions in a turbulent boundary layer

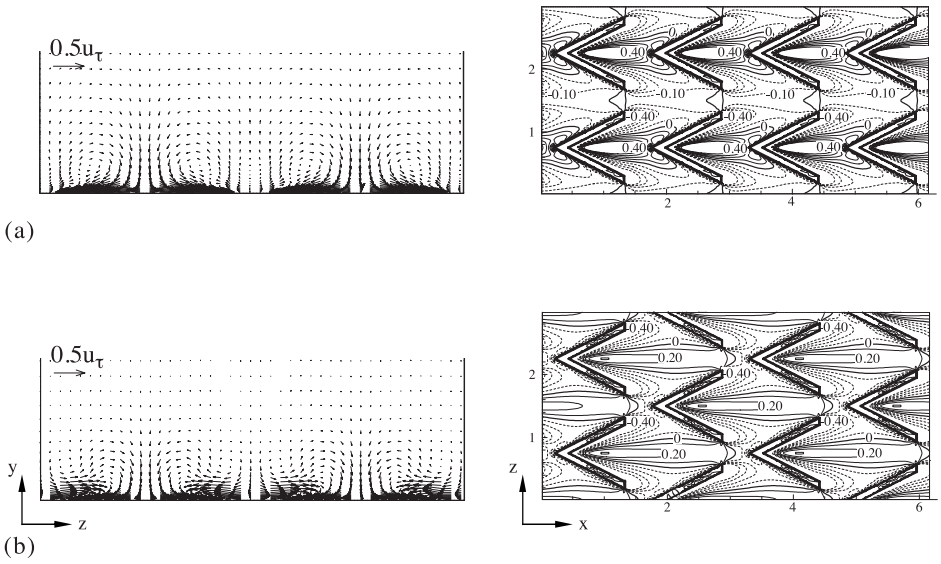

Figure 3.13: Results from DNS for the chevron-shaped protrusions in a parallel (a) and a staggered (b) arrangement; the left column shows the mean cross-flow vector (v, w) in a cross-section at the (streamwise) middle of the protrusions; the right column shows a plan view of the wall with the contours of mean shear-stress variation; from Sagong et al. (2008)

Study	Type	DR	Test range	Comments
Sirovich et al. (1998b)	experimental, channel flow	13.5%	$Re = 12600$ (7 m/s)	–
Sirovich and Karlsson (1997)	experimental, channel flow	10%	$750 < Re_\tau < 2000$	Drag from pressure drop
Monti et al. (2001)	experimental, external flow	30%	$2000 < Re_\theta < 4500$ (10 – 19 m/s)	Drag from von Kármán integral relation
Sagong et al. (2008)	experimental, external flow	≈ 0%	$4400 < Re_\theta < 8300$ (15 – 30 m/s)	Drag from balance
Sagong et al. (2008)	numerical, external flow	−5%	$4400 < Re_\theta < 8300$ (15 – 30 m/s)	–

Table 3.5: Overview of drag reduction (DR) with chevron-shaped protrusions in different studies; note that a negative DR corresponds to a drag increase

application is the range of Reynolds numbers over which a drag reduction is achieved. This behaviour is likely due to the change in boundary layer thickness with increasing distance, which is not observed in a fully developed turbulent channel flow (Monti et al., 2001). Variable scales for the protrusion geometry could be considered to counteract this effect (Sirovich et al., 1998b).

The drag reduction is achieved at its full potential for arrays with fully randomised protrusion rows; several other parameters that can be randomised are proposed (Sirovich et al., 1998b). However, in a practical implementation, complete randomisation may not be viable (e.g. due to manufacturing techniques and cost); in these cases, the repetition of a large randomised pattern might be the wisest choice, as proposed by the inventors in the same patent.

Other practical considerations are the structural integrity of the protrusion elements under actual operating conditions of an aircraft, the weight of the elements, or their effect on drag with a certain degree of erosion or dirt. For example, the protrusions may lead to an increased accumulation of particles on the surface during flight, negatively affecting its effect or directly leading to an undesired drag increase. The reviewed publications did not discuss these matters, probably due to the early stage of the technique development. Furthermore, some of these considerations depend on the chosen materials and manufacturing techniques and thus, will be discussed in section 5. A more detailed discussion of the

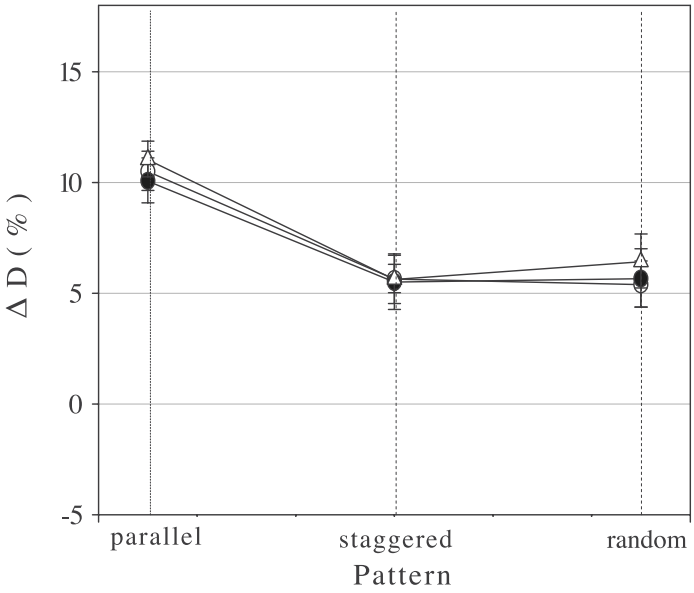

Figure 3.14: Drag change results by Sagong et al. (2008) with the array presented in 3.12 for three chevron leg thickness values: $20\delta_\nu$ (white circle), $30\delta_\nu$ (black circle), and $40\delta_\nu$ (white triangle)

practical considerations of this technique is presented in section 9.3.

3.6. Final remarks

As presented in this section, there is no scientific consensus on the effectiveness of protrusions for drag reduction: while some scholars report that this method is effective for channel flows (Sirovich and Karlsson, 1997; Sirovich et al., 1998b) and for turbulent boundary flows (Monti et al., 2001), others (Sagong et al., 2008) were not able to reproduce the results and even found the opposite effect when making use of chevron-shaped protrusions. This uncertainty motivates the first research question of this Master thesis and proves the need for replication.

Furthermore, only a very narrow area of the available design space has been explored. Configurations such as cavities instead of protrusions or the randomisation of several parameters have not been studied, or at least no results could be found in the literature; this knowledge gap is addressed in research question two. Moreover, modern flow measurement and visualisation techniques such as particle image velocimetry (PIV) can be beneficial in better understanding the flow mechanics, which could result in more effective designs. In the scope of this literature review, no flow visualisation of a flow with protrusion elements was found. Research question three has been formulated to address this gap. Moreover, only two publications (Monti et al., 2001; Sagong et al., 2008) looked into this technology for turbulent boundary layers experimentally; a repetition of the experiments under similar conditions could help confirm (or correct) their results and increase the knowledge of this technology in the scientific community.

II

Design and production of chevron-shaped protrusions

4

Rationale for the selected designs

Before starting manufacturing the models for the experimental campaign, it is necessary to decide on the scope of the tests and the required models to accomplish the goals defined in chapter 1. This chapter aims to summarise the possible design parameters and to present the protrusion array designs selected for the experimental investigation.

4.1. Design parameters

Many relevant design parameters of a protrusion array have been mentioned in chapter 3. Every researcher used a slightly different nomenclature and parameter set. This section briefly presents all relevant parameters in the definition considered for the rest of this thesis. All parameters can be divided into two main categories: element parameters and array parameters. The former refers to parameters that define the geometry of every element, while the latter includes the parameters that specify the arrangement of the elements in the array.

Element parameters

Shape The shape of the elements that form the array can be varied. The most common shape found in literature is a *chevron*, sometimes also referred to as 'vee-shape' or 'v-shape' (e.g. Monti et al., 2001). Inspired by the sailfish (Sagong et al., 2008), it is also possible to use *delta*-shaped elements. These elements can be thought of as a simplified version of the chevron-shaped elements, where the two legs are connected to form a closed triangle. Although not found in literature, other shapes are possible as long as these trigger the same mechanism as the aforementioned ones. In this thesis report, the discussion will be centred around chevron and delta-shaped elements. A schematic representation of some element shapes is presented in figure 4.1.

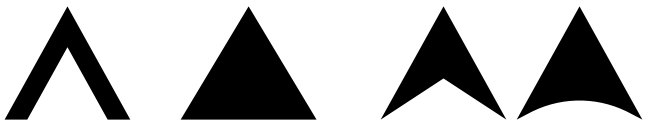

(a) Chevron (b) Delta (c) Alternative shapes

Figure 4.1: Schematic of several element shapes

Type Although the elements that form the array are commonly referred to as *protrusions*, this is only one of two possible element types. If the element extends above the surface, then it is a protrusion. If the element is realised as a pocket in the surface, it is a *cavity*. The generalisation towards protrusions comes from the fact that these are more common in literature. Both types are illustrated in figure 4.2.

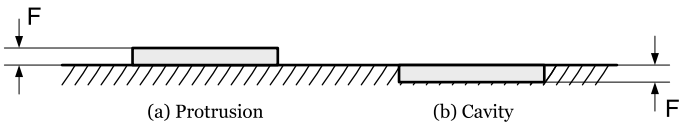

Figure 4.2: Schematic of the element type: protrusion and cavity with the respective height or depth

Length of an element (B) Indicates the size of an element from its apex to the rear edge. With respect to the direction of the mean free-stream flow, the length of the element can also be thought of as its streamwise size. This dimension is exemplarily depicted with several more in figure 4.3.

Width of an element (C) Indicates the size of an element in the direction transversal to the mean free-stream flow direction.

Element height (F) In the case of protrusion elements, the height quantifies the extension above the surface. In the case of a cavity, this parameter indicates the depth of the pocket, as shown in figure 4.2.

Apex angle (α) Simplifying the element geometry as a triangle, the apex angle is the angle opposite to the base. This parameter is not required to characterise the element when its length and width are given; however, it is included in this list since it is used in literature (Monti et al., 2001).

Thickness of chevron legs (T) For a chevron-shaped element, the thickness of the legs is required to define its geometry fully. Many of the array descriptions found in the literature omit this parameter, making a replication of the experimental setup difficult.

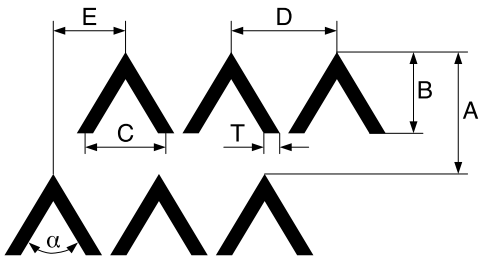

Figure 4.3: Schematic of the array design from a top view

Array parameters

Separation between rows (A) The elements in the array are arranged in rows perpendicular to the flow direction. The separation between the rows is the parameter that indicates the streamwise distance between one row and the next.

Separation between elements in a row (D) The distance between elements in the direction transversal to the mean free-stream flow is defined with this parameter.

Offset between rows (E) Considering two consecutive rows, the offset defines the shift between both rows in the direction transversal to the mean free-stream flow.

Type of offset The offset can be of different types, namely *constant*, *random* or *zero*. In the case of a constant offset, the value of the offset is the same for any two consecutive rows. If the offset value does not follow any pattern, it is random. Moreover, if the elements in two consecutive rows are perfectly aligned, the offset is zero. These three offset types are illustrated in figure 4.4.

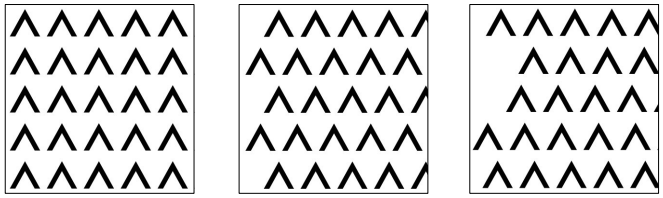

(a) Zero (aligned) (b) Constant (c) Random

Figure 4.4: Schematic of the different types of offset

Orientation The elements in the array can have different orientations with respect to the mean free-stream velocity. In the example of a chevron or delta-shaped element, its apex can point against the flows, which will be called *apex upstream* in this thesis report, or its apex can point in the same direction as the flow, called *apex downstream*, as shown in figure 4.5.

(a) Apex upstream (b) Apex downstream

Figure 4.5: Schematic of upstream and downstream apex orientations

For all relevant studies found in literature and discussed in chapter 3, the parameters defined in this section have been summarised in table A.1, which can be found in appendix A. Notice that some entries had to be left blank because a full description was unavailable. In these cases, an educated guess was made for replicating the designs.

More parameters could be provided for a more accurate description of the element array, such as element roughness or tolerances. Since none of the reviewed publications dealing with this type of flow control technique gives any indications of these parameters, it was decided to limit the description to the previously presented ones for this Master thesis. However, the following chapter will describe the manufacturing materials and techniques to facilitate a complete replication of the experiments presented in this report.

4.2. Selected designs for balance measurement

Considering the twelve parameters introduced in the previous section and the potential values these can have, it is easy to realise that there are infinite possible combinations and, hence, an infinite number of possible arrays. Due to limited resources, selecting a reasonable number of array designs to reach the goals defined in chapter 1 is required.

To select designs in an organised and coherent manner that allows answering research questions one and two, three categories of designs were defined: replication, parameter sweep, and hypotheses.

4.2.1. Replication

The replication category contains all relevant designs for which results could be found in the literature. The two groups tested in this category are aligned patterns (drag increase) and random patterns (drag reduction). The designs selected for replication are summarised in figure 4.6.

Aligned patterns

The drag increase group contains the aligned design by Sirovich and Karlsson (1997), design 3 from Sirovich et al. (1998b), and the aligned design by Sagong et al. (2008). Please note that Sagong et al. (2008) is not clear on the used geometry since two values are reported for each parameter (see figure 3.12). For the replication of their experiments, it was decided to use the geometry from Sirovich and Karlsson (1997) (i.e. the left column in figure 3.12). Sagong et al. (2008) and Sirovich and Karls-

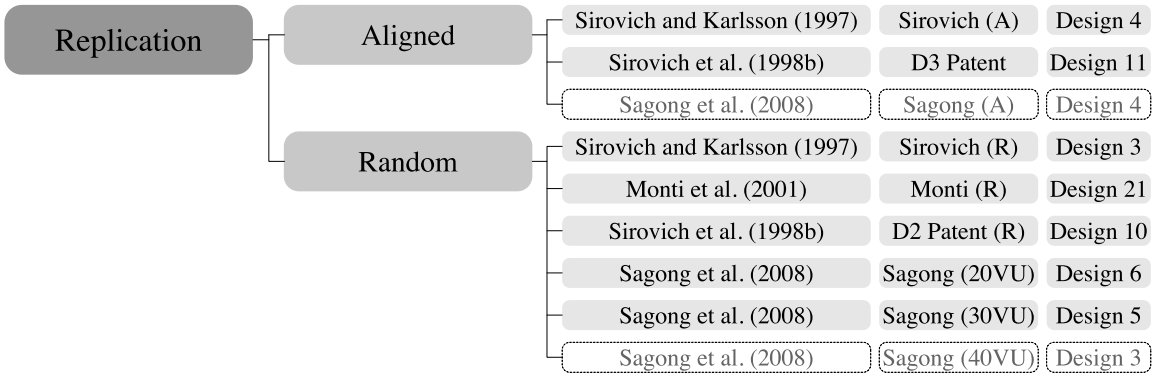

Figure 4.6: Overview of selected replication designs; entries in boxes with dashed lines correspond to designs already introduced

son (1997) use the same geometry; nevertheless, both are included in the replication because of their different testing conditions and reported results.

Random patterns

The drag decrease group contains the random design by Sirovich and Karlsson (1997), the random design by Monti et al. (2001), design 2 with a random offset from Sirovich et al. (1998b), and three random designs tested by Sagong et al. (2008) with different chevron leg thicknesses.

In total, this category contains nine designs with the goal of answering the first question of this research. For this category, it was chosen to test all designs reported to decrease drag since these are of great interest to this Master thesis. With respect to drag-increasing designs (i.e. aligned patterns), only a selection of the most relevant ones was chosen to validate the experimental results found in the literature. Some aligned designs, such as D4, D5, D6, and D7 (see section 3.1) were not replicated.

4.2.2. Parameter study

In order to answer research question number two: 'How do the individual parameters of the protrusion array affect its performance?', it is necessary to selectively vary the parameters of the protrusion array and test the accomplished effect. For this Master thesis, the separation between rows, the separation between elements in a row, and the chevron leg thickness were selected. Note that the first two are array parameters, while the last one is an element parameter. The reason for this choice is that the array parameters are considered key for drag performance of the flow control technique, while the thickness of the chevron leg is included to test if this parameter, which is omitted in most publications, has a large effect on the results. The variation of the chevron leg thickness overlaps with the replication category since Sagong et al. (2008) also performed a leg thickness study. For all parameter sweeps, the random array design by Sirovich and Karlsson (1997) was taken as a baseline, and new designs were constructed by varying only the parameter of interest. An overview of the designs selected for this category is presented in figure 4.7.

Separation between rows

In the case of 'separation between rows', the baseline is $300\delta_v$, which corresponds to the random array design by Sirovich and Karlsson (1997). Three further separations were defined considering the envelope used in literature: $230\delta_v$, $350\delta_v$, and $400\delta_v$.

Separation between elements in a row

For the 'separation between elements in a row', Sirovich and Karlsson (1997) used $260\delta_v$, the three additional separations that have been selected are $300\delta_v$, $350\delta_v$, and $400\delta_v$.

Chevron leg thickness

Finally, for the 'thickness of chevron legs', the values used by Sagong et al. (2008) were selected: $20\delta_v$, $30\delta_v$, and $40\delta_v$. All three categories in the parametric study contain at least three variations to make

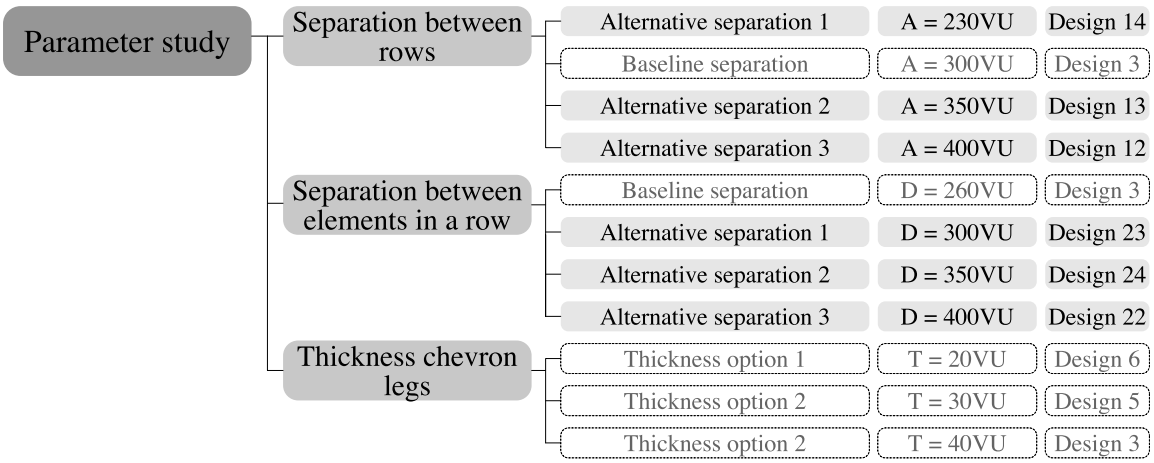

Figure 4.7: Overview of selected parameter study designs; entries in boxes with dashed lines correspond to designs already introduced

identifying trends in the data possible.

Note that this category only includes parameters that can have a continuous numerical value. Discrete and categorical parameters (e.g. shape, type, type of offset, and orientation) are covered in the next group (i.e. hypotheses).

4.2.3. Hypotheses

This last category of selected designs includes all additional designs for which a hypothesis has been formulated (or was found in literature), which are not replications or sweeps of continuous parameters. The tested parameters are shape, type, offset (type and value), and orientation. Furthermore, the effect of different Reynolds numbers on the drag performance is included. These categories and the corresponding designs are depicted in figure 4.8.

Deltas

As explained previously, the elements can have different shapes, such as 'chevron' or 'delta'. The manufacturing of chevron-shaped protrusions is more complicated and time-consuming than the manufacturing of delta-shaped protrusions (for more details, refer to section 5.2). Considering that the elements act as little vortex generators, it can be argued that a delta should have a comparable effect to a chevron. Hence, the following hypothesis is formulated: *with a lower manufacturing effort, a delta-shaped protrusion array can yield a comparable drag performance to a chevron-shaped protrusion array*. This hypothesis is tested by comparing the random and the aligned arrays by Sirovich and Karlsson (1997) to an exact copy of these designs where the chevrons have been replaced by deltas.

Cavities

According to Sirovich et al. (1998b), using cavities instead of protrusions yields the same flow modification, although protrusions are the preferred method. From this finding, the following hypothesis is formulated: *the use of cavities instead of protrusions results in an array of comparable performance, where the protrusion array is more effective in reducing drag*. This hypothesis is tested analogously to the previous one: the random and the aligned arrays by Sirovich and Karlsson (1997) are compared against their 'cavity' counterpart.

Offset

The effect of different types of offsets and values for these offsets is very relevant: according to literature (e.g. Sirovich and Karlsson, 1997), the choice of a random offset instead of a zero offset can turn a drag-reducing technique into a drag-increasing one.

Aligned The first hypothesis formulated for the offset is: *an aligned array pattern leads to an increase in drag with respect to a flat plate, while the same pattern arranged randomly leads to a de-*

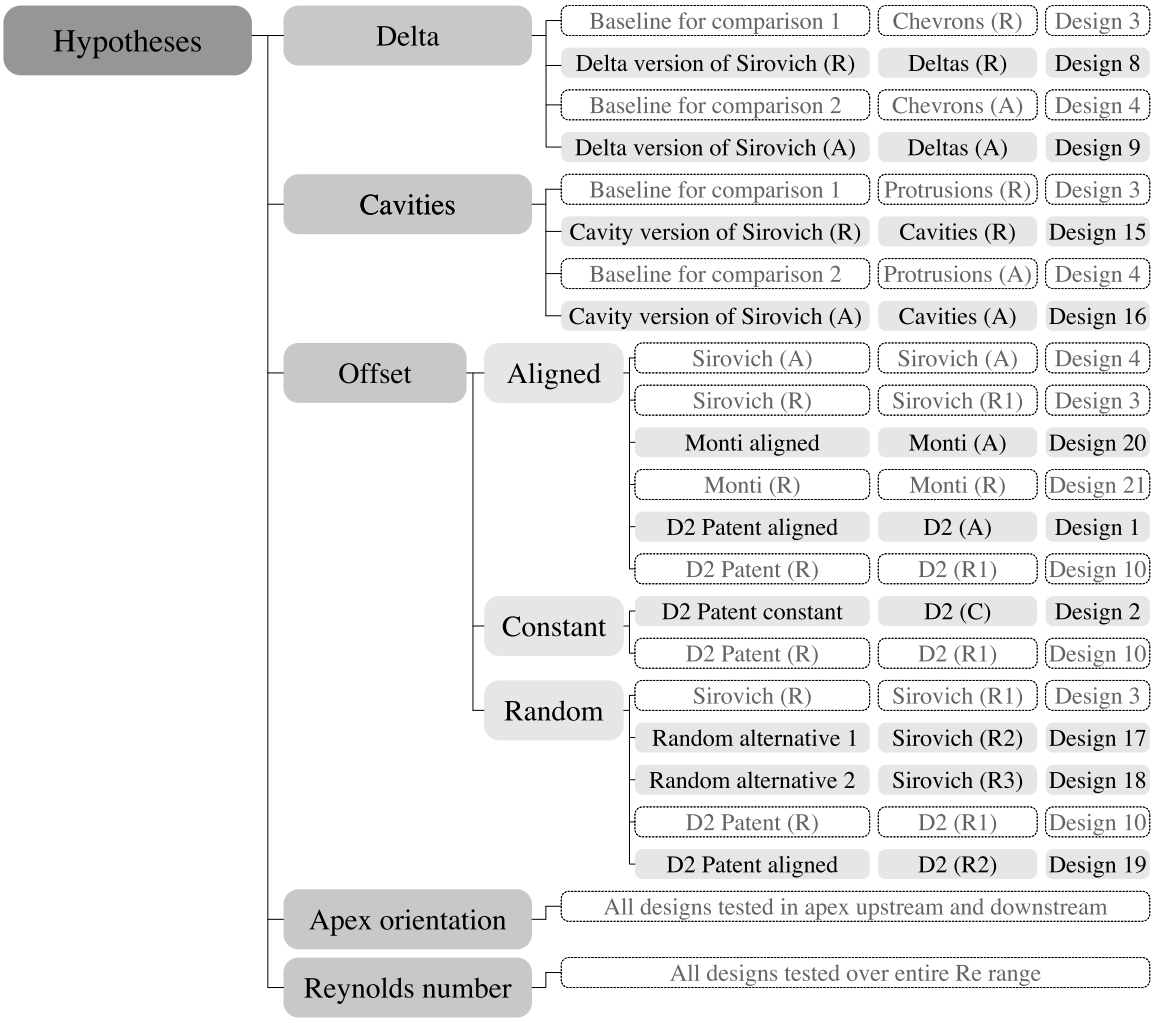

Figure 4.8: Overview of selected hypotheses designs; entries in boxes with dashed lines correspond to designs already introduced

crease in drag. This hypothesis is covered by comparing the random and aligned designs by Sirovich and Karlsson (1997). Furthermore, an aligned alternative for the designs by Monti et al. (2001) and D2 from Sirovich et al. (1998b) has been selected.

Constant The second 'offset' hypothesis is: *an array with a random offset is more effective in reducing drag than an array with a constant (non-zero) offset*. This hypothesis is checked by comparing the random array in D2 by Sirovich et al. (1998b) with an alternative design where the offset is constant.

Random The last 'offset' hypothesis is defined as: *if the drag reduction is truly the effect of a fully random offset, different random offsets should have the same drag performance*. In order to test this hypothesis, two alternative randomisations for the design by Sirovich and Karlsson (1997) and one alternative randomisation for design D2 by Sirovich et al. (1998b) are tested.

Apex orientation

The elements in the array can have different orientations, two of which are of particular interest: apex upstream and apex downstream. The motivation for choosing an orientation reverse to the one initially found in literature is the skin structure found on the sailfish, as explained by Sagong et al. (2008). Since testing these two orientations does not require new models, the effect of different orientations is tested for all designs. The hypothesis to be tested in this case is: *a reverse element orientation leads to higher drag values (i.e. a reduced drag-reducing performance)*.

Reynolds number

Finally, the flow control technique's drag performance for different Reynolds numbers is examined. In external flows, according to Monti et al. (2001), the drag reduction is only accomplished over a limited range of Reynolds numbers. Hence, in this case, the hypothesis is: *the flow control technique is effective over a limited range of Reynolds numbers*. To test this hypothesis no further designs are required; instead, all existing designs are tested in the range of approximately $550,000 < Re_1 < 2,200,000$ (or $630 < Re_\tau < 1850$).

With the designs selected in this section, it is possible to test the effect of all the design parameters except for the element length, width, and height. The reason why these parameters that directly describe the size of the elements were not included is threefold: first, these parameters are very consistent in literature (i.e. all authors use the same element length of $200\delta_\nu$, and almost the same width of $200\delta_\nu$ with a maximum deviation of 9%); hence, the large spread in published results is not thought to come from these parameters. Second, due to manufacturing constraints detailed in section 5.2, a variation in height is not feasible. Third, the limited resources made a prioritisation of designs necessary, and these three parameters are a logical bundle that can be excluded without interfering with other results. Furthermore, this bundle can autonomously be tested in a future campaign.

The selected designs include 24 unique test plates that are tested in two orientations and for a Reynolds number range of approximately $550,000 < Re_1 < 2,200,000$. Table 4.1 details the exact parameters used for the different designs.

4.3. Selected designs for PIV

While 24 unique test plate designs tested in two orientations have been chosen for the balance measurements, this amount of plates and configurations for the PIV experiments would not be feasible within the scope of this Master thesis, the time requirements for testing, the required storage, and the post-processing needs would exceed the ones available. Furthermore, it is not necessary to test all test plates and configurations to adequately answer research question number three: 'Do the flow characteristics and coherent structures in the flow support the working mechanism hypothesis presented by Sirovich and Karlsson (1997)?'. For this reasons, the following test cases are selected for the PIV experiments:

- The aligned and the random arrays proposed by Sirovich and Karlsson (1997) are tested to address the research question directly.
- The aligned and random delta designs are tested to understand if these two protrusion shapes yield the same or a comparable flow manipulation. Understanding the similarity between chevron and delta-shaped elements is of interest because of reasons concerning the manufacturing, which will be detailed in chapter 5.
- Every PIV design is tested in apex upstream and apex downstream configuration to determine if the orientation plays a role in the effect the protrusions have on the flow. This information is relevant for the definition of new protrusion geometries.
- A reference smooth test plate is also tested in the same experimental setup to have reference data.

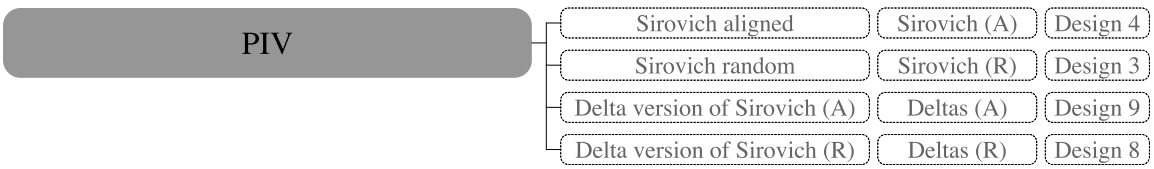

Figure 4.9: Overview of selected designs for PIV; entries in boxes with dashed lines correspond to designs already introduced

In total, four protrusion designs which will be tested in two orientations have been selected for the PIV experiments. These four designs are depicted in figure 4.9.

4.4. Overview of designs

This section provides reference information to uniquely identify the parameters used for the designs selected for this Master thesis. Table 4.1 contains a list with 24 designs, their respective category, and their parameters. For more information on the different randomisations (i.e. the parameter 'E-value'), please refer to section 5.1. An overview of designs and the corresponding label used in the presentation of the results and additional reference tables can be found in appendix B.

Design	Category	A [-]	B [-]	C [-]	D [-]	T [-]	E type	E value [-]
1	Hypotheses | Offset (aligned) | D2 patent 1998 (aligned)	278	200	182	270	40	zero	0
2	Hypotheses | Offset (constant) | D2 patent 1998 (constant/ staggered)	278	200	182	270	40	constant	135
3	Replication | Random pattern | Sirovich and Karlsson 1997 (random)	300	200	200	260	40	random	RAND_E
4	Replication | Aligned pattern | Sirovich and Karlsson 1997 (aligned)	300	200	200	260	40	zero	0
5	Replication | Random pattern | Sagong (30VU)	300	200	200	260	30	random	RAND_E
6	Replication | Random pattern | Sagong (20VU)	300	200	200	260	20	random	RAND_E
8	Hypotheses | Shapes delta | Randomised pattern with equivalent deltas	300	200	200	260	40	random	RAND_E
9	Hypotheses | Shapes delta | Aligned pattern with equivalent deltas	300	200	200	260	40	zero	0
10	Replication | Random pattern | D2 patent 1998 (randomised)	278	200	182	270	40	random	2 x RAND_E
11	Replication | Aligned pattern | D3 patent 1998 (aligned)	730	300	250	394	40	zero	0
12	Parameter sweep | Separation between rows | $400\delta_v$	400	200	200	260	40	random	2 x RAND_E
13	Parameter sweep | Separation between rows | $350\delta_v$	350	200	200	260	40	random	2 x RAND_E
14	Parameter sweep | Separation between rows | $230\delta_v$	230	200	200	260	40	random	RAND_E
15	Hypotheses | Cavities | Randomised pattern with cavities	300	200	200	260	40	random	RAND_E
16	Hypotheses | Cavities | Aligned pattern with cavities	300	200	200	260	40	zero	0
17	Hypotheses | Offset (random) | Alternative 1 to Sirovich (R)	300	200	200	260	40	random	RAND_E_2
18	Hypotheses | Offset (random) | Alternative 2 to Sirovich (R)	300	200	200	260	40	random	RAND_E_D18
19	Hypotheses | Offset (random) | Alternative 1 to D2 patent (random)	278	200	182	270	40	random	RAND_E_D19
20	Hypotheses | Offset (aligned) | Monti (aligned)	300	200	180	260	30	zero	0
21	Replication | Random pattern | Monti (random)	300	200	180	260	30	random	RAND_E_M
22	Parameter Sweep | Separation between elements in a row | $400\delta_v$	300	200	200	400	40	random	RAND_E
23	Parameter Sweep | Separation between elements in a row | $300\delta_v$	300	200	200	300	40	random	RAND_E
24	Parameter Sweep | Separation between elements in a row | $350\delta_v$	300	200	200	350	40	random	RAND_E
30	Initial proof of concept - not part of the selected designs	344	333	200	294	27	zero	0

Table 4.1: Table of designs, categories, and parameters

Please note that design 30 corresponds to the initial proof of concept and will not be further discussed here; since this design was tested in the wind tunnel and its drag data is presented in appendix C, the corresponding parameters are included in the table.

Figures 4.10 and 4.11 show a 50×50 mm^2 detail of the 24 designs presented in table 4.1. The left side of the details corresponds to the left side of the test plate; hence this side is irregular for the designs with a random and a constant (non-zero) offset. A scale has been included for reference.

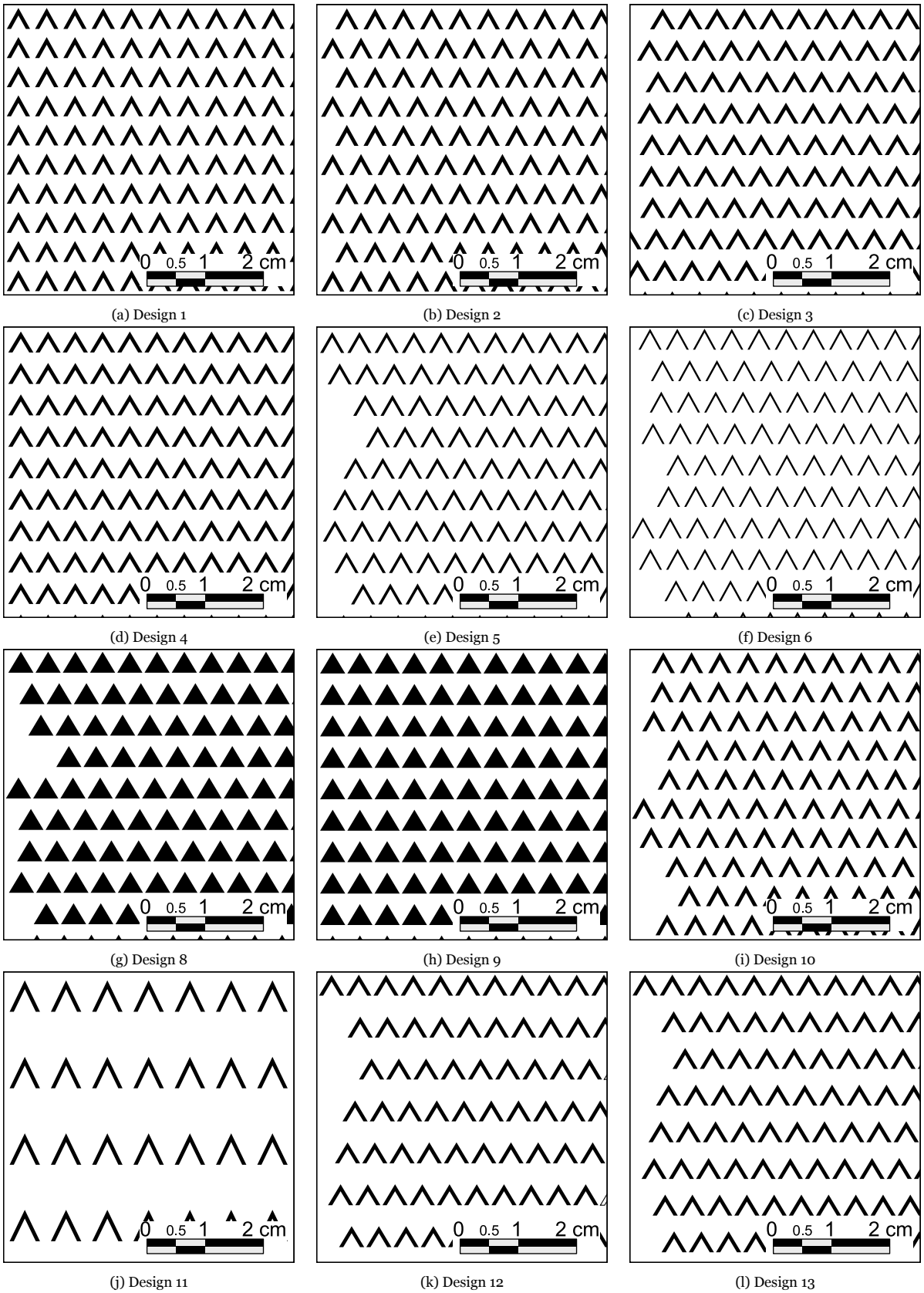

(a) Design 1 (b) Design 2 (c) Design 3

(d) Design 4 (e) Design 5 (f) Design 6

(g) Design 8 (h) Design 9 (i) Design 10

(j) Design 11 (k) Design 12 (l) Design 13

Figure 4.10: Designs; black area represents the vinyl, white represents the aluminium

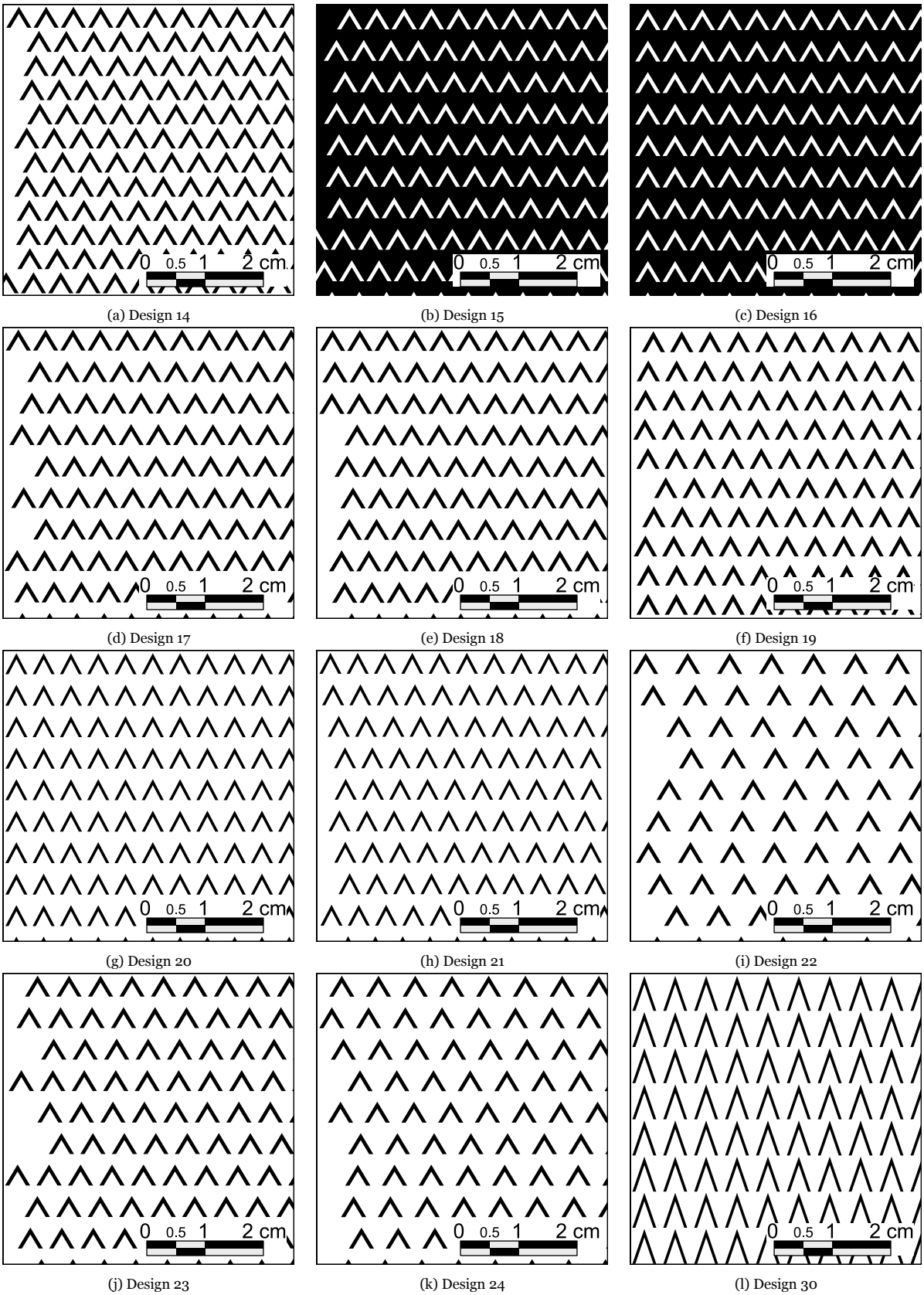

(a) Design 14 (b) Design 15 (c) Design 16

(d) Design 17 (e) Design 18 (f) Design 19

(g) Design 20 (h) Design 21 (i) Design 22

(j) Design 23 (k) Design 24 (l) Design 30

Figure 4.11: Designs (continued); black area represents the vinyl, white represents the aluminium

5

Design, manufacturing, and validation

In the previous chapter, the array configurations selected for the wind tunnel experiments have been presented, and the choices have been explained. The current chapter will address the design process and motivate the design choices for the selected arrays in section 5.1. The manufacturing of the balance measurement models is covered in section 5.2. Next, some remarks about the manufacturing of the PIV test plates are made in section 5.3. Finally, the validation process is detailed in section 5.4.

5.1. Test plate design

This section outlines the design choices made to convert the designs selected in the previous chapter into an actual geometry suitable for the experimental campaign. Next, the design process is briefly discussed.

5.1.1. Design choices

The main design choices that will be motivated here are the selection of a viscous unit length, the randomisation used for the offset values, and the test plate dimensions.

Viscous unit length

The test plate design involves converting parametric array descriptions into a physical model suitable for the available wind tunnel and experimental setup. The main parameter in the literature for characterising the element and array geometry is the viscous unit length (δ_ν or VU). In order to determine the physical dimensions of the array, it is necessary to determine the viscous unit length, which can be accomplished using the power-law equations introduced in section 2.1.

For the computation, the density (ρ), the kinematic viscosity (ν) and the Reynolds number ($Re_x = \frac{\rho U_\infty x}{\mu}$) are required. Table 5.1 contains the values used for the computation to facilitate the reproduction of the results.

Name	Variable	Value	Unit
Density	ρ	1.225	[kg/m^3]
Kinematic viscosity	ν	1.5×10^{-5}	[m^2/s]
Dynamic viscosity	μ	1.81×10^{-5}	[kg/m /s]
Free stream velocity	U_∞	20	[m/s]
Characteristic length	x	1.05	[m]

Table 5.1: Values used for the computation of the viscous unit

The choice of free-stream velocity is given by the available velocity range: $0 < U_\infty \lessapprox 35$ m/s. 20 m/s is a velocity located roughly in the middle of the available velocity range, offering enough flexibility to test

at higher and lower velocities. Furthermore, experimental data is available for this velocity, enabling the validation of the theoretical viscous unit length computation, as will be demonstrated later.

This paragraph briefly introduces the experimental setup to motivate the chosen characteristic length. Figure 5.1 shows the plate as it is installed in the wind tunnel. The plate fits into a custom balance called 'the Hill' and, when mounted, has a total length of roughly 900 mm. In the selected configuration, 'the Hill' is preceded by a device consisting of a flat plate and an elliptical leading edge with a floor opening. The floor opening removes the boundary layer from the wind tunnel and somewhat reduces the blockage effect. The primary function of this extension is to initiate a turbulent boundary layer at a distance of 600 mm from the leading edge of the test plate. For this purpose, a strip of large carborundum particles is located at the elliptical leading edge of the extension. More details on the experimental setup can be found in section 6.1.

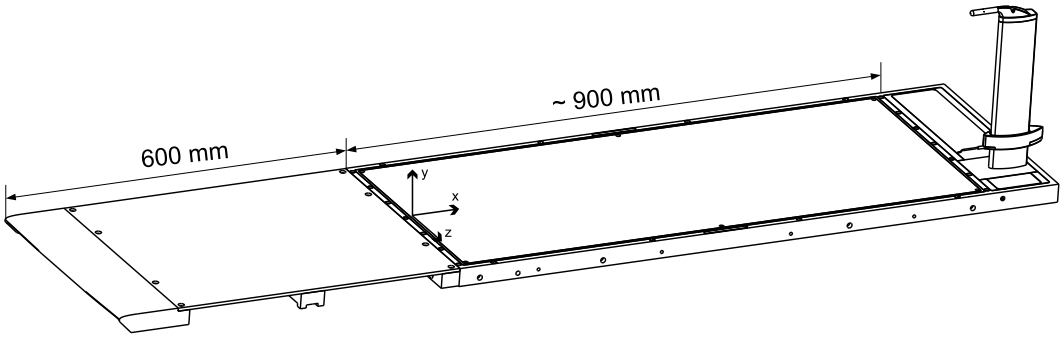

Figure 5.1: Development length of the boundary layer for the Hill, modified from van Nesselrooij et al. (2022)

In the computations for the boundary layer thickness and the viscous unit length, the characteristic length is the boundary layer development length, or in other words, the distance to the trimming location (i.e. the leading edge of the 'Hill' extension). Figure 5.2 shows the values for the boundary layer thickness and the viscous unit length for a distance of up to 2 m from the trimming position. Note that the location of the test plate is illustrated by a thick grey line on the horizontal axis and two vertical thin grey dash-dotted lines. Over the length of the plate, the boundary layer thickness experiences an increase of 119%, while the viscous unit length has a comparatively lower increase of 6.8%. Due to the low increase of the viscous unit length (18 times smaller than the increase in boundary layer thickness), it is assumed for the designs that the viscous unit length remains constant (i.e. no variation of the viscous unit length is considered in the streamwise direction). The value for the viscous unit length used for the designs corresponds to the computed value at a boundary layer development length of $x = 1.05$ m or the centre of the test plate, namely: $\delta_v = 18\ \mu$m.

The computation is validated by comparing the results with the viscous unit length and the boundary layer thickness from experimental data by Hartog (2021), which is depicted in figure 5.2. At first glance, it can be seen that the theoretical and experimental data have a better match in the case of the viscous unit length. This observation is supported by the normalised root-mean-square deviation (NRMSD). Note that the root-mean-square deviation (RMSD) alone is insufficient for comparing two different data sets because it has a dimension. Since no standard means of computing the NRMSD is available in the literature, the procedure used for this analysis is briefly explained. The first step is to compute the RMSD:

$$RMSD = \sqrt{\frac{\sum_{n=1}^{N}(\tilde{y_n} - y_n)^2}{N}}, \tag{5.1}$$

where $\tilde{y_n}$ is the experimental data and y_n is the theoretical value. Next, the RMSD is normalised by the mean of the theoretical values $\bar{y_n}$:

$$NRMSD = \frac{RMSD}{\bar{y_n}}. \tag{5.2}$$

For the viscous unit length, the NRMSD value between experimental and theoretical data is 4.11%,

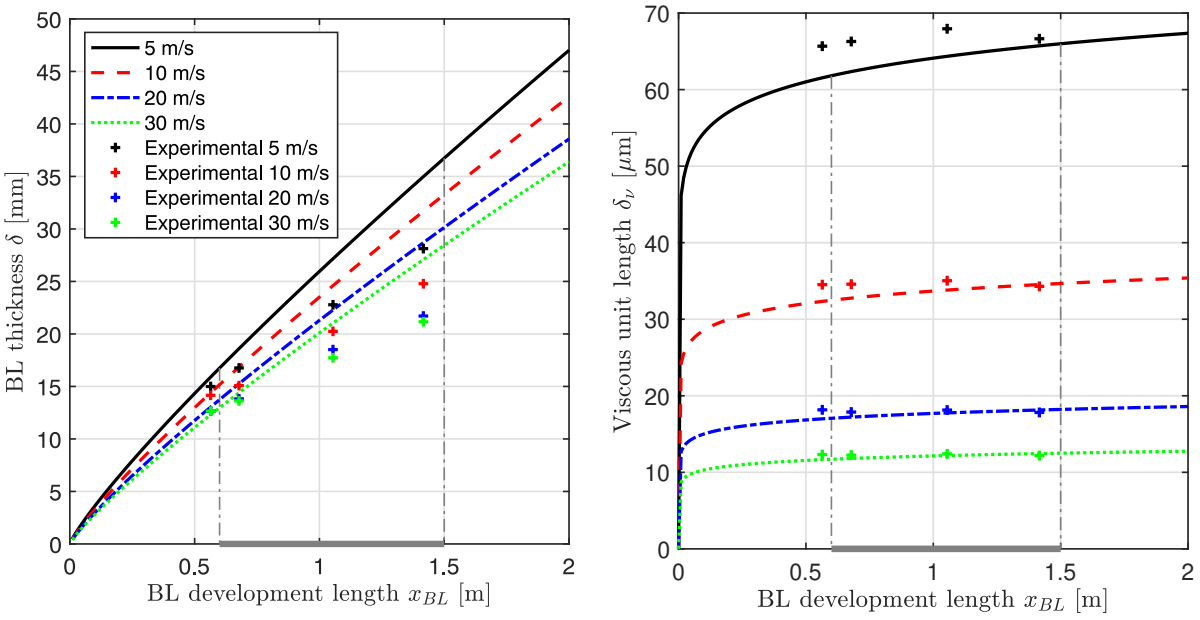

Figure 5.2: Theoretical and experimental boundary layer thickness (left) and viscous unit development (right) over the test plate for a free-stream velocity of 20 m/s, experimental data from Hartog (2021)

and for the boundary layer thickness, it is 20.45%. The deviation between theory and experiments can have several sources, such as the fact that the experimental setup is not a perfect zero gradient turbulent boundary layer or measurement errors. The good match between theory and experiments for the viscous unit length gives confidence in the chosen value of $\delta_\nu = 18$ μm to scale the designs.

Offset randomisation

Five different offset randomisations have been selected for the designs, as shown in table 4.1. Note that, in this context, the same randomisation means that the same values have been used to define the offset. In this way, it can be ensured that the observed effect comes from the intended parameter change and not from an undesired change in offset. For parameter designs with more rows than random values available, the randomisation values were repeated for the remaining rows (these cases are indicated with '2×' in the table). The five randomisations are briefly presented here:

RAND_E This offset randomisation contains values selected from a standard normal distribution multiplied by the initial row offset of $130\delta_\nu$. The command used in MATLAB to generate these values is: `130 * randn(rows,1)`, where `rows` is the number of rows of the protrusion array.

RAND_E_2 This offset randomisation is obtained running the same command as presented for RAND_E a second time, which yields a different set of values.

RAND_E_D18 For this randomisation, the values that are multiplied with the initial offset are obtained from a uniform distribution between 0 and 1. The corresponding MATLAB code is as follows: `260 * rand(rows,1).`

RAND_E_D19 This set of random values uses the same code as presented for RAND_E_D18.

RAND_E_MONTI For the design by Monti et al. (2001), the target set of random offset values is given by figure 3.7. As mentioned by the researchers, the offset follows a Gaussian distribution. The initial offset is chosen to match the range of values used by Monti et al. (2001). A good normal distribution of the values is ensured by selecting a set of values with acceptable skewness and kurtosis values.

The chosen randomisation has a skewness of 0.0091 (ideal normal distribution: 0) and a kurtosis value of 2.9157 (ideal: 3). The corresponding MATLAB command is `100 * randn(rows,1)`.

Test plate dimensions

The array designs should cover a test plate with the dimensions $881.3 \times 366.3 \times 5$ mm^3, leaving approximately 10 mm clearance at the leading and trailing edges of the test plate to avoid damage during storage and transportation. These dimensions are dictated by the balance setup selected for the experiments, as will be detailed in section 6.

5.1.2. Design process

With the array configurations selected (chapter 4) and the relevant dimensions defined (section 5.1.1), the last step of the test plate design is to prepare the geometry files to be manufactured from vinyl sheets using a vinyl cutter, as will be detailed in the next section (section 5). The manufacturing technique requires a 2D geometry definition, for which a vector graphics editor was chosen. Concretely, TikZ was used, a LaTeX package to produce vector graphics. The advantage of TikZ over other alternatives is the possibility to define the entire geometry by script with a simple syntax, which opens the door for parameterisation.

For this purpose, a Matlab script that takes the parameters defined in chapter 4, the required test plate size, and the desired viscous unit length was prepared. The full script for the example of the geometry for the random design by Sirovich and Karlsson (1997) (design 3) can be found in appendix D. The output of this script is a '.tex' text file that can be compiled with a LaTeX compiler to obtain a PDF file with the geometry of the test plate design. An image of the design generated using TikZ is shown in figure 5.3. This file is directly used for manufacturing, as explained in the next section.

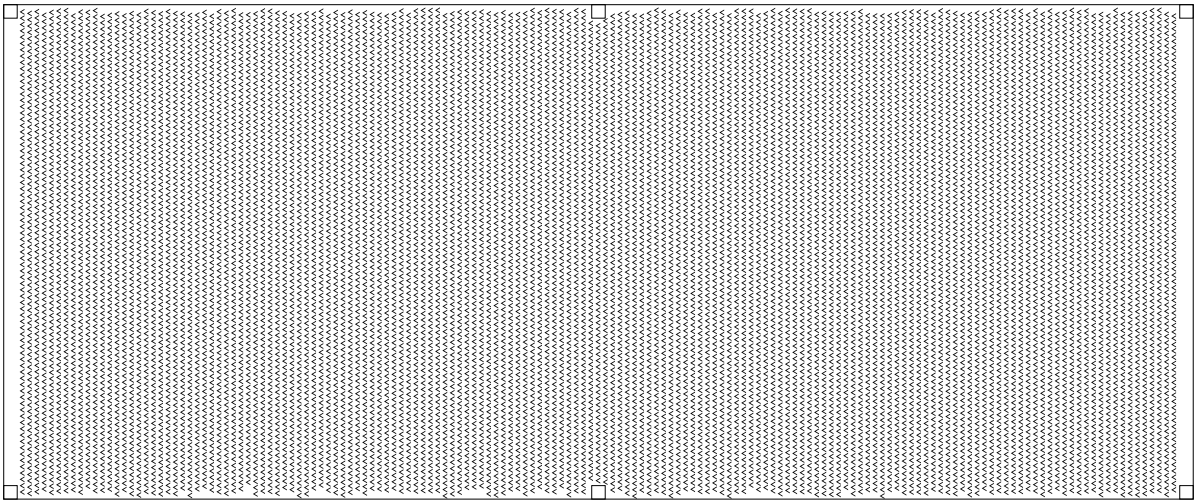

Figure 5.3: Test plate generated with TikZ corresponding to the array design 3 inspired by Sirovich and Karlsson (1997); image render of the geometry file

5.2. Manufacturing of balance measurement test plates

This section focuses on the manufacturing of the test plates required prior to the start of the experimental campaign. In this step, the theoretical designs envisioned for the measurements are converted into physical objects that can be placed inside the wind tunnel. A large number of models is required to reach the objectives of this thesis; hence, a quick and cost-effective manufacturing technique is important. An added difficulty is that very few details about the manufacturing techniques used in previous studies were known, so an original solution had to be found.

The target geometry for the model is given by the experimental setup selected for this thesis, in particular, by the dimension of the test plate required for the 'Hill': $881.3 \times 366.3 \times 5$ mm^3. Aluminium plates of the indicated length and width are used as base test plates, and the array elements are added on top. The selected technique to manufacture the array elements would then dictate the required plate

height. In this section, first, the choice of the selected technique will be motivated (5.2.1), and next, the manufacturing process will be outlined (5.2.2).

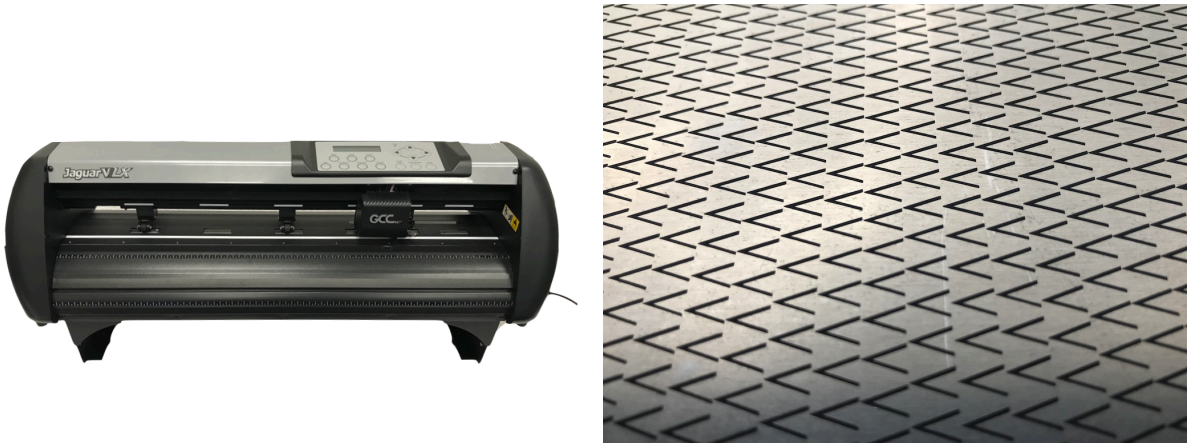

(a) Vinyl cutter

(b) Protrusion array manufactured from vinyl

Figure 5.4: Vinyl cutter and example for vinyl protrusions

5.2.1. Motivation for selected technique

Several techniques were considered for manufacturing the test plates, such as electroerosion, plasticine-stamp or clay, 3D printing, UV printing, and vinyl. The advantages, disadvantages, and known applications of the different techniques were discussed in detail in a previous literature review report. Table 5.2 summarises the findings.

Manufacturing technique	Advantage	Disadvantage
Electroerosion	Very accurate geometry possible	Very slow process, electrode with the target geometry has to be manufactured in advance
Plasticine-stamp or clay	Quick and cheap process, malleable material can be reused	Possibly inaccurate for shallow geometries and edges, no complete randomisation possible, each new geometry requires the manufacturing of a new stamp
3D Printing	Direct manufacturing without intermediate step of any protrusion geometry possible	Print size constraint by the size of the printer
UV printing	Protrusions can be printed directly onto a flat test plate	Print size constraint by the size of the printer, very expensive
Vinyl	Very quick and cheap, suitable for retrofitting of existing aircraft	Only discrete sizes possible dictated by the available foils

Table 5.2: Advantages and disadvantages of manufacturing techniques for protrusion elements

From the assessment, vinyl appears to be the most suitable material for manufacturing many protrusion plates for an experimental campaign in which a large area of the design space wants to be covered. It offers quick and cheap manufacturing, albeit the limitation in protrusion height (i.e. the height has to coincide with an available vinyl sheet thickness). It has to be noted that a scan through currently available vinyl foil shows that many foil thicknesses are available, ranging from 25 μm to 350 μm, where foils in the range of 60 to 80 μm are the most common ones (Metamark, 2021). Furthermore, this technique is very flexible and could even be used as the final manufacturing technique as the protrusion sticker can easily be attached to an existing aircraft fuselage and wings. While vinyl is not very common in fluid dynamics, it has been used for wind tunnel tests in the past. For example, Gramola et al. (2019) used

vinyl in combination with a vinyl cutter for a photogrammetry study to obtain accurate deformation measurements in a supersonic wind tunnel. The pattern tracked by the photogrammetry system was manufactured from vinyl foil.

For the use of vinyl, two techniques manufacturing techniques were considered: laser-cutting and knife-cutting. Microscope images showing the geometry obtained with the two techniques are shown in figure 5.5. The laser-cut geometry presents very irregular edges and an accumulation of material due to the melting process. The knife-cut geometry has very clean and regular edges in comparison and was hence selected for manufacturing the models. For cutting vinyl, a vinyl cutter from the manufacturer GCC, model Jaguar V LX 61, has been used (see figure 5.4). This machine cuts media of up to 610 mm in width and has virtually no limitation in the model length since the media comes in rolls of 50 m. This device enables the manufacturing of the protrusion arrays in one piece and offers the flexibility to increase the length if required.

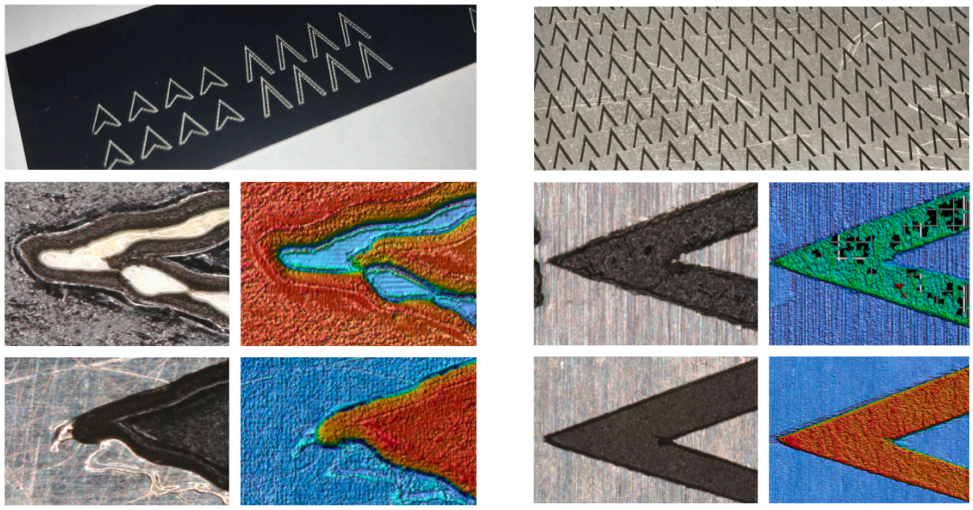

(a) Laser-cut vinyl (b) Knife-cut vinyl

Figure 5.5: Comparison between laser-cut and knife-cut vinyl; microscope images in the second and third rows were taken with a wide-area 3D measurement microscope, model *Keyence VR-5000*

Several types of vinyl sheets were tested, and the Metamark 7 Series Black Matt (M7-111M) was selected for its quality, surface finish, thickness, and cutting properties. The selected foil is polymeric calendered PVC with a nominal gauge of 70 μm (Metamark (UK) Limited, 2021). The height of the protrusion elements obtained with this vinyl coincides with the required thickness specified in the literature. For this reason, the base plate was chosen to have the thickness required for the 'Hill' (i.e. 5 mm) with the protrusions made out of vinyl glued to the surface. For the base test plates, CNC aluminium plates with the dimensions specified previously are (i.e. $881.3 \times 366.3 \times 5$ mm^3). The test plates also include six holes at the edges that can be used to screw the plate and the 'Hill' together for safety. However, this is not critical at the low-velocity range for the planned experiments and was therefore not done. Furthermore, the repeatability of the measurements was found to be worse when screws were used to secure the plate. The base plates were used on both sides for efficiency, meaning that one test plate has two sides with two different designs.

5.2.2. Process

The manufacturing process can be split into several steps that are detailed below:

Cutting vinyl The first step is to cut the vinyl. For this, the vinyl roll is installed into the vinyl cutter. Before cutting the design, it is necessary to adjust the cutting parameters. The parameters depend on the cut design, the wear of the blade, and the vinyl; therefore, checking the settings before every cut is necessary. The main parameters set are: force, speed, and offset. The 'force' refers to the amount of force applied to the blade when it is in contact with the vinyl. Ideally, the force setting is such that

the blade cuts through the vinyl but does not cut the liner. For reference, a force of 80 gf[1] was used. The speed refers to the velocity at which the knife is moved over the vinyl to cut the design. Note that, for the selected vinyl cutter, the knife can only move along the width of the vinyl; the vinyl is moved using several rollers to cut along the length. A typical speed used for the manufacturing of the models was 72 cm/s. This setting was increased to up to 120 cm/s to speed up the cutting time with easier designs. Last, the offset is relevant when cutting sharp geometries, especially corners. It indicates the distance between the centre of the knife holder and the blade's position that is actually in contact with the material and does the cutting. The offset was set to 0.2 mm for the used cutter blade.

The design is uploaded to the vinyl using the software GreatCut 4 by GCC. The exact duration of the cutting process depends on the complexity of the design and the number of elements; for reference, the mean duration is 1.5 hours. After the cut, the piece of vinyl containing the cut design is separated from the rest of the roll using a knife.

Transfer the design Once the design has been cut, the design is transferred onto the surface of the base plate. For this, the exposed (non-sticky) side of the vinyl is covered with transfer foil using a scraper. Then, the liner of the vinyl is removed, leaving the sticky side of the vinyl exposed. At this point, the design is laid on a flat table with the sticky side up. Tape is used to ensure the vinyl sheet is flat and no wrinkles or bubbles form. Next, the aluminium base plate can be aligned with an outline of the same shape cut around the design by placing the base plate with the long side next to the vinyl sheet. Once the long side is aligned, the plate is moved closer to the vinyl until there is contact between the surface and the vinyl. The next step is to use a scraper to ensure the vinyl is adhered well and remove any possible air bubbles. Then, the transfer foil can be removed, exposing the cut design on the base plate surface.

Please note that, in the case of cavities, the elements are removed using tweezers before transferring the design. This order was found to yield a better result. The process of manually removing every protrusion and only leaving the cavities is very tedious and takes on average 8 to 10 hours for each cavity design. Considering that a design has roughly $12,000$ elements, $1,500 - 1,200$ have to be removed per hour.

Weed After the transfer step, the entire vinyl sheet is pasted on the surface of the base plate. However, only the protrusions are needed; the remaining vinyl surrounding them has to be removed (note that this is different for the cavities, as indicated previously). Removing the unwanted vinyl is known as weeding. Especial care is required during this process to avoid damaging the protrusions or the base plate with the scalpel and tweezers used for weeding. Missing or damaged protrusions are replaced manually. The weeding is a tedious step that takes on average 3 hours per plate. The exact duration depends on the number of protrusions and their design. Chevron-shaped protrusions required more care to weed than delta-shaped protrusions. This difference is also reflected in the weeding time of only 30-40 minutes for the delta plates.

Rolling Once the designs are weeded, a large metallic cylinder is rolled with pressure over the test plate to ensure that all the protrusions adhere properly. This step can also be done using the scraper tool, but it was found to be less convenient and more prone to errors, such as unwillingly removing some elements.

Cover patches The last step before installing the test plate in the wind tunnel is to cover the holes of the base plate. For this purpose, patches were manufactured using vinyl. The advantage of the custom-made patches compared to using tape is that the patches have the exact form of the corners. Furthermore, the same patches are used for all plates, increasing repeatability.

5.3. Manufacturing considerations for PIV test plates

Performing PIV involves illuminating a plane of the flow field with very bright laser light. Glossy or polished surfaces, such as the aluminium of the test plates, can lead to reflections, either reflecting

[1]Note that the unit used for the force setting by the manufacturer is gram force (gf)

scattered light or when hit directly by the laser beam. These reflections can negatively affect the quality of the measurements and should be avoided. Furthermore, the reflections can be hazardous since laser light is dangerous for eyesight. A common practice when performing PIV experiments is to use matte black models to minimise the effect of reflections.

The models manufactured for the balance measurement use a test plate made out of untreated aluminium, which has a glossy surface and is very unsuited for PIV experiments. Three options were explored to manufacture suitable PIV test plates: painting the existing test plates, painting a base plate before attaching the protrusions, and using an anodised base plate.

The most straightforward approach to obtaining matte black models is to take the existing test plates and paint them black with spray paint. This approach was tested, and the result was assessed by examining the sample under a wide-area 3D measurement microscope, model *Keyence VR-5000* (Keyence Corporation of America, 2016), which is available in the Delft Aerospace Structures and Materials Laboratory (DASML) at TU Delft. The result of this examination is shown in figure 5.6a. This figure shows a microscope image of a protrusion array; half of this array has been painted with one matte black spray paint coat. The height profile corresponding to a spanwise cut through the protrusion array is presented in figure 5.6b. This profile is used to assess the effect of the paint on the geometry. The area that has been painted is overall approximately 10 μm thicker. Furthermore, the edges are less sharp, and the surface of the protrusions, which was flat, looks bumpy. These observations confirm that the geometry of the arrays is modified, and the conclusion is drawn that painting existing models is unsuitable.

(a) Microscope image showing top view and line for height profile evaluation

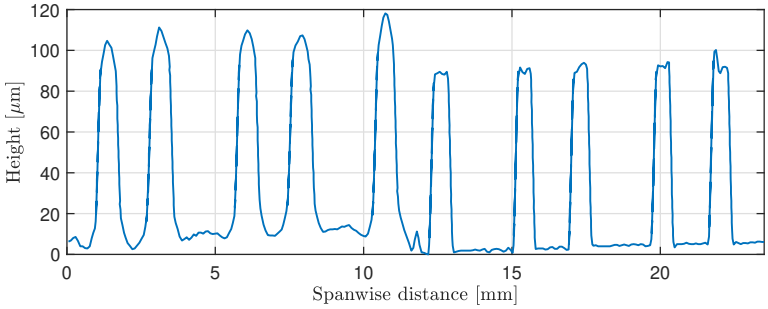

(b) Height profile evaluated along the line shown in the top view

Figure 5.6: Comparison between painted and raw protrusion elements; data obtained with a wide-area 3D measurement microscope, *model Keyence VR-5000*

The second approach was to paint the base plates without any protrusions attached. Once the plate is uniformly black, the protrusions are attached following the procedure described before. The problem, in this case, is that some of the paint comes off during the weeding step, leaving exposed areas of glossy aluminium. This is shown in figure 5.7a.

Finally, black anodised aluminium plates are used for the PIV models. The anodised surface is more resistant to scratches and general wear than paint, making it ideal for the required application. The process described previously was used to apply the array onto the anodised plate. The result is a clean matte black surface as shown in figure 5.7b. Since the surface of the base plates for PIV is different from the one used for the balance measurements, these test plates are included in the direct force measurements; the results will be compared with their non-anodised counterparts.

5.4. Validation

The manufactured models are validated to ensure that these accurately represent the original design. All the models were visually inspected for manufacturing errors or damage. Some selected ones were scanned using the microscope (model *Keyence VR-5000*), which was introduced previously. The measurements from the scan were compared with the intended design to validate the dimensions. A microscope image taken for validation and the corresponding comparison with the design values are shown in figure 5.8 and table 5.3, respectively. The quality of the protrusions in terms of manufacturing tolerance was considered acceptable, with the largest deviations being around 2%.

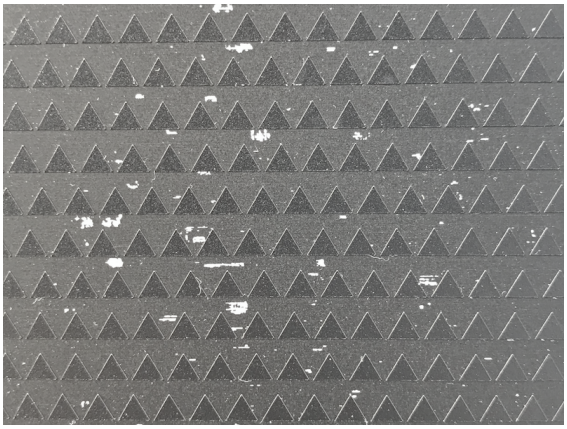

(a) Spray painted PIV test plate showing paint damage after the weeding step

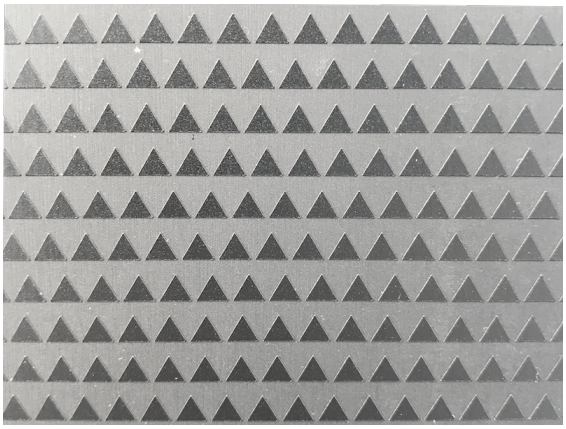

(b) Anodised PIV test plate as used for the final experiments

Figure 5.7: PIV test plates in comparison

While the array elements were satisfactory, the base plates were not. Originally, CNC milled base plates had been ordered after some initial tests with plates manufactured in different ways (mainly CNC milled plates and water jet cut aluminium sheet). However, the base plates that were delivered had only been CNC milled around the edges; the main surfaces of the plate were not CNC milled and presented the roughness natural to the production of aluminium sheet. Moreover, this roughness was not constant: some plates presented roughness grooves in horizontal and others in vertical direction. An error metric has been introduced to quantify the uncertainty of the flat base plate, as will be detailed in section 6.1.3.

After the drag measurements, the data revealed that some plates were not moving freely inside the balance, giving wrong results. The problem was identified to be a slight curvature along the long side of some plates. Due to the design of the balance selected for the measurements, when the curvature exceeds a particular value, the frame that supports the test plate is pushed against the balance's internal structure, creating a physical contact between the frame and the structure. The frame is designed to swing freely and is only supported by four flexures at the corners; the physical contact with the structure due to the plate's curvature constraints the free swing of the frame (and plate), yielding wrong measurements. The consequence of this issue was that the measurements had to be repeated after straightening the test plates.

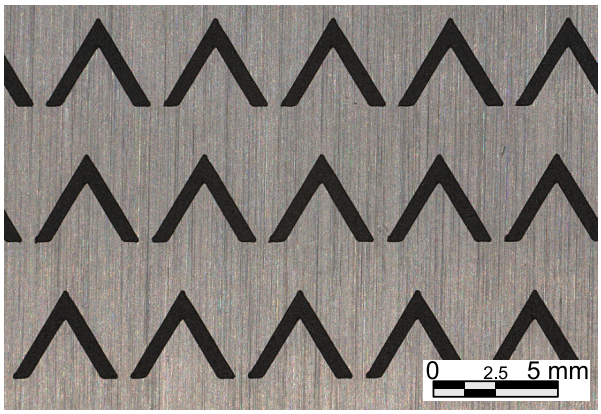

Figure 5.8: Microscope image of portion of TP0094A with design 3 obtained with a wide-area 3D measurement microscope, model *Keyence-5000* used to determine the actual sizes of the model

Further examination of the plates revealed that many of the test plates were slightly curved, although only in some cases the curvature was a problem for the frame. Since the curvature of the plate can affect the balance measurements, all the test plates were straightened. The plates were covered with transfer

	Designed value [mm]	Measured value [mm]	Difference [%]
A	5.4	5.4	0
B	3.6	3.52	2.2
C	3.6	3.63	0.8
D	4.68	4.67	0.2
F	0.09 – 0.108	0.09	within range
T	0.7	0.69	1.43

Table 5.3: Comparison of design dimensions and measured dimensions for TP0094A with design 3

foil to protect them from scratches and other damage and straightened using a roll bender. A schematic showing the working mechanism of a roll bender can be found in figure 5.9. The 'workpiece' (i.e. the test plate) is introduced between three steel rolls arranged in a pyramid form. The top roll can be moved up and down and determines the curvature that the workpiece experiences. While this machine is usually employed to bend metals, a careful choice of the position of the rolls can straighten metal plates. This task was carried out with help of the Dienst Elektronische en Mechanische Ontwikkeling (DEMO) at TU Delft.

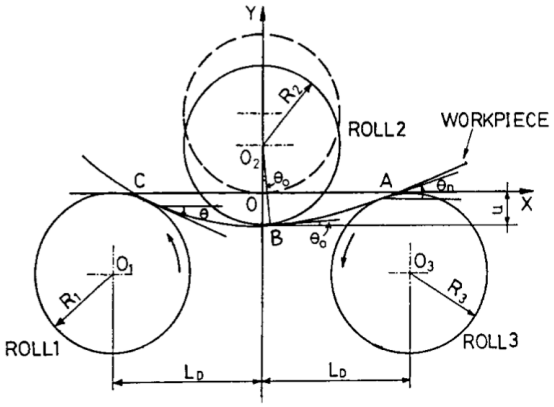

Figure 5.9: Schematic of a pyramid type three-roll bending machine, from Yang and Shima (1988)

After the rolling, it had to be verified that the geometry of the protrusions had not changed, especially the height. The previously introduced wide-area 3D measurement microscope, model *Keyence VR-5000* was used for this purpose. The height profiles of an unrolled and a rolled plate were used to determine the mean protrusion height; a comparison of the two confirmed that the height had not been affected by the rolling. In both cases, the height of the protrusions was approximately 90 μm.

While the rolling did solve the problem for most of the plates that were not swinging initially, two of them did not swing after several repetitions of the rolling process. Eventually, these two models had to be manufactured a second time.

In this second part of the report, the selected test plate designs have been motivated. Then the process to create the geometric models has been explained, followed by a description of the manufacturing and validation method. These are all required steps to create the necessary test plates. In the next part of the report, the experimental apparatus is detailed before presenting and discussing the results of the measurements.

III

Wind tunnel experiments

6

Experimental apparatus

This chapter presents the experimental setup and the measurement techniques used in this Master thesis. The setup and the techniques have been chosen to answer the research questions adequately. The drag performance is quantified by means of a direct force measurement, which yields the integrated skin friction force over the entire plate. Section 6.1 gives a detailed explanation on the direct force measurement. For the quantitative visualisation of flow structures, for example, to analyse the coherent structures close to the wall or to visualise the flow in the corners of the wind tunnel, particle image velocimetry (PIV) was used, as discussed in section 6.2. Finally, the technique of fluorescent oil visualisation is briefly addressed in section 6.3 as an option to visualise the flow on the wind tunnel walls or other surfaces exposed to the flow.

All experiments were performed in the M-tunnel in the Low-Speed Laboratory at the Delft University of Technology. This open-circuit wind tunnel has a maximum velocity of around 35 m/s, a turbulence intensity of approximately 0.7% at 24.7 m/s free stream velocity (Lin, 2021) and a test section of 400 × 400 mm^2. Figure 6.1a shows an image of the M-tunnel, where the relevant components have been labelled. As introduced in section 5.1.1, the boundary layer has a development length of 600 mm before reaching the leading edge of the test plate, thanks to an extension used to initiate a turbulent boundary layer, which has been introduced in section 5.1.1. Depending on the desired measurement (i.e. direct force measurement or PIV), the extension is followed by a custom balance called the 'Hill' or by a 3D printed mock-up referred to as the 'PIV-Hill' or 'PHill'. The test section has two transparent acrylic walls for optical access: one on the top (ceiling) and one on the side. The side wall also acts as a sliding door to access the test section, for example, to install a test plate. The position of the extension and the 'Hill' assembly inside the test section is shown in figure 6.1b. When the assembly is installed inside the test section and a test plate is in place, the available test section is reduced by 30 mm in height to 400 × 370 mm^2 (width × height).

6.1. Direct force measurements

In simple terms, a direct force measurement involves attaching the element that will experience a force to a load cell and reading the output from said load cell. However, this technique presents several challenges for skin friction measurements because the occurring forces (or force changes) are very low, sometimes falling within the measuring tolerance of the load cell itself. A straightforward approach to solve this problem is to choose the test plate as large as possible and to test at the highest velocities possible to increase the skin friction and, hence, the load captured by the sensor (Oguri and Kohama, 1996). Nonetheless, there are limitations to this 'solution', namely the size of the wind tunnel section and the fact that most initial test campaigns are performed at low-speed wind tunnel facilities. A further challenge of balance measurements is that of unwanted force contributions: while only the shear force of the test plate is of interest, other force components can interfere with the measurements due to the three-dimensional nature of the test specimen. Some examples of unwanted contributions are gravity, suspension forces and pressure differentials (van Nesselrooij et al., 2022).

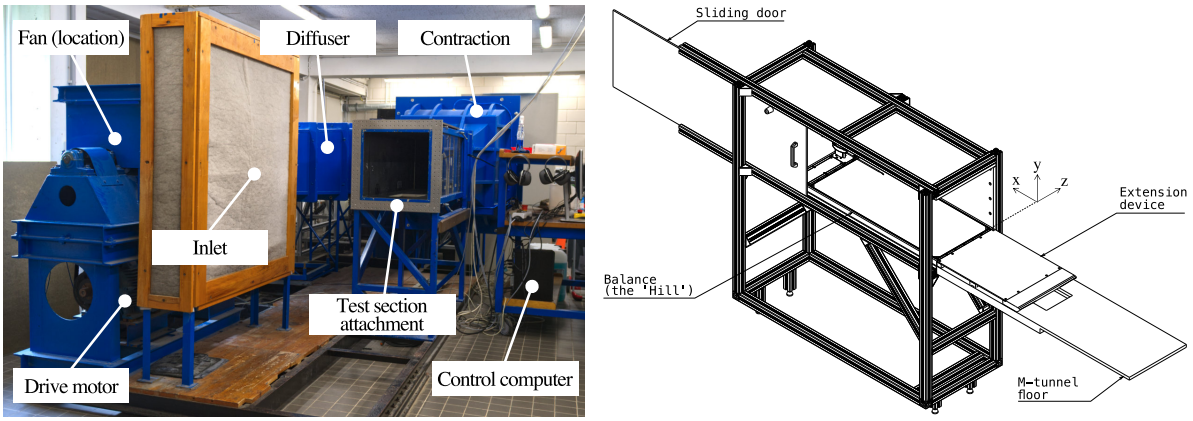

(a) M-tunnel in an open-circuit configuration without the test section installed

(b) Test section with the 'Hill' and the extension device, modified from Lai (2021)

Figure 6.1: Main M-Tunnel components and CAD drawing of the test section

To circumvent possible challenges, the 'Hill', a device specifically developed to study skin friction reduction applications with an effect of 0.5% or higher, was used for the experiments. This apparatus for flat plate drag measurements has been developed by van Nesselrooij et al. (2022). The researchers report a root-mean-square repeatability of less than 0.2% of the drag coefficient for this instrument at drag values > 1 N. The device takes test plates with a dimension of $881.3 \times 366.3 \times 5$ mm^3 and is designed to provide an almost automated measurement of the skin friction force over that plate, automatically correcting for pressure differentials and other sources of errors. Figure 6.2 shows a detailed illustration of the core of the measurement system where all components have been labelled. This core is combined with extensions depending on the desired configuration or wind tunnel facility. As mentioned previously, the extension with an elliptical leading edge and an opening was chosen for the experiments. The invention is also equipped with a so-called 'data periscope' that features a Pitot tube on the top, a hot-wire transverse probe, and a temperature and humidity sensor. These probes and sensors collect data on the flow conditions in addition to the force measurements (van Nesselrooij et al., 2022).

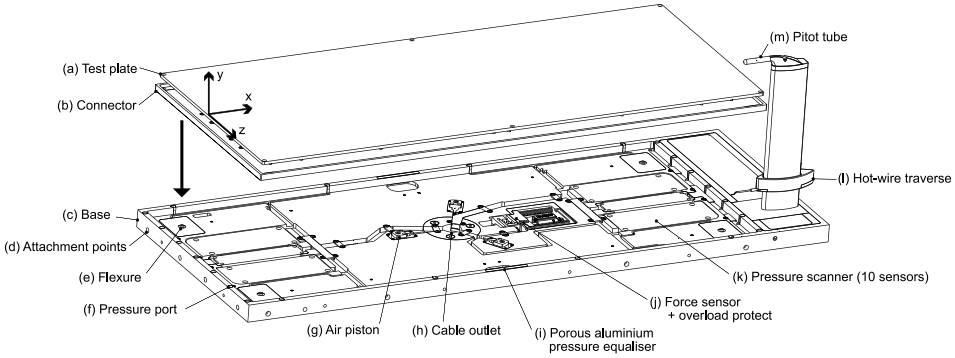

Figure 6.2: Detailed illustration of the components of the measurement system with names, from van Nesselrooij et al. (2022)

6.1.1. Methodology

In their paper, van Nesselrooij et al. (2022) also present a methodology to use their apparatus correctly to obtain very accurate and precise measurements. The test plate with the surface modification is measured in combination with a reference smooth test plate in a process involving seven velocity sweeps of increased velocities. The measurements of the modified test plate are always preceded and followed by the measurement of a smooth reference plate (i.e. measurements 1, 3, 5, and 7 are with the smooth test plate installed, and measurements 2, 4, and 6 are performed with the modified test plate). The accuracy of the measured drag coefficient for the modified plate is increased by considering the reference measurements at the same Reynolds number.

For the experimental campaign presented in this Master thesis, 57 configurations had to be tested (without counting trial runs and repeated measurements). For efficiency reasons, the proposed methodology was modified to test four plates in one round ('quadruple sandwich'). The exact measurement sequence is depicted in table 6.1. A warm-up round is recommended at the beginning of the 'sandwich'. Each measurement takes approximately eight minutes and is followed by a five minutes wind tunnel cool-down. During the eight minutes, an initial measurement is taken for a free-stream velocity of 0 m/s. Next, ten measurements are taken between 25% and 100% of the wind tunnel rotational speed (maximum: 2900 rpm), followed by the last measurement at 0 m/s. The data acquisition time is 15 s. The advantage of measuring in a 'quadruple sandwich' becomes apparent when comparing the total duration of 216 minutes (or 1 hour 36 minutes) with four times the duration of a 'single sandwich'; namely four times 99 minutes, or 396 minutes. The measurement of four plates in a 'quadruple sandwich' is 45.5% quicker than four 'single sandwiches' measurements. Of course, this concept can be applied to a different number of plates; for time-constraint reasons, the sandwich was also made with a different number of plates on some occasions.

Index		Name	Duration [min]
0		Warm-up (TP0000)	8 + 5
1		Reference (TP0000)	8 + 5
2	2-1	Design 1	8 + 5
	2-2	Design 2	8 + 5
	2-3	Design 3	8 + 5
	2-4	Design 4	8 + 5
3		Reference (TP0000)	8 + 5
4	4-1	Design 1	8 + 5
	4-2	Design 2	8 + 5
	4-3	Design 3	8 + 5
	4-4	Design 4	8 + 5
5		Reference (TP0000)	8 + 5
6	6-1	Design 1	8 + 5
	6-2	Design 2	8 + 5
	6-3	Design 3	8 + 5
	6-4	Design 4	8 + 5
7		Reference (TP0000)	8
		Total duration	216

Table 6.1: Measurement sequence for a quadruple sandwich with the Hill

6.1.2. Processing and analysis

During the measurement, the data is written to three text files that contain the force values, the pressure values, and ambient conditions, respectively. These files are post-processed using a MATLAB code specifically developed for handling the 'Hill' data. This code computes the drag difference between the desired design and a reference test plate (ΔC_D). For the reference plate, TP0000 was used. A pressure and a null force correction are applied to the results. The pressure correction takes into account the secondary drag force that can arise from pressure differences in the gap between the free-swinging element and the stationary part of the 'Hill'. Pressure taps are installed in the air gap to monitor the pressures in order to quantify the magnitude of the additional force and correct it. Concretely, 7 pressure taps are distributed horizontally (i.e. spanwise) along the leading edge and 8 along the trailing edge air gaps of the plate. The additional pressure tap in the trailing edge gap offers information about the vertical variation in pressure at the plate's midspan. Eight additional pressure taps along the long edge of the apparatus (four on each side) monitor the pressure gradient in the streamwise direction (van Nesselrooij et al., 2022). For the null force correction, the first and the last measurements (i.e. the measurements at $U_\infty = 0$) are compared, and possible discrepancies are taken into account. The null force correction is also used as an indication of the quality of the measurement; a high correction usually points toward a problem with the test plate, for example, that it is not swinging freely, as discussed in section 5.4.

The main output of the post-processing used for the results presented in the next chapter (7) is the corrected and averaged drag difference values for each configuration. These values are available for the ten measurement points as a function of Re_1, which is the Reynolds number per metre:

$$Re_1 = \frac{\rho U_\infty}{\mu} = \frac{U_\infty}{\nu}. \tag{6.1}$$

Since the rotational speed of the tunnel at which the measurements are taken is always the same, but the ambient conditions change, the Re_1 values for which data points are available vary between plates. In order to compare the results of different plates, a Re_1 value is selected within the measured range, and the corresponding drag difference (ΔC_D) value is determined by linear interpolation.

6.1.3. Measurement error metric

In order to quantify the effect of using different aluminium base plates for the models, five arbitrary flat plates have been measured. The drag difference between these plates and the reference smooth plate (TP0000) is depicted in figure 6.3. The error bar included in the figure indicates the RMSD between repeated measurements. It can be seen that the RMSD values are very low, 0.22% on average, indicating good repeatability of the measurements.

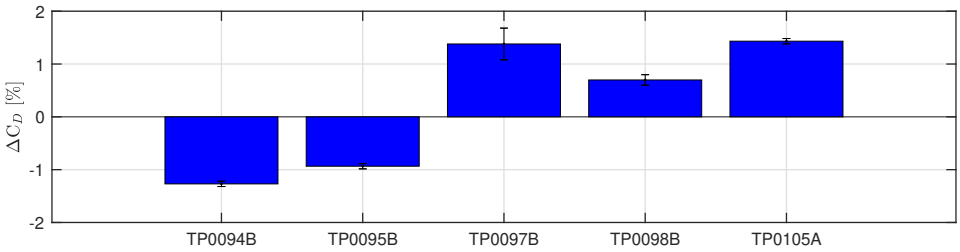

Figure 6.3: Drag difference between five randomly selected smooth plates and the reference flat plate TP0000 at $Re_1 = 2 \times 10^6$; the error bars indicate the repeatability RMSE of the measurements

As can be observed in figure 6.3, the drag difference (ΔC_D) between the five randomly selected flat plates and the reference flat plate (TP0000) is in the order of 1% for the selected Re_1. This result means that a measured drag difference between a protrusion model and TP0000 will have a contribution from the base plate that is independent of the protrusion design. With these results in mind, it is considered inadequate to use the RMSD value for repeatability as an error bar when comparing different configurations. For this reason, a new error metric has been defined that includes the uncertainty of a randomly selected flat plate. This new error metric is computed as the RMSD of the ΔC_D values of the five flat plates with respect to the expected value of zero. Since the RMSD value for repeatability is much lower than the RMSD for flat plate uncertainty, it is considered negligible, and only the latter will be used in the results.

6.2. Particle image velocimetry

Particle image velocimetry (PIV) is a non-intrusive quantitative flow visualisation technique that yields the instantaneous velocity vectors in a selected plane of the flow field. The acquired data can be further post-processed to display other flow values, such as vorticity. For PIV, so-called tracer particles are introduced in the flow; these particles are small enough to follow the flow without altering its properties. Laser light is shaped into a light sheet covering the plane of interest through several optics. The bright laser light illuminates the particles going through the laser sheet plane, which scatter light that is captured by an optical sensor, such as a digital camera. From an image pair taken within a short time interval, the displacement of the tracer particles can be evaluated, and, since the time interval is known, also the velocities can be determined. Compared to other methods such as HWA, an advantage of PIV is that it provides the instantaneous velocities of the entire flow field; this is required to observe coherent structures in the flow and other features that do not appear in the averaged velocity flow field.

There are several types of PIV depending on the number of cameras and quantities of interest. According to the objectives of this thesis, the primary purpose of the visualisation is to verify the working

mechanism hypothesis, for which planar PIV suffices. Planar PIV captures two velocity components in a two-dimensional space; hence it is considered a two-dimensional two-component technique or 2D-2C for short. A typical arrangement for planar PIV is shown in Figure 6.4. For information on alternative types of PIV setups and practical resources on using PIV, please refer to Raffel et al. (2018).

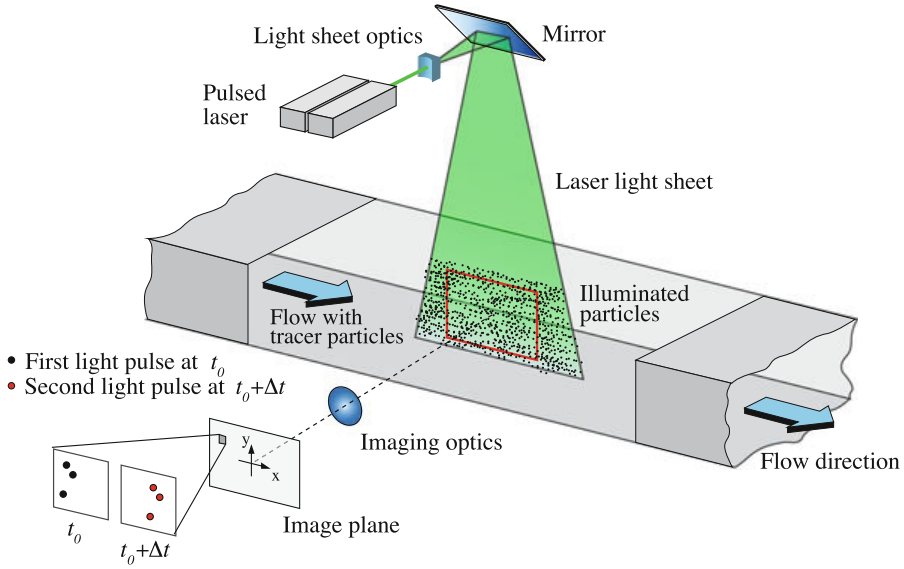

Figure 6.4: Schematic arrangement for a planar 2D-2C PIV measurement in a wind tunnel, from Raffel et al. (2018)

From Figure 6.4, it can be seen that the PIV setup has many components and an overall high level of complexity. This figure also shows schematically how the particle displacement can be determined from the image pair.

6.2.1. Experimental setup

The PIV measurements were performed in the M-tunnel in the Low-Speed Laboratory at the Delft University of Technology. Figure 6.5 shows a picture of the experimental setup used for the wall-parallel plane, the relevant components of the setup have been labelled.

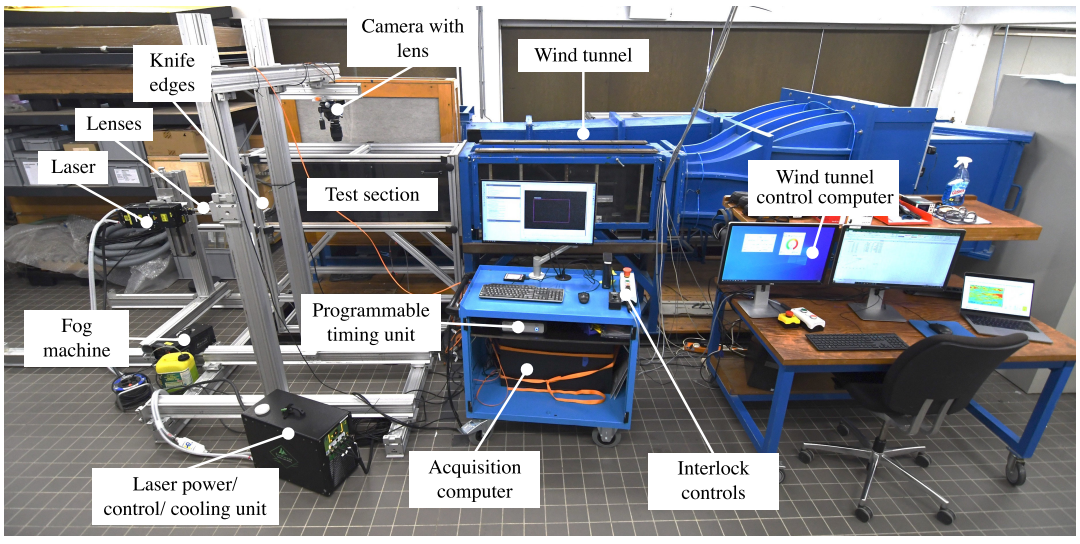

Figure 6.5: PIV setup in the M-tunnel for wall-parallel x-z-plane

Wind tunnel The PIV experiments are performed in the M-tunnel, which is controlled using a LabView application from the **wind tunnel control computer**. The test plate of interest is in the 'PHill',

installed inside the **test section**. For the different measurements, the wind tunnel is run between 5 m/s and 20 m/s. The wind tunnel control computer gives a velocity reading different from the one used for the balance measurements because both use probes situated in different locations. In order to match the conditions from the PIV experiments as closely as possible to the balance measurements, the fan rotational speed corresponding to different velocities measured by the 'Hill' was considered instead of the live velocity reading provided by the wind tunnel control computers. The rotational speeds corresponding to the velocities of interest for the PIV experiments are shown in table 6.2. This table also includes the wind tunnel's operational point, computed as the ratio between the selected rotational speed and the maximum rotational speed of 2900 rpm. Please note that due to changing ambient conditions, the velocities that are obtained with a set rotational speed vary. For convenience, the velocities will be used in the discussion of the results (although it is the rotational speed that remains constant).

Velocity [m/s]	5	10	20
Fan rotational speed [rpm]	420	840	1680
Operational point [%]	14.48	28.97	57.93

Table 6.2: Fan rotational speeds corresponding to different free stream velocities

Fog generator When the wind tunnel is running, the tracer particles are introduced using a SAFEX Fog 2010+ fog generator located close to the wind tunnel inlet. The fluid SAFEX-Inside-Nebelfluid 'Normal/Power Mix' is used to produce water-glycol droplets with an approximate diameter of 1 μm.

Laser The fog particles are illuminated using a double-pulsed ND:Yag Evergreen 200 laser by Lumibird (Quantel laser). Some technical details of the laser can be found in table 6.3. The laser head is mounted on a micrometre slider to allow for a precise adjustment of the laser height. A series of **lenses** attached to the laser head shape the laser beam into a thin sheet. The lenses used to shape the laser beam are a combination of plano-convex round cylindrical lenses ('cylindrical positive'), plano-concave lenses ('spherical negative'), and bi-convex lenses ('positive spherical'). All the lenses are manufactured from N-BK7 optical glass and are coated with a broadband anti-reflection coating on both sides for the wavelength range: $350 - 700$ nm (Thorlabs, Inc., 2022). The thickness and orientation of the laser sheet depend on the desired plane and will be detailed in section 6.2.2. To further shape the laser sheet and eliminate reflections, **knife edges** are positioned following the lens setup. The laser head is connected through a cable and two cooling pipes to an **external unit** which acts as a power, control, and cooling unit.

During the laser operation, laser safety goggles must be worn. Furthermore, The laser is connected to an **interlock** system by Lasermet. This system ensures that the laser cannot be operated if the laboratory door is open and instantaneously shuts down the laser if the door is opened during operation. Furthermore, safety screens were installed in the lab for the duration of the PIV experiments.

Wavelength	[nm]	532
Pulse repetition rate	[Hz]	15
Energy	[mJ]	200
Near field beam diameter	[mm]	<6.35
Beam divergence	[mrad]	<4

Table 6.3: Technical details Evergreen 200 laser (Lumibird, 2020)

Camera The illuminated plane with the tracer particles is captured by a digital camera positioned perpendicular to the illuminated plane. The Imager sCMOS CLHS camera by LaVision has a resolution of 2560×2160 pixels with a pixel size of 6.5×6.5 μm^2 and a digital output of 16 bit. The exposure can be set between 15 μs and 100 ms. The camera has an F-mount for attaching **lenses** (LaVision, 2020). The used lens depends on the required field of view (FOV) and will be specified in section 6.2.2, where the individual planes are presented.

Acquisition computer An acquisition computer controls the measurement using the DaVis 10 by LaVision. The images from the camera are acquired via a direct optical fibre connection between the camera and the computer. For synchronising the laser pulse with the camera's shutter, a programmable timing unit (PTU X, by LaVision) is used. The camera trigger, the laser Q switches, and the lamp switches are connected to this device, which communicates with the acquisition software. The PTU X controls the timing of the laser and the exposure of the camera in double frame mode. A schematic of the trigger sequence is shown in figure 6.6.

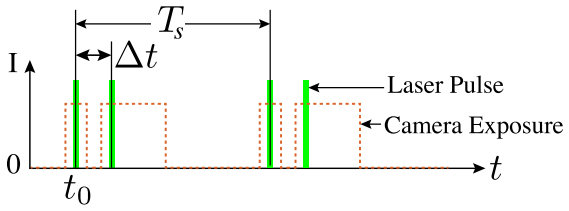

Figure 6.6: Laser and camera synchronisation diagram, modified from Rius Vidales (2022)

The orange dashed line represents the camera exposure, and the green bars illustrate the laser pulse. The time between two image pairs is denoted by T_s, which is related to the sampling frequency f_s as:

$$f_s = \frac{1}{T_s}, \tag{6.2}$$

for good PIV measurements, the sampling frequency must be chosen such that subsequent image pairs are uncorrelated. In other words, T_s has to be large enough to allow a particle to travel through the entire FOV. A sampling frequency of $f_s = 30$ Hz was used for the PIV measurements. It was checked that this frequency is adequate for uncorrelated measurements since it is lower than the lowest required frequency of 64 Hz for 5 m/s in the x-z plane.

The time between images or frames in a pair is denoted by Δt. The time between image pairs has to be adjusted to ensure an adequate particle displacement; a common rule of thumbs to determine Δt is the one-quarter rule, which states that no more than one-quarter of the particles in the frame should leave the FOV in Δt. This value depends on the velocity and the FOV; the values used for the different planes will be presented in section 6.2.2.

6.2.2. PIV planes

The PIV technique was used for two purposes in this thesis: to visualise the low-speed streaks in the flow region close to the wall and to visualise the flow in the corner regions of the wind tunnel. These two applications required different planes and settings, which are detailed in this section.

x-z plane: coherent structures

For the visualisation of the coherent structures close to the wall, a wall-parallel x-z plane was chosen. The objective of this plane is to visualise the low-speed streaks, which are located in the buffer layer ($5 \leq y^+ \leq 30$) and are most energetic around $y^+ \approx 15$, as discussed in section 2.2. It is known that the theoretical viscous length scale is roughly 30 μm at a free-stream velocity of 10 m/s (see figure 5.2). With this value for the viscous length scale, the target layer is located between 150 μm and 900 μm away from the wall. These values show that the laser sheet has to be very close to the wall (0.15 mm) and that it has to be very thin (< 750 μm). For reference, a typical PIV laser sheet is between 1.5 mm and 2 mm thick. The spanwise and streamwise sizes of the FOV are chosen much larger than the expected spanwise spacing ($100\delta_v$) and streamwise lenght ($1000\delta_v$). With this criterion in mind, the FOV was given by the closest position of the camera to the wind tunnel with the available lens (f = 105 mm). Last, the position of the FOV was chosen as close as possible to the trailing edge and roughly at the mid-span of the plate so that the BL has the longest development length possible and has the maximum thickness without any disturbances from potential corner vortices. The exact location of the plane with respect to the test plate is shown in figure 6.7a. For this setup, the laser head was positioned at the outflow of the wind tunnel pointing towards the flow and the camera was positioned perpendicular to the test plate above the test section, as shown in figure 6.5.

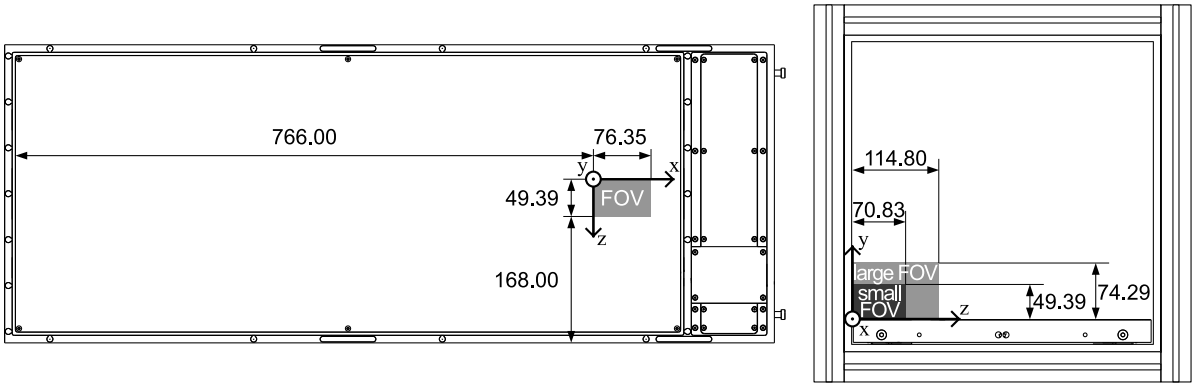

(a) Field of view for x-z plane

(b) Field of view for y-z planes (large and small)

Figure 6.7: Size, position, and local coordinate systems for the fields of view for the PIV experiments; all dimensions in mm

For the x-z plane, a lens combination consisting of a spherical negative lens (focal length f = −50 mm), followed by two spherical negative lenses (focal length f = −100 mm), and a cylindrical positive lens (focal length f = +100 mm) was used. The distance between the lenses is shown in figure 6.8a. With this lens setup in combination with the laser and sharp knife edges, a thin laser sheet with an estimated laser sheet thickness of 0.71 mm was obtained. This sheet meets the requirements discussed previously. The thickness is determined with the help of millimetre paper; the paper is placed at a 45° plane to increase the projected laser sheet thickness and have a more accurate reading (figure 6.9b). The read value is corrected by dividing it by $\sqrt{2}$. The constant thickness of the laser sheet over the FOV can be verified using the same method (figure 6.9a). Once the laser sheet is ready, the laser head is lowered as much as possible to get very close to the wall without having strong reflections affecting the results. Figure 6.8b shows the final laser sheet over the plate and the knife edge setup.

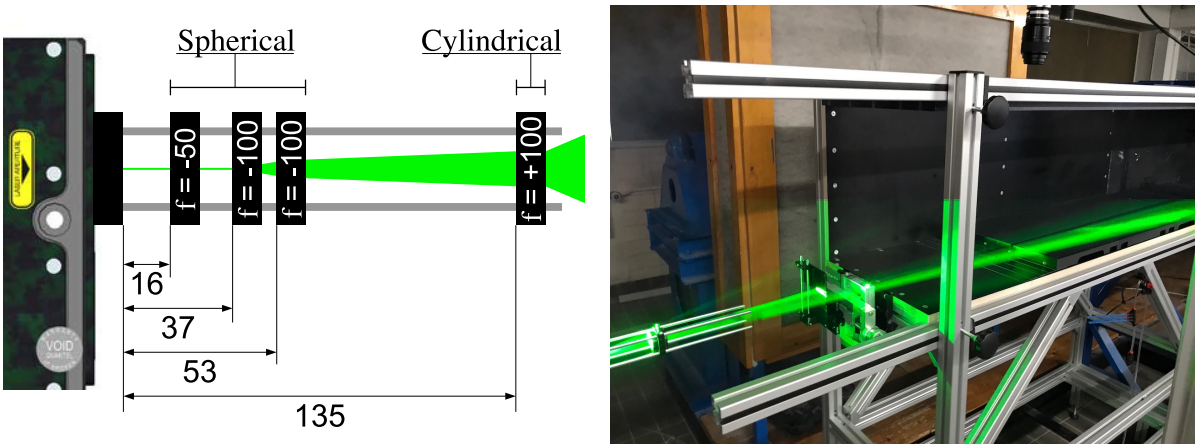

(a) Lenses for PIV thin sheet; focal length and dimensions in mm; not to scale; laser head illustration from Lumibird (2020)

(b) Laser sheet over the test plate

Figure 6.8: Lens setup and final PIV laser sheet over the test plate

The camera calibration was performed with a millimetre paper placed on the test plate (i.e. the location of the laser sheet). An image of the millimetre paper was taken in DaVis, where the origin and a length scale can be indicated to compute the magnification and define the axes. In order to check the perpendicularity of the camera with respect to the FOV, the pixel size of each side of the largest square in the calibration image was compared (top: 1344 px, bottom: 1339 px, left: 1343 px, right 1342 px); the maximum difference was found to be of 5 px or 0.37%, which is considered negligible and, hence, no perspective correction is deemed necessary.

This plane was tested at 5 m/s, at 10 m/s, and at 20 m/s. The 20 m/s were selected because the pro-

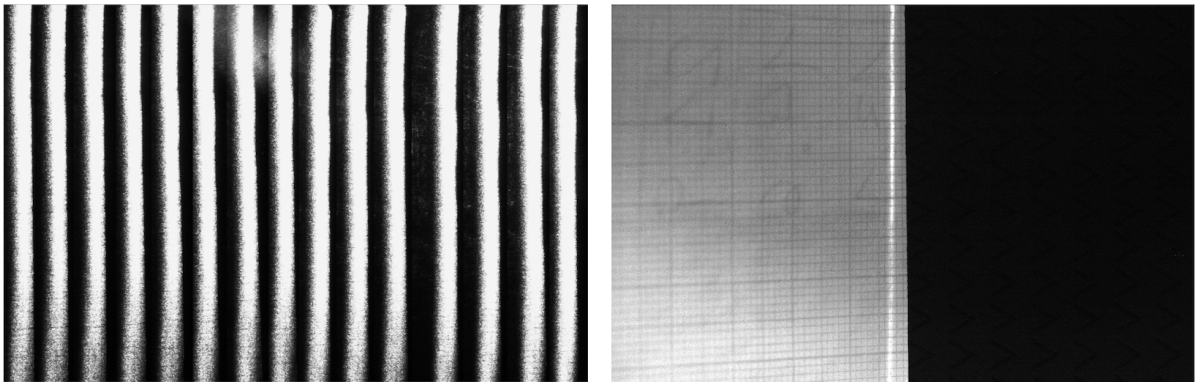

(a) Initial laser sheet thickness over the entire FOV, laser sheet reflection on 45°plane

(b) Laser sheet on a 45°plane at 60% power

Figure 6.9: Laser sheet thickness estimation with millimetre paper

trusions had been designed for this velocity. The 5 m/s were selected because of the thicker boundary layer and larger viscous length scale at lower velocities. Finally, the 10 m/s were chosen to have a measurement in between to analyse trends in the data. No tests were performed above 20 m/s because the boundary layer becomes too thin, and it is not possible to reach the position and thickness targets. The time between frames in a pair (Δt) was chosen to achieve a particle displacement of roughly 10 px for all three velocities. For this purpose, a time between frames Δt of 80 μm for 5 m/s, 40 μm for 10 m/s, and 20 μm for 20 m/s was chosen. Due to the proximity to the wall, the wall-normal velocity component led to many particles leaving the laser sheet for longer Δt values. A too short particle displacement is also not ideal since it can lead to noise in the measurements. A displacement of 10 px was found to be a good compromise. For the x-z plane, 600 image pairs were recorded for every configuration. Further details of this plane can be obtained from table 6.4.

		x-z plane	y-z plane (small FOV)	y-z plane (large FOV)
Test plates	[-]	TP0000 Sirovich aligned$^{\Delta}$ Sirovich random$^{\Delta}$ Delta aligned$^{\Delta}$ Delta random$^{\Delta}$	TP0000	
Field of view	[mm × mm]	76.35 × 49.39	70.83 × 45.82	114.8 × 74.29
Image size	[px × px]	2560 × 1656		
Scale factor	[px/ mm]	33.53	36.14	22.29
Focal length	[mm]	105	200	
F-stop	[-]	8		
Exposure time	[μs]	15		
Laser power	[%]	60		
Image pairs	[mm]	600	1200	
Velocities	[m/s]	5 10 20	5 10 20	
Δt	[μm]	80 40 20	100 and 50 / 50 and 25 / 25 and 12	
Max particle displacement	[px]	≈10	≈1.8 and ≈0.85	≈0.65 and ≈0.3

Table 6.4: PIV settings; '$^{\Delta}$': test plates measured in apex upstream and apex downstream orientations

y-z plane: corner vortices

For the second round of PIV experiments, the corner region of the wind tunnel had to be captured. For this purpose, the y-z wall-normal plane was chosen. The laser was positioned on the side of the wind tunnel, and the camera in the outflow pointing towards the flow (small FOV). Since the camera shake was noticeable at higher velocities, the setup was modified, and the camera was positioned right outside

of the outflow, pointing towards a mirror positioned in the outflow at 45°(large FOV). The final setup is shown in figure 6.10.

(a) General view

(b) Detailed view: camera and mirror assembly

Figure 6.10: PIV setup for y-z wall-normal plane

These measurements aimed to understand the flow in the corner regions and quantify the size of possible corner vortices. Since the exact extent of the corner vortices is unknown, the size was approximated from the thickness of the boundary layer, namely ≈ 35 mm at the trailing edge of the test plate for 5 m/s (figure 7.1); note that the side wall boundary layer is not trimmed and is hence expected to be larger. With this in mind, two FOVs were selected: a small one (70.83 mm × 45.82 mm) to capture the corner in detail with a high resolution and a large one (114.8 mm × 74.29 mm) to identify larger flow structures. The position of the FOV is shown in 6.7b. The bottom left corner (in the orientation shown in the figure) was chosen for convenience since it is the only corner where two black walls come together. The same flow behaviour is expected in all four corners. The y-z plane was chosen very close to the trailing edge (800 mm from the plate's leading edge) since larger corner vortices are expected downstream.

The lenses used to transform the laser beam into a sheet were the same as presented for the x-z plane. However, the distance between these lenses was adjusted, and the knife edges were removed to obtain a thicker laser sheet. Since the particles that move with the free-stream velocity cross the laser sheet perpendicularly, a particle enters and leaves the laser sheet very quickly. For this reason, it is advantageous to have a thicker laser sheet (which means a longer time from entering to leaving the illuminated volume). The maximum thickness obtained was 2 mm, since the laser had a defect and projected a shadow in the centre of the beam, which became noticeable for thicker sheets. The velocities selected for this plane were also 5 m/s, 10 m/s, and 20 m/s. The thickness of the laser sheet and the selected velocities determine the maximum allowable Δt for the tests, as shown in table 6.5. The row 'max Δt' indicates the time that a particle needs to cross the illuminated volume assuming a path perpendicular to the laser sheet (computed as thickness/ velocity). 'max Δt 1/4 rule' is the maximum Δt that can be used for the measurements according to the one-quarter rule. The last row gives half the one-quarter rule value. For the measurements, the values in bold font were used. In summary, twelve measurements were taken for this plane: six for each FOV. For each FOV, three velocities were tested with two different Δt values. All the measurements were performed for the smooth reference plate TP0000.

Velocity	[m/s]	5	10	20
max Δt	[μs]	400	200	100
max Δt 1/4 rule	[μs]	**100**	**50**	**25**
half max Δt 1/4 rule	[μs]	**50**	**25**	**≈12**

Table 6.5: Δt estimation for three different velocities for the y-z plane with 2 mm thickness

The same calibration procedure and check for perpendicular position of the camera as explained for the x-z plane were used in this case. For more details about the settings used for this plane, please refer to table 6.4. For the y-z plane, 1200 image pairs were recorded for every configuration.

6.2.3. Processing and analysis

Once the image pairs have been captured, the next step is to process them.

- First, the image pairs are pre-processed to eliminate unwanted reflections and improve the results in later steps in DaVis.
- Next, the velocity vector field is determined from a cross-correlation analysis of the images performed in DaVis.
- Finally, the vector fields are post-processed in MATLAB.

In this section, these three steps are explained in more detail.

Pre-processing

The raw images have some reflections and background noise that affect the cross-correlation result. A Butterworth high pass filter with a length of seven images was applied to remove these unwanted reflections. This filter can remove reflections ('low frequencies') but comes at the cost of reduced image intensity. However, the remaining intensity was sufficient for the subsequent steps. A comparison between the raw and Butterworth-filtered image for the x-z plane can be found in figure 6.11.

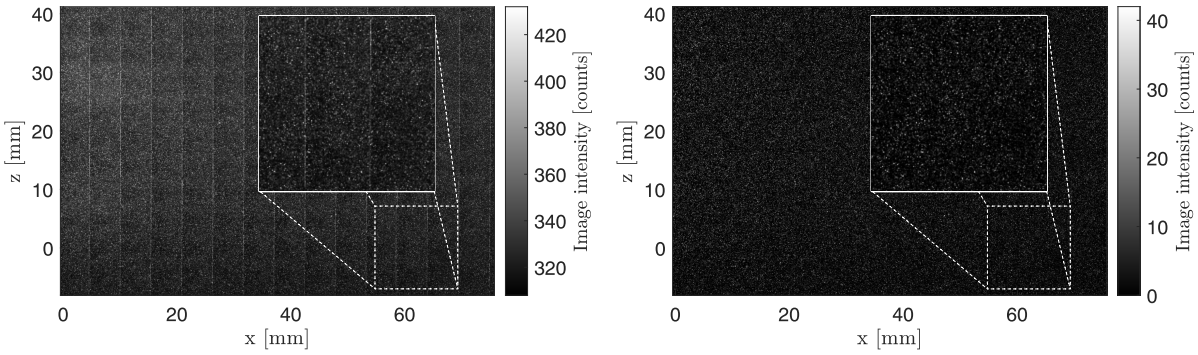

(a) Raw image (b) Pre-processed image

Figure 6.11: Comparison between the raw and pre-processed image for the x-z plane; the area in the dashed square has been enlarged

In the case of the y-z plane, the same filter was applied. Additionally, the image area close to the wall was masked to eliminate very strong reflections that could not be removed with the filter. The reflections were more pronounced than for the x-z plane because the laser was pointing directly against the wall. The filtered image (before the masking) can be found in figure 6.12.

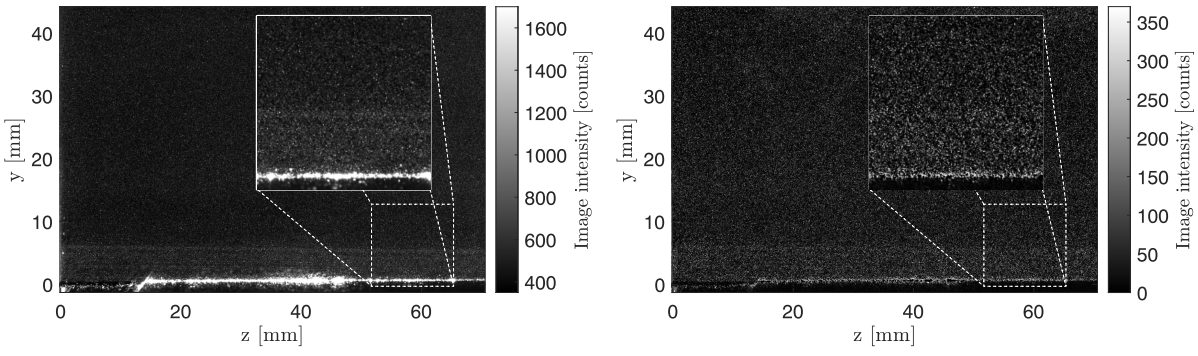

(a) Raw image (b) Pre-processed image

Figure 6.12: Comparison between the raw and pre-processed image for the y-z plane (small FOV); the area in the dashed square has been enlarged

Cross-correlation

By applying the cross-correlation to an image pair, it is possible to determine the instantaneous particle displacement from the correlation peaks and, ultimately, the instantaneous particle velocities. For this, the image is divided into interrogation windows; each interrogation window yields a displacement/ velocity value. A multi-pass approach was chosen for the cross-correlation analysis, meaning that the cross-correlation is performed several times with decreasing window sizes. The settings used for the different PIV planes are presented in table 6.6. These settings were selected following several tests and best practices.

		x-z plane	y-z plane
Initial	Window size	96 × 96	64 × 64
	Shape	square 1:1	ellipse 2:1
	Overlap	75%	75%
	Passes	1	1
Final	Window size	16 × 16	48 × 48
	Shape	square 1:1	ellipse 2:1
	Overlap	75%	75%
	Passes	2	2
Geometric mask		Off	On

Table 6.6: Cross-correlation settings

An example of a test to determine the cross-correlation parameters is shown in figure 6.13. The smaller the final pass interrogation window size, the more vectors are present in the final vector field; hence, the smaller the flow features that can be resolved. However, if the window size is too small, the results become noisy. This behaviour is because not enough particles are present in the small interrogation window to determine the flow velocity accurately. In the mentioned figure, the final window sizes 12 × 12 and 16 × 16 are compared. It can be seen that the results are much noisier in the case of 12 × 12. Furthermore, 16 × 16 already resolves the flow features of interest (i.e. the streaky regions of low velocity). For the mentioned reasons, the final pass interrogation window size of 16 × 16 was chosen for the cross-correlation of the x-z plane images.

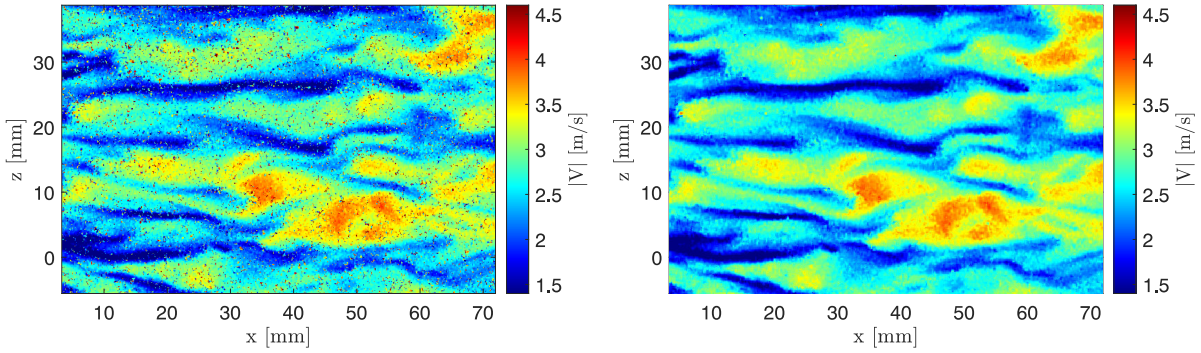

(a) 12 × 12 final pass window size

(b) 16 × 16 final pass window size

Figure 6.13: Comparison between final pass window sizes for the x-z plane; instantaneous velocity field for TP0109A at 5 m/s

Post-processing

For the x-z plane, basic post-processing, such as the computation of the mean vector field and the standard deviation, was done in DaVis. For more complex analyses, the vector data was exported as a .dat file to be used in MATLAB. One of the analyses performed with MATLAB is the two-point correlation used to determine the characteristics of the low-speed streaks, as explained in section 2.2.3. Furthermore, the standard deviation was used as a proxy for the strength of the low-speed streaks.

For the y-z plane, the average flow field was computed in DaVis before exporting the data to MATLAB for visualisation. The length scales were made non-dimensional with the boundary layer thickness for better comparison with literature data.

6.2.4. Uncertainty quantification

The relative uncertainty of the instantaneous velocity fields is computed using a correlation factor based on the measurement uncertainties of modern digital cameras used for PIV ($\epsilon_{\Delta x_{px}}$) and the average pixel displacement in the plane ($\overline{\Delta x_{px}}$). Raffel et al. (2018) proposes a correlation factor of $\epsilon_{\Delta x_{px}} = 0.1$ px, which will be employed here:

$$\epsilon_u = \frac{\epsilon_{\Delta x_{px}}}{\overline{\Delta x_{px}}}, \tag{6.3}$$

the average pixel displacements can be substituted by the mean velocity ($\bar{u}$), the scale factor (M), and the time between frames (Δt), yielding:

$$\epsilon_u = \frac{\epsilon_{\Delta x_{px}}}{\bar{u} \times M \times \Delta t}. \tag{6.4}$$

The uncertainty in the statistical quantities used in this report is also analysed. According to Sciacchitano and Wieneke (2016), the uncertainty of the mean velocity in streamwise direction is defined as:

$$\epsilon_{\bar{u}} = \frac{\sigma_u}{\sqrt{N}}, \tag{6.5}$$

the uncertainty of the standard deviation is defined as:

$$\epsilon_{\sigma_u} = \frac{\sigma_u}{\sqrt{2(N-1)}}, \tag{6.6}$$

and the uncertainty of the variance as:

$$\epsilon_{\sigma_u^2} = \sigma_u^2 \sqrt{\frac{2}{(N-1)}}, \tag{6.7}$$

where N is the number of independent samples. The same is valid for other velocity components, where u is replaced by v or w. These equations are valid for large sample sizes $N \leq 30$ with an accuracy of 1% (Ahn and Fessler, 2003). The use of these equations is justified in the cases considered here ($N = 600$ and $N = 1200$) since both have a number of frames larger than 30. Note that the uncertainty in time is neglected since it is much lower than the spatial uncertainty (in the order of 100 times smaller). The uncertainty quantification is performed on the vector fields after cropping margins and reflections.

Tables 6.7 and 6.8 show the uncertainties for the x-z and y-z planes, respectively. Note that for brevity, only a selection of the results for TP0000 is presented in the tables. The full uncertainty data for all PIV test cases can be found in appendix E for the x-z plane (table E.1) and in appendix F for the y-z plane (table F.1). Note that only the relevant uncertainty parameters have been computed for each plane.

U_∞ [m/s]	ϵ_u [%]	ϵ_w [%]	$\epsilon_{\bar{u}}$ [m/s]	$\epsilon_{\bar{w}}$ [m/s]	$\epsilon_{\sigma(u)}$ [m/s]	$\epsilon_{\sigma(w)}$ [m/s]	$\epsilon_{\sigma(u)^2}$ [m^2/s^2]	$\epsilon_{\sigma(w)^2}$ [m^2/s^2]
5	1.38	359.5	0.0236	0.0127	0.0167	0.0090	0.0194	0.0056
10	1.22	302.0	0.0406	0.0263	0.0287	0.0186	0.0573	0.0240
20	1.16	172.7	0.1029	0.0704	0.0728	0.0498	0.3813	0.1767

Table 6.7: Selection of PIV uncertainty values for the x-z plane with TP0000

6.3. Fluorescent oil visualisation

This qualitative flow visualisation technique is a quick manner to visualise the flow at a surface, more concretely, the flow velocity close to a surface. It is commonly used to visualise flow separation, shocks, and boundary layer transition, among others. This section briefly explains the technique based on Lu (2010), followed by a description of its application in this Master thesis.

FOV [-]	U_∞ [m/s]	Δt [μ s]	ϵ_v [%]	ϵ_w [%]	$\epsilon_{\bar{v}}$ [m/s]	$\epsilon_{\bar{w}}$ [m/s]	$\epsilon_{\sigma(v)}$ [m/s]	$\epsilon_{\sigma(w)}$ [m/s]
large	5	100	906.5	32.62	0.0061	0.0074	0.0043	0.0052
small	5	100	10.0	16.25	0.0058	0.0061	0.0041	0.0043
large	10	50	3290.1	29.10	0.0095	0.0107	0.0067	0.0076
small	10	50	9.4	14.32	0.0115	0.0122	0.0082	0.0087
large	20	25	2474.3	28.20	0.0162	0.0191	0.0115	0.0135
small	20	25	8.9	13.83	0.0217	0.0230	0.0154	0.0163

Table 6.8: Selection of PIV uncertainty values for the y-z plane with TP0000

Working mechanism

A thin layer of mineral oil (roughly 0.1 mm thick) is applied to the surface using a brush. The oil contains fluorescent particles that glow when illuminated with an ultraviolet light source. Differences in thickness of the oil layer (such as oil accumulation or the absence of oil) are visible as different brightness levels.

The case where no oil is present is considered to understand the working mechanism and validity of this technique. If no oil is present between the flow and the surface, the velocity is zero at the wall. However, the gradient $\left(\frac{\partial u}{\partial y}\right)$ increases with the proximity to the wall and achieves a maximum at $\left(\frac{\partial u}{\partial y}\right)_{y=0}$. When a thin layer of oil is present on the wall, the velocity is not zero at the interface between the flow and the oil; the oil is entrained due to this non-zero velocity (and the shear force). While the velocity at the air-oil interface is continuous, the velocity gradient is not. The velocity gradient decreases from air to oil. Furthermore, the velocity profile in the oil is linear due to the low Reynolds number (Stokes regime). In equilibrium conditions, the shear stress has to be continuous at the interface. Recalling equation 2.1 introduced in chapter 2:

$$\tau = \mu_{air}\left(\frac{\partial u}{\partial y}\right)_{y_f+\pi} = \mu_{oil}\left(\frac{\partial u}{\partial y}\right)_{y_f-\pi}, \tag{6.8}$$

where y_f is the height of the oil film, and π is an arbitrarily small distance. Knowing that $\mu_{air} << \mu_{oil}$, it follows that the velocity gradient in the oil region is much smaller than the one in the air region. Considering the small velocity gradient, the small thickness of the oil layer, and the non-slip condition at the wall, the velocity at the air-oil interface must be very low. Fluorescent oil visualisation can be considered non-intrusive because of the combination of the low velocity of the oil and the linear velocity profile in the layer of oil.

Despite this technique's ease of use and low complexity, some limitations must be considered. Oil visualisation cannot be used in applications where the body forces dominate, such as spinning rotor blades. It is also not suitable for studying natural convection. Moreover, the oil can be tedious to clean and can cause damage to delicate instruments if not handled correctly.

Application in experimental campaign

In this experimental campaign, fluorescent oil visualisation was used to visualise the effect of the corner vortices on the bottom and side wall of the test section. 'Ondina oil 32' produced by Shell was selected after some test runs with oils with higher and lower viscosity. To prevent the oil from entering the 'Hill' and damaging delicate electronics, the oil visualisation was performed with the 'PHill'; furthermore, the wind tunnel corner where the oil was applied was covered with a glossy white vinyl foil, which was removed and disposed of after the measurements.

The fluorescent oil visualisation was conducted for three free-stream velocities: 10 m/s, 20 m/s and 30 m/s. In all cases, the tunnel was run for a minimum of 10 minutes, and pictures were taken with a digital single-lens reflex (DSLR) camera (Nikon D500 with a Nikkor 24-70 mm f/2.8 lens at a focal length of 24 mm). The images were qualitatively analysed on a computer for any signs of vortex lines. A selection of the acquired images can be found in appendix G.

7

Direct force measurements

This chapter presents the results from the parametric sweep performed for this Master thesis. A total of 33 test plates have been considered in a total of 61 configurations[1] to replicate the results found in the literature and to understand the effect of individual parameters on the drag performance.

First, the results are presented in section 7.1 following the categories introduced in chapter 4, namely: replication, parameter sweep, and hypotheses. Next, the results are discussed, and some hypotheses for further investigation are formulated in section 7.2.

7.1. Results

In this section, only a selection of the data is presented in a manner that targets the research questions. For a complete overview of the data acquired for every configuration, please refer to appendix C. The ΔC_D data presented in this section already contains the pressure and null-force corrections (see section 6.1.2). The error bar included in the presented data is the error metric for 'flat plate uncertainty' introduced in 6.1.3. In the case of values from the literature, error bars are only included where available.

7.1.1. Replication

When comparing results against data from the literature, it is important to consider the different test conditions and setups. These differences could be crucial to understanding possible differences and are required to match the experimental results from literature with own research data. For this reason, these conditions are summarised for all studies replicated in this thesis in table 7.1.

	Sirovich and Karlsson (1997) (and Sirovich et al., 1998b)	Monti et al. (2001)	Sagong et al. (2008)	Current thesis
Wind tunnel	fully developed turbulent channel flow	open circuit, downstream blower	open circuit, suction type	open circuit, blower upstream (M-tunnel)
Test section size (LWH)	$8500 \times 750 \times 56.8$ mm^3	$6000 \times 300 \times 400$ mm^3 ($1500 \times 300 \times 100$ mm^3)^i	$2000 \times 300 \times 400 - 420$ mm^3 ^{ii}	$1500 \times 400 \times 370$ mm^3
Turbulence intensity	-	-	0.5% (at 20 m/s)	$\approx$ 0.7% (at 24.7 m/s)
Test regime	$15,000 < Re < 40,000^{iii}$ $750 < Re_\tau < 2,000$ $(10,800 < Re < 18,000^{iii})$	$750 < Re_\theta < 4,250$ 5 m/s $< U_{cl}^{iv} <$ 20 m/s	$4,400 < Re_\theta < 8,300^v$ 15 m/s $< U_\infty <$ 30 m/s	$5.5e5 < Re_1 < 2.2e6$
Measurement	Pressure drop	Von Kármán integral relation	Floating element apparatus (balance)	'The Hill' (balance)
Model size (LW)	8530 × 750 mm^2	900 × 300 mm^2	598 × 298 mm^2	881.3 × 366.3 mm^2

Table 7.1: Testing conditions for different studies; the source of the information is indicated in the header; '^{i}': indicates the initial test section size, with which no drag reduction was obtained; '^{ii}': wind tunnel height slightly divergent to obtain a zero pressure gradient; '^{iii}': Reynolds number based on the centerline velocity (and the channel height); '^{iv}': velocity measured at the centerline; '^{v}': with θ at right before the plate

[1] 24 unique designs in two flow directions, four PIV designs in two flow directions, and five reference plates

Looking at the row 'Test regime' in table 7.1, it is obvious that different references are used to describe the test regime, for example, Re_τ, Re_θ, and Re_1. In order to compare experimental results, the test regimes for the experiments presented in this thesis are 'translated' to Re_τ and Re_θ. Please, note that for the conversion, the centre of the test plate is considered (i.e. the friction velocity u_τ and the momentum thickness θ are computed at the centre of the test plate for a given free stream velocity, or the BL development length is 1.05 m), the variation of these quantities along the test plate for different free-stream velocities is shown in figure 7.1. For the computation of u_τ and θ, the simplified equations introduced in section 2.1 were used.

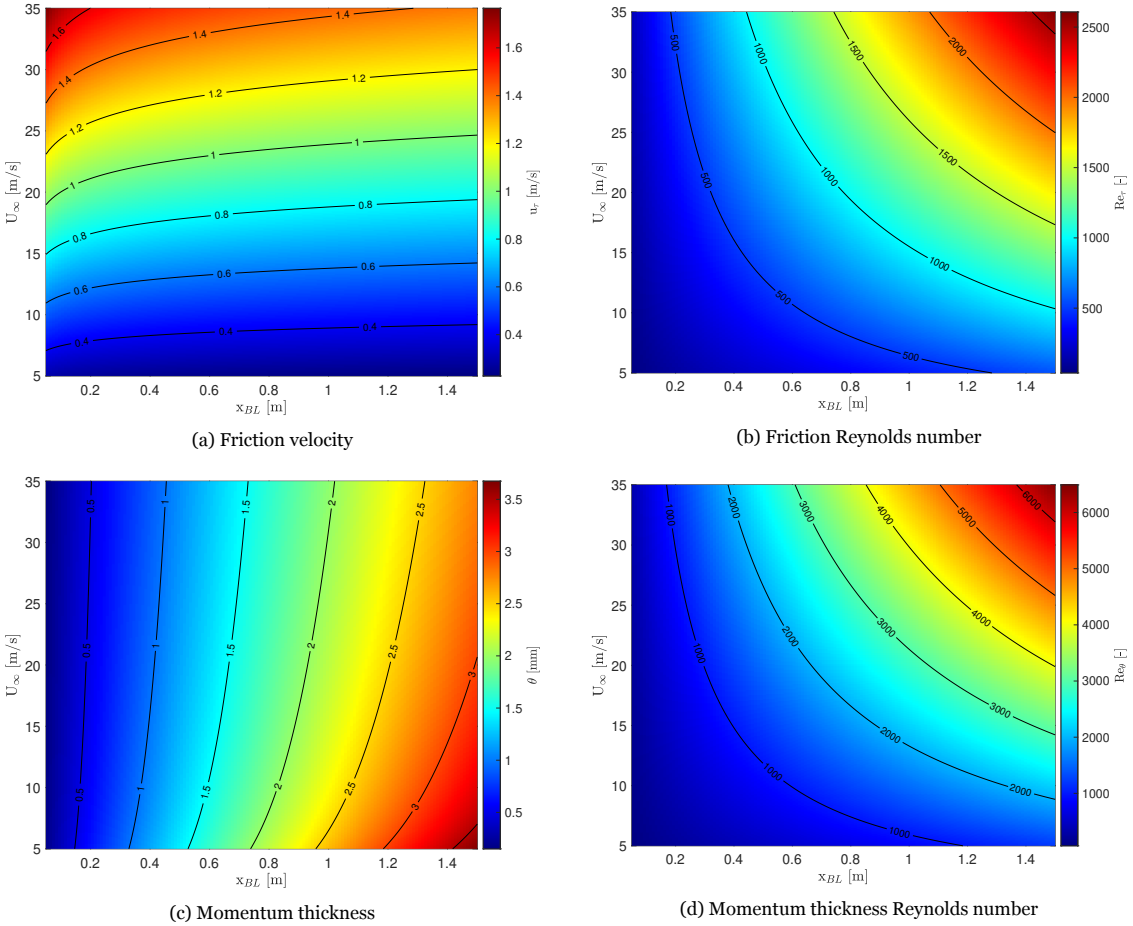

(a) Friction velocity

(b) Friction Reynolds number

(c) Momentum thickness

(d) Momentum thickness Reynolds number

Figure 7.1: Theoretical boundary layer values over the development and test plate lengths for the range of velocities achievable with the M-tunnel

The measurements performed for this Master thesis were in the range of $5.5 \times 10^5 < Re_1 < 2.2 \times 10^6$. Assuming a kinematic viscosity of 1.5×10^{-5} m^2/s, this corresponds to a free stream velocity range of 8.25 m/s $< U_\infty <$ 33 m/s. Using the power-law equations in section 2.1: 2.525×10^{-3} m $< \theta < 2.071 \times 10^{-3}$ m or $1388.75 < Re_\theta < 4556.64$. Similarly: $625.49 < Re_\tau < 1858.95$. Comparing these ranges with the ones presented in table 7.1 shows overlap with all previous experimental studies; hence, comparing the results is possible. The exact cases which have been replicated and the corresponding flow regime are indicated in table 7.2. Note that the two sources (literature and own experiments) are compared only at one Reynolds number. This Reynolds number has been selected to match the one where the reported effect of the flow control technique is the highest. Where the effect is constant, a reasonable Reynolds number has been selected. However, it has been verified that the selected Reynolds number represents the test case over the entire tested range of Reynolds numbers. No clear indication of the Reynolds number was found for the results by Sagong et al. (2008). In this case, a Reynolds number close to the lower bound of the range has been selected.

The result of the replication is shown in the form of a bar chart in figure 7.2. Note that the first three

Name	Source	Reynolds number	Comment
Sirovich (A)	Sirovich and Karlsson (1997)	$Re_\tau = 1500$ $Re_1 = 1.67 \times 10^6$	N/A
D3 Patent	Sirovich et al. (1998b)	$Re_\tau = 630$ $Re_1 = 5.55 \times 10^5$	N/A
Sagong (A)	Sagong et al. (2008)	$Re_\theta = 4199.19$ $Re_1 = 2 \times 10^6$	No Re_θ indicated in original source; same test plate as 'Sirovich (A)'
Sirovich (R)	Sirovich and Karlsson (1997)	$Re_\tau = 1500$ $Re_1 = 1.67 \times 10^6$	N/A
Monti (R)	Monti et al. (2001)	$Re_\theta = 3300$ $Re_1 = 1.51 \times 10^6$	N/A
D2 Patent (R)	Sirovich et al. (1998b)	$Re_\tau = 630$ $Re_1 = 5.55 \times 10^5$	N/A
Sagong (20VU)	Sagong et al. (2008)	$Re_\theta = 4199.19$ $Re_1 = 2 \times 10^6$	No Re_θ indicated in original source
Sagong (30VU)	Sagong et al. (2008)	$Re_\theta = 4199.19$ $Re_1 = 2 \times 10^6$	No Re_θ indicated in original source
Sagong (40VU)	Sagong et al. (2008)	$Re_\theta = 4199.19$ $Re_1 = 2 \times 10^6$	No Re_θ indicated in original source; same test plate as 'Sirovich (R)'

Table 7.2: Replicated test cases with source and Reynolds number

entries correspond to aligned array designs, while the remaining six correspond to designs with random offsets. The designs corresponding to the labels used in the bar plot can be found in table 7.2 or appendix B. For the moment, the blue and the grey bars are of interest. The red bar will be addressed later in this section.

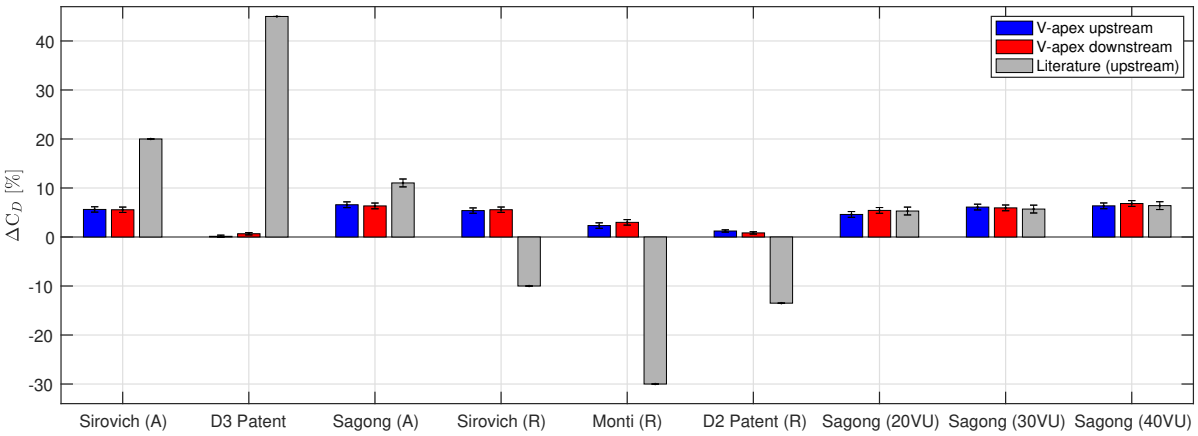

Figure 7.2: Replication; categories detailed in table 7.2; note that every replication case is at a different Reynolds number and that literature values only depict the apex upstream orientation

A preliminary observation when looking at figure 7.2 is that there is a large deviation between the replication and the literature values, except for the cases from Sagong et al. (2008). This result is unexpected because the Reynolds number to replicate the test cases by Sagong et al. (2008) had to be estimated, while it was exactly matched for the others.

For the aligned arrays, both the replication and the literature values go in the same direction (i.e. both show drag increase), albeit the already mentioned large difference between the values. For 'Sirovich (A)', the reported value is roughly 3.5 times larger than the experimental drag increase. This discrep-

ancy is accentuated for 'D3 Patent', where the literature value is over 320 times larger than the experimental one. This result is very unexpected since 'D3 Patent' is presented in Sirovich et al. (1998b) as a reference for a good model to increase mixing; hence, the largest drag increase was expected for this test plate. Upon further examination, it was found that the design 'D3 Patent' is the design with the lowest number of designed protrusion elements in the entire set with $3,185$ elements (for reference, the average of the entire set is $11,571$). The low number of protrusion elements seems to correlate with the low drag penalty of this design. This correlation indicates that the measured drag increase is, at least partially, an effect of the surface roughness produced by the elements. This observation will be further examined when the parameter sweep results are discussed (section 7.1.2).

The last aligned replication case is 'Sagong (A)', where the literature value is comparable to the experimental one (70% higher without accounting error bars), especially considering that Sagong et al. (2008) did not specify the exact Reynolds number at which the test was performed. Due to the available range in experimental data, the replication was done close to the lower bound specified by Sagong et al. (2008). Considering the trend in the data with increasing Reynolds number (see section 7.1.3), it is possible that a better replication would have been obtained at higher Reynolds numbers.

For the replication of random array designs, two distinct groups can be identified: a group where a drag increase was found as opposed to the drag reduction reported in the literature ('Sirovich (R)', 'Monti (R)', and 'D2 Patent (R)') and a group where the trend in the literature coincides with the one from the experiments ('Sagong (20VU)', 'Sagong (30VU)', 'Sagong (40VU)').

Starting with the first group, the drag reduction found by Sirovich and Karlsson (1997) ('Sirovich (R)') is roughly twice as large as the drag increase found experimentally. In other words, the ΔC_D difference between both measurements is $15.39 \pm 0.55\%$. For 'Monti (R)', the difference between both values is even higher ($32.33 \pm 0.56\%$). The same trend is identified for 'D2 Patent (R)': a small drag increase measured ($\Delta C_D = 1.22$) versus a large reported drag reduction ($\Delta C_D = -13.5$). As a reminder, it is important to note that it is not possible to compare values across replication cases because every case has an individual Reynolds number, as specified in table 7.2.

The trend is different in the second group: here, the difference between experimental data and reported values is very low (compared to the previous replication cases). Without considering the error bars, the reported values differ by 15% (20VU), -6.6% (30VU), and 0.6% (40VU) from the experimental values. When the error bars are considered, no difference between measured and reported values can be observed, in other words, the replication is exact within the error margins.

Looking at the good replication of data by Sagong et al. (2008), it is natural to ask why the replication is so good in this case and so bad in the others. Going back to table 7.1, it can be seen that Sagong et al. (2008) is the only other study that also used a balance measurement for determining the drag change. Furthermore, the size of the test sample and wind tunnel test section used in their study is comparable to the one used for this Master thesis. In the other studies considered in this thesis, the drag measurement was done indirectly using pressure values. Other differences are the much longer test section size and the larger model size in the case of Sirovich and Karlsson (1997). More details on the possible causes to explain the discordance between this study and the literature are provided in section 7.2.

7.1.2. Parameter study

Three parameter sweeps were tested in this campaign: separation between rows, separation between elements in a row, and thickness of the chevron legs. The results for the three sweeps are shown in figure 7.3. The solid lines with the markers (square and circle) represent the measured data. The 'flat plate uncertainty error' is included in the form of a shaded area around the solid lines. A new metric has been introduced in these figures, namely the 'plate coverage ratio'. Following the initial observation that the low drag increase of replication 'D3 Patent' seems to correlate with the low number of protrusion elements, a metric was required to represent the roughness introduced by the presence of the protrusion elements. This metric is the dimensionless 'plate coverage ratio' or the 'plate coverage' expressed in [%],

which is defined as:

$$\text{Plate coverage} = \frac{A_{\text{protrusion}} \times N_{\text{elements}}}{A_{\text{test plate}}} \times 100[\%], \tag{7.1}$$

where $A_{\text{protrusion}}$ is the area of a single protrusion, N_{elements} is the number of protrusion elements, and $A_{\text{test plate}}$ is the area of the test plate exposed to the flow. While $A_{\text{test plate}}$ is constant for all test plates ($322,820.19\ \text{mm}^2$), $A_{\text{protrusion}}$ depends on the geometry of the protrusion. For reference, the three values considered for the plots are presented here: $A_{\text{protrusion}}$ (20VU) $= 2.56\ \text{mm}^2$, $A_{\text{protrusion}}$ (30VU) $= 3.20\ \text{mm}^2$, and $A_{\text{protrusion}}$ (40VU) $= 4.26\ \text{mm}^2$.

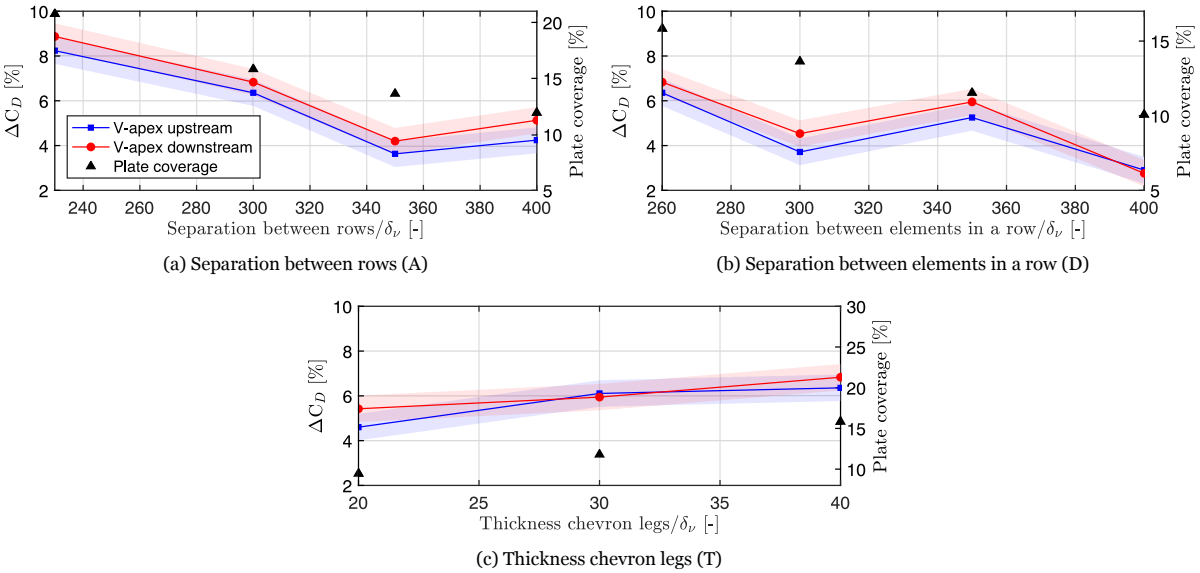

(a) Separation between rows (A)

(b) Separation between elements in a row (D)

(c) Thickness chevron legs (T)

Figure 7.3: Parameter sweep results for $Re_1 = 2 \times 10^6$

Separation between rows

For the separation between rows, the values $230\delta_\nu$, $300\delta_\nu$, $350\delta_\nu$, and $400\delta_\nu$ were tested. It can be seen in figure 7.3a that the plate coverage ratio decreases with increasing separation between rows. This trend is because the larger the distance between rows, the lower the number of rows that fit on the test plate.

The ΔC_D data follows, in general, the same trend as the plate coverage ratio: ΔC_D decreases from 8.23% at $230\delta_\nu$ to 4.24% at $400\delta_\nu$. However, there is an exception to this general trend: at $350\delta_\nu$, ΔC_D achieves a minimum value of 3.63%, which indicates that this spacing is beneficial for the drag behaviour beyond a mere roughness effect.

Separation between elements in a row

The results for the separation between elements in a row sweep are shown in figure 7.3b. The separations $260\delta_\nu$, $300\delta_\nu$, $350\delta_\nu$, and $400\delta_\nu$ were tested. Also, in this case, the plate coverage ratio decreases with increasing separation because fewer elements fit onto the plate.

ΔC_D decreases from 6.36% at $260\delta_\nu$ to 2.91% at $400\delta_\nu$, which is the lowest drag increase for this sweep. Despite of the minimum drag decrease being at the largest separation, there is a local minimum at $300\delta_\nu$ ($\Delta C_D = 3.71$), were ΔC_D drops below the value for $350\delta_\nu$ ($\Delta C_D = 5.25$). This local behaviour shows again that the 'protrusion roughness' is not the only parameter that determines the value of ΔC_D.

Chevron leg thickness

The results of the last parameter sweep are shown in figure 7.3c. There, ΔC_D and the plate coverage ratio are shown for a chevron leg thickness of $20\delta_\nu$, $30\delta_\nu$, and $40\delta_\nu$. In this case, the plate coverage ratio increases slightly with increasing thickness. This trend is explained by the increasing area of the chevron elements with increasing leg thickness (while the number of elements remains roughly constant).

ΔC_D follows a similar trend as observed for the plate coverage ratio; namely, it increases with increasing leg thickness. Considering the measurement uncertainty, it is not possible to distinguish between ΔC_D for $30\delta_\nu$ and $40\delta_\nu$.

7.1.3. Hypotheses

This section presents experimental results to verify or refute the hypotheses formulated in section 4.2.3. The hypotheses are split into the following categories: deltas, cavities, offset, apex orientation, Reynolds number, and anodised PIV models.

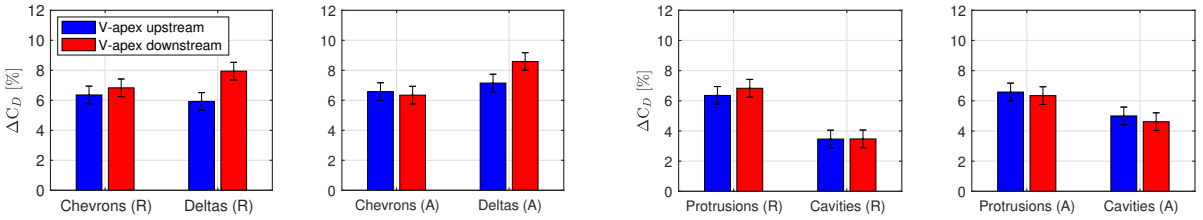

(a) Delta hypothesis

(b) Cavity hypothesis

Figure 7.4: Results for the delta and Cavity hypotheses at $Re_1 = 2 \times 10^6$

Deltas

The hypothesis formulated relative to the use of deltas is: *with a lower manufacturing effort, a delta-shaped protrusion array can yield a comparable drag performance to a chevron-shaped protrusion array*. To test this hypothesis, it is necessary to check if deltas and protrusions lead to the same ΔC_D. The results are shown in figure 7.4a. Currently, only the blue bars corresponding to V-apex upstream are of interest. The figure contains two plots: the left one shows the randomised array and its delta counterpart, while the right one shows the same for an aligned array. The ΔC_D of the chevron and delta arrays coincide within the flat plate uncertainty for both randomised and aligned arrays.

Cavities

For the cavities hypothesis, the results are shown in figure 7.4b. This figure contains two plots: the left one shows the results for a random pattern and the right one for an aligned pattern. The hypotheses based on a statement by Sirovich et al. (1998b) is as follows: *the use of cavities instead of protrusions results in an array of comparable performance, where the protrusion array is more effective in reducing drag*. The experimental data do not support this hypothesis. First, neither the protrusions nor the cavities reduce drag; hence, it is not possible to indicate which one is 'more effective in reducing drag'. Second, it can be argued that the performance is not comparable: ΔC_D for a random array with cavities is roughly half the value of the protrusion counterpart; for the aligned case, this difference is less pronounced, and the cavities value is roughly 25% lower than the protrusion value. In general, the following can be said for cavities: the use of cavities leads to a drag increase that is lower in magnitude than the protrusion counterpart both for random and aligned patterns.

Offset

According to the literature, a critical parameter for the performance of the flow control technique is the offset between rows. Three hypotheses have been formulated for this parameter to cover the aligned, constant, and random offset scenarios. The experimental results are shown in 7.5 and will be discussed in detail in the next paragraphs. Again, only the dark blue bars in the figures are of interest for the moment. In order to have a varied sample, variations of three different reference designs were used: Sirovich and Karlsson (1997) (figure 7.5a), Sirovich et al. (1998b) (figure 7.5b), and Monti et al. (2001) (figure 7.5c).

Aligned *An aligned array pattern leads to an increase in drag with respect to a flat plate, while the same pattern arranged randomly leads to a decrease in drag.*

To test this hypothesis, 'Sirovich (A)' and 'Sirovich (R1)' (figure 7.5a), 'D2 (A)' and 'D2 (R1)' (figure 7.5b), and 'Monti (A)' and Monti (R) (figure 7.5c) are compared. In none of the cases a drag reduction was observed for arrays with a random offset (or with any other offset). In fact, for the first case ('Sirovich

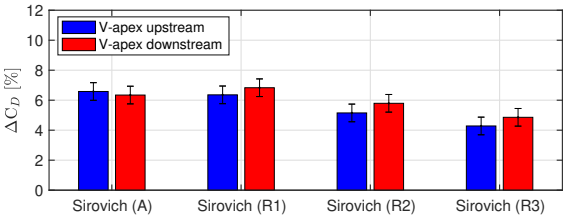

(a) Sirovich and Karlsson (1997); (A) aligned and (R1, R2, R3) three randomisations

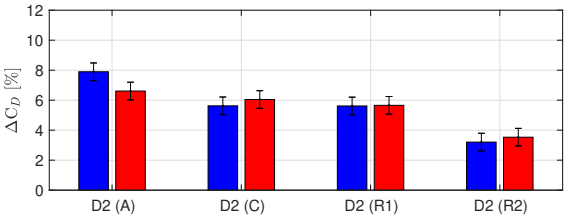

(b) Design 2 (D2) from Sirovich et al. (1998b); (A) aligned, (C) constant, and (R1, R2) two randomisations

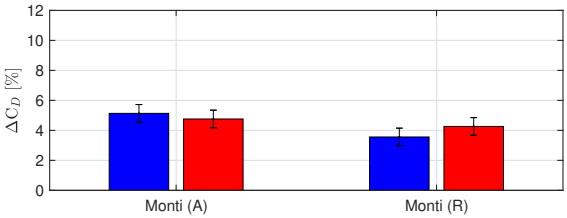

(c) Monti et al. (2001); (A) aligned and (R) random

Figure 7.5: Effects of different offset types and values on the drag performance at $Re_1 = 2 \times 10^6$

(A)' and 'Sirovich (R1)'), the ΔC_D are equal, considering the 'flat plate uncertainty'. In the other two cases, the aligned array leads to a higher drag increase than its random counterparts. This statement also holds when the alternative randomisations and the design with a constant offset are considered. In any case, the hypothesis cannot be supported.

Constant *An array with a random offset is more effective in reducing drag than an array with a constant (non-zero) offset.*

This hypothesis is tested by comparing 'D2 (C)' with 'D2 (R1)' and 'D2 (R2)' in figure 7.5b. The first realisation is that none of the configurations leads to a reduction in drag; hence, the hypothesis does not hold. Comparing 'D2 (C)' with 'D2 (R1)', no difference in ΔC_D can be established considering the 'flat plate uncertainty'. When comparing 'D2 (C)' and 'D2 (R2)', it can be seen that the constant offset leads to a higher drag increase, with a ΔC_D difference of $2.42\% \pm 0.59\%$. From the observations, it can be said that a constant offset array design leads to an equal or higher drag increase than its random offset counterpart.

Random *If the drag reduction is truly the effect of a fully random offset, different random offsets should have the same drag performance.*

Figures 7.5a and 7.5b show different variations of the random array design by Sirovich and Karlsson (1997) (R1, R2, and R3) and Sirovich et al. (1998b) (R1, R2), respectively. The only difference between variations is the offset between rows; each variation has a different set of random values that define the offset, as explained in section 5.1.2.

It can be seen at first glance that the experimental evidence cannot support the hypothesis: all random variations have a different drag performance, except for 'Sirovich (R2)' and 'Sirovich (R3)', where the ΔC_D values coincide within the 'flat plate uncertainty'. The largest differences between random array designs are found when comparing 'Sirovich (R1)' with 'Sirovich (R3)' and 'D2 (R1)' with 'D2 (R2)'; in these two cases, the second variation leads to a roughly 37% smaller drag increase (without considering the 'flat plate uncertainty'). It can be stated that the randomisation of the offset between rows has a noticeable impact on the drag performance of the design.

Apex orientation

Monti et al. (2001) and Sagong et al. (2008) introduce the idea of protrusions with an orientation opposite to the one originally proposed by Sirovich and Karlsson (1997), namely 'apex downstream'. This idea is (at least partially) motivated by the structures found on the sailfish's skin, as explained in chapter 3. All measurements have been conducted in both configurations ('apex upstream' and 'apex down-

stream') to test the effect of the reverse orientation. The results are included as red bars or data points in the figures discussed previously. The tested hypothesis is as follows: *a reverse element orientation leads to higher drag values (i.e. a reduced drag-reducing performance).* The first remark on the hypothesis is that no drag-reducing performance was observed.

The apex downstream orientation leads, in general, to higher ΔC_D values for random or constant (non-zero) offsets, while it leads to lower ΔC_D values for aligned protrusion arrays. However, the effect of the orientation on ΔC_D falls within the 'flat plate uncertainty' with very few exceptions. The first exception is 'D2 (A)' in figure 7.5b, where there is a minimum difference of $\Delta C_D = 0.11\%$ when the uncertainty ranges are considered. The second exception are the delta array designs presented in figure 7.4a ('Delta (R)' and 'Delta (A)'). In these cases, the reverse orientation leads to an increased ΔC_D value. In general, it can be stated that the orientation of the elements in the array has a negligible effect on the drag reduction performance, with the only noteworthy exception being the delta array, where the reverse orientation leads to higher drag values.

Reynolds number

The arrays have been designed with a specific Reynolds number in mind, corresponding to a free-stream velocity of 20 m/s, as explained in chapter 5.1. For this reason, the designs are expected to perform especially well at their design Reynolds number. Furthermore, Monti et al. (2001) show that in external flows, the drag reduction is only achieved over a narrow range of Reynolds numbers (see figure 3.8). For this reason, the following hypothesis has been formulated: *the flow control technique is effective over a limited range of Reynolds numbers.*

In order to test this hypothesis, ΔC_D over the entire range of Re_1 is examined. For convenience and brevity, the test plate corresponding to the random design by Sirovich and Karlsson (1997) has been selected and is shown in figure 7.6. The behaviour of this test plate is representative of the entire set (a collection of ΔC_D over the entire range of Reynolds numbers for all plates and configurations can be found in appendix C).

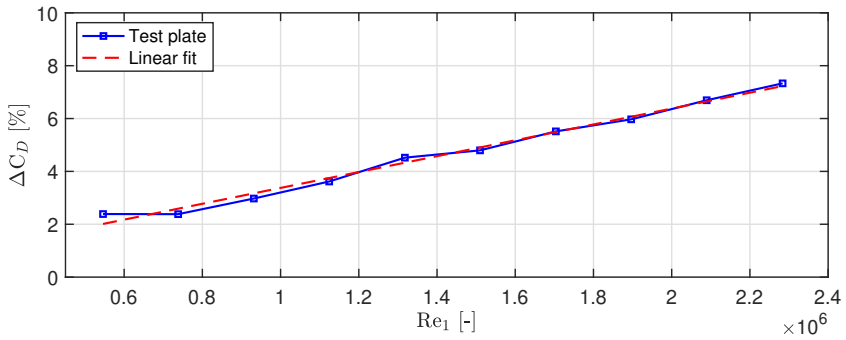

Figure 7.6: ΔC_D over different values of Re_1 for TP0094A in V-apex upstream orientation ('Sirovich (R)')

It can be seen in figure 7.6 that the drag difference increases almost linearly with increasing Reynolds number. There is no sign of 'particularly good performance' at the design Reynolds number of the protrusions and no indication of a limited range of Reynolds number for which drag reduction is obtained.

The same trends identified and discussed in this section for $Re_1 = 2 \times 10^6$ hold for other Reynolds numbers. For reference, figures 7.3, 7.4, 7.5, and 7.7 are presented in appendix H for $Re_1 = 10^6$. There it can be seen that the same general trends apply, with lower ΔC_D values.

Anodised PIV models

The last comparison that is of interest concerns the PIV models. As explained in section 5.3, the use of glossy aluminium plates is not recommended for the PIV experiments due to the bright reflections that appear when the laser light hits the aluminium surface. Matte black models are preferred to reduce reflections, and after some testing, black anodised test plates were selected as an alternative to the glossy aluminium ones. The four models chosen for PIV were manufactured a second time with the new plates. This subsection compares the four anodised test plates to the original ones. The result of

this comparison is shown in figure 7.7. The figure contains two plots: the left one includes the test plates with protrusion elements, and the right one includes the test plates with delta elements. Every test plate group consists of four bars, two for the original test plate in two orientations and two for the PIV anodised models in two orientations.

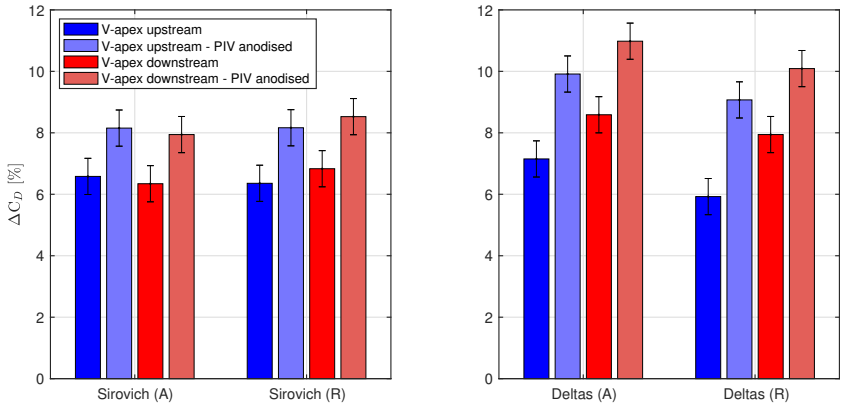

Figure 7.7: Direct force measurement results for the anodised plates for PIV at $Re_1 = 2 \times 10^6$

A quick inspection of figure 7.7 shows that the anodised models present a larger drag increase in all four cases and in both orientations. Since the array designs are the same on both the original and anodised plate, the increase should be solely an effect of the increased surface roughness due to the anodising process. If that is the case, the increase should be constant for all measurements. A computation of the drag increase between original and anodised models yields the following values: 1.57%, 1.6%, 1.8%, 1.7%, 2.76%, 2.39%, 3.15%, and 2.15% (from left to right in figure 7.7). Considering that the flat plate uncertainty has an absolute value of 1.17%, the increase can be considered constant and is attributed to the anodising process.

7.2. Discussion and working hypotheses

The main outcomes from the parametric study are summarised to start the discussion about the result:

1. No drag reduction has been observed.
2. Only the experimental results from Sagong et al. (2008) could be replicated successfully.
3. In general, the drag change data follows the same trend as the plate coverage, pointing towards a large impact of the 'protrusion roughness' on the plate's drag performance.
4. However, the parameter sweeps show that the 'protrusion roughness' is not the only relevant parameter that determines the value of ΔC_D:
   (a) for the separation between rows, the lowest ΔC_D is obtained at $350\delta_v$;
   (b) for the separation between elements in a row, there is a local minimum at $300\delta_v$.
5. Deltas can replace chevrons in the V-apex upstream orientation without any measurable effect on the drag performance.
6. The use of cavities leads to a drag increase that is lower in magnitude than the protrusion counterpart for random and aligned patterns.
7. Several observations were made concerning the offset type:
   (a) an aligned pattern leads to a drag increase equal to or larger than its constant or random counterparts;
   (b) a constant offset array design leads to an equal or higher drag increase than its random offset

counterpart;

(c) the randomisation of the offset between rows has a noticeable impact on the drag performance of the design; hence, not all randomisations seem to interact with the coherent structures equally.

8. The orientation of the elements in the array has a negligible effect on the drag reduction performance, with the only noteworthy exception being delta arrays, where the reverse orientation leads to higher drag values. In general, the orientation is less relevant than other parameters, such as the array configuration and its effect is thus considered negligible.

9. ΔC_D increases (quasi)linearly with increasing Reynolds number (Re_1) for all test plates and configurations tested. No indication for a limited range over which drag reduction is obtained nor a particular behaviour at the design Reynolds number was observed.

10. The anodising process adds a drag penalty with respect to the aluminium models without surface treatment. In the examined case of $Re_1 = 2 \times 10^6$, the drag increase is on average $\Delta C_D = 2.14\% \pm 0.59\%$.

While all the outcomes are of great interest to understanding the performance of the proposed flow control technique, results number one and two are deemed more significant. No drag reduction was observed for any of the designs. Furthermore, many results reported in the literature could not be corroborated. Hence, it is considered necessary to explore the reasons for this discrepancy. There are many possible causes for the obtained results; the ones believed to be relevant are discussed in this section. The reasons that will be discussed can be grouped into the following categories: 'low-quality turbulent boundary layer', 'incorrect scaling', 'different testing conditions', and 'ineffective flow control technique'. Please note that the categories are not mutually exclusive, i.e. it can be argued that a low-quality turbulent boundary layer leads to an erroneous scaling; instead, these are logical groups of ideas to present possible causes in a structured manner.

Low-quality boundary layer

The first possible explanation for the discrepancy between the experiments and the values found in the literature could be a low-quality turbulent boundary layer. The literature shows that the proposed flow control technique is suitable for a fully developed turbulent flow. Furthermore, the protrusions are thought to interact with the low-speed streaks, which can only happen if the coherent structures are not disrupted and present in the flow. In this regard, two possible issues can be considered.

Corner vortices

In the current setup, the test section is 400 mm wide, and the test plate with the protrusion elements takes up 366.3 mm. In other words, the test plate takes up almost the entire test section width. At the corners of the wind tunnel, the boundary layers of two walls interact and form a so-called corner vortex. In the corner vortex region, the flow differs from the turbulent boundary layer flow in the middle (half-span) of the test plate. Hence, the low-speed streaks targeted by the flow control technique may be disrupted (or have a spacing different from those in the undisturbed region). If this is the case, the protrusions are ineffective in the area covered by the corner vortices; moreover, they might increase the pressure drag without any benefits to the skin friction. Depending on the size of the corner vortex area, the increased pressure drag could outweigh the skin friction reduction in the undisturbed area, leading to a net drag increase. Note that the corner vortices have not been a problem for other techniques tested in the 'Hill' such as riblets, for which the experimental setup has been validated by van Nesselrooij et al. (2022).

In order to address this possible cause, the first step is to determine the size of the corner vortices and, in particular, how much width is taken up by them. This size could be estimated analytically (using numerical simulation results for similar test sections) or experimentally. Since only the spanwise extent of the corner vortices is of interest, fluorescent oil visualisation over the test plate surface could be used. Alternatively, the corner region could be visualised using PIV.

Longer test section

As explained in previous chapters, the current turbulent boundary layer has a development length of 600 mm until the beginning of the test plate. This length is dictated by the current setup and has been used in many similar studies that also required a turbulent boundary layer flow (e.g. Hartog, 2021; Lai, 2021). However, the possibility exists that a longer development length is required for the protrusions to work. As mentioned in section 3.4, Monti et al. (2001) changed their original test section ($1500 \times 300 \times 100$ mm^3) to a larger one ($6000 \times 300 \times 400$ mm^3) because 'it was recognised that the length was insufficient' (Monti et al., 2001); note that the researchers do not explain the reasons why the length was found to be insufficient.

However, the Reynolds numbers of the tests performed in the current test section are already comparable to the ones of the studies that could not be replicated, which should indicate that flow similarity exists. Another drawback of a longer test section in the current configuration is that the influence of the corner vortices discussed previously would be increased as these would take up more space.

Nevertheless, if a test in a longer test section is desired, this could be realised with relatively low effort using the extension built for the M-tunnel, which adds 2.40 m to the development length.

Incorrect scaling

The protrusions are scaled using the viscous unit δ_ν, as explained in section 5.1.1. A correct scaling is necessary for the protrusions to interact with the right coherent structures. Hence, the observed results could be the effect of incorrect scaling. Several causes for incorrect scaling have been identified and will be discussed here.

Effect of internal boundary layer

For the design of the test plates, the viscous unit δ_ν considering a boundary layer development length of 600 mm before the leading edge of the test plate has been used. However, the protrusion elements do not start at the trimming location but at the beginning of the test plate. The protrusion elements can be considered roughness elements, and it is known that a change in roughness can lead to the initiation of an internal boundary layer. That means that the development length of the actual boundary layer over the plate (the internal one) has a much shorter development length; hence, the chosen scaling is incorrect.

The easiest way to target the effect of an internal boundary layer is to extend the area covered by elements. Practically, this means covering the extension device with protrusions so that there is no roughness change at the beginning of the test plate.

Viscous unit incorrect

Another possible reason for an incorrect scaling could bluntly be that the estimated viscous unit (δ_ν) in section 5.1.1 is wrong. While this is a possible scenario, it is considered very unlikely. Extreme care has been put into the estimation of δ_ν, and the computed theoretical values have been compared with experimental data obtained from PIV measurements of the x-y wall-normal plane using the same experimental setup. As explained in the respective chapter, the experimental data match the theory with an NRMSD of 4.11%.

Low-speed streak separation

As explained previously, the protrusion elements are thought to interact with the flow inhibiting low-speed streaks. For this purpose, the protrusions are designed to introduce disturbances into the flow at a scale comparable to the near-wall streak spacing. However, no experimental evidence for the interaction between the near-wall streaks and the protrusions has been found in the literature. A study of the low-speed streaks and the effect the protrusions have on these coherent structures is considered beneficial. The results of the proposed study would show if the protrusions act according to the working mechanism found in the literature.

The study of the coherent structures near the wall, particularly low-speed streaks, can be conducted by means of PIV measurement of an x-z wall parallel plane.

Wrong scaling parameter

Following all publications on the topic, the flow control technique proposed in this thesis has been scaled with the viscous unit. However, the possibility exists that this inner scaling parameter has been incorrectly chosen. A different scaling of the protrusions, for example, an outer scaling, can be explored.

Different testing conditions

For the replication of the results reported in the literature, the testing conditions have been matched as closely as possible; however, the available experimental facilities and resources pose a constraint and make an exact replication unfeasible. Table 7.1 gives an overview of the testing conditions for the different studies. In particular, three aspects have been identified to be very unalike; these are presented here.

Protrusion area smaller

While the model size (or: area covered with elements) used by Monti et al. (2001) and Sagong et al. (2008) is very close to the one used for the experiments in this thesis, there is a large difference to the model size used by Sirovich and Karlsson (1997). Concretely, the area covered with protrusions for the experiments in this thesis is only 5% of the covered area in the mentioned study. For reference, the length is ten times smaller and the width half the one used by Sirovich and Karlsson (1997).

The longer area with protrusions could have several effects: the boundary layer is fully developed, and only then the protrusions have an effect, or the large area is just necessary for the interactions between the protrusions and the coherent structures to have a noticeable effect.

Measurement technique

The second difference, which has been pointed out earlier in this report, is the measurement technique. The studies that could be replicated successfully also used a balance measurement, while the ones that could not be replicated determined the skin friction using pressure measurements. For the assessment of the proposed flow control technique as a means of reducing turbulent skin friction drag, the use of a balance is preferred. There are various examples of technologies that, while effective according to indirect measurements, were found not to work when directly measuring the force; that is why some authors propose direct force measurements as the preferred approach to determining skin friction drag (Baars et al., 2016; van Nesselrooij et al., 2022).

Channel flow

The last difference that will be pointed out here is that Sirovich and Karlsson (1997) use a channel flow instead of an external flow. The main difference between the two flows is that, in the fully developed turbulent channel flow, parameters such as the boundary layer thickness remain constant (Monty et al., 2009). The possible implication of testing in an external flow was already pointed out by Monti et al. (2001). A possibility to get closer to the conditions in Sirovich and Karlsson (1997) is to test the protrusions in a channel flow.

Erroneous experimental results in the literature

The last explanation for the discrepancy with the reported values in the literature is that the measurement results found in some of the publications are erroneous. Many possible reasons could lead to wrong measurements, ranging from the choice of an inadequate technique to the incorrect use of an adequate one. This last hypothesis is a very strong statement and cannot be answered directly. The outcome of the previous considerations will determine if this is the case or not.

While all the possible causes listed in this section are interesting and worth exploring, not all of them can be further investigated in this Master thesis. For example, to study the results in a longer test section, in a channel flow, with a much larger protrusion area, or with a different scaling parameter, the experiments must be repeated, which is outside the scope of this thesis. For other causes, such as the validity of the selected viscous unit and the measurement technique, enough evidence has been provided already to justify that the choices made in this thesis are correct. Finally, the hypothesis of erroneous results in literature cannot be addressed directly, as explained previously

Considering the causes that have been excluded, three possible causes discussed in this section are left and have been selected for further study. These are the ‘corner vortices’, the ‘internal boundary layer’, and the ‘low-speed streak separations’. The following chapter will present a detailed investigation of these three aspects.

8

Detailed flow investigation

Following the results from the parametric study in chapter 7, a detailed investigation is performed to understand the results better and obtain insights that could result in a new, improved design. In particular, three areas have been selected for further study: the extent of the corner vortices in the test section used for the experiments (section 8.1), the effect of the protrusions on the low-speed streaks (8.2), and the effect of the internal boundary layer (8.3).

8.1. Corner vortices

As outlined in section 7.2, the possibility exists that the regions of the test plate closest to the side walls are experiencing a flow different from the one in the middle region of the plate due to the presence of corner vortices. These could lead to the protrusions not interacting as intended with the coherent structures so that, in the worst scenario, the drag increase in this region could outweigh the drag reduction in the unaffected area, leading to a net drag increase. This effect of the corner vortices would explain the large deviations observed with the values from the literature. Notice that the width of the test plate used by Sagong et al. (2008) was also roughly the width of the test section; hence, their results could be affected by the same phenomenon.

Over the wind tunnel walls, boundary layers develop; these boundary layers interact at the corners where two walls come together, creating a so-called corner vortex. This section aims to determine the size of these corner vortices, particularly the extent of the affected region into the bottom wall of the wind tunnel. Several approaches exist (analytical, numerical, and experimental); the experimental approach has been chosen for this investigation because the wind tunnel and experimental setup are available and because it is thought to be the most effective approach in providing the required information quickly and reliably.

Oil flow visualisation experiments

The first attempt at determining the extent of the corner vortices into the width of the test plate was made using fluorescent oil visualisation. For details on this flow visualisation technique, please refer to the explanation given in section 6.3. As mentioned, experiments were performed at 10 m/s, 20 m/s, and 30 m/s. However, no effect of the corner vortex was observed (such as an oil accumulation). In order to test the setup, a vortex generator was installed. The effect of this vortex was clearly visible in the layer of oil, validating the setup. A selection of the results can be seen in appendix G. The absence of any signs of a corner vortex can be explained in several manners. First, the vortex could be too weak to affect the oil layer. Second, the streamwise direction of the flow could be dominant over the spanwise motion of the vortex, hence, 'deleting' any spanwise trace from the oil layer. In any case, the results from the fluorescent oil visualisation experiments are inconclusive, and further investigation is required.

PIV experiments

Due to the inconclusive results from the first experiments, an alternative technique is required. Various methods are suitable for investigating the corner vortices, from rudimentary ones, such as tufts, to more advanced ones, such as using (an array of) pitot tubes, hot wire anemometry (HWA), or PIV. Since a PIV setup is available (as it is used for a different investigation in this Master thesis), this technique was chosen. For the details on PIV and the y-z plane setup, please refer to the explanation provided in section 6.2.2. In the case of the corner vortices, only the mean flow is of interest; for this purpose, 1200 instantaneous vector fields were averaged. An overview of the mean flow and the corresponding standard deviation for the twelve measurements performed can be found in appendix F. For the sake of this discussion, the mean velocity field and the standard deviation for the small FOV with a $\Delta t = 100$ μs and 5 m/s are shown in figure 8.1. This choice is motivated in the following paragraphs.

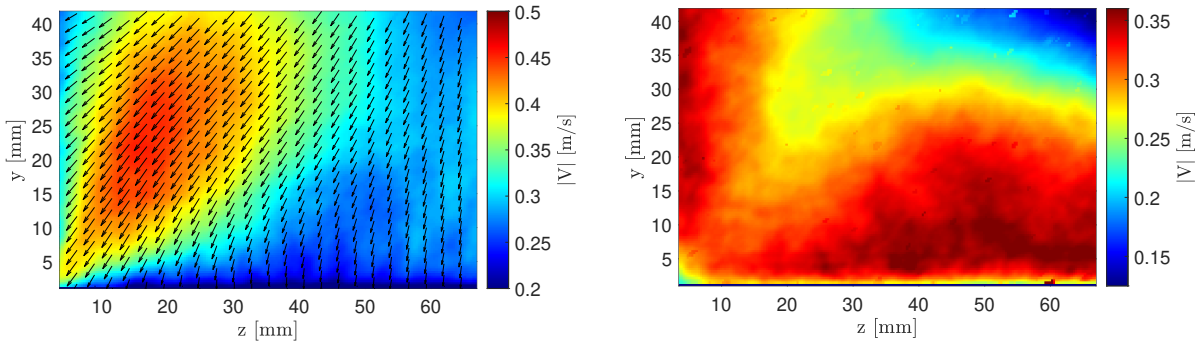

(a) Average velocity field

(b) Standard deviation

Figure 8.1: Average and standard deviation for y-z plane at 5m/s and $\Delta t = 100$ μs; small FOV

In general, the results from the twelve measurements show the same characteristics: the main flow is characterised by an area of high velocity shaped like an inverted droplet inclined at 45° from the corner. The flow direction in this area is towards the corner. The further away from the 45° line, the more the flow direction points perpendicularly to the side or bottom wall, whichever is closer. As expected, the lowest velocity is found in the regions closest to the wall. Please note that the coordinate $(y, z) = (0, 0)$ indicates the position of the corner and that some regions very close to the wall have been masked to eliminate the effect of reflections. The standard deviation increases with decreasing distance to the wall, which is expected, as weaker velocity fluctuations are expected in the mean flow than in the turbulent boundary layer region. The region of high standard deviation coincides with the estimated thickness of the boundary layer over the flat test plate at the location of the measurements ($\approx$ 35 mm).

It can be seen in appendix F that the results for the large FOV are generally noisier than those for the small FOV. This observation is explained by the lower scale factor in the large FOV and, consequently, the lower maximum particle displacement as shown in table 6.4. The particle displacement is at subpixel level (0.65 px and 0.3 px for the larger and shorter Δt, respectively), making the results very susceptible to noise. Furthermore, some level of camera shake was present due to the position in the outflow. In the results for the large FOV, the area of high velocity is not separated from the side wall, and the low-velocity region close to this wall is missing. The low quality of the large FOV results is also reflected in the error quantification shown in table 6.8 and appendix F. For the reasons mentioned in this paragraph, the large field of view is only used qualitatively and will not be considered further in this section.

The difference between the two chosen times between frames (Δt) is less pronounced than the difference between large and small FOV discussed in the previous paragraph. The two Δt values yield comparable results, where the longer one tends to be noisier. The explanation for this observation is simple: a longer Δt gives more time for particles to leave the illuminated plane and accentuates the effect of camera shake.

The velocity is the last consideration in selecting the measurement used for the rest of the discussion. It has already been established that the area of most fluctuations is related to the thickness of the bound-

ary layer. Hence, the measurements with the thickest boundary layer have to be used to establish a margin that is valid for the entire range of velocities. The thickest boundary layer is observed for the measurement at the lowest velocity. For all these reasons, the measurement of the y-z plane with a small FOV at 5 m/s and a Δt of 100 μs has been chosen (see figure 8.1).

Comparison of results with the literature

In order to validate the results obtained from PIV, comparable data were searched in the literature. Please note that the validation is only required qualitatively since only the extent and not the exact velocity values are of interest. The wind tunnel test section can be seen as a square duct; similarly, the flow inside can be interpreted as a square duct flow. This type of flow has been widely studied in literature due to its relevance for engineering applications (e.g. ventilation ducts and heat exchangers). In particular, the so-called secondary motions present in these flows are of interest for the current discussion (Modesti et al., 2018). These motions were first identified by Prandtl (1926) and Nikuradse (1930).

As explained by Pirozzoli et al. (2018), 'the secondary motions in square ducts are known to come in the form of eight counter-rotating eddies bringing high-momentum fluid from the duct core towards the corners'. Two of these vortices can be seen in 8.2a; note that the flow in the duct is symmetric around $(y, z) = (1, 1)$.

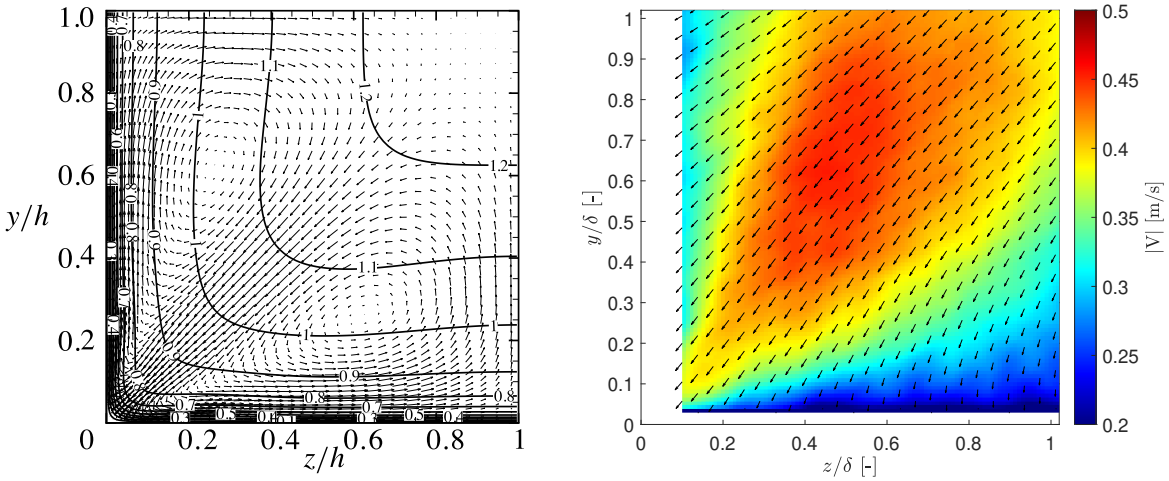

(a) Mean streamwise velocity contours (continuous black line) and mean cross-stream vectors (black arrows); modified from Pirozzoli et al. (2018)

(b) Experimental data from PIV measurements; the white area has been masked, and no velocity data is available there; axes normalised with the estimated boundary layer thickness of δ = 35 mm

Figure 8.2: Secondary motions in a square duct flow

For comparison, the mean velocity field introduced previously has been plotted in figure 8.2b. Since Pirozzoli et al. (2018) are considering a fully developed turbulent flow in a square duct, the coordinates are scaled with the duct half side h. For a better comparison, the experimentally obtained velocity field is scaled using the estimated boundary layer thickness at the measurement plane and velocity, namely δ = 35 mm. It can be seen that the experimental data only captures the region between the two vortices (i.e. the region at an angle of 45° from the bottom left corner). This region has the highest cross-stream velocity (i.e. the velocity in the y-z plane). Considering that the maximum velocity present in the red region corresponds to a displacement of $\approx$ 1.8 px, it is reasonable to assume that the much lower velocity present in the vortices (up to 10× smaller judging by the scale of arrows in figure 8.2a) falls under the threshold measurable with the available setup. Notice that the chosen time between frames Δt is the maximum allowed by the one-quarter rule. In order to capture smaller velocities, a thicker laser sheet, a tighter FOV, or a higher resolution sensor would be needed. Additionally, the region closest to the wall had to be masked to remove the effect of reflections.

Furthermore, the captured (maximum) velocity of these vortices is larger than expected, namely 8–10% of the free stream velocity, while in literature, it is stated that the secondary motions are roughly 1–2% the strength of the bulk velocity (Brundrett and Baines, 1964; Gessner and Jones, 1965). A possible

explanation for this observation is the high uncertainty of the experimental results of around 10 – 20% for the instantaneous fields. However, as mentioned earlier, the magnitude of the velocities is not so relevant as the geometry of the vortex.

Estimation of the spanwise effect of the corner vortex

The velocity profile over a horizontal cut at $y = 20.94$ mm in the small FOV is considered (see figure 8.1) to assess the spanwise extent of the corner vortices. The chosen position corresponds to half of the height captured in the FOV and, from a visual inspection of the average velocity field, it is considered a conservative representation of the corner vortex effect on the near bottom wall. The velocity profile is shown in figure 8.3 together with a curve that depicts the velocity variation in the spanwise direction. This figure shows that the corner vortex effect fades out at around $z \approx 50$ mm, where a lower, more constant velocity is reached. The spanwise velocity variation confirms this observation: from $z \approx 50$ mm onwards, the variation oscillates around 0 m/s. From this analysis, it is concluded that the effect of the corner vortex extends 50 mm in the spanwise direction.

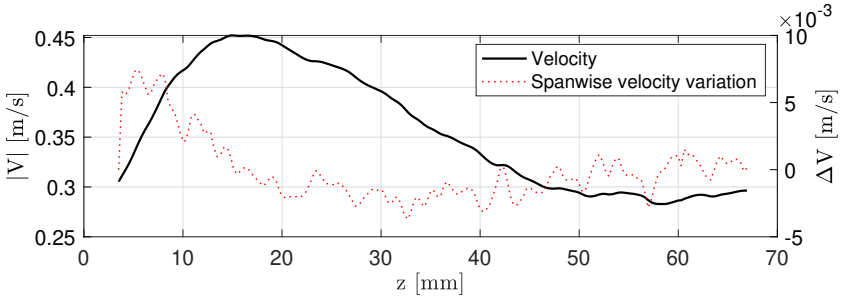

Figure 8.3: Velocity profile over a horizontal cut at $y = 20.94$ in the small FOV

Recommendation

From the observation made regarding the corner vortices, keeping a distance to the wall of 50 mm from each side is advisable. By keeping this margin smooth, the effect of the secondary motions in the tunnel on the smooth reference plate will be (almost) equal to the effect on the test plate, making sure that the measured drag difference ΔC_D only comes from the manipulation of the flow in the undisturbed middle region. Considering that the plate is 366.3 mm and the tunnel is 400 mm wide, there is already a margin of 16.85 mm on each side, corresponding to the 'Hill' frame. For future designs, an additional margin of at least 33.15 mm has to be left in smooth conditions on both sides of the test plate. Note that the smaller the area covered with the passive flow manipulator, the smaller the force difference measured between the plates, and the more inaccurate the results become. For this reason, the margin on both sides cannot be arbitrarily increased.

8.2. Effect of the protrusion on low-speed streaks

The study of the flow and the coherent structures very close to the wall serves several purposes in this Master thesis. First, the instantaneous streamwise velocity fields close to the wall can give some indication of the structures that are being targeted by the protrusions. Sirovich and Karlsson (1997) formulate the hypothesis that the elements of the array interact with the low-speed streaks, as explained in chapter 3. Hence, the low-speed streaks are of special relevance in this study; in particular, to verify their occurrence and investigate the effect the protrusions have on them. Second, the streamwise velocity variation in the field is used as a proxy for the strength of the coherent structures and the turbulence level to understand if this strength is affected by the array design. For this, a simple analysis using the velocity variance in the field will be presented as a proxy for the turbulent energy.

From the theory discussed in chapter 3, it is expected that, with respect to a flat reference plate (called 'TP0000'), the strength of the low-speed streaks increases for an aligned protrusion pattern. The contrary is expected for a random protrusion pattern, namely a reduction in strength or occurrence of the low-speed streaks. Recalling the hypothesised working mechanism: the random protrusion pattern is expected to inhibit the low-speed streaks. Considering the comparable drag performance of chevron and delta-shaped protrusions observed in chapter 7, at least in the apex upstream orientation, it is expected that both types of protrusions lead to a similar flow field behaviour.

PIV experiments

For this investigation, the quantitative flow visualisation technique particle image velocimetry (PIV) has been chosen to visualise an approximately 40×75 mm^2 region of the flow parallel to the test plate (x-z plane). Details about the technique and the chosen plane can be found in section 6.2. It is not possible to include all the obtained velocity fields ($16,200$) in this report reasonably. To still give a good overview of the results, the average velocity field, the corresponding standard deviation, and an instantaneous velocity field are included for every test case in appendix E. Please note that these plots show the absolute velocity (combination of streamwise and spanwise); however, the streamwise velocity component is dominant and will be considered for the computations and analyses presented in this section. Furthermore, the shown velocity fields have been first cropped for the analyses in order to remove noise, zero-values and the effect of some reflections at the edges (5% of the length removed from each side).

The best representation of low-speed streaks (or wall-near streaks) is obtained for the measurements at 5 m/s. The streaks become less clear for 10 m/s and are barely visible at 20 m/s. A possible explanation for this observation is that the laser sheet height (expressed in viscous units) is too high at the higher velocities and the visualised region is too distant from the wall for the near-wall streaks to be discernible. For 5 m/s, the viscous unit length is the largest; with increasing velocity, the viscous unit length becomes smaller so that the relative height of the laser sheet (which is at the same absolute position for all measurements) increases.

As discussed in section 2.2, the low-speed streaks originate at the wall and rise from there, extending into the logarithmic region. Although their separation is defined as $l^+ = 100$, it increases with the distance to the wall, as depicted in figure 2.5. The streaks are most energetic in the buffer layer ($5 \leq y^+ \leq 30$) and become less discernible further away from the wall. Other turbulent events, such as burst events, can be more prominent for visualisations at a larger distance from the wall. In fact, in the instantaneous field for 20 m/s, small pockets of very low velocity can be seen; these could correspond to the low-momentum flow transported from the wall into higher regions in the boundary layer, as explained in section 2.2. These initial thoughts will be supported later with experimental evidence.

A streamwise velocity gradient is present in the average velocity fields; an example for the case of TP0000 at 5 m/s is shown in figure 8.4 next to the corresponding standard deviation. The cause for this gradient can be a slightly diverging laser sheet or a misalignment between the laser sheet and the test plate. The development of the boundary layer can also lead to a streamwise velocity gradient; however, this is not the case here, as the gradient should be in the opposite streamwise direction. The fact that this gradient is most pronounced for the lowest velocity tested is explained by the fact that the laser sheet is relatively higher for higher velocities. Although the physical inclination of the laser sheet is the same for all cases, for higher velocities, the illuminated region is higher in the boundary layer and is hence less sensitive to slight variations in the height (lower $\left(\frac{\partial u}{\partial y}\right)$).

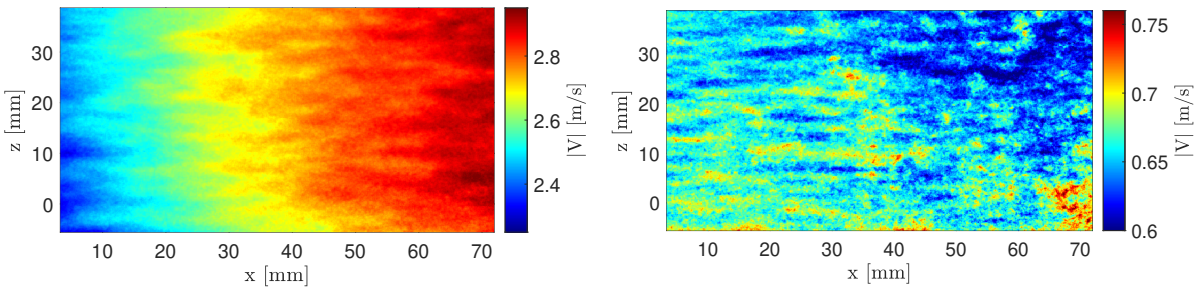

(a) Average velocity field

(b) Standard deviation

Figure 8.4: PIV data for TP0000 at 5 m/s

Before starting the assessment of the laser sheet height, a quick plausibility check is presented in figure 8.5. This figure shows a near-wall x-z plane at a comparable wall distance obtained from a numerical simulation by Rosti and Brandt (2017) next to a measured instantaneous velocity field. Both show similar features, which can be considered rudimentary validation of the experimental data.

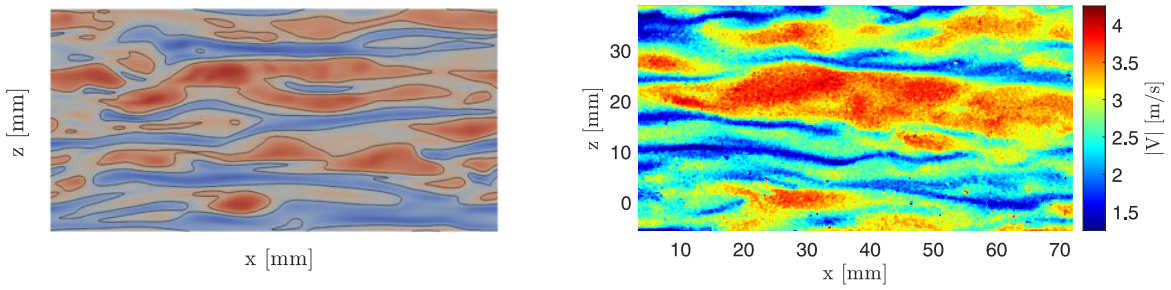

(a) Near wall x-z plane from Rosti and Brandt (2017)

(b) Measured instantaneous velocity field for TP0000 at 5 m/s

Figure 8.5: Plausibility check of measured instantaneous streamwise fluctuations

Two-point statistics analysis

The height of the measured planes is determined from the mean velocity using a characteristic velocity profile. First, the mean of the average velocity field is computed. The values obtained for the different velocities and test plates are shown in 8.6a. For 5 m/s and 10 m/s, the mean velocities are very similar and close to the mean velocity over the smooth reference plate. For 20 m/s, the mean velocity over the chevron-shaped protrusions is consistently higher than for the reference plate; the opposite is true for the delta-shaped protrusions. A likely explanation for this behaviour is that the plates were installed at slightly different heights: the current setup consists of a 3D printed frame where the plate is installed. The exact height of the plate is adjusted using metallic spacers, which does not guarantee consistency. It is also possible that the protrusions lead to a shift of the velocity profile.

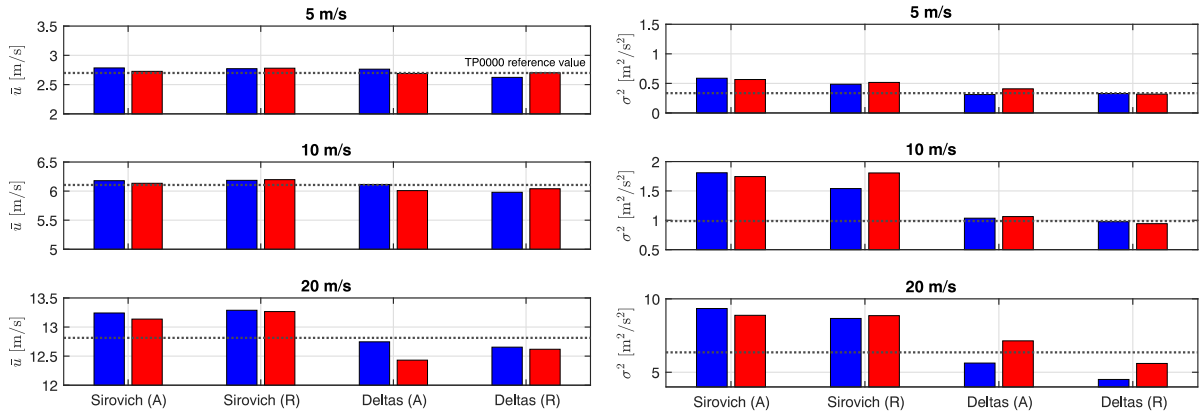

(a) Mean streamwise velocity

(b) Variance

Figure 8.6: Comparison between different plates in terms of mean and variance (averaged over the plate); blue columns (left) correspond to apex upstream; red columns (right) correspond to apex downstream

Using experimental data for the friction velocity u_τ from a previous study by Hartog (2021), u^+ is computed for every test case. Velocity profiles over the reference test plate at the required velocities using the same experimental setup were available from the same dataset by Hartog (2021). These profiles are shown in figure 8.7a and were used to determine y^+ from the experimental velocity data. The final values for the distance from the wall are shown in figure 8.7b. These results confirm the initial hypothesis for the laser sheet height. For 5 m/s the laser sheet is at $y^+ \approx 17$, for 10 m/s at $y^+ \approx 30$, and for 20 m/s at $y^+ \approx 59$.

For 5 m/s, the target region is illuminated since the most energetic streaks are expected around $y^+ \approx 15$. The measurement for 10 m/s is at the upper limit of the buffer layer. And the measurements for 20 m/s are well inside the overlap layer. The region of every measurement already indicates the expected flow structures. The expected spacing can also be estimated from figure 2.5: for $y^+ \approx 15$, the streak spacing is $l^+ = 120 - 150$; for $y^+ \approx 30$, $l^+ = 144 - 216$; and for $y^+ \approx 59$, $l^+ = 202 - 322$. Note that these values are based on the DNS and experimental results only.

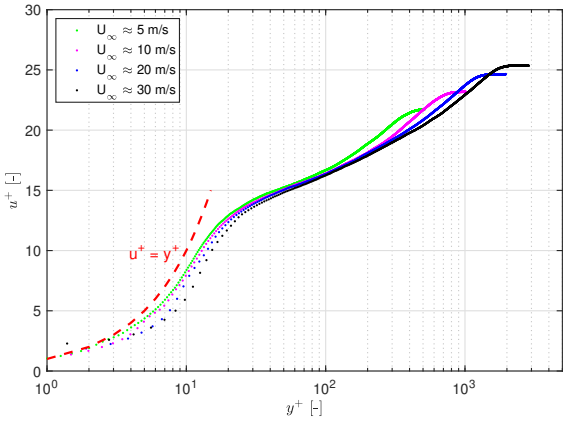

(a) Velocity profiles; modified from Hartog (2021)

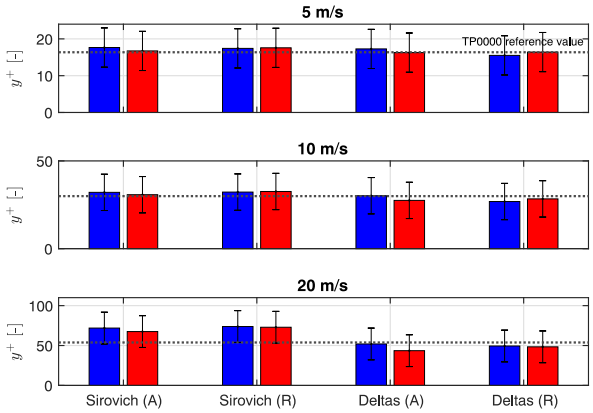

(b) Position of laser sheet above the wall; blue columns (left) correspond to apex upstream; red columns (right) correspond to apex downstream; the estimated laser sheet thickness is indicated as an error bar

Figure 8.7: Velocity profiles and laser sheet height

From the previous calculation, it is clear that the measurements at 10 m/s and 20 m/s are on the high side, and low-speed streaks may not be distinguishable in those regions. However, the analysis is continued with these velocities because some low-speed streak 'footprint' could be detected. As a reminder from section 2.2, closest to the wall, the near-wall streaks (i.e. the ones that are being targeted here) are most prominent; with increasing distance from the wall, hairpin packets or trains of packets are found; finally, increasing the distance to the wall further, very large scale motions (VLSM) are present.

To better understand the difference in the flow fields for different test plates, the structures in the flow are characterised using two-point statistics as introduced in section 2.2.3. For this, the two-point correlation is computed for every flow field, yielding a correlation map as shown in figure 8.8a for TP0000 at 5 m/s. Note that the respective mean velocity field is subtracted from the instantaneous fields for the two-point correlation. For readability, contours are shown in steps of $R_{uu} = 0.02$; the highest contour value is $R_{uu} = 1$; the zero contours ($R_{uu} = 0$) have been skipped; positive contours are represented by solid lines and negative contours, by dashed lines. Furthermore, the two-dimensional correlation map and the central streamwise and spanwise cuts are plotted, as shown in figure 8.8. This process has been automated with MATLAB so that the instantaneous velocity fields are imported, the individual correlations are computed, the average of all correlation plots is determined, and spanwise spacing and streamwise length of the structures in viscous units are calculated. Note that the spanwise spacing is interpreted as the peak-to-peak distance and the streamwise length as the 0.1 crossing integral length scale, as explained in section 2.2.3. The correlation maps for all the flow cases can be found in appendix E.3.

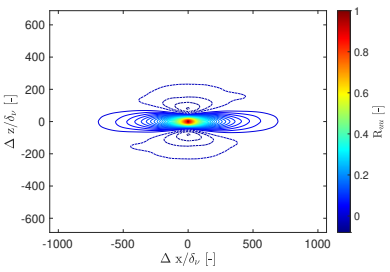

(a) Two-point correlation

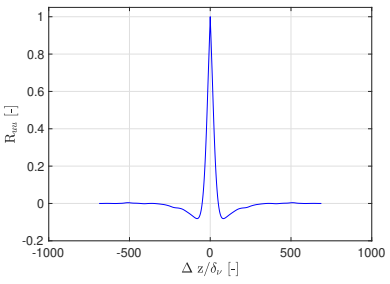

(b) Central spanwise cut ($\Delta x/\delta_\nu = 0$)

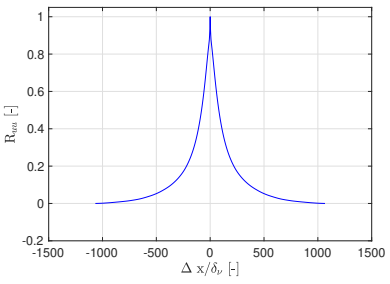

(c) Central streamwise cut ($\Delta z/\delta_\nu = 0$)

Figure 8.8: Two-point statistics for TP0000 at 5 m/s

The two-point correlation (figure 8.8a) shows a region of positive correlation flanked by two regions of negative correlation, which is an indication of some organisation in the flow and shows that the behaviour is not completely broadband. An analysis of the spanwise spacing and streamwise length for

the different test cases is carried out to understand if the protrusions affect the near-wall streaks. The distances are computed using 600 instantaneous velocity fields. Figure 8.9 shows the convergence of the spacing with the number of image pairs.

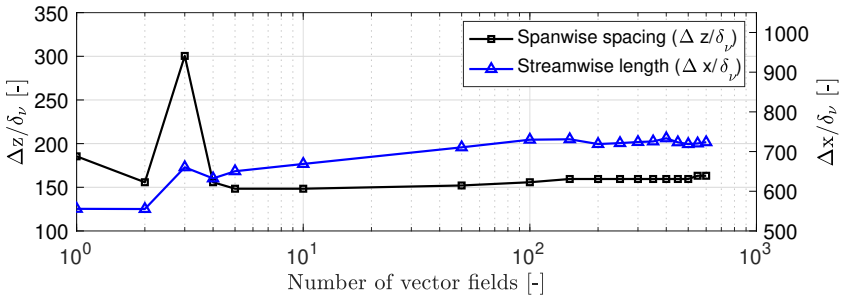

Figure 8.9: Convergence of the spanwise spacing and streamwise length with an increasing number of vector fields for TP0000 at 5 m/s

The computed spacing and length values are shown in figure 8.10 for all 27 test cases. Considering the smooth reference plate: a spanwise spacing of $l^+ = 163$ and a streamwise length of $d^+ = 723$ are observed for 5 m/s; $l^+ = 529$ and $d^+ = 1005$ for 10 m/s; and $l^+ = 820$ and $d^+ = 754$ for 20 m/s. Comparing these values with the expected low-speed streak separation presented previously, it is clear that the experimental results only come close to the expected ones in the case of 5 m/s. Although it is unlikely that the values for 10 m/s and 20 m/s are solely characteristic of the near-wall streaks, these are characteristic of the coherent structures present in the flow and show that some level of organisation can be identified in the flow field in a statistical sense.

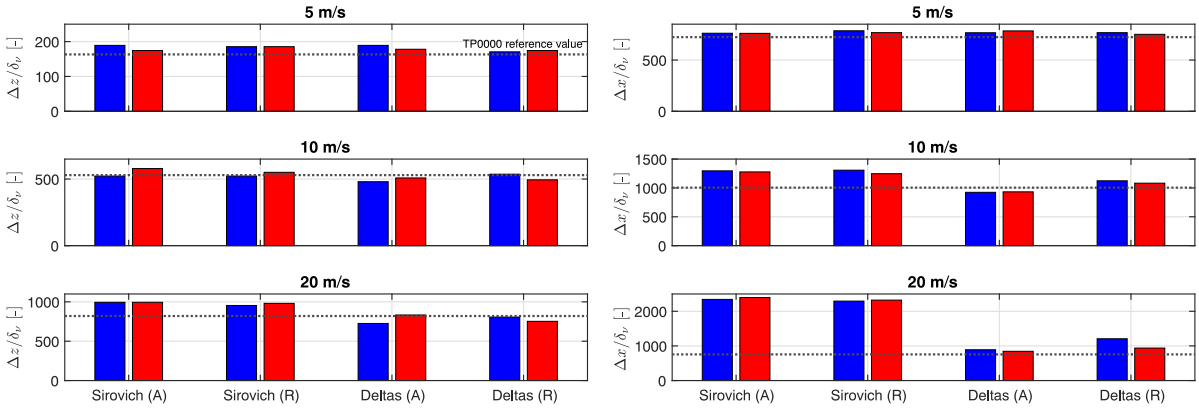

(a) Spanwise spacing

(b) Streamwise length

Figure 8.10: Comparison between the results from the two-point statistic analysis; blue columns (left) correspond to apex upstream; red columns (right) correspond to apex downstream

For the lowest velocity tested, 5 m/s, the spacing l^+ and the length d^+ for the test plates with protrusions are consistently higher and close to the reference value. In the case of l^+, the maximum deviation from the reference value is $l^+ \approx 26$, or $\approx 16\%$ higher (on average $l^+ \approx 17.8$, or $\approx 11\%$ higher). A similar behaviour is observed for d^+, with a maximum deviation from the reference value of $d^+ \approx 62$, or $\approx 8.5\%$ higher (on average $d^+ \approx 44.5$, or $\approx 6\%$ higher). No consistent difference is observed between the two offset types (aligned and random) or between the two orientations (apex upstream and downstream). As expected, the chevron-shaped protrusions and the delta-shaped protrusions behave in a very similar manner. The results for 5 m/s do not support the hypothesis formulated previously: the similar values for aligned and random offsets indicate that none of the designs leads to a diminishing of the near-wall streaks.

Observing the result in figure 8.10 for 10 m/s, it can be seen that the spacing values (l^+) for the protrusion designs are very close to the reference value. The maximum deviation is of $l^+ \approx 49$ or less than

10%. On average, the spacing for the chevron-shaped protrusion designs is higher than the reference value and the one for the delta-shaped protrusions. A similar behaviour can be observed for the length d^+: the chevrons consistently lead to higher values than the deltas. The difference with respect to the reference length is larger than in the case of the spacing: the maximum deviation is of ≈ 30% (on average ≈ 20%); hence, the length values appear to be more sensitive to different protrusion arrays than the spacing values. No definite trend can be observed in terms of array orientation. Furthermore, no clear difference in the spacing and length values can be observed between the aligned and the random offset designs. The only difference observed in the results for 10 m/s is between chevrons and deltas, as discussed previously. The higher values obtained for chevrons and the lower values obtained for deltas can be linked to the difference in mean velocities presented in figure 8.6a and the corresponding difference in laser sheet height in figure 8.7b.

The same trends reported for 10 m/s can be observed more pronounced for the case of 20 m/s. The chevron designs lead to a larger spacing and the delta designs to a lower spacing, with a maximum deviation from the reference value of ≈ 21% and an average deviation of ≈ 15%. The same is true for the streamwise length; here, the chevron designs lead, on average, to ≈ 209% higher length values, indicating a much lower level of streamwise periodicity in the flow compared to the reference case. The length values for the delta designs are closer to the reference value with a maximum deviation of ≈ 60% and a mean deviation of ≈ 28%. As discussed previously, the differences observed between the protrusion types are connected to the mean velocity (figure 8.6a) and the laser sheet height (figure 8.7b). No clear trend is visible between aligned and random offset patterns; both lead to comparable spacing and length values. There is also no clear trend in the use of different apex orientations; in most cases, both orientations perform similarly. The only noteworthy exception is the case 'Deltas (R)', where the apex upstream orientation leads to a ≈ 30% higher distance value than the apex downstream orientation.

Summarising the discussion of the results in figure 8.10, no relevant effect of the type of offset was observed; hence, the hypothesis formulated previously that protrusion arrays with a random offset diminish the near-wall streaks cannot be supported. However, the similar behaviour for different offset types is consistent with the direct force measurements. The two protrusion orientations result in similar spanwise spacing and streamwise length values, as expected from the balance measurements. The delta-shaped protrusions at a velocity of 20 m/s are the only exception to this general trend. Finally, chevron-shaped protrusions lead to larger spacing and length values than the reference case, while delta-shaped protrusions lead to lower spacing and length values. This discrepancy with the balance measurement results is explained by the higher and lower mean velocities measured for chevrons and deltas, respectively. The different velocities can result from slightly different installation heights or a shift in the velocity profile. Note that, due to the different heights for 5 m/s, 10 m/s, and 20 m/s, a direct comparison of the spacing and length values between the three velocities is not possible. For this reason, the discussion in this section was limited to the effect of different array designs for a constant velocity.

Turbulence energy in the flow

In the two-point correlation analysis, it was concluded that no significant change in the spanwise spacing and streamwise length was observed for different types of offset; hence, the working mechanism hypothesis could not be supported. This means that the protrusions do not affect the flow in a manner that the periodicity of the coherent structures present in the flow is affected. This second analysis explores the possibility that the protrusions affect the strength of the structures in the flow. As mentioned previously, the variance of the velocity field is used as a proxy for the strength of the structures.

Figure 8.6b shows the computed variance for the 27 test cases. In general, the variance is higher than the reference value for chevron-shaped protrusions and almost the same or slightly lower for delta-shaped protrusions. Concretely, the chevrons lead to an average increase of approximately 61%, 74%, and 40% for 5 m/s, 10 m/s, and 20 m/s, respectively. The deltas lead to lower deviations from the reference value of 10%, 5%, and 20% for 5 m/s, 10 m/s, and 20 m/s, respectively. This result does not match the findings from the balance measurements: according to the measurements, chevrons and deltas were expected to be equivalent. However, the large difference can be linked to the trend observed in the mean velocity (figure 8.6a). There, the chevrons have higher mean velocities, and the deltas have

lower mean velocities than the reference case.

In terms of array orientation, both apex upstream and apex downstream configurations lead to comparable variance values, with a noteworthy exception being the case of deltas for a velocity of 20 m/s. This exception is in line with the balance measurement results, where an increased drag for the apex downstream orientation was observed for the delta-shaped protrusions (see figure 7.4a).

Despite the visible difference between protrusion types, no clear trend can be observed for different types of offset: both random and aligned offset designs lead to comparable variance values, suggesting that the level of turbulence in both cases is similar. Hence, the initial theory for the working mechanism cannot be supported.

Please note that this is a second-order statistical approach. More detailed analyses, such as counting the occurrence of certain events or using pattern recognition algorithms, are considered too specific for this initial study.

8.3. Internal boundary layer

The last aspect considered in this detailed investigation is the effect on an internal boundary layer. As outlined in previous sections, the current setup consists of a test plate mounted on a balance (the 'Hill') preceded by a flat plate with an elliptical leading edge. A strip of carborundum particles at the leading edge of the extension is used to initiate a new turbulent boundary layer. The length (600 mm) of the extension plate corresponds to the development length of the flow until it reaches the test plate with the protrusions. This development length has been considered in chapter 5.1 to compute the viscous length scale δ_ν used to scale the array designs.

The possibility exists that the protrusion elements that are adhered to the test plate appear to the flow as a rough surface. In this case, the transition from the extension to the test plate would be equivalent to a smooth-to-rough transition (STR). It is well known that, in this case, a so-called internal boundary layer (IBL) is initiated, as explained in the review by Kadivar et al. (2021). Figure 8.11 shows a schematic of the formation of an IBL over a roughness step. With the beginning of an internal boundary layer, the flow experienced by the protrusions close to the wall does not correspond to the assumed one with a development length of 600 mm, but rather to the one of a developing boundary layer. Hence, the values used for scaling the array designs would be wrong.

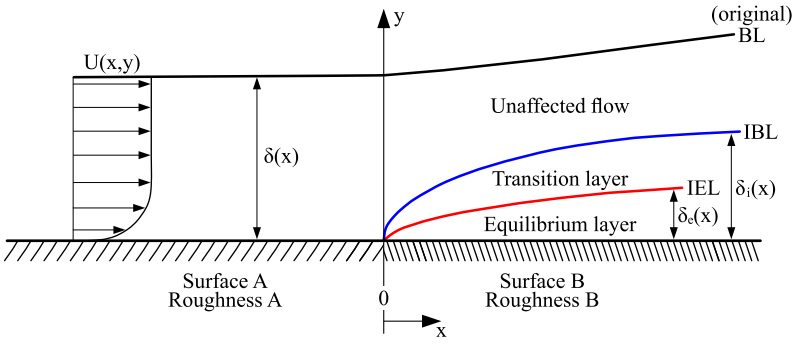

Figure 8.11: Internal boundary layer (IBL) and internal equilibrium layer (IEL) formation for a turbulent boundary layer flow over a roughness step; inspired by Kadivar et al. (2021)

Since the relevant parameter, in this case, is thought to be the viscous length scale, the effect of the internal boundary layer on the scaling is not expected to be large. To support this claim with concrete values, figure 5.2 in chapter 5.1 is considered. Currently, a $\delta_\nu = 0.01775$ mm ≈ 0.018 mm is used for a development length of $x = 1.05$ m until the middle of the plate. Using the same approach, a $\delta_\nu = 0.01669$ mm ≈ 0.017 mm is found for a development length of $x = 0.44$ m, which correspond to the middle of the test plate, i.e. the boundary layer initiates at the leading edge of the plate. The difference between both values is roughly 1 μm or 6%. For comparison, if the boundary layer thickness were the relevant scaling parameter, this difference would be over 110%. While the value of δ_ν in

the middle of the test plate with or without IBL, the difference between the required δ_ν at the leading and trailing edge of the test plate is substantial ($\approx$ 38%, starting at 10 mm to avoid division by zero); for comparison, this difference is of $\approx$ 6.4% for the original design with 600 mm development length. Hence, the assumption that the viscous unit can be assumed constant over the plate does not hold in the case of an internal boundary layer. This very simplified calculation illustrates the difference between the assumed conditions without IBL and the conditions with IBL and stresses the relevance of a correct understanding of the actual boundary layer over the test plate.

Internal boundary layer theory

A brief review of IBLs shows that most of the early work is dedicated to micrometeorology and the study of the atmospheric boundary layer over roughness steps, such as the transition from ocean to land or from smooth terrain to forest (Rao et al., 1974; Garratt, 1990). The main interest of the research appears to be the estimation of the height of the IBL and, in particular, when equilibrium conditions are re-established.

Looking back at figure 8.11, the interface between two surfaces with different roughness values can be seen. The requirement for an IBL is just a change in surface roughness, meaning that the transition can occur from smooth to rough (Antonia and Luxton, 1971), as in the case at hand, or from rough to smooth (Antonia and Luxton, 1972). It is assumed that the turbulent boundary layer is fully developed at the moment of the transition and has a thickness of $\delta(x)$. At the origin of surface change ($x = 0$), an IBL and an internal equilibrium layer (IEL) are initiated with the layer thickness $\delta_i(x)$ and $\delta_e(x)$, respectively. In the region known as IBL, the equilibrium state of the near-wall flow is altered by the new surface roughness. Above this layer, the flow remains unaltered. The region of the IBL where the equilibrium state is re-established is known as the IEL (Kadivar et al., 2021). According to the researchers, the thickness of the IBL is a relevant parameter for the flow recovery after the roughness step. However, despite the many studies and publications addressing this topic, the phenomenon is not yet fully understood (Li et al., 2019). The many different models proposed in the literature to estimate the height of the IBL are an example of the complexity and lack of agreement on the matter: Savelyev and Taylor (2005) present 23 different formulas proposed by different researchers.

There is also no clear answer to the required streamwise distance until a new equilibrium state is established after a smooth-to-rough transition. To give some examples, Antonia and Luxton (1971) find that, in the smooth-to-rough transition, the boundary layer adjusts to the new surface roughness at a distance smaller than 20δ from the step. Li et al. (2019) conclude in their study that the equilibrium state in the viscous region is recovered close to instantaneously (Kadivar et al., 2021). Rouhi et al. (2019) performed a DNS study on the effect of a rough-to-smooth and a smooth-to-rough transition in an open channel flow. The researchers conclude that a streamwise distance of 2.5δ is required in the case of smooth-to-rough transition for the equilibrium assumption to hold.

IBL over the test plates and recommendation

Considering that the thickest boundary layer is present at the lowest velocity tested, namely 5 m/s, a quick calculation can be performed using the criteria mentioned in the previous paragraphs (20δ and 2.5δ for re-established equilibrium). At 5 m/s, the boundary layer thickness is $\delta = 16.75$ mm at the smooth-to-rough transition. Hence, the equilibrium is re-established after 335 mm (according to Antonia and Luxton, 1971) or after 41.9 mm (according to Rouhi et al., 2019). Although both values largely differ, it is clear that a relevant extent of the test plate is affected by the IBL.

To address this issue, and given the large uncertainty around the determination of flow parameters in the IBL, it is recommended to apply the protrusion elements over the extension device so that the smooth-to-rough transition occurs further upstream and the test plate is not affected by the IBL. The previous computations show that the available distance of 600 mm is more than required to re-establish the equilibrium.

8.4. Concluding remarks

This chapter has explored the spanwise extent of the corner vortices over the test plate, the effect of the protrusions on the low-speed streaks, and the impact of the internal boundary layer on the viscous

unit length. These three aspects were selected as possible causes for the discrepancy between the drag performance obtained in this study and the one reported in the literature.

First, it has been verified that the corner vortices affect a region of approximately 33 mm on each side of the test plate. This region should be kept smooth (i.e. without protrusions) to determine an accurate drag performance of the models without the effects of the experimental facility.

The investigation of the low-speed streaks has concluded that the working hypothesis reported in the literature cannot be supported. The models with an aligned and a random offset seem to interact with the coherent structures in a similar manner, and none was found to affect the spacing or length of the structures in the flow considerably. The similar performance of aligned and random offset designs is in line with the direct force measurements and suggests that the flow manipulators are not targeting the near-wall streaks efficiently.

The roughness step in the current experimental setup leads to flow conditions that differ from the design conditions over the test plate. The extension that precedes the balance is long enough for the flow to recover equilibrium conditions after a smooth-to-rough transition; hence, applying the flow manipulators already over the extension is recommended.

IV

Discussion, conclusions, and recommendations

9 Discussion

In this chapter, the main outcomes of the experimental study are revisited in section 9.1. Based on these outcomes, an improved design is proposed in section 9.2. Finally, the implementation of protrusions as a flow control technique in real-world implementations is addressed in section 9.3.

9.1. Key outcomes

The direct force measurement results have been discussed extensively in section 7.2, and the detailed investigation results have been presented and addressed in chapter 8. In this section, the key outcomes of this thesis will be revisited.

Direct force measurements

- No drag reduction has been observed, and only the results by Sagong et al. (2008) could be replicated. A low-quality boundary layer in the experiments, an incorrect scaling of the model, differing testing conditions, and possibly erroneous results reported in the literature are explored as conceivable causes to explain the measured drag increase.
- The use of different methods to determine the skin friction drag has been regarded as a potential cause for large deviations in the results. Due to the high confidence in the selected measurement method (van Nesselrooij et al., 2022), it can be assumed that the drag performance is quantified better than with an indirect method.
- The direct force measurement results have consistently shown that the drag performance is not solely determined by the 'protrusion roughness':
  - The optimum design parameter values do not always coincide with the design with fewer protrusion elements.
  - The drag performance is very sensitive to the array randomisation, even for designs with the same number of elements.

  These observations prove that a meaningful interaction occurs between the protrusions and the flow.
- The (quasi)linear drag performance with the Reynolds number indicates an inadequate choice of scaling parameter. For a flow control technique specifically designed for a free-stream velocity of $U_\infty = 20$ m/s, at least some distinct performance at the corresponding Reynolds number can be expected.
- The equivalent drag performance of delta-shaped protrusions opens the door for models that are easier to manufacture and more robust.

- The distribution of the elements appears to be more relevant than their orientation.

Corner vortices

- The corner vortices extend roughly 33 mm into each side of the test plate at $U_\infty = 5$ m/s.
- The area affected by the corner vortices should be left smooth to limit the comparison between the tested design and the reference plate to the undisturbed area.

Low-speed streaks

- No substantial difference in the spanwise spacing or the streamwise length has been observed between aligned and random protrusion arrays.
- No substantial difference in the velocity variance has been observed between aligned and random protrusion arrays.
- The observed flow behaviour does not support the working mechanism hypothesis found in the literature.
- However, the results agree with the findings from the direct force measurements and suggest that protrusions are not interacting with the low-speed streaks effectively.

Internal boundary layer

- The theoretical effect of the internal boundary layer on the validity of the scaling is not negligible.
- The protrusions should be applied over the extension preceding the test plate to eliminate the effect of the smooth-to-rough transition.

9.2. Improved design

Up to this point in the thesis report, questions one, two, and three have been addressed. In this section, the fourth and last question will be tackled: *can a design with improved drag performance or overall characteristics be defined?*

To address the first requirement set by the research question, namely the improved drag characteristics, the best values for the individual parameters found in section 7.1 are combined. Concretely, a separation between rows of $350\delta_\nu$ and a separation between elements in a row of $400\delta_\nu$ are selected. For their equivalent drag performance, delta-shaped protrusions are chosen; thus, no leg thickness is required. Testing several sets of random offsets is recommended since this parameter has been found to be very sensible. For the design presented in this section, the randomisation RAND_E_D19 is chosen because it is the one that has yielded the lowest drag increase. An overview of the parameters selected for the improved design is shown in table 9.1.

Category	A [-]	B [-]	C [-]	D [-]	T [-]	E type	E value [-]
Improved design	350	200	200	400	40	random	RAND_E_D19

Table 9.1: Improved design parameters

The choice of delta-shaped protrusions improves the overall characteristics of the flow control technique since the manufacturing is quick, and the array is less prone to damage than chevron-shaped protrusions.

Note that extreme cases such as D3 in Sirovich et al. (1998b) which yield a very small drag increase are not considered due to their low plate coverage. In these cases, the effect of the protrusions is so small that they can be regarded as flat plates and are thus not of interest to this discussion.

Besides the direct improvements in the design of the array, some considerations from the detailed investigation in chapter 8 have to be taken into account. First, the protrusion elements must be limited to the area of the test plate with undisturbed flow conditions. Concretely, this means that a margin of

at least 33.15 mm has to be kept smooth (i.e. free of protrusions) at each (long) side of the test plate. In the design presented in this section, this margin has a width of 40 mm. Second, the protrusions might act as roughness elements, introducing an internal boundary layer. It is required the eliminate the roughness step to ensure a correct scaling. For this, it is recommended to cover the extension device with protrusion elements. An image render of the geometry file for the optimised design is shown in figure 9.1. Note that the gap between the test plate has been left clean, and cutting lines have been added to facilitate the installation.

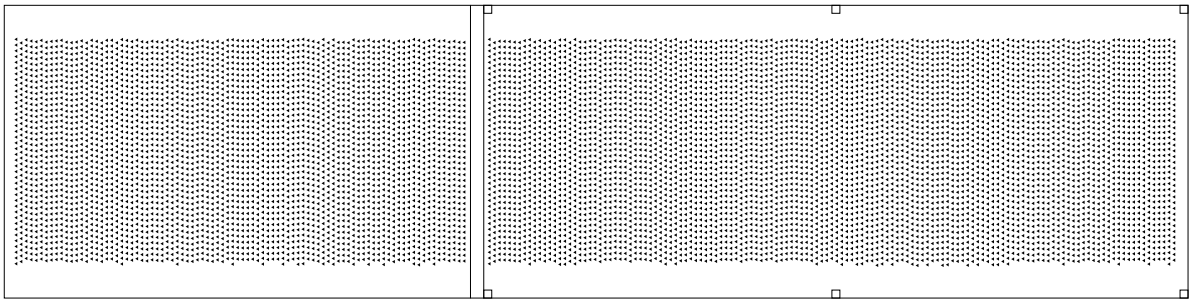

Figure 9.1: Improved protrusion array design generated with TikZ; image render of the geometry file

This combination of design parameters should yield a drag performance equal to or better (i.e. lower drag increase) than the measurements for the individually selected parameters. Furthermore, the improved test plate designs should allow the protrusions to perform at their best and enable accurate measurements with fewer sources of errors.

9.3. Practical considerations

The increasing pressure to reduce the carbon footprint of aviation (and other means of transport) demands solutions that can be implemented practically and are suitable for large-scale industrial applications. The most promising of techniques is not valuable for the common goal of cleaner aviation if an application in operational conditions is not feasible and its working principles cannot be applied elsewhere. For these reasons, it is deemed very relevant to devote a chapter in this thesis to the discussion of the practical implementation of chevron-shaped protrusions as a passive flow control technique for turbulent drag reduction. The discussion will be divided into scale considerations, manufacturability and application, and flow mechanical considerations.

Scale considerations

The protrusions produced for the experiments were scaled according to the flow conditions in the wind tunnel used for the measurements. However, the scales in the experiments differ from those in real-world applications. In this section, the required size for two applications will be examined.

Variable	Unit	Vessel	Aircraft	M-Tunnel
ρ	[kg/m^3]	1,025	0.4135	1.225
ν	[m^2/s]	1.853×10^{-6}	3.526×10^{-5}	1.5×10^{-5}
μ	[kg/ m/ s]	0.00109	1.458×10^{-5}	1.81×10^{-5}
U_∞	[m/s]	12.34	250	30

Table 9.2: Environment conditions for aircraft and vessels; vessels: sea water at 20°; aircraft: 10 km cruising altitude

For this discussion, two means of transport are considered: cargo vessels and airliners. The global supply chain relies on ultra-large container vessels (ULCV), which can transport between 21,000 – 25,000 TEU[1]. These vessels have a length overall of approximately 400 m (Rodrigue, 2020). Moreover, air transport has become ubiquitous in today's society: business trips, leisure trips, transport of critical goods, and many more. Aircraft manufacturers and operators are in the spotlight and already advertise

[1]TEU: Twenty-foot Equivalent Unit; a unit commonly used to express the capacity of cargo vessels in containers

with the improved fuel efficiency of their aircraft. In this discussion, two of the latest airliners will be considered: the A350-1000 by Airbus and the 777X-9 by Boeing. These two aircraft have a length of 73.79 m (Airbus, 2022) and 76.72 m (Boeing, 2022), respectively. Table 9.2 summarises the values used to compute the viscous unit length for the three cases considered here.

Using the values from table 9.2 and the power-law equations introduced in section 2.1, the viscous unit length over the development length of an aircraft, a container vessel, and the M-tunnel is computed. The viscous unit length for these three cases is shown in figure 9.2 together with the friction Reynolds number. Please note that a semi-logarithmic and a full logarithmic representation were chosen for the viscous unit length and the friction Reynolds number, respectively, since this was an adequate axis scaling to allow for easy comparison between the three cases. Considering the middle of the total length in every case: for the aircraft, the viscous length scale is ≈ 4.9 μm; for the ship, it is very similar with a value of ≈ 6 μm; and for the M-tunnel at 30 m/s it is ≈ 12 μm.

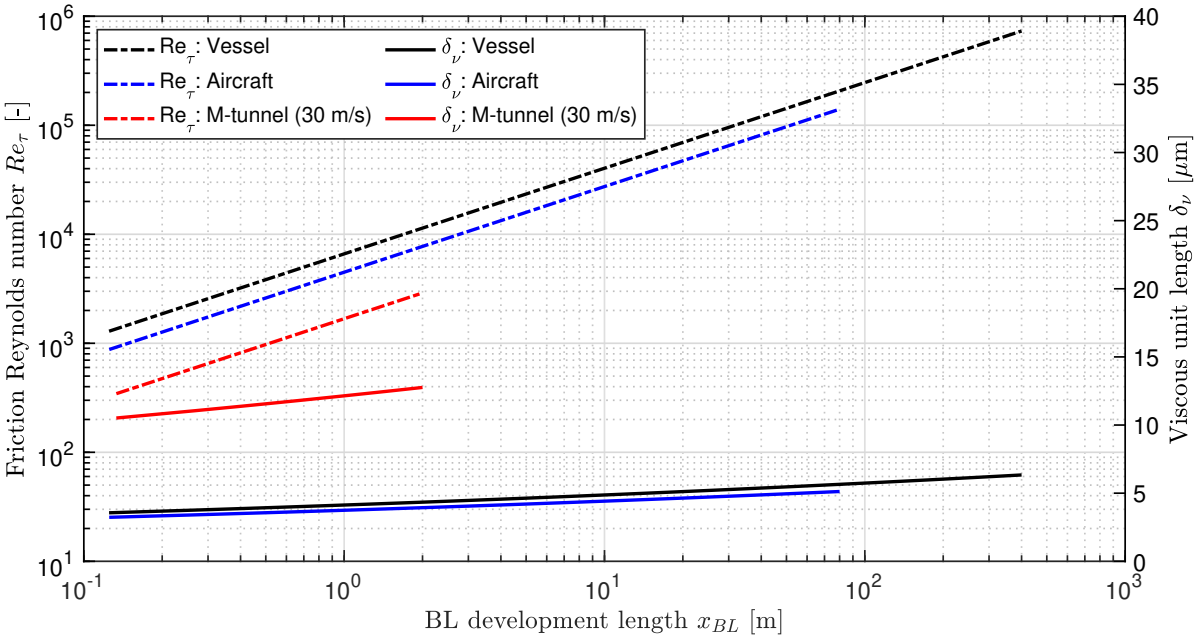

Figure 9.2: Viscous unit length development and friction Reynolds number for a container vessel, commercial aircraft, and the M-tunnel

The feasibility of the viscous unit length values is assessed by considering the smallest size of the protrusions, namely their height. The protrusions are approximately 6 viscous units high, which translates to 29.4 μm for an aircraft, 36 μm for the vessel, and 72 μm for the M-tunnel. These values are at a scale that can be manufactured (as will be discussed next) and are, hence, considered viable.

Manufacturability and application

The required sizes of the flow manipulators can be manufactured with the technique used in this thesis since off-the-shelf vinyl foils with a thickness of 30 μm are available. This material is also known in the aerospace industry, and aircraft-certified vinyl foil exists and has been tested for this Master thesis (3M™Exterior Aircraft Graphic Film A7322, 3M-ID B00026401, provided by the company Omnimark B.V.).

The small required thickness also opens the door to alternative manufacturing techniques, for example, paint or textured foil. The required thickness corresponds to $2 - 3$ layers of spray paint; hence, the protrusions could be painted onto the aircraft's skin or the vessel's hull using a stencil. Another alternative is to use textured foil with the protrusion geometry applied directly onto the skin.

Despite the many possibilities for manufacturing, it is also relevant to stress that the flow manipulators can easily be retrofitted, are low-cost and have a light weight. Assuming a weight of 280 g/m^2 for the vinyl foil and a coverage ratio of 20%, the protrusions add roughly 130 kg (or less than six standard

suitcases) when applied on an A350[2] aircraft.

Flow mechanical considerations

To truly understand the benefits of a flow control technique in a practical application, knowing how the drag reduction obtained with said technique in the laboratory translates into a final fuel burn reduction is necessary. This section discusses several aspects that must be considered and presents a possible quantification of the potential benefits of chevron-shaped protrusions. For the quantification, it is assumed that the technology yields a 10% wall drag reduction as reported by Sirovich and Karlsson (1997). In particular, five topics will be considered: applicability, Reynolds number scaling, skin friction share in total drag, flight altitude, and fuel weight savings.

Applicability In the ideal scenario tested in the laboratory, the flow control technique is applied over an entire reference test area, and the wall drag reduction with respect to the smooth reference area is determined. In a practical implementation, assuming that the surface modification will be applied over the entire aircraft skin is not realistic. Bechert et al. (1997) estimate that approximately only 70% of the aircraft skin can be covered with a flow control device such as the protrusions, areas of high erosion such as the leading edge of the wings, other areas where the device will interfere with other systems such as the de-icing system, and windows should be kept clean.

Knowing that only 70% of the skin can be covered with protrusion arrays, the reported skin friction reduction is reduced by 30%, yielding the ideal skin friction reduction of the flow control technique when applied to an aircraft.

Reynolds number scaling As addressed at the beginning of this section, the friction Reynolds number at which the tests were performed ($Re_\tau \approx 1.8 \times 10^3$) differs from the ones found in practical cases, such as an airliner in cruise ($Re_\tau \approx 8 \times 10^4$). These values have been determined using figure 9.2 at the middle of the tunnel or aircraft length. The extrapolation of the drag reduction at low friction Reynolds number to large Reynolds number is a current research topic. For example, Marusic et al. (2010, 2021) study the effect of Reynolds number scaling. They point out that, with increasing Reynolds number, the contribution of the small scales remains roughly constant. However, with an increasing Reynolds number, the large scales have an increasing contribution, which means that the contribution of the small scales becomes relatively smaller with an increasing Reynolds number. The drag-reducing contribution of any technique that targets the small-scale structures is also relatively reduced with increasing Reynolds number. A schematic of the effect expressed in the wall stress spectrum is shown in figure 9.3.

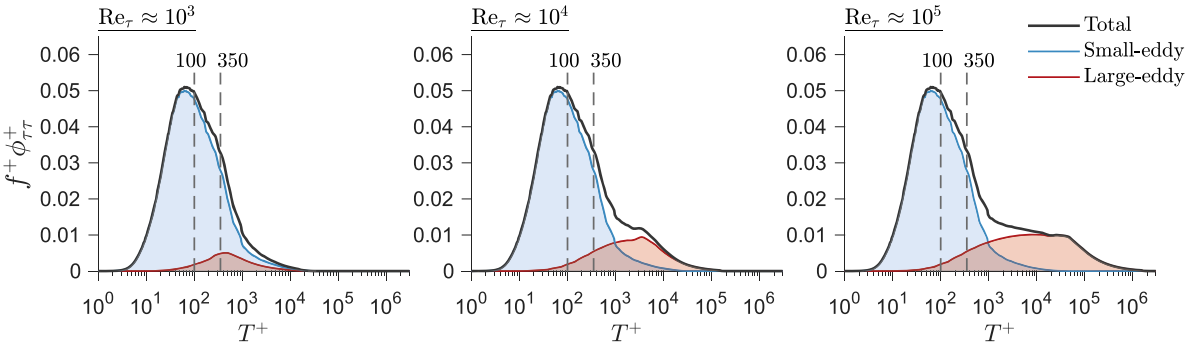

Figure 9.3: Wall stress spectrum dependence on Reynolds number, from Marusic et al. (2021)

Baars (2020) also discussed the effect of Reynolds number scaling. He notes that there is no scale separation at low Reynolds numbers (Re_τ). In this regime, it is theoretically possible to perfectly trim the passive flow control device to a specific flow condition to obtain the maximum drag reduction. However, bands of low and high Reynolds numbers appear as the Reynolds number increases. Due to the larger range of Reynolds numbers present in the flow, the manipulators are not operating at their optimal conditions and their performance drops.

[2]Simplified analysis assuming a total area of 2,253.6 m^2 (1,381.6 m^2 for the fuselage and 872 m^2 for the wings).

Gatti and Quadrio (2016) quantify the Reynolds number scaling as shown in figure 9.4. This quantification is based on an analytical calculation where the friction law, which essentially gives the relation between the skin friction and the friction Reynolds number, is evaluated for the cases with and without flow control. Please note that Gatti and Quadrio (2016) present the results specifically for a skin-friction reduction induced by a spanwise forcing; hence, it is not universally applicable. However, for the sake of argument, the same approach is followed to quantify the Reynolds-number dependence of the wall drag reduction obtained with chevron-shaped protrusions.

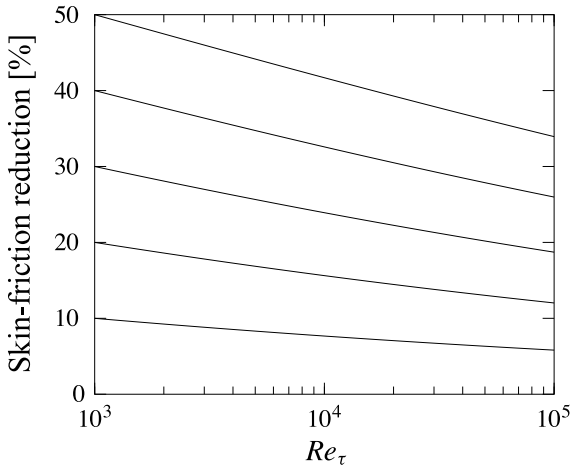

Figure 9.4: Extrapolated drag reduction values with Re_τ, modified from Gatti and Quadrio (2016)

Following the initial assumption, the protrusions yield a drag reduction of 10% for a friction Reynolds number of $Re_\tau \approx 10^3$. Looking at figure 9.4, it can be seen that this efficiency is reduced to a 6% drag reduction when scaled for $Re_\tau \approx 8 \times 10^4$, corresponding to a 40% decrease in drag reduction.

Skin friction share in total drag The reported reduction of 10% by Sirovich and Karlsson (1997) refers to a skin-friction reduction (actually to a wall-tangential force reduction, as discussed previously). It is well known that skin friction accounts for approximately 50% of the total drag of an aircraft (Bechert et al., 1997; Spalart and McLean, 2011). Hence, the skin-friction reduction obtained for the application area and adjusted for the higher friction Reynolds numbers is reduced by half to obtain the contribution of the flow control technique to the total drag reduction of an aircraft.

Flight altitude Spalart and McLean (2011) point out some beneficial aspects for skin-friction reduction techniques in a practical implementation. They explain that a pilot would adjust the flight altitude as a consequence of the skin-friction reduction to adjust the balance between viscous and pressure drag. In doing this, the reduced viscous drag accounts for half of the total drag with the benefit of reduced pressure drag. The researchers estimate that this effect leads to a small increase of 3.33% of the drag reduction (Spalart and McLean, 2011).

Fuel weight saving The second beneficial effect of a drag reduction is that the amount of fuel required to fly a certain distance is smaller so that an aircraft needs to carry less fuel, which reduces the aircraft's weight and its drag. This effect leads to a 16.67% increase in drag reduction (Spalart and McLean, 2011).

Figure 9.5 shows how the 10% wall drag reduction translates into a final fuel burn reduction of 2.53% and a breakdown of the contribution of every aspect that was discussed previously. Although the final fuel burn reduction is smaller than the assumed wall drag reduction, it has to be noted that it is very substantial. Following an estimation by Kornilov (2015), a 1% drag reduction can lead to 400,000 L of fuel saved per year in the case of an A340-300 aircraft. Consequently, the 2.53% translate to a saving of over one million litres per year per aircraft.

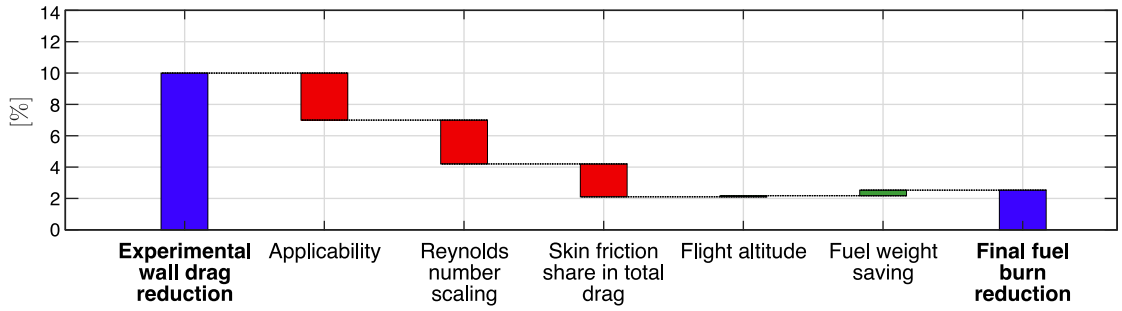

Figure 9.5: Skin friction reduction to final fuel burn reduction breakdown; blue bars show total quantities, such as wall drag reduction or fuel burn reduction; red bars indicate negative contributions (i.e. drag increasing contributions) and green bars indicate positive contributions (i.e. drag reducing contributions)

For its feasible dimensions in industrial applications, straightforward manufacturing, and potentially substantial final fuel burn reduction, chevron-shaped protrusions are considered a highly interesting technique. For its potential and since this is only an initial investigation into this passive flow control technique, it is recommended to extend the research, as will be detailed in section 10.2.

10

Concluding remarks and future outlook

Chevron-shaped protrusions have a distinct set of benefits for real-world applications: the required dimensions of the protrusions are feasible, these can easily be (retro)fitted to aircraft by means of a foil, and the final potential drag reduction is substantial. These benefits over other passive flow control techniques make a study of chevron-shaped protrusions of particular interest.

In this thesis, chevron-shaped protrusions have been studied as a passive flow control technique for reducing drag in a turbulent boundary layer. Four research questions have been formulated to address the research opportunities identified in the literature. The required designs to answer these questions have been selected and prepared for manufacturing using vinyl protrusion of roughly $5\delta_\nu - 6\delta_\nu$ in thickness (for the design Reynolds number of $Re_\tau = 1270$) attached to an aluminium base plate. Direct force measurements have been performed in the M-tunnel over a Reynolds number range of approximately $630 < Re_\tau < 1850$ to determine the drag performance.

A detailed investigation has been performed to explore the possible causes of the observed drag increase. The corner vortices present in the test section have been measured, and their spanwise extent has been quantified. Furthermore, the coherent structures have been characterised by means of 2D-2C PIV of a wall-parallel plane at a minimum distance of $17\delta_\nu$ from the wall. Last, the effect of an internal boundary layer has been explored as a possible cause for badly scaled protrusions in the current setup.

The main contributions of this study to the field of chevron-shaped protrusions are the replication data for previous studies, the first data published on the effect of individual design parameters on the drag performance, and the first flow visualisations of the near-wall flow over arrays of protrusions. The conclusions that can be drawn from these three main outcomes are presented below:

- **Replication of experiments presented in prior studies.**
  The results from Sagong et al. (2008) have been replicated successfully. However, all other previous experimental studies could not be replicated. The possible causes for the discrepancy in the results have been discussed extensively. The choice of an external flow instead of a channel flow, different measurement techniques, and limitations in the used experimental setup have been identified as the most likely causes. It is concluded that further tests addressing the identified causes for the discrepancy are required to support or dismiss the results from previous studies conclusively.

- **First data published on the effect of individual design parameters on the drag performance.**
  The data reflects the effect of eight design parameters on the drag performance. No drag reduction has been observed for any of the tested configurations. The results consistently have shown that the added roughness due to the presence of protrusions is not the only parameter that determines the drag performance. Furthermore, the drag performance has been found to be highly

sensitive to the randomisation of the array. From these data, it is concluded that a meaningful interaction occurs between the protrusions and the flow.

- **First flow visualisation of the near-wall flow over arrays of protrusions.**
  No substantial change in spanwise spacing or streamwise length of the near-wall turbulent structures has been observed between aligned protrusions, random protrusions, and the smooth reference case. The level of turbulence, analysed as the velocity variance, does also not support the hypothesis regarding the working mechanism presented in previous studies. It is concluded that the protrusion designs tested in this study do not interact with the coherent structures as described in the literature. However, the results agree with the behaviour observed from the direct force measurements, leading to the second conclusion that the protrusions are badly scaled and do not interact with the low-speed streaks effectively.

Further details on the main outcomes are provided in the following section, where the individual research questions will be addressed.

10.1. Research questions

In section 1.2, four research questions have been formulated, which have been targeted in this report. This section aims to summarise the answers to these research questions.

1. ***Can the results found in the literature be reproduced?***

   The sub-questions will be discussed before addressing the overall question.

   (a) *How can the reported designs/ experimental setup be replicated in the available experimental facilities? Is there missing information for which assumptions have to be made?*

   The experimental setup was chosen to be comparable to the ones used in the literature. In particular, the Reynolds numbers for the tests were matched with the ones in previous studies, and the models were scaled according to the viscous unit length in the M-tunnel. The most notable difference between the used test setup and the one by Sirovich and Karlsson (1997) is that the protrusions were tested in an external flow instead of a channel flow. The same external flow setup is used by Monti et al. (2001) and Sagong et al. (2008). Some differences are also observed in the size of the test plate: while the chosen size is comparable to the one used by Sagong et al. (2008) and Monti et al. (2001), it is much smaller than the one used by Sirovich and Karlsson (1997) (only 5% of the area). Finally, the measurement techniques selected for the experiments differ: a direct force measurement as used by Sagong et al. (2008) is selected for this campaign, while Sirovich and Karlsson (1997) and Monti et al. (2001) determine the drag force indirectly using pressure measurements. Regarding the geometry of the protrusion arrays, only the thickness of the chevron legs was not defined in Sirovich and Karlsson (1997). The geometry used by Sagong et al. (2008) was somewhat ambiguous. In both cases, an educated choice has been made. An overview of the testing condition for the different studies can be found in table 7.1.

   (b) *What is the difference in drag force measured between the various configurations and the reference smooth flat plate? And, in particular, can the reported drag reduction be reproduced?*

   An overview of the drag difference with respect to a flat reference plate for all replication test cases can be found in figure 7.2. The values range between a $0.14 \pm 0.24\%$ and $6.58 \pm 0.59\%$ drag increase; no relevant drag reduction has been observed.

   (c) *How can differences between the performed measurements and the reported results be explained?*

   The differences between the performed measurements and the reported results can have different sources that are addressed in section 7.2. The first possibility is a low-quality turbulent boundary layer, in particular, due to the effect of the corner vortices and an insufficient de-

velopment length. The second option is that the chosen scaling is incorrect due to the effect of an internal boundary layer or a wrong estimation of the viscous unit length. The scaling might also be wrong if the low-speed streak separation is not the correct proxy or the viscous unit length is the wrong choice of scaling parameter altogether. The difference in the testing conditions is the third possible cause for the deviations, especially the smaller protrusion area, the measurement technique, and the channel flow. Lastly, the experimental results reported in the literature may be erroneous.

To answer the overall question, not all results reported in the literature could be reproduced. Only the findings from Sagong et al. (2008) have been replicated within the measurement uncertainty. For all other results, large deviations have been observed. Especially relevant is that none of the reported drag reductions could be observed in the measurements.

The second question addresses the different parameters that characterise the protrusion array and aims to understand their effect on the drag performance of a given protrusion array.

2. ***How do the individual parameters of the protrusion array affect its performance?***

   Again, the sub-questions will be addressed first, followed by an answer to the general question.

   (a) *What granularity of the design parameter space can feasibly be tested?*

   It is not feasible to experimentally test all parameter combinations and alternative designs due to the limited time and resources available. For this reason, the required design parameters to describe an array of protrusions have been defined, and the relevant ones for testing have been identified. The parameters can be grouped into two categories: element parameters that describe a single element (such as shape, type, length, width, height, apex angle, and thickness of the chevron legs) and array parameters that describe the arrangement of the elements (such as separation between rows, separation between elements in a row, offset between rows, type of offset, and orientation). In this Master thesis, all parameters except for the element length, width, and height are tested. The main reason for this choice is that the array parameters are expected to have a larger effect on the performance than the element parameters, judging from the available literature. For every parameter, between two and four different values are tested. A detailed explanation of the cases selected for testing is provided in chapter 4.

   (b) *How do changes in the individual design parameters affect the drag force difference with respect to a smooth reference plate and, in particular, the achieved drag reduction?*

   No drag reduction has been observed for any of the tested parameter variations; hence, the answer will focus on how the different parameters affect the measured drag increase (ΔC_D). For the separation between rows and the separation between elements in a row, the ΔC_D is lower with increasing separation, in general. An optimal separation has been found at $350\delta_\nu$ for the separation between rows and at $300\delta_\nu$ for the separation between elements in a row. In the case of the chevron leg thickness, an increasing value leads to an increase in ΔC_D. In all three cases, the general trend follows the trend observed for the plate coverage: the larger the coverage, the larger ΔC_D. The exceptions to this trend indicate that the added roughness due to the presence of the protrusions is not the only parameter that determines the drag performance; hence, a meaningful interaction between the protrusions and the flow occurs.

   Deltas have been found to perform as protrusions in the apex upstream configuration. Moreover, cavities led to a lower ΔC_D than protrusions. Regarding the offset, an aligned pattern leads to a ΔC_D of the same magnitude or higher than a random or constant array. Similarly, the arrays with a constant offset lead to a ΔC_D equal to or higher than their random counterparts. Finally, different randomisations lead to very different drag performance, showing the high sensitivity of the drag performance and providing more evidence to support that the protrusion roughness is not the only relevant parameter. The last parameter tested, namely the orientation, has, in general, a negligible effect on the performance. The complete

overview of results can be found in section 7.1.

(c) *Can an outer envelope of drag-reducing designs be defined? Does this envelope change with Reynolds number?*

An outer envelope of drag-reducing design cannot be defined since no drag reduction has been observed. ΔC_D increases (quasi)linearly with the Reynolds number and no sudden change in performance has been observed.

The effect of the individual parameters on the drag performance has been covered in the sub-questions. The details of the parametric study are well documented in chapter 7.

While the first two questions have focused on the concrete drag performance for different configurations, question number three addresses the hypothesised working mechanism.

3. ***Do the flow characteristics and coherent structures in the flow support the working mechanism hypothesis presented by Sirovich and Karlsson (1997)?***

(a) *Can low-speed streaks be visualised over the smooth reference test plate with the available experimental setup?*

The low-speed streaks at $y^+ = 17$ have been visualised over a smooth test plate for a free-stream velocity of 5 m/s. A two-point correlation analysis has been performed to determine the spanwise spacing and streamwise separation of these streaks; the computed spacing is in the order of the expected values at the respective distance from the wall. A similar analysis was performed for 10 m/s and 20 m/s, also showing some level of coherence in the flow. However, the distance from the wall was too high for these two velocities to capture the effect of near-wall streaks solely.

(b) *Can the low-speed streaks be removed or be evidently weakened with a protrusion design that was shown to reduce skin friction?*

In the direct force measurements, no design was found to reduce drag. For this reason, this test is performed with a design with a random array that has been reported to reduce drag in previous studies. A comparison of the spacing and length of the structures present in the flow with the smooth reference case shows no evidence of affected low-speed streaks.

(c) *Can the low-speed streaks be evidently enhanced with an aligned protrusion design that was shown to increase skin friction?*

The tests performed with an aligned protrusion design show similar spacing and separation values as found for the flat reference plate; hence, the aligned protrusion patterns do not affect the low-speed streaks notoriously.

(d) *Do the turbulence statistics support the working mechanism hypothesis?*

A simple second-order statistical analysis has been performed. The variance of the streamwise velocity in the flow field is very similar for the pairs of random and aligned offset designs tested, suggesting that the level of turbulence in both cases is similar. All random cases analysed show no indication of a decreased turbulent activity that could support the hypothesis. The velocity variance for drag-increasing chevron designs is 40% – 70% higher than for the reference case; however, this increase was not observed for drag-increasing delta designs.

In general, no relevant variation could be observed in the characteristic spacing and length of the structures present in the flow nor in the variance of the velocity in the flow field. These observations lead to the conclusion that the flow characteristics and coherent structures analysed in this study do not support the working mechanism proposed in the literature.

Finally, the last question aimed at defining a better design based on the previous findings is addressed:

4. **To what extent can a design with improved drag performance or overall characteristics be defined?**

   (a) *What problems identified during the campaign can be addressed to lead to an improved design?*

   Possible causes for the measured drag performance have been addressed in a detailed flow investigation. In particular, the effect of the corner vortices, the low-speed streaks, and the internal boundary layer were examined. The outcome of this investigation is translated into clear design recommendations: a margin of at least 33 mm should be left smooth on each (long) side of the test plate; moreover, the protrusion design should be applied over the extension device to remove the smooth-to-rough step at the leading edge of the test plate and ensure equilibrium conditions.

   (b) *What aspects, next to drag performance, can be improved in the array design?*

   Next to the drag performance, the results found in the initial direct force campaign can be used to design an array that is easier to manufacture and less prone to damage. A concrete example is the use of delta-shaped protrusions instead of the original chevron-shaped ones.

An improved design has been defined by combining the best values for the parameters tested in this experimental study ($A = 350$, $D = 400$, RAND_E_D19) with easy to manufacture and robust delta-shaped protrusions. Furthermore, the test plate design has been improved to remove large sources of errors and yield more accurate results overall. A detailed explanation of the envisioned design is included in section 9.2. Although all preparations have been completed, the experimental test using the improved design remains open and is included as a recommended starting point for future research.

10.2. Recommendations for future research

Future research into the flow control technique of protrusions is deemed relevant due to the combination of large drag reduction found in prior studies, the advantages in practical applications, and the novel opportunities for further investigation identified in this thesis. This section summarises the recommendations for future research.

Test the improved design

The first recommendation is to perform direct force measurements of the improved design presented in section 9.2 in the M-tunnel. All the preparations required for this test have been conducted, and it is a good starting point to continue research on the performance of the protrusions in turbulent boundary layer flows. In particular, the main uncertainties of the current setup can be disregarded with the new improved design.

Test the element parameters

The element parameters that have been excluded from this study can be tested in order to complete the parametric study. The different element width and length values can easily be manufactured using the methods presented in this thesis. Furthermore, vinyl foils for different protrusion heights have been already selected and purchased.

Replicate experiments in a channel flow

The most evident difference between the experimental setup used for this thesis compared to the initial publication on protrusions (Sirovich and Karlsson, 1997) is the type of flow. A replication of the work by Sirovich and Karlsson (1997) using a channel flow would be an important contribution to the scientific community, as it would add evidence to support or dismiss the reported findings. This replication should become possible over the coming months as the construction of the improved channel 'DC40' is concluded.

In the channel flow, an exhaustive investigation of the flow mechanics can be conducted to understand the working mechanism, confirm or correct the scaling parameter, and eventually translate the technology to an external flow.

Use a longer development length

Generally, the tests should be performed using a larger area covered with protrusions and at higher Reynolds numbers. Both can be accomplished by using a longer test section to which the flow manipulators are applied. A test section extension with a length of 2.40 m has been recently built and is available for experimental campaigns with the 'Hill' in the M-tunnel.

Study the x-y plane

In this thesis, the x-z and the y-z plane have been studied. The flow field close to the protrusions can be examined in more detail using HWA or measuring the x-y plane with PIV to characterise the boundary layer at different streamwise positions. These data would make it possible to determine the mean boundary layer velocity profile and, in particular, if a vertical shift of the logarithmic region can be observed, analogous to other drag-reducing techniques like riblets.

Quantify the effect of the protrusion roughness

The direct force measurements have shown a strong correlation between the plate coverage ratio and the drag performance. This result suggests that the added roughness due to the presence of the protrusions ('protrusion roughness') is a major contributor to the observed drag increase. There is sufficient evidence to support that the protrusion roughness is not the only relevant parameter affecting the drag performance. However, more research is required to understand its exact magnitude.

Reduce the 'flat plate uncertainty'

The use of flatter test plates is recommended to avoid some of the problems experienced during the experimental campaign. In particular, the 'flat plate uncertainty' can be reduced in this case, enabling a more accurate study of the differences between configurations. An alternative to flatter plates is to test against the same test plate before applying the vinyl so that the largest source of error in the measurements, namely the 'flat plate uncertainty', is eliminated.

Use a more rigid support structure for the PIV experiments

Finally, for repeated measurements of the x-z plane very close to the wall, it is strongly recommended to build a new support structure for the test plate. The current one (the 'PHill') is unreliable and does not ensure an exact positioning of the test plate.

These recommendations should provide a good starting point for continuing the research on protrusions as a passive flow control technique for turbulent drag reduction.

Bibliography

Adrian, R. J., Meinhart, C. D., & Tomkins, C. D. (2000). Vortex organization in the outer region of the turbulent boundary layer. *Journal of Fluid Mechanics*, *422*, 1–54. https://doi.org/10.1017/S0022112000001580

Ahn, S., & Fessler, J. A. (2003). Standard errors of mean, variance, and standard deviation estimators. *EECS Department, The University of Michigan*, *1*(2).

Airbus. (2022). A350-1000: Shaping the future of air travel. Retrieved June 1, 2022, from https://aircraft.airbus.com/en/aircraft/a350/a350-1000

Al Zahrani, S., Islam, M. S., Xu, F., & Saha, S. C. (2020). Thermal performance investigation in a novel corrugated plate heat exchanger. *International Journal of Heat and Mass Transfer*, *148*, 119095. https://doi.org/10.1016/j.ijheatmasstransfer.2019.119095

Antonia, R. A., & Luxton, R. E. (1971). The response of a turbulent boundary layer to a step change in surface roughness Part 1. Smooth to rough. *Journal of Fluid Mechanics*, *48*(4), 721–761. https://doi.org/10.1017/S0022112071001824

Antonia, R. A., & Luxton, R. E. (1972). The response of a turbulent boundary layer to a step change in surface roughness. Part 2. Rough-to-smooth. *Journal of Fluid Mechanics*, *53*(4), 737–757. https://doi.org/10.1017/S002211207200045X

Baars, W. J. (2020). *Spectral properties of turbulence kinetic energy in turbulent boundary layers* [Online seminar]. Australasian Fluid Mechanics Seminar Series. https://www.afms.org.au/events.html#Webinars

Baars, W. J., Squire, D. T., Talluru, K. M., Abbassi, M. R., Hutchins, N., & Marusic, I. (2016). Wall-drag measurements of smooth- and rough-wall turbulent boundary layers using a floating element. *Experiments in Fluids*, *57*(5), 90. https://doi.org/10.1007/s00348-016-2168-y

Bechert, D. W., Bruse, M., Hage, W., & Meyer, R. (1997). Biological surfaces and their technological application - laboratory and flight experiments on drag reduction and separation control. *28th Fluid Dynamics Conference*. https://doi.org/10.2514/6.1997-1960

Bechert, D. W. (1999). Passive control methods: Riblets, vortex generators and self-activating flaps. In G. E. A. Meier & P. R. Viswanath (Eds.), *IUTAM Symposium on Mechanics of Passive and Active Flow Control. Fluid Mechanics and its Applications* (pp. 107–108). Springer, Dordrecht. https://doi.org/10.1007/978-94-011-4199-4_17

Bewley, G. P., Chang, K., & Bodenschatz, E. (2012). On integral length scales in anisotropic turbulence. *Physics of Fluids*, *24*(6), 061702. https://doi.org/10.1063/1.4726077

Blackwelder, R. F. (1988). Coherent structures associated with turbulent transport. *Transport Phenomena in Turbulent Flows: Theory, Experiment, and Numerical Simulation*, 69–88. https://ui.adsabs.harvard.edu/abs/1988tptf.proc...69B

Boeing. (2022). BOEING 777X: Meet the 777X. Retrieved June 1, 2022, from https://www.boeing.com/commercial/777x/

Brundrett, E., & Baines, W. D. (1964). The production and diffusion of vorticity in duct flow. *Journal of Fluid Mechanics*, *19*(3), 375–394. https://doi.org/10.1017/S0022112064000799

CAN & ICSA. (2018). *Contribution of the global aviation sector to achieving Paris Agreement climate objectives* (Conference Proceedings). https://unfccc.int/sites/default/files/resource/156_CAN%20ICSA%20Aviation%20TD%20submission.pdf

Canton, J., Örlü, R., Chin, C., Hutchins, N., Monty, J., & Schlatter, P. (2016). On large-scale friction control in turbulent wall flow in low reynolds number channels. *Flow, Turbulence and Combustion*, *97*(3), 811–827. https://doi.org/10.1007/s10494-016-9723-8

Chernyshenko, S. I., & Baig, M. F. (2005). The mechanism of streak formation in near-wall turbulence. *Journal of Fluid Mechanics*, *544*, 99–131. https://doi.org/10.1017/S0022112005006506

Choi, K. S. (2006). The rough with the smooth. *Nature*, *440*(7085), 754–754. https://doi.org/10.1038/440754a

Coles, D. (1956). The law of the wake in the turbulent boundary layer. *Journal of Fluid Mechanics*, *1*(2), 191–226. https://doi.org/10.1017/S0022112056000135

Corrsin, S. (1957). Some current problems in turbulent shearflows. *Nat. Acad. Sci. Naval Hydrodynamics, Publ.*, *515*. https://ci.nii.ac.jp/naid/10006919593/en/

Dennis, D. J. C. (2015). Coherent structures in wall-bounded turbulence. *Anais da Academia Brasileira de Ciências*, *87*(2), 1161–1193. https://doi.org/10.1590/0001-3765201520140622

Du, Y., & Karniadakis, G. E. (2000). Suppressing wall turbulence by means of a transverse traveling wave. *Science*, *288*(5469), 1230–1234. https://doi.org/10.1126/science.288.5469.1230

Du, Y., Symeonidis, V., & Karniadakis, G. E. (2002). Drag reduction in wall-bounded turbulence via a transverse travelling wave. *Journal of Fluid Mechanics*, *457*, 1–34. https://doi.org/10.1017/s0022112001007613

Fiedler, H. E. (1987). Coherent structures. In G. Comte-Bellot & J. Mathieu (Eds.), *Advances in turbulence* (pp. 320–336). Springer Berlin Heidelberg. https://doi.org/10.1007/978-3-642-83045-7_37

Fransson, J. H. M., Talamelli, A., Brandt, L., & Cossu, C. (2006). Delaying transition to turbulence by a passive mechanism. *Physical review letters*, *96*(6), 064501. https://doi.org/10.1103/PhysRevLett.96.064501

Gad-el-Hak, M. (2000). *Flow control: Passive, active, and reactive flow management*. Cambridge University Press. https://doi.org/10.1017/CBO9780511529535

Ganapathisubramani, B., Hutchins, N., Monty, J. P., Chung, D., & Marusic, I. (2012). Amplitude and frequency modulation in wall turbulence. *Journal of Fluid Mechanics*, *712*, 61–91. https://doi.org/10.1017/jfm.2012.398

Garratt, J. R. (1990). The internal boundary layer — A review. *Boundary-layer meteorology*, *50*, 171–203. https://doi.org/10.1007/BF00120524

Gatti, D., & Quadrio, M. (2016). Reynolds-number dependence of turbulent skin-friction drag reduction induced by spanwise forcing. *Journal of Fluid Mechanics*, *802*, 553–582. https://doi.org/10.1017/jfm.2016.485

Gessner, F. B., & Jones, J. B. (1965). On some aspects of fully-developed turbulent flow in rectangular channels. *Journal of Fluid Mechanics*, *23*(4), 689–713. https://doi.org/10.1017/S0022112065001635

Glauert, H. (1933). *Wind tunnel interference on wings, bodies and airscrews in a two-dimensional-flow wind tunnel* (No. 1566). British A. R. C. https://apps.dtic.mil/sti/pdfs/ADA953012.pdf

Gramola, M., Bruce, P. J. K., & Santer, M. (2019). Photogrammetry for accurate model deformation measurement in a supersonic wind tunnel. *Experiments in Fluids*, *60*(1), 1–11. https://doi.org/10.1007/s00348-018-2652-7

Handler, R. A., Levich, E., & Sirovich, L. (1993). Drag reduction in turbulent channel flow by phase randomization. *Physics of Fluids A: Fluid Dynamics*, *5*(3), 686–694. https://doi.org/10.1063/1.858652

Hartog, F. H. (2021). *Turbulent boundary layers over surfaces with streamwise-preferential permeability - Experimental investigation into the drag and flow mechanics* [Master thesis, Delft University of Technology]. Delft University of Technology Repository. http://resolver.tudelft.nl/uuid:0797d3d4-ff30-460c-a5b6-6ff732eb6ffd

Head, M. R., & Bandyopadhyay, P. (1981). New aspects of turbulent boundary-layer structure. *Journal of Fluid Mechanics*, *107*, 297–338. https://doi.org/10.1017/s0022112081001791

Hu, Z., & Sandham, N. D. (2001). Large-domain simulations of plane couette and poiseuille flow. *Second Symposium on Turbulence and Shear Flow Phenomena*.

Hussain, A. K. M. F. (1986). Coherent structures and turbulence. *Journal of Fluid Mechanics*, *173*, 303–356. https://doi.org/10.1017/S0022112086001192

Hutchins, N., & Marusic, I. (2007). Evidence of very long meandering features in the logarithmic region of turbulent boundary layers. *Journal of Fluid Mechanics*, *579*, 1–28. https://doi.org/10.1017/S0022112006003946

Hutchins, N., Monty, J. P., Ganapathisubramani, B., Ng, H. C. H., & Marusic, I. (2011). Three-dimensional conditional structure of a high-Reynolds-number turbulent boundary layer. *Journal of Fluid Mechanics*, *673*, 255–285. https://doi.org/10.1017/S0022112010006245

Kadivar, M., Tormey, D., & McGranaghan, G. (2021). A review on turbulent flow over rough surfaces: Fundamentals and theories. *International Journal of Thermofluids*, *10*, 100077. https://doi.org/10.1016/j.ijft.2021.100077

Keyence Corporation of America. (2016). Wide-Area 3D Measurement System. Retrieved January 21, 2022, from https://indico.fnal.gov/event/19329/contributions/51481/attachments/32024/39256/611883_VR-3200_Brochure.pdf

Kline, S. J., Reynolds, W. C., Schraub, F. A., & Runstadler, P. W. (1967). The structure of turbulent boundary layers. *J. Fluid Mech*, *30*(4), 741–773. https://doi.org/10.1017/S0022112067001740

Kornilov, V. I. (2015). Current state and prospects of researches on the control of turbulent boundary layer by air blowing. *Progress in Aerospace Sciences*, *76*, 1–23. https://doi.org/10.1016/j.paerosci.2015.05.001

Lagraa, B., Labraga, L., & Mazouz, A. (2004). Characterization of low-speed streaks in the near-wall region of a turbulent boundary layer. *European Journal of Mechanics - B/Fluids*, *23*(4), 587–599. https://doi.org/https://doi.org/10.1016/j.euromechflu.2003.12.005

Lai, Y. J. C. (2021). *Turbulent viscous drag reduction in air by compliant surfaces* [Master thesis, Delft University of Technology]. Delft University of Technology Repository. http://resolver.tudelft.nl/uuid:a470acae-1238-4e47-a986-11fc69378f6b

LaVision. (2020). Imager sCMOS CLHS. Retrieved June 1, 2022, from https://www.lavision.de/en/products/cameras/cameras-for-piv/

Lee, M., & Moser, R. D. (2015). Direct numerical simulation of turbulent channel flow up to $Re_\tau \approx 5200$. *Journal of Fluid Mechanics*, *774*, 395–415. https://doi.org/10.1017/jfm.2015.268

Levich, E., Shtilman, L., & Tur, A. V. (1991). The origin of coherence in hydrodynamical turbulence. *Physica A: Statistical Mechanics and its Applications*, *176*(2), 241–296. https://doi.org/10.1016/0378-4371(91)90290-S

Levich, E. (2009). Coherence in turbulence: New perspective. *Concepts of Physics*, *6*(3), 239–457. https://doi.org/10.2478/v10005-009-0007-0

Li, M., de Silva, C. M., Rouhi, A., Baidya, R., Chung, D., Marusic, I., & Hutchins, N. (2019). Recovery of wall-shear stress to equilibrium flow conditions after a rough-to-smooth step change in turbulent boundary layers. *Journal of Fluid Mechanics*, *872*, 472–491. https://doi.org/10.1017/jfm.2019.351

Lin, Y. Y. (2021). *Numerical investigation of the turbulent boundary layer over dimpled surfaces* [Master thesis, Delft University of Technology]. Delft University of Technology Repository. http://resolver.tudelft.nl/uuid:e4e11548-f4f8-4728-8213-98f313d800c6

Lu, F. K. (2010). Surface oil flow visualization. *The European Physical Journal Special Topics*, *182*(1), 51–63. https://doi.org/10.1140/epjst/e2010-01225-0

Lumibird. (2020). Evergreen Double-pulse Nd:YAG lasers for PIV (03/20-REV A). Retrieved June 1, 2022, from https://www.quantel-laser.com/tl_files/client/docs_produits/EverGreen2_Specs_EN_032020REVA.pdf

Lumley, J. L. (1970). *Stochastic tools in turbulence*. Academic Press, Inc.

Marusic, I., Chandran, D., Rouhi, A., Fu, M. K., Wine, D., Holloway, B., Chung, D., & Smits, A. J. (2021). An energy-efficient pathway to turbulent drag reduction. *Nature Communications*, *12*(1), 5805. https://doi.org/10.1038/s41467-021-26128-8

Marusic, I., Mathis, R., & Hutchins, N. (2010). High Reynolds number effects in wall turbulence. *International Journal of Heat and Fluid Flow*, *31*(3), 418–428. https://doi.org/10.1016/j.ijheatfluidflow.2010.01.005

Metamark. (2021). Product catalogue - self adhesive signvinyl, digital media and speciality materials. Retrieved January 20, 2022, from https://www.metamark.co.uk/media/support/catalogues/m20169_Metamark_Product_catalogue_v3_RGBCOVER_.pdf

Metamark (UK) Limited. (2021). Metamark 7 Series: High Performance Calendered Sign Vinyl. Retrieved June 1, 2022, from https://www.metamark.co.uk/mwdownloads/download/link/id/366/

Mikosz, S. (2021). Fly net zero: Airline commitment to net zero 2050 [Press Release No. 66 after the 77th IATA Annual General Meeting in Boston, USA]. Retrieved January 10, 2022, from https://www.iata.org/en/iata-repository/pressroom/presentations/environment-net-zero-carbon-at-iata-agm-2021/

Modesti, D., Pirozzoli, S., Orlandi, P., & Grasso, F. (2018). On the role of secondary motions in turbulent square duct flow. *Journal of Fluid Mechanics*, *847*, R1. https://doi.org/10.1017/jfm.2018.391

Monti, R., De Ponte, S., & Levich, E. (2001). Effects on the resistance and on the separation of v shapes passive manipulators in a turbulent boundary layer. In A. Soldati & R. Monti (Eds.), *Turbulence structure and modulation* (pp. 255–267). Springer Vienna. https://doi.org/10.1007/978-3-7091-2574-8_9

Monty, J. P., Hutchins, N., NG, H. C. H., Marusic, I., & Chong, M. S. (2009). A comparison of turbulent pipe, channel and boundary layer flows. *Journal of Fluid Mechanics*, *632*, 431–442. https://doi.org/10.1017/S0022112009007423

Murakami, Y., Shtilman, L., & Levich, E. (1992). Reducing turbulence by phase juggling. *Physics of Fluids A: Fluid Dynamics*, *4*(8), 1776–1781. https://doi.org/10.1063/1.858399

Nieuwstadt, F. T. M., Westerweel, J., & Boersma, B. J. (2016). *Turbulence*. Springer International Publishing. https://doi.org/10.1007/978-3-319-31599-7

Nikuradse, J. (1930). Untersuchungen über turbulente Strömungen in nicht kreisförmigen Rohren. *Ing. arch*, *1*, 306–332. https://doi.org/10.1017/jfm.2017.617

Oguri, E., & Kohama, Y. (1996). Drag reduction by micron-sized distributed surface geometry on a flat plate [In Japanese]. *Nippon Kikai Gakkai Ronbunshu, B Hen/Transactions of the Japan Society of Mechanical Engineers, Part B*, *62*(597), 1754–1761. https://doi.org/10.1299/kikaib.62.1754

Pirozzoli, S., Modesti, D., Orlandi, P., & Grasso, F. (2018). Turbulence and secondary motions in square duct flow. *Journal of Fluid Mechanics*, *840*, 631–655. https://doi.org/10.1017/jfm.2018.66

Prandtl, L. (1926). Über die ausgebildete Turbulenz. *International Congress for Applied Mechanics*.

Raffel, M., Willert, C. E., Scarano, F., Kähler, C. J., Wereley, S. T., & Kompenhans, J. (2018). *Particle image velocimetry : A practical guide*. Springer. https://doi.org/10.1007/978-3-319-68852-7

Rao, K. S., Wyngaard, J. C., & Coté, O. R. (1974). The structure of the two-dimensional internal boundary layer over a sudden change of surface roughness. *Journal of Atmospheric Sciences*, *31*(3), 738–746. https://doi.org/10.1175/1520-0469(1974)031<0738:TSOTTD>2.0.CO;2

Rius Vidales, A. F. (2022). *Influence of a forward-facing step on crossflow instability and transition: An experimental study in a swept wing boundary-layer* (Doctoral dissertation). Delft University of Technology. https://doi.org/10.4233/uuid:6fd8a152-ab7a-4ecd-a817-61945d431bef

Rius Vidales, A. F., & Kotsonis, M. (2021). Impact of a forward-facing step on the development of crossflow instability. *Journal of Fluid Mechanics*, *924*, A34. https://doi.org/10.1017/jfm.2021.497

Robinson, S. K. (1991). Coherent motions in the turbulent boundary layer. *Annual Review of Fluid Mechanics*, *23*(1), 601–639. https://doi.org/10.1146/annurev.fl.23.010191.003125

Rodrigue, J. P. (2020). *The geography of transport systems* (5th ed.). Routledge. https://doi.org/10.4324/9780429346323

Rosti, M. E., & Brandt, L. (2017). Numerical simulation of turbulent channel flow over a viscous hyper-elastic wall. *Journal of Fluid Mechanics*, *830*, 708–735. https://doi.org/10.1017/jfm.2017.617

Rouhi, A., Chung, D., & Hutchins, N. (2019). Direct numerical simulation of open-channel flow over smooth-to-rough and rough-to-smooth step changes. *Journal of Fluid Mechanics*, *866*, 450–486. https://doi.org/10.1017/jfm.2019.84

Sagong, W., Kim, C., Choi, S., Jeon, W. P., & Choi, H. (2008). Does the sailfish skin reduce the skin friction like the shark skin? *Physics of Fluids*, *20*(10), 101510. https://doi.org/10.1063/1.3005861

Savelyev, S. A., & Taylor, P. A. (2005). Internal Boundary Layers: I. Height Formulae for Neutral and Diabatic Flows. *Boundary-Layer Meteorology*, *115*, 1–25. https://doi.org/10.1007/s10546-004-2122-z

Schoppa, W., & Hussain, F. (1998). A large-scale control strategy for drag reduction in turbulent boundary layers. *Physics of Fluids*, *10*(5), 1049–1051. https://doi.org/10.1063/1.869789

Sciacchitano, A., & Wieneke, B. (2016). PIV uncertainty propagation. *Measurement Science and Technology*, *27*(8), 084006. https://doi.org/10.1088/0957-0233/27/8/084006

Sillero, J. A., Jiménez, J., & Moser, R. D. (2014). Two-point statistics for turbulent boundary layers and channels at Reynolds numbers up to $\delta+ \approx 2000$. *Physics of Fluids*, *26*(10), 105109. https://doi.org/10.1063/1.4899259

Sirovich, L., Ball, K. S., & Handler, R. A. (1991). Propagating structures in wall-bounded turbulent flows. *Theoretical and Computational Fluid Dynamics*, *2*(5), 307–317. https://doi.org/10.1007/BF00271470

Sirovich, L., Ball, K. S., & Keefe, L. R. (1990). Plane waves and structures in turbulent channel flow. *Physics of Fluids A: Fluid Dynamics*, *2*(12), 2217–2226. https://doi.org/10.1063/1.857808

Sirovich, L., Bronicki, L., & Levich, E. (1993). *Method and apparatus for controlling turbulence in a wall-bounded fluid flow field* (Patent No. 0 543 647 A1). European Patent Office.

Sirovich, L., & Karlsson, S. (1997). Turbulent drag reduction by passive mechanisms. *Nature*, *388*(6644), 753–755. https://doi.org/10.1038/41966

Sirovich, L., & Levich, E. (1993). *Method of and apparatus for controlling turbulence in a wall-bounded fluid flow field* (US Patent No. 5.263.793). United States Patent and Trademark Office.

Sirovich, L., Levich, E., & Bronicki, L. (1994). *Method of and apparatus for controlling turbulence in a wall-bounded fluid flow field* (US Patent No. 5.362.179). United States Patent and Trademark Office.

Sirovich, L., Levich, E., & Bronicki, L. (1997). *Method of and apparatus for controlling turbulence in boundary layer and other wall-bounded fluid flow fields* (US Patent No. 5.595.205). United States Patent and Trademark Office.

Sirovich, L., Levich, E., & Bronicki, L. (1998a). *Method and apparatus for controlling turbulence in boundary layer and other wall-bounded fluid flow fields* (US Patent No. 5.797.414). United States Patent and Trademark Office.

Sirovich, L., Levich, E., Bronicki, L., & Karlsson, S. (1998b). *Apparatus for controlling turbulence in boundary layer and other wall-bounded fluid flow fields* (US Patent No. 5.833.389). United States Patent and Trademark Office.

Sirovich, L., Levich, E., Bronicki, L., & Karlsson, S. (1998c). *Method and apparatus for controlling turbulence in boundary layer and other wall-bounded fluid flow fields* (Patent No. EP 0 850 832 A1). European Patent Office.

Sirovich, L., Maxey, M., & Tarman, H. I. (1989). An eigenfunction analysis of turbulent thermal convection. In J. C. Jean-Claude Andre, F. Durst, B. Launder, F. W. Schmidt, & J. H. Whitelaw (Eds.), *Turbulent Shear Flows 6* (pp. 66–77). Springer, Berlin, Heidelberg. https://doi.org/10.1007/978-3-642-73948-4_7

Smith, C. R. (1984). A synthesized model of the near-wall behavior in turbulent boundary layers. In G. K. Patterson & J. L. Zakin (Eds.), *Proceedings of 8th symp. on turbulence*. University of Missouri-Rolla. https://apps.dtic.mil/sti/pdfs/ADA137029.pdf

Smith, C. R., & Metzler, S. P. (1983). The characteristics of low-speed streaks in the near-wall region of a turbulent boundary layer. *Journal of Fluid Mechanics*, *129*, 27–54. https://doi.org/10.1017/S0022112083000634

Spalart, P. R., & McLean, J. D. (2011). Drag reduction: enticing turbulence, and then an industry. *Philosophical Transactions of the Royal Society A: Mathematical, Physical and Engineering Sciences*, *369*(1940), 1556–1569. https://doi.org/10.1098/rsta.2010.0369

Tameike, H., Yakeno, A., & Obayashi, S. (2021). Influence of small wavy roughness on flatplate boundary layer natural transition. *Journal of Fluid Science and Technology*, *16*(1), JFST0008. https://doi.org/10.1299/jfst.2021jfst0008

Tani, I. (1988). Drag reduction by riblet viewed as roughness problem. *Proceedings of the Japan Academy, Series B*, *64*(2), 21–24. https://doi.org/10.2183/pjab.64.21

Theodorsen, T. (1955). The structure of turbulence. In H. Görtler & W. Tollmien (Eds.), *50 Jahre Grenzschichtforschung: Eine Festschrift in Originalbeiträgen* (pp. 55–62). Vieweg+Teubner Verlag, Wiesbaden. https://doi.org/10.1007/978-3-663-20219-6_6

Thorlabs, Inc. (2022). N-BK7 Bi-Convex Lenses (AR Coating: 350 - 700 nm). Retrieved June 1, 2022, from https://www.thorlabs.com/newgrouppage9.cfm?objectgroup_id=4848

Tian, G., Zhang, Y., Feng, X., & Hu, Y. (2022). Focus on bioinspired textured surfaces toward fluid drag reduction: Recent progresses and challenges. *Advanced Engineering Materials*, *24*(1), 2100696. https://doi.org/10.1002/adem.202100696

Tugluk, O., & Tarman, H. I. (2016). Drag reduction via phase randomization in turbulent pipe flow. In B. Karasözen, M. Manguoğlu, M. Tezer-Sezgin, S. Göktepe, & Ö. Uğur (Eds.), *Numerical Mathematics and Advanced Applications ENUMATH 2015* (pp. 463–470). Springer International Publishing. https://doi.org/10.1007/978-3-319-39929-4_44

van Nesselrooij, M., van Campenhout, O. W. G., van Oudheusden, B. W., Schrijer, F. F. J., & Veldhuis, L. L. M. (2022). Development of an experimental apparatus for flat plate drag measurements and considerations for such measurements. *Measurement Science and Technology*, *33*(5), 055303. https://doi.org/10.1088/1361-6501/ac527f

Walsh, M. (1982). Turbulent boundary layer drag reduction using riblets. *20th aerospace sciences meeting* (p. 169). https://doi.org/10.2514/6.1982-169

Wang, H., Wang, Z., Luo, K., Hawkes, E. R., Chen, J. H., & Fan, J. (2021). Direct numerical simulation of turbulent boundary layer premixed combustion under auto-ignitive conditions. *Combustion and Flame*, *228*, 292–301. https://doi.org/10.1016/j.combustflame.2021.02.005

White, F. M. (2006). *Viscous fluid flow* (3rd international ed.). McGraw-Hill.

Yang, M., & Shima, S. (1988). Simulation of pyramid type three-roll bending process. *International Journal of Mechanical Sciences*, *30*(12), 877–886. https://doi.org/https://doi.org/10.1016/0020-7403(88)90071-9

Zhang, Y., Yan, C., Chen, H., & Yin, Y. (2020). Study of riblet drag reduction for an infinite span wing with different sweep angles. *Chinese Journal of Aeronautics*, *33*(12), 3125–3137. https://doi.org/10.1016/j.cja.2020.05.015

Zhou, H., Zhu, Y., Tian, G., Feng, X., & Zhang, Y. (2021). Experimental investigations of the turbulent boundary layer for biomimetic surface with spine-covered protrusion inspired by pufferfish skin. *Arabian Journal for Science and Engineering*, *46*(3), 2865–2875. https://doi.org/10.1007/s13369-020-05235-6

V

Appendices

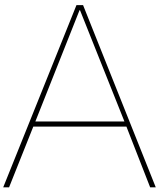

Table of designs from literature

In chapter 3 of this Master thesis, several studies that have tested protrusions in the past are reviewed. The corresponding array designs used in these studies are also introduced and briefly discussed. In particular, the drag decreasing designs (or: non-zero offset designs) are of relevance for this Master thesis. This appendix gives an overview of the relevant array parameters used in literature in table A.1. Notice that only drag-reducing designs are included; concretely, the presented designs are:

- Sirovich et al. (1998b), design range reported in the patent for the different parameters.
- Sirovich et al. (1998b), best drag reduction design reported in the patent (D2).
- Sirovich and Karlsson (1997), random protrusion array design.
- Monti et al. (2001), random protrusion array design.
- Sagong et al. (2008), two reported array designs with a random and constant offset.

A detailed explanation of the individual parameters can be found in chapter 4.

		Sirovich et al. (1998b) Design Range	Sirovich et al. (1998b) Drag reduction design	Sirovich and Karlsson (1997)	Monti et al. (2001)	Sagong et al. (2008)
Shape (Chevron [C], delta [D], other [O])	–	C	C	C	C	C
Type (Protrusion [P], cavity [CY])	–	P	P	P	P	P
Separation between rows (streamwise distance)	A	200 - 400	278	300	300	278/300
Length of an element (streamwise size)	B	150 - 250	200	–	200	200
Width on an element (transversal size)	C	–	182	200	180	182/200
Separation between elements in a row (transversal distance)	D	200 - 300	270	260	260	270/260
Offset between rows (transversal)	E	–	135	130	Figure 3.7	130/135
Type offset (Random [R], constant [CT], zero [Z])	–	R, CT, Z	R, CT	R	R	R, CT
Element height (or: depth)	F	5 - 15	5	5-6	5	5/5-6
Apex angle	α	20 - 90°	–	–	60°	–
Thickness of the chevron legs	T	–	–	–	–	20/ 30/ 40

Table A.1: Summary of design parameters in protrusion arrays; unless otherwise stated, the values are given in viscous units (δ_ν)

B

Table of designs and test plates

For this Master thesis, 33 test plates were tested in a total of 61 configurations. This number of configurations includes 24 unique test plate designs tested in two orientations, four PIV test plates tested in two orientations, and smooth reference plates for the error bar calculation. This appendix can be seen as a supplement to table 4.1 presented in section 4 and provides two reference tables to quickly identify design number, labels, and test plates.

In the discussion of the results, labels are used to refer to the different designs to facilitate the interpretation of these. The used labels are introduced in chapter 4. For quick reference, an overview of designs and the corresponding labels are presented in table B.1.

Design	Label
1	D2 (A)
2	D2 (C)
3	Sirovich (R), Sagong (40VU), A = 300VU, D = 260VU, T = 40VU, Chevrons (R), Protrusions (R), Sirovich (R1)
4	Sirovich (A), Sagong (A), Chevrons (A), Protrusions (A)
5	Sagong (30VU), T = 30VU
6	Sagong (20VU), T = 20VU
8	Deltas (R)
9	Deltas (A)
10	D2 Patent (R), D2 (R1)
11	D3 Patent
12	A = 400VU
13	A = 350VU
14	A = 230VU
15	Cavities (R)
16	Cavities (A)
17	Sirovich (R2)
18	Sirovich (R3)
19	D2 (R2)
20	Monti (A)
21	Monti (R)
22	D = 400VU
23	D = 300VU
24	D = 350VU
30	Trial TP

Table B.1: Designs and corresponding labels

The designs are geometric descriptions of a specific protrusion (or cavity) array. The physical objects used for the wind tunnel experiments are test plates. Table B.2 gives an overview of the test plates (TP) and the respective array designs. Note that every TP has two sides referred to as 'A' and 'B'. A 'quality check' column indicates if the model has no imperfections ('ok') or if it is damaged. The possible damages included in the table are 'no swing' to indicate that the test plate is bent and does not swing

freely when installed in the balance; and 'paint damaged' and 'damaged' to indicate that the base paint or the vinyl are not in good condition for use. The reference smooth plate (TP0000) is not included in the table.

Plate Number	Side	Design number	Quality check
TP0091	A	1	ok
TP0091	B	5	ok
TP0092	A	2	ok
TP0092	B	N/A	No swing
TP0093	A	11	ok
TP0093	B	N/A	No swing
TP0094	A	3	ok
TP0094	B	21	ok
TP0095	A	12	ok
TP0095	B	17	ok
TP0096	A	10	ok
TP0096	B	17	No swing
TP0097	A	13	ok
TP0097	B	27	ok
TP0098	A	4	ok
TP0098	B	16	ok
TP0099	A	8	ok
TP0099	B	18	ok
TP0100	A	9	ok
TP0100	B	23	ok
TP0101	A	5	No swing
TP0101	B	24	ok
TP0102	A	6	ok
TP0102	B	16	Damaged
TP0103	A	14	ok
TP0103	B	19	ok
TP0104	A	22	ok
TP0104	B	20	ok
TP0105	A	29	ok
TP0105	B	N/A	No swing
TP0106	A	30	ok
TP0106	B	15	ok
TP0107	A	9	paint damaged
TP0107	B	N/A	ok
TP0108	A	8	paint damaged
TP0108	B	N/A	N/A
TP0109	A	4	ok
TP0109	B	N/A	N/A
TP0110	A	3	ok
TP0110	B	N/A	N/A
TP0111	A	9	ok
TP0111	B	N/A	N/A
TP0112	A	8	ok
TP0112	B	N/A	N/A

Table B.2: Table of test plates and corresponding designs

C

All drag data and corrections

This appendix contains the drag data acquired for the 61 tested configurations. The results shown here correspond to the final measurements after rolling. Note that data for test plate TP0106A with design 30, which was manufactured as a proof of concept, is included in figures C.50 and C.51, although this test plate is not discussed in the main part of this report.

The figures are presented in ascending order of test plate number. Figures on the same page correspond to the same test plate in apex upstream and apex downstream configurations. In order to keep this order, the test plates measured in smooth conditions are shown individually on a single page.

Every figure is formed by five plots: 'RMSE', 'w/o pressure correction', 'null force correction', 'pressure correction', and 'final result'. 'RMSE' contains the root-mean-square error of the three repeated measurements of a test plate. 'w/o pressure correction' shows the actual drag difference measured between the test plate and a smooth reference plate (TP0000); each line stands for the values of one of the three repetitions. 'Null force correction' and 'pressure correction' show the magnitude of the respective corrections that are applied to the measured values in 'w/o pressure correction' to obtain the 'final result'. Note that the values presented and discussed in the main part of this thesis correspond to the averaged 'final result'. The 'RMSE' is the measurement repetition error metric; however, a different error metric has been introduced in section 6.1.3 to facilitate the comparison between plates.

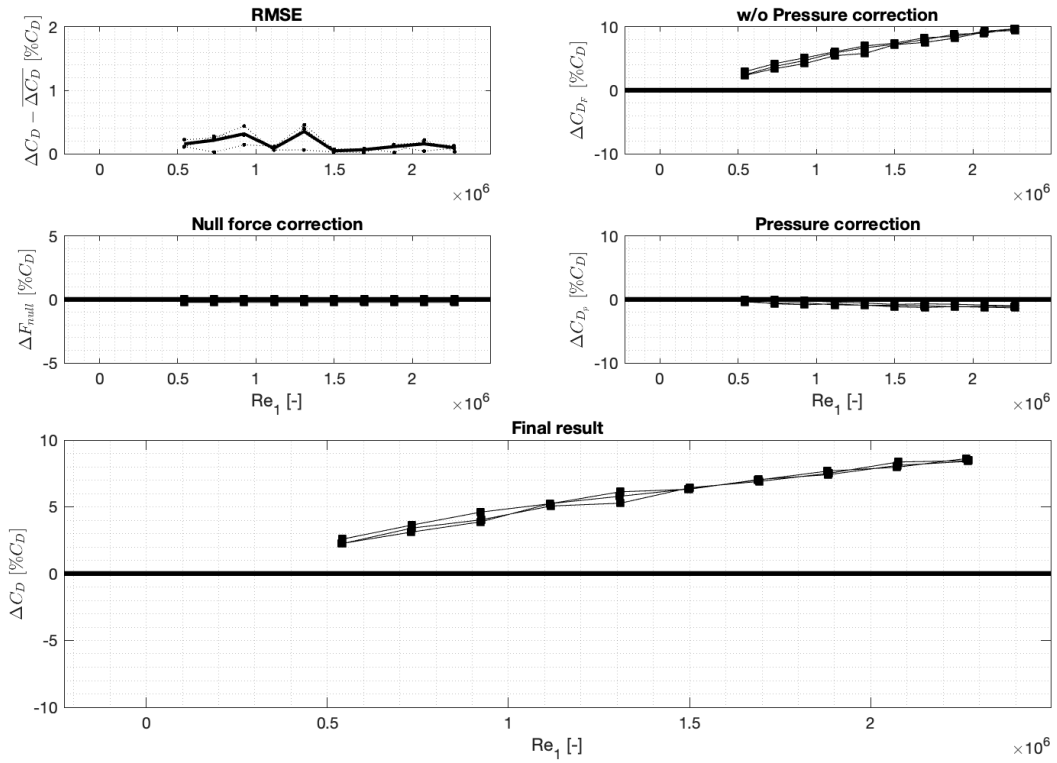

Figure C.1: Data for TP0091A in apex upstream configuration

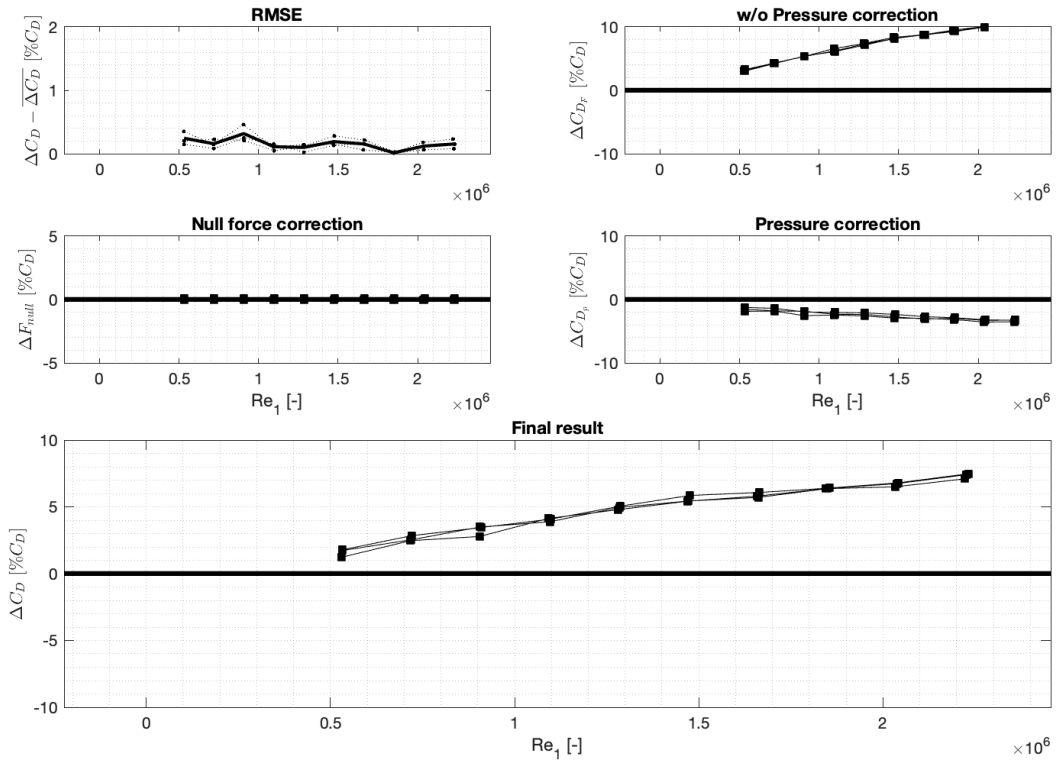

Figure C.2: Data for TP0091A in apex downstream configuration

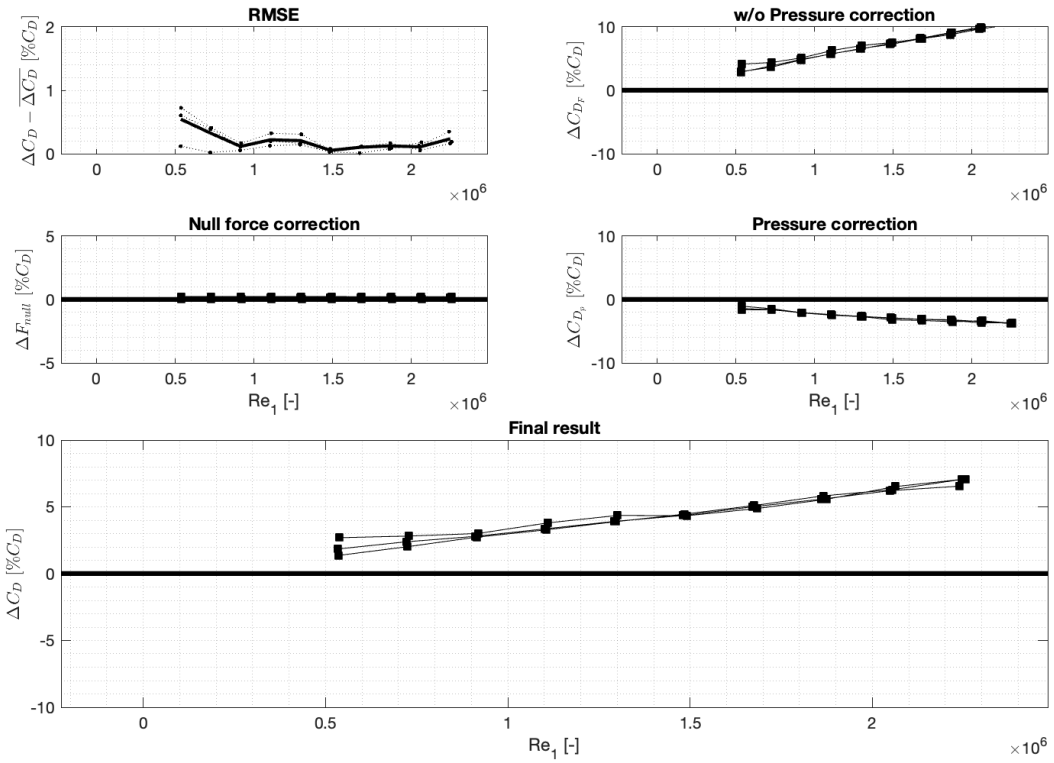

Figure C.3: Data for TP0091B in apex upstream configuration

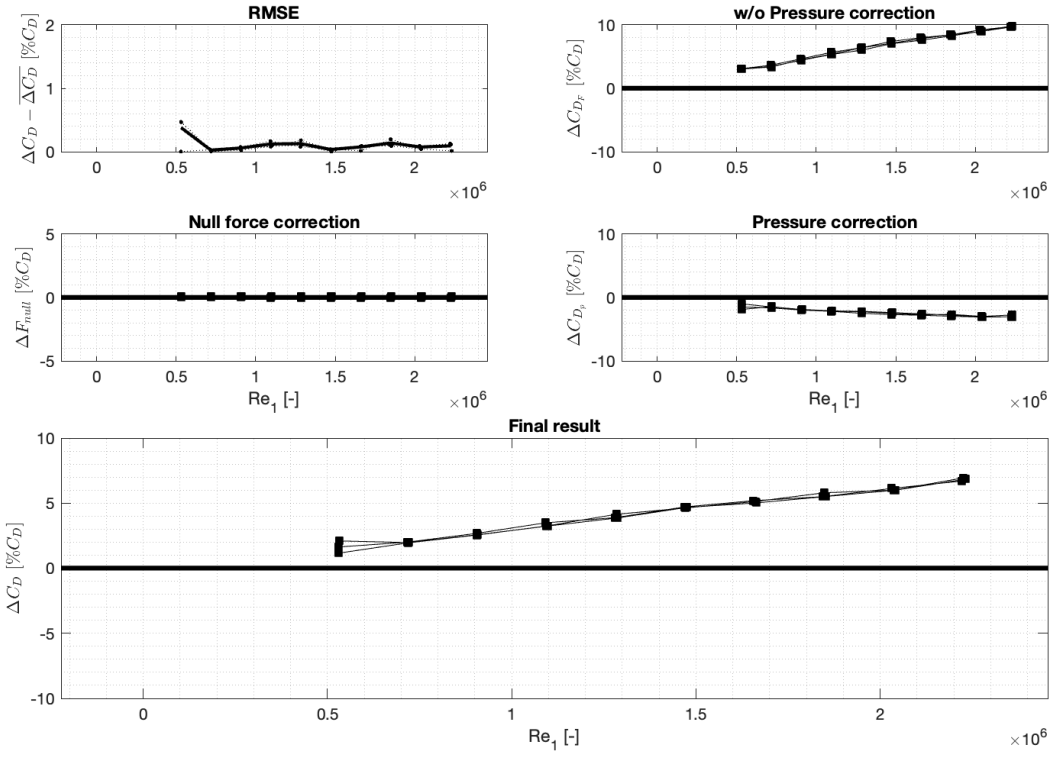

Figure C.4: Data for TP0091B in apex downstream configuration

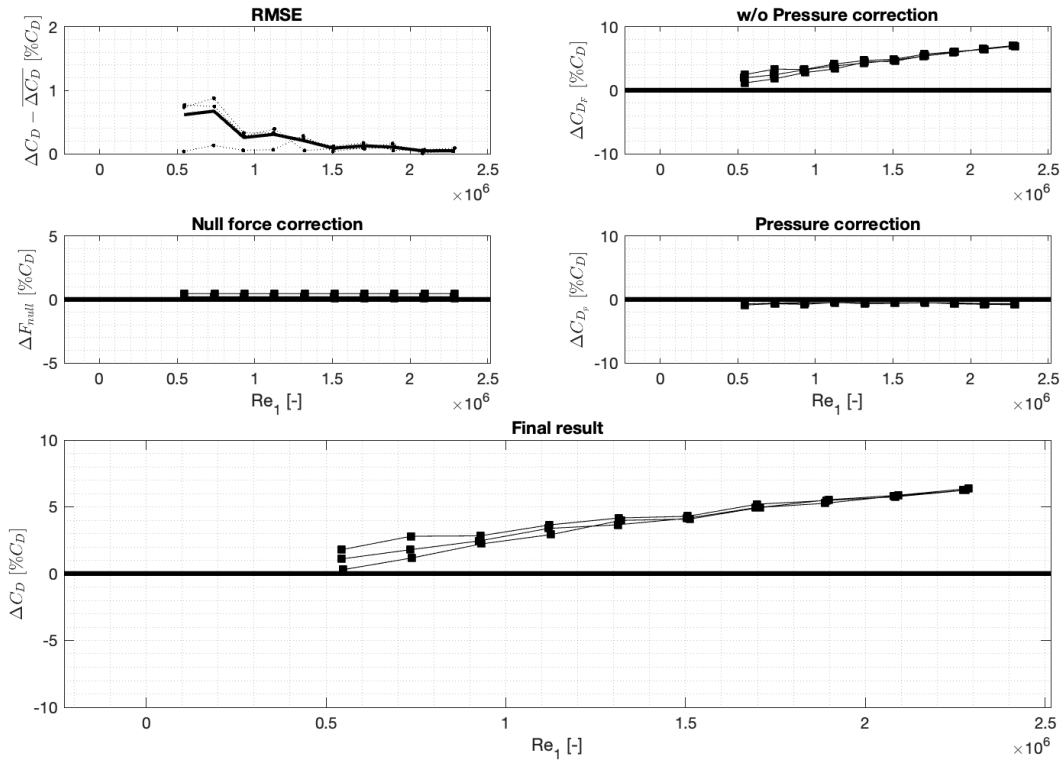

Figure C.5: Data for TP0092A in apex upstream configuration

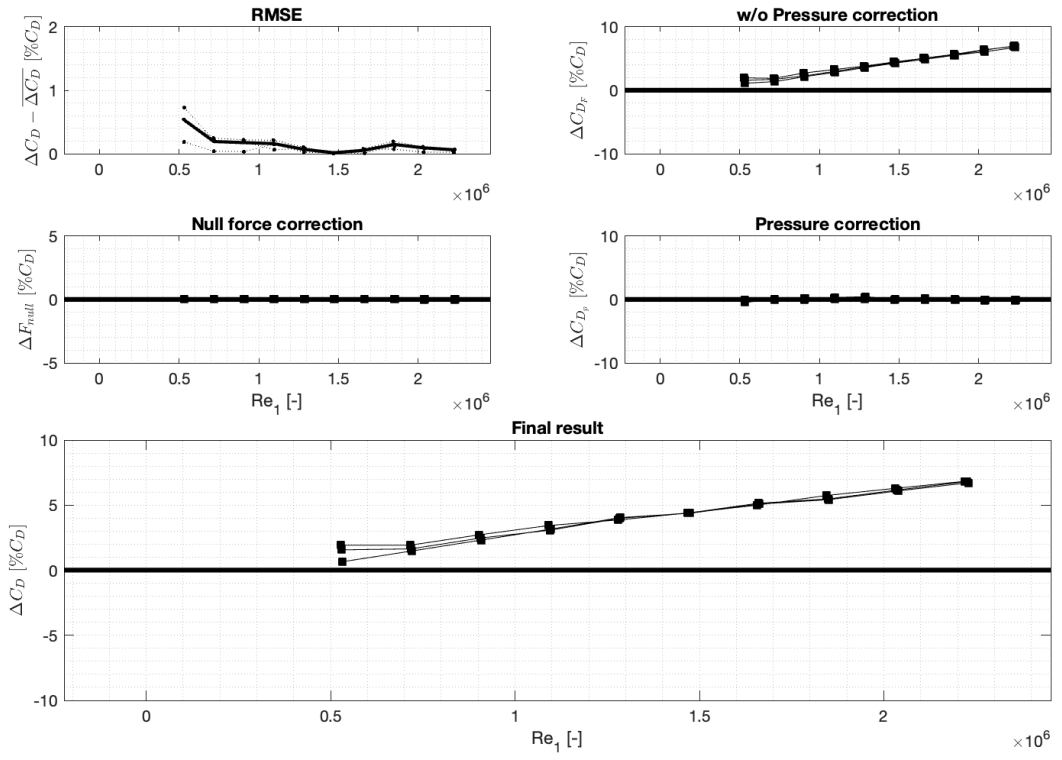

Figure C.6: Data for TP0092A in apex downstream configuration

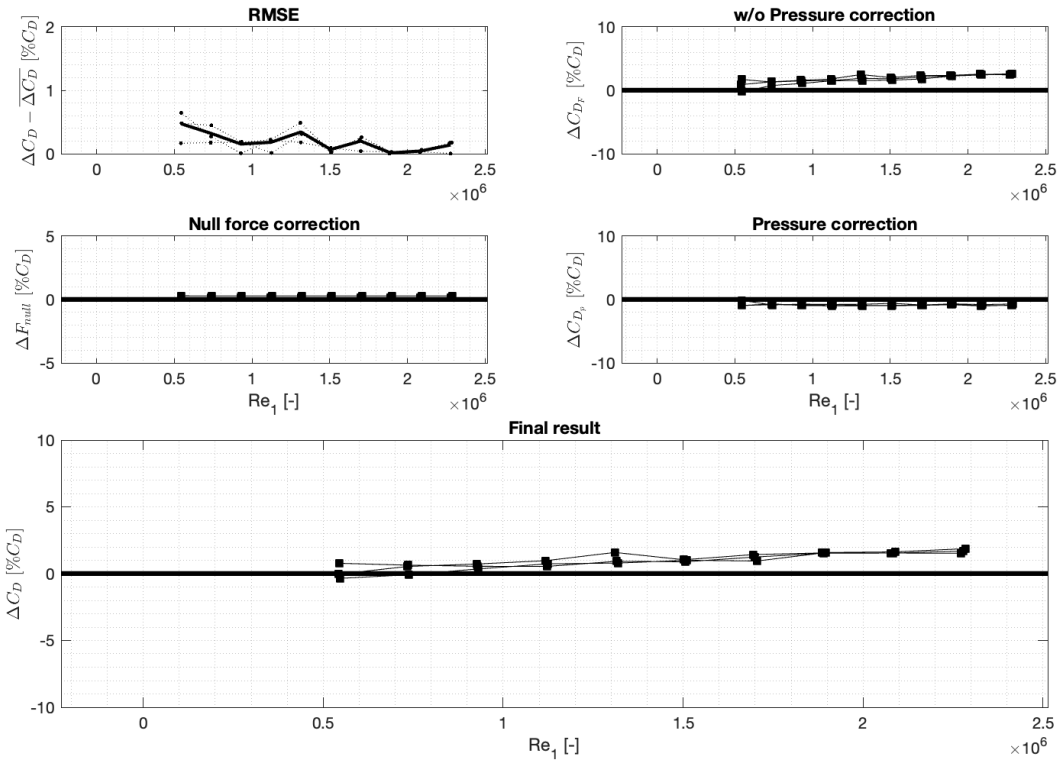

Figure C.7: Data for TP0093A in apex upstream configuration

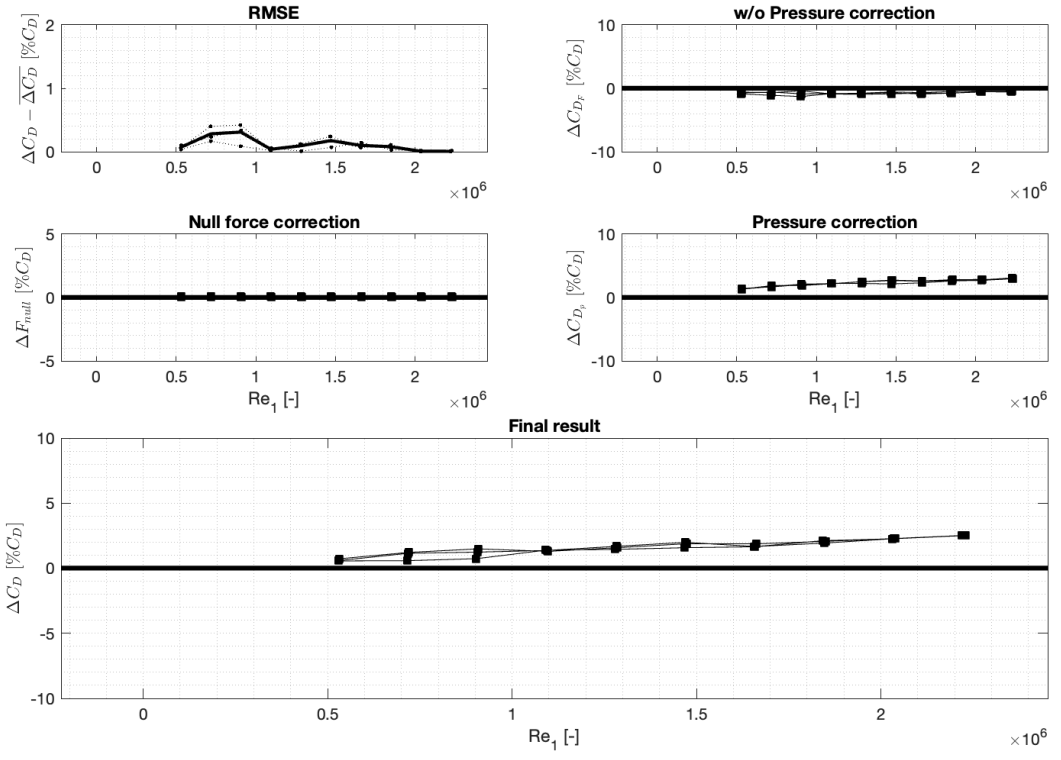

Figure C.8: Data for TP0093A in apex downstream configuration

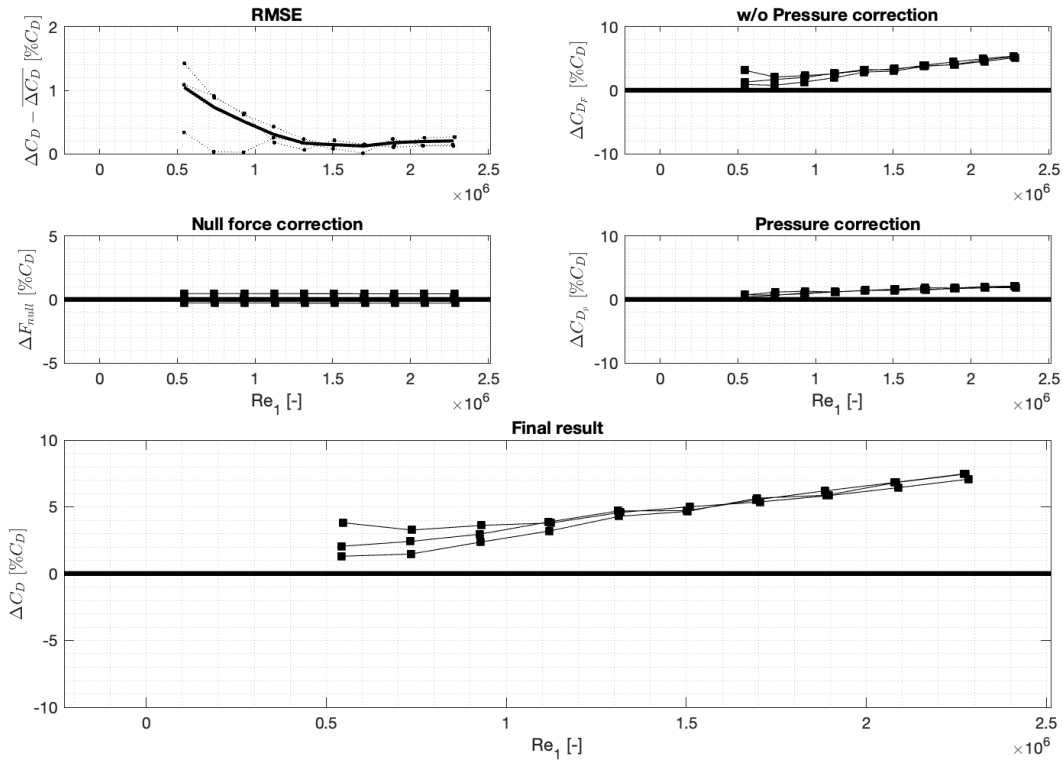

Figure C.9: Data for TP0094A in apex upstream configuration

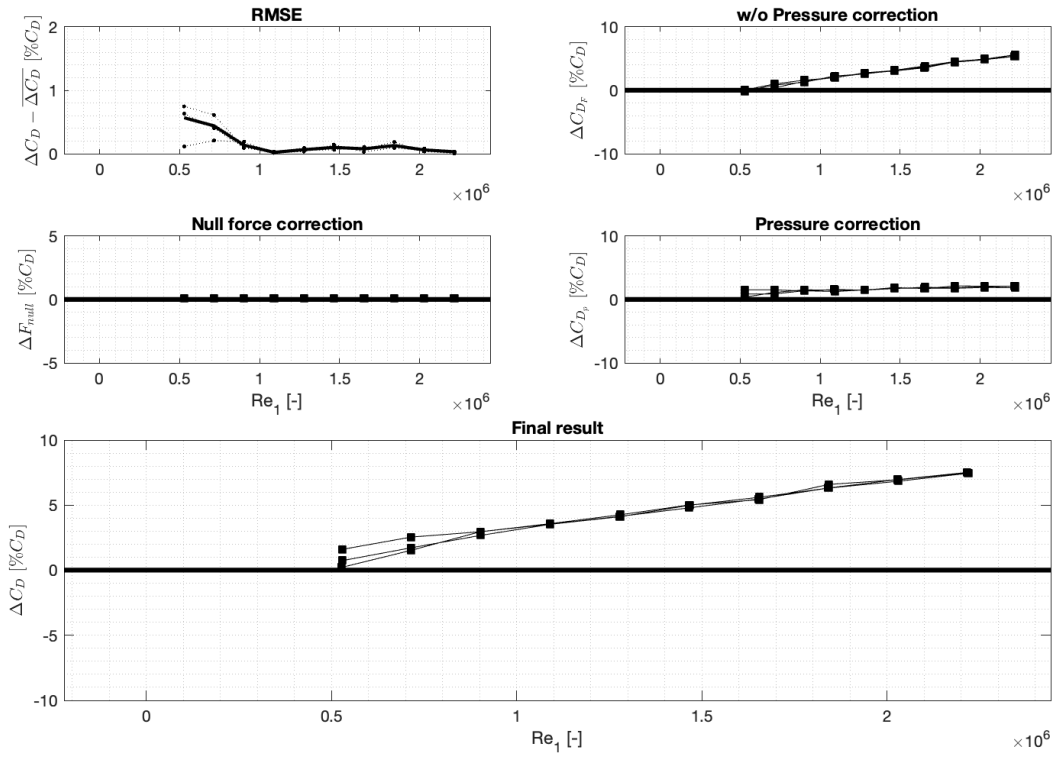

Figure C.10: Data for TP0094A in apex downstream configuration

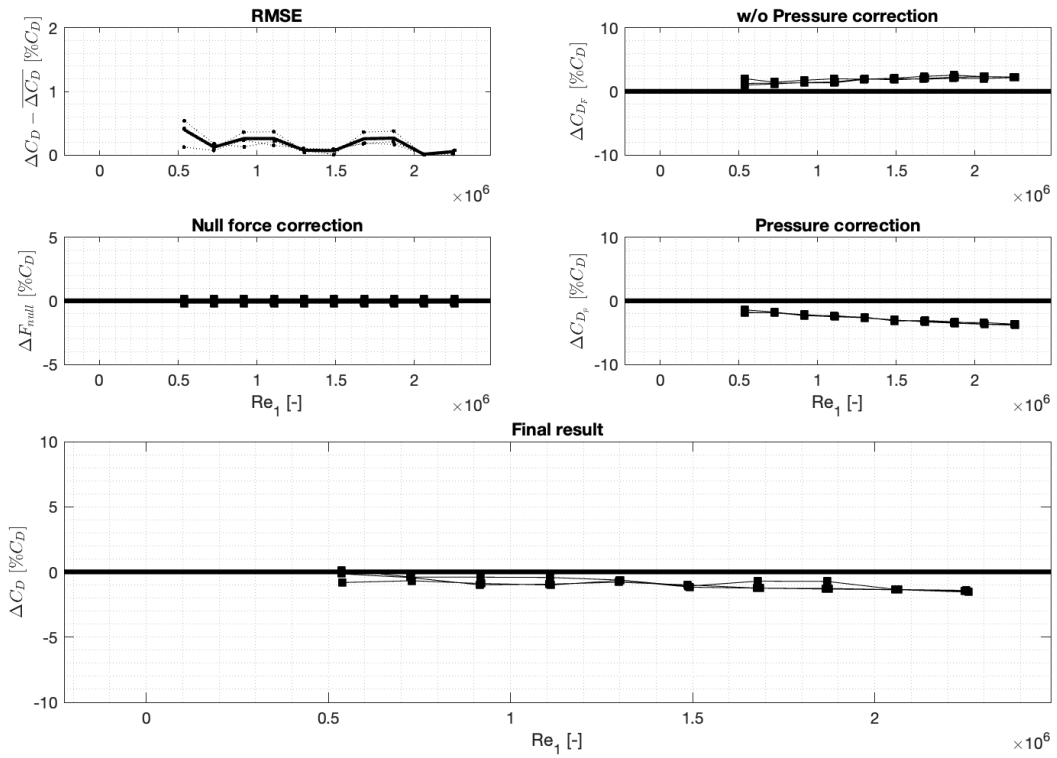

Figure C.11: Data for TP0094B as reference flat plate, before covering it with a vinyl array

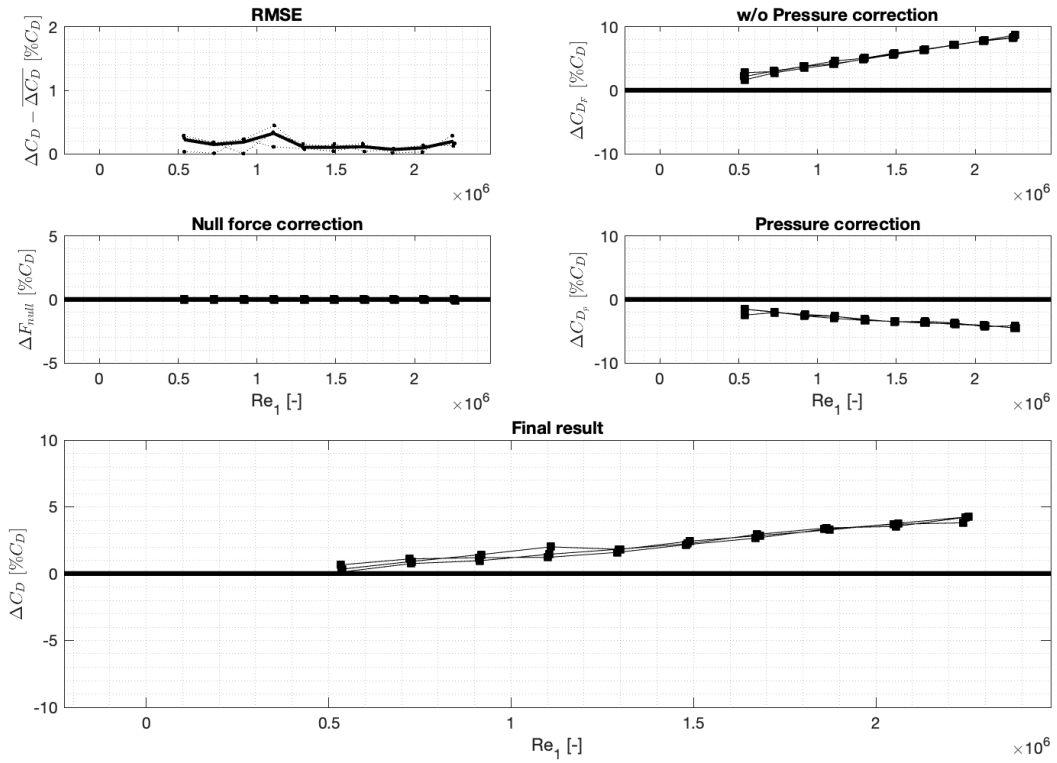

Figure C.12: Data for TP0094B in apex upstream configuration

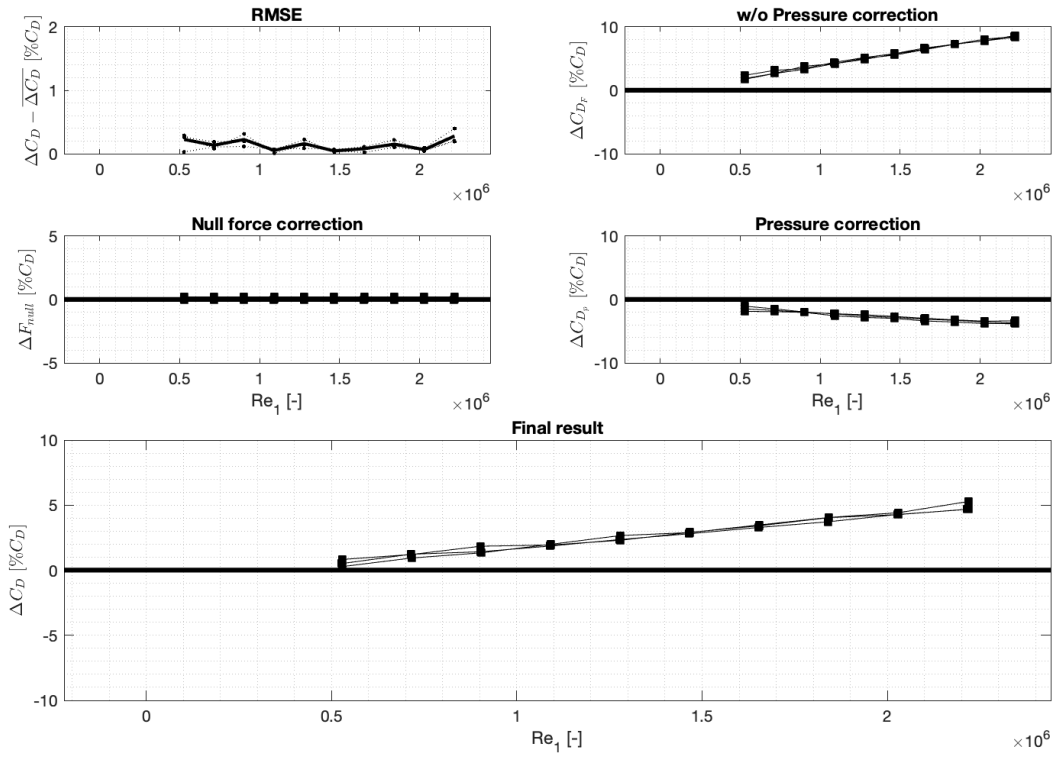

Figure C.13: Data for TP0094B in apex downstream configuration

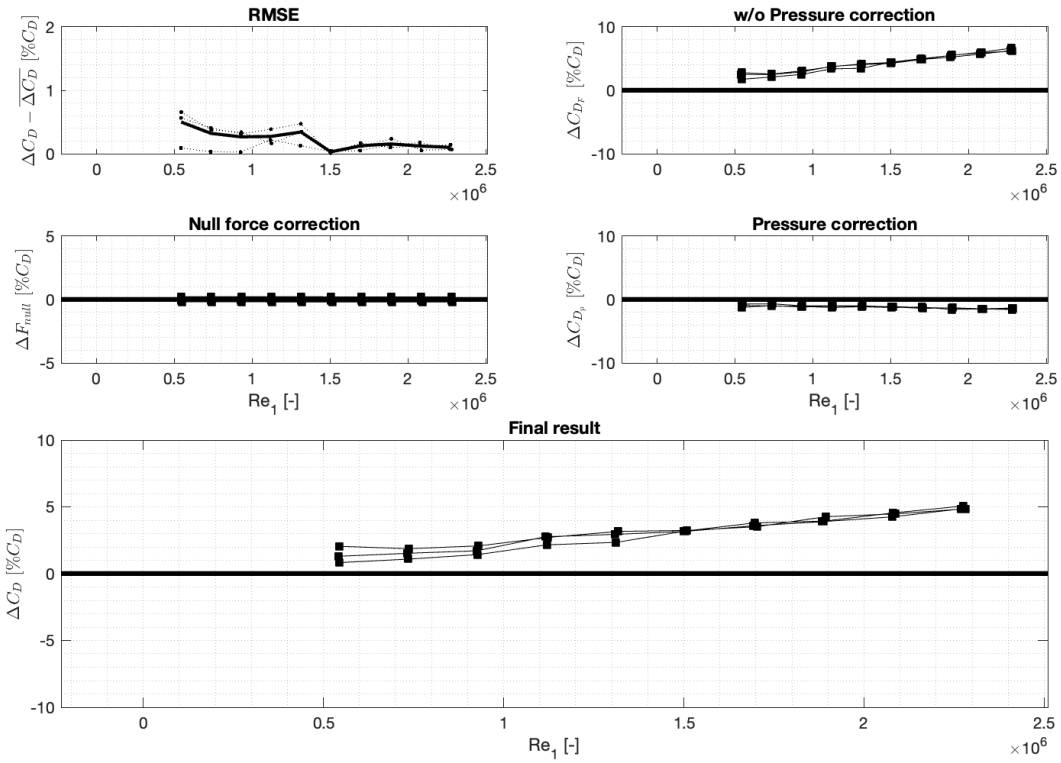

Figure C.14: Data for TP0095A in apex upstream configuration

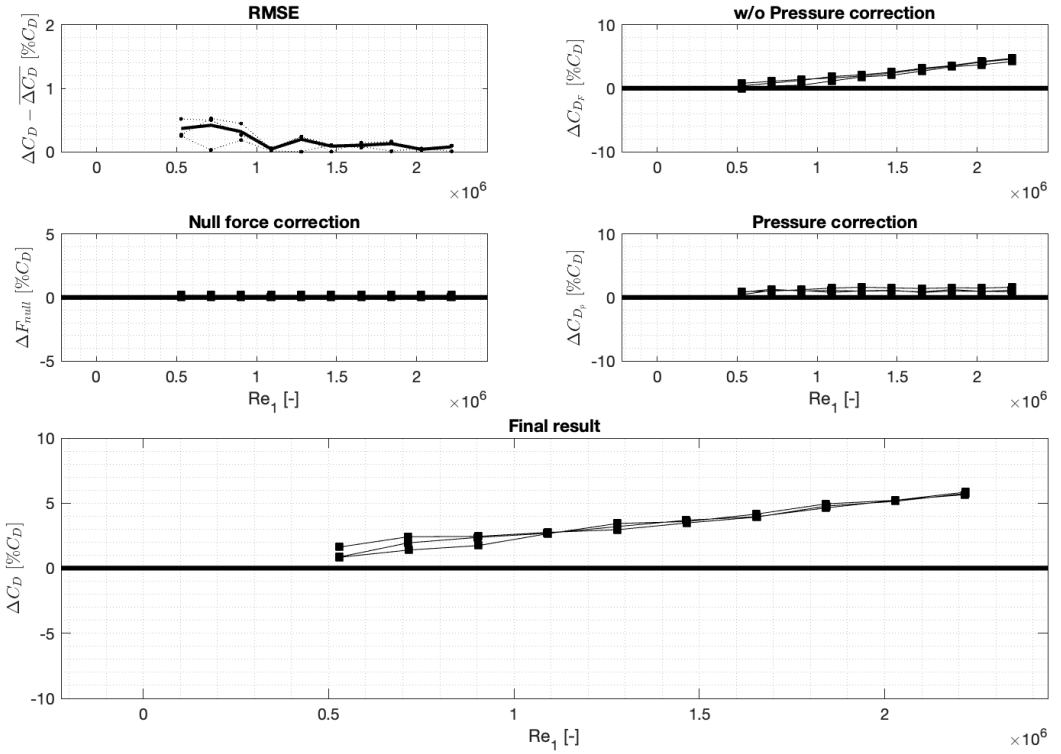

Figure C.15: Data for TP0095A in apex downstream configuration

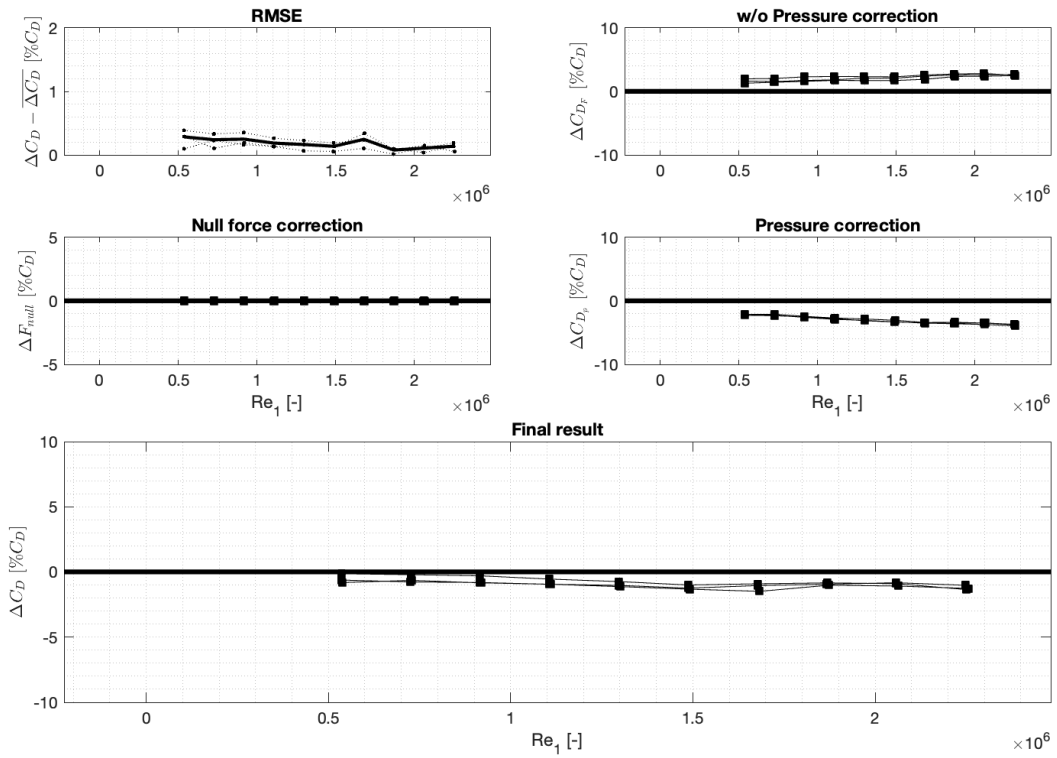

Figure C.16: Data for TP0095B as reference flat plate, before covering it with a vinyl array

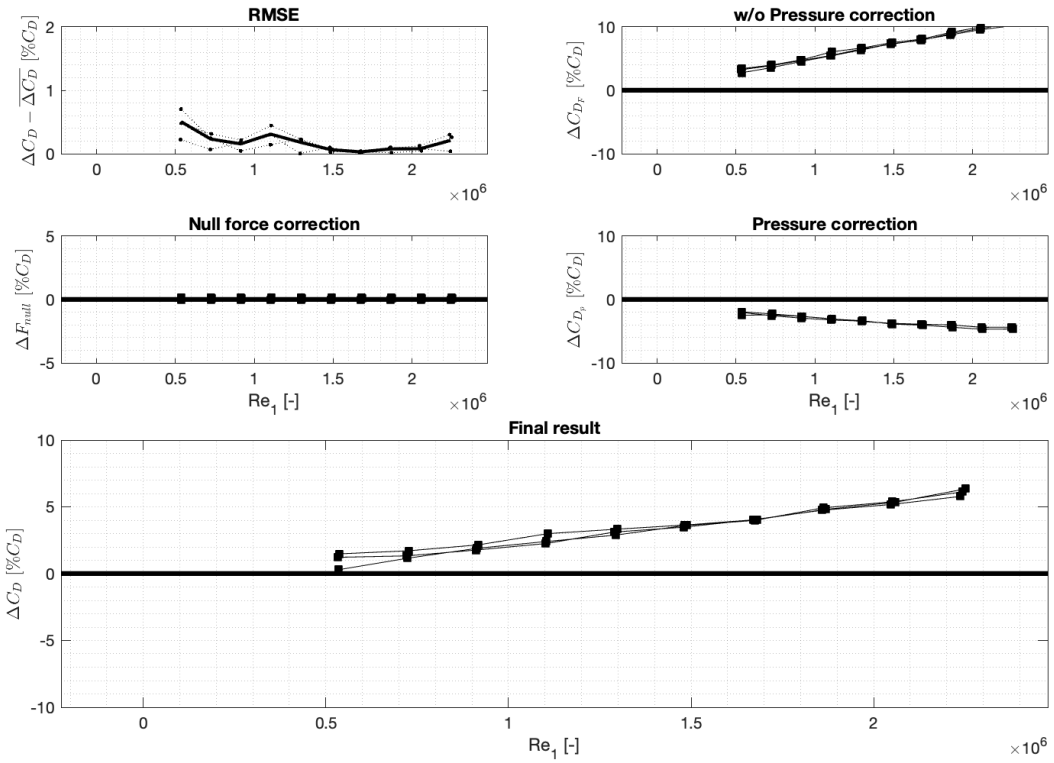

Figure C.17: Data for TP0095B in apex upstream configuration

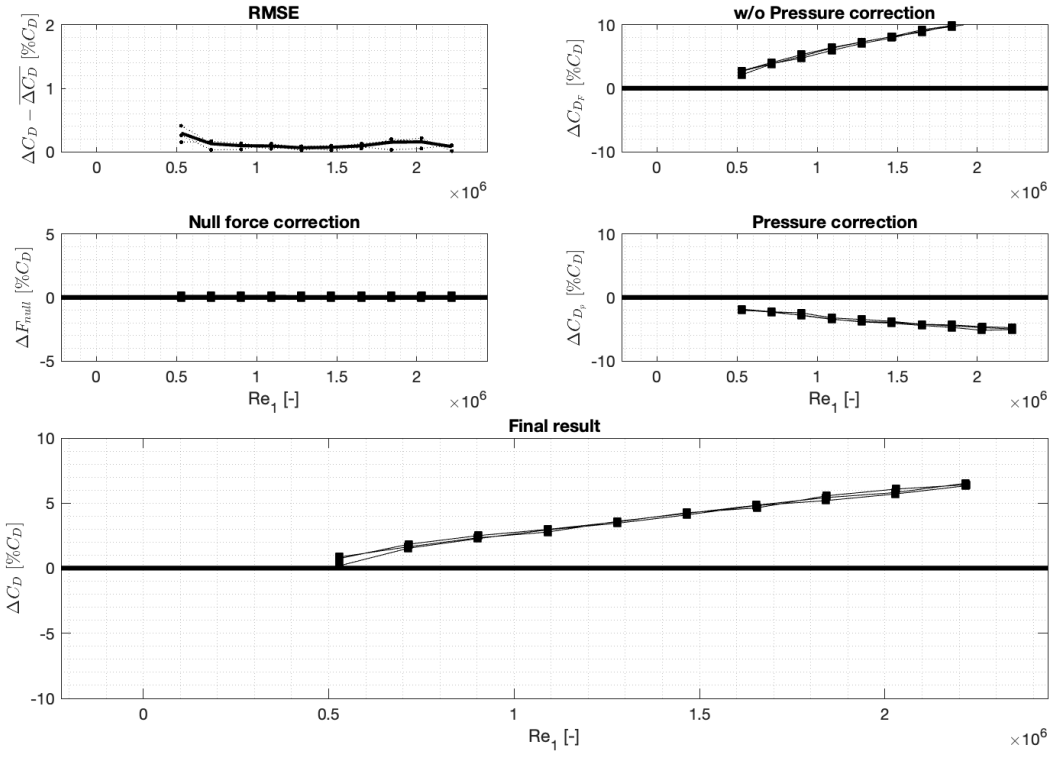

Figure C.18: Data for TP0095B in apex downstream configuration

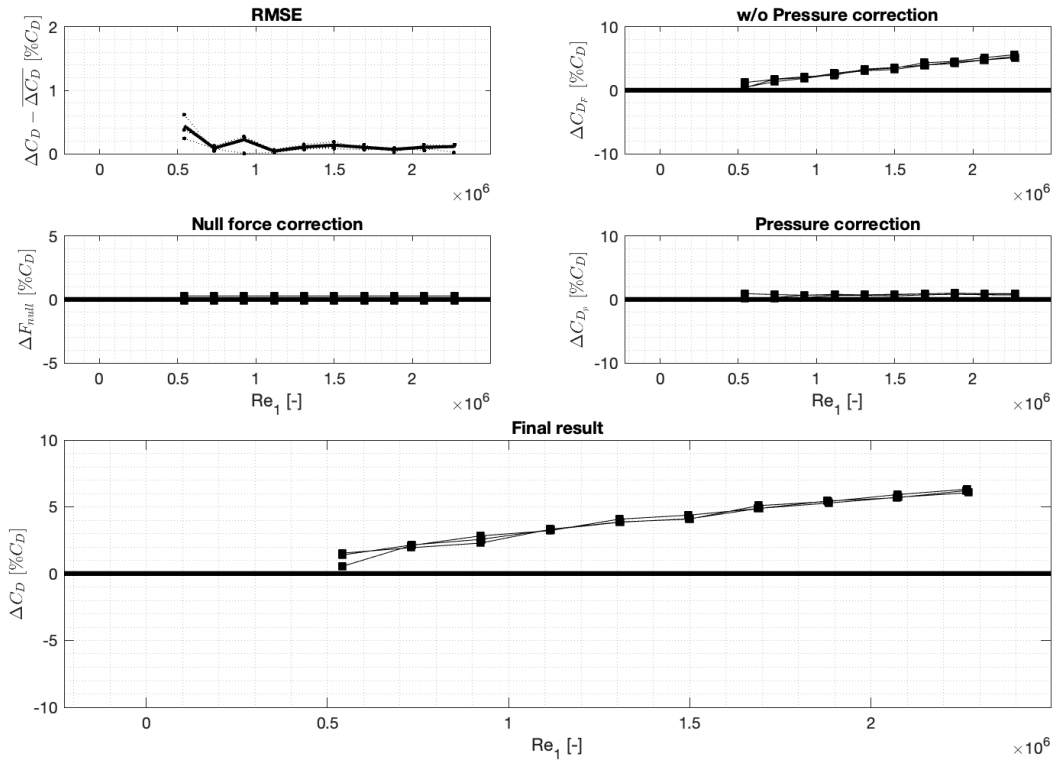

Figure C.19: Data for TP0096A in apex upstream configuration

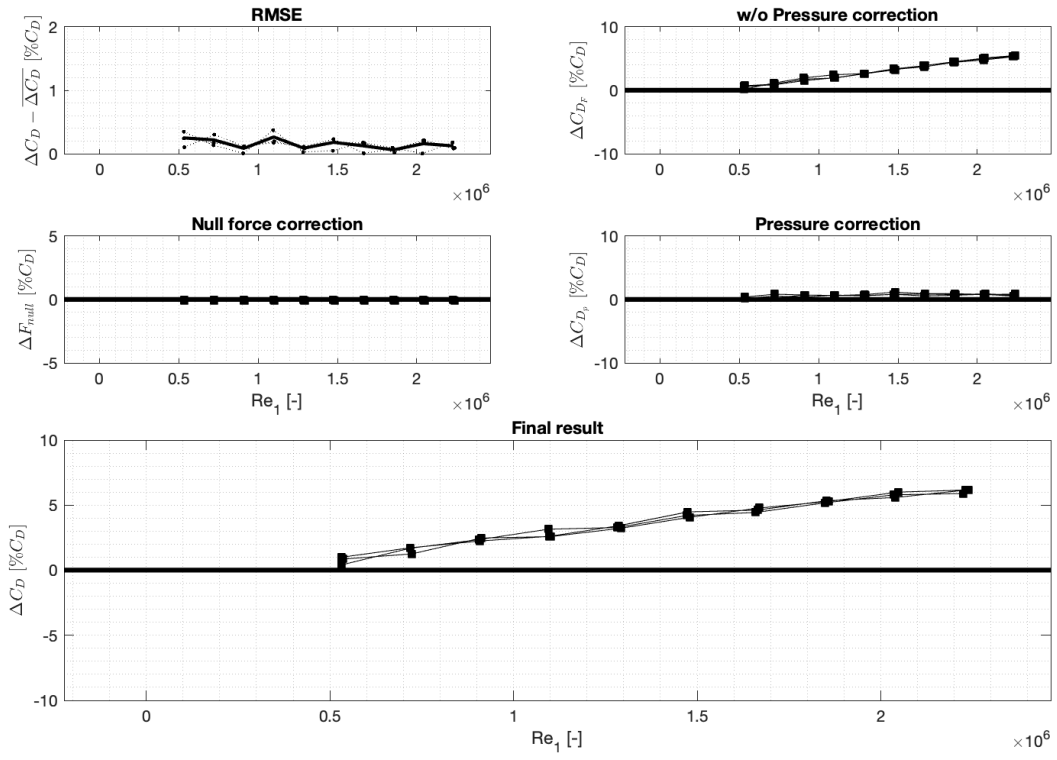

Figure C.20: Data for TP0096A in apex downstream configuration

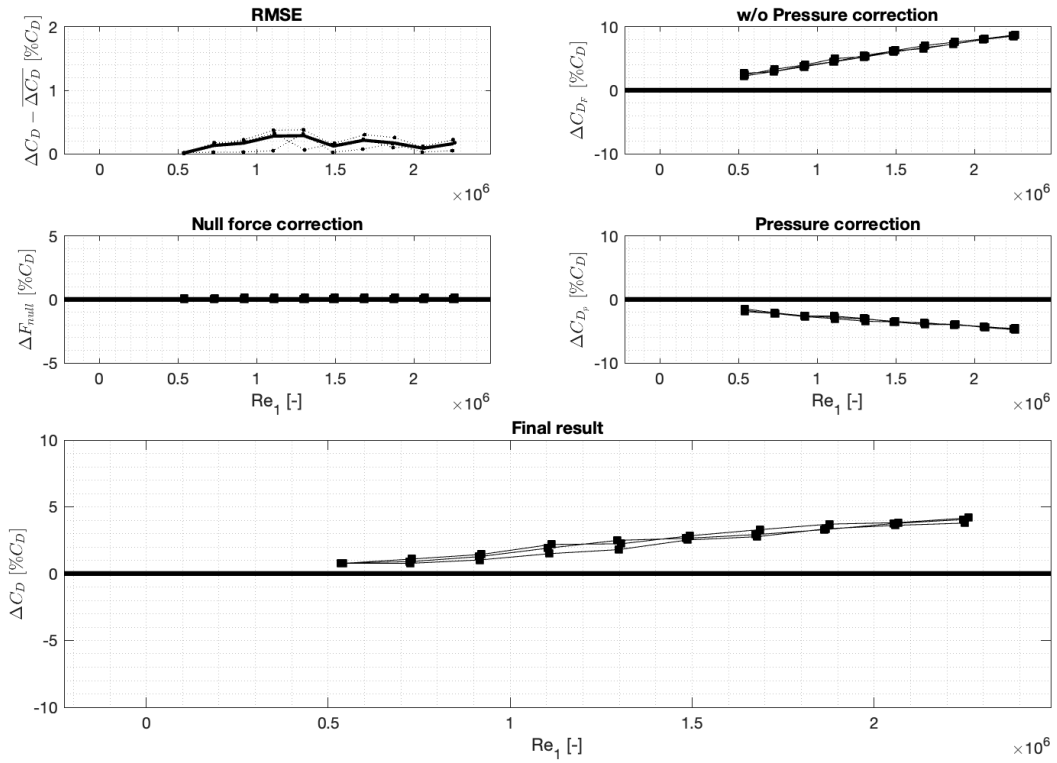

Figure C.21: Data for TP0097A in apex upstream configuration

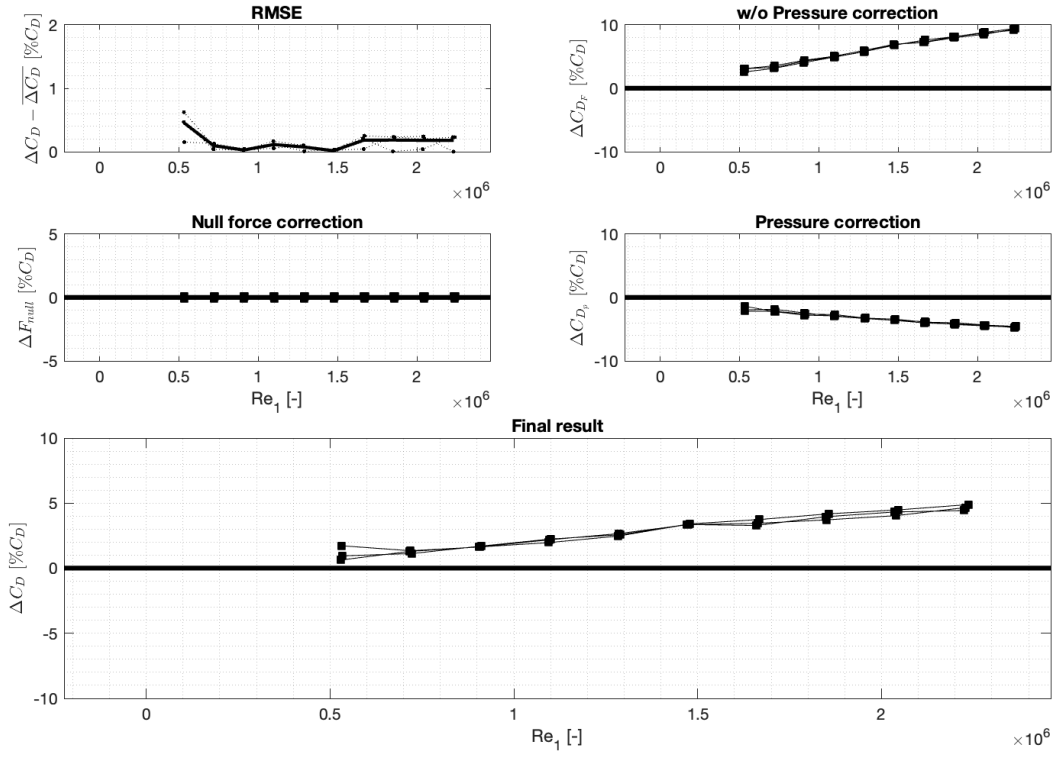

Figure C.22: Data for TP0097A in apex downstream configuration

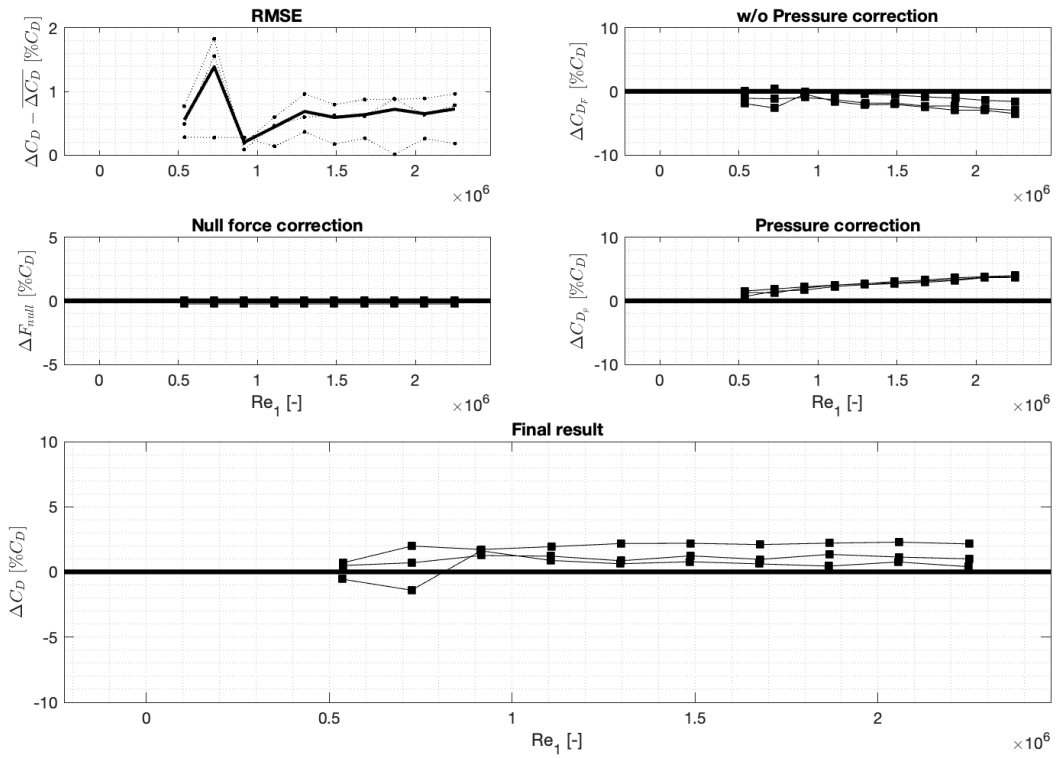

Figure C.23: Data for TP0097B as flat plate

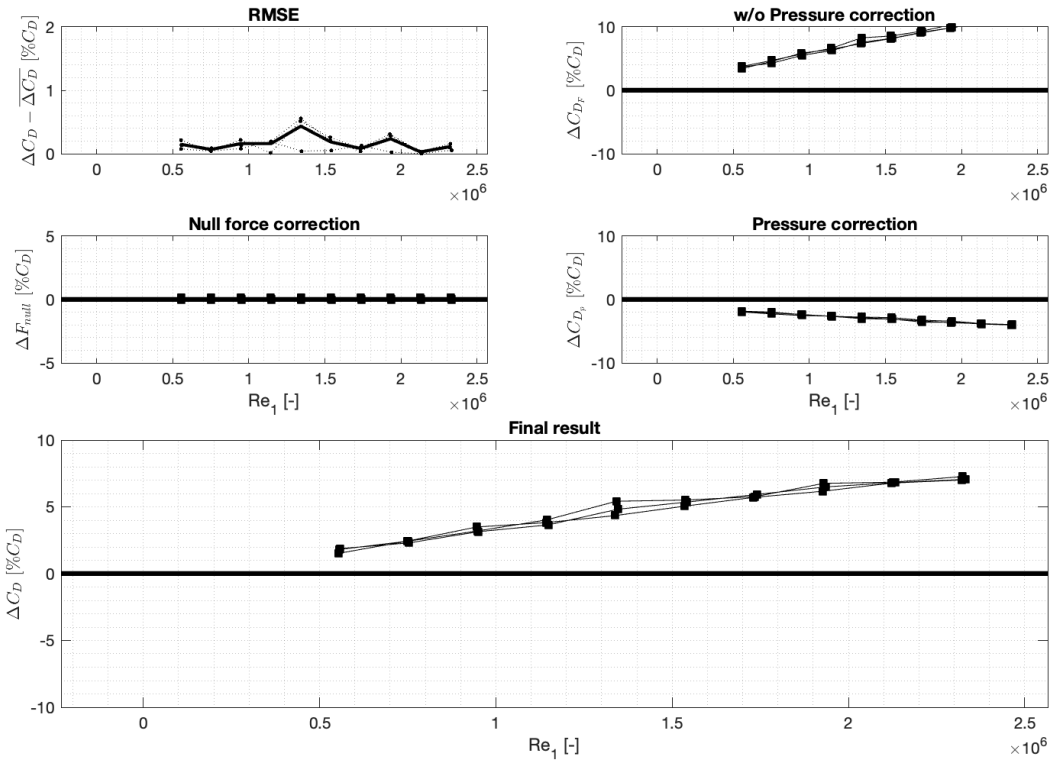

Figure C.24: Data for TP0098A in apex upstream configuration

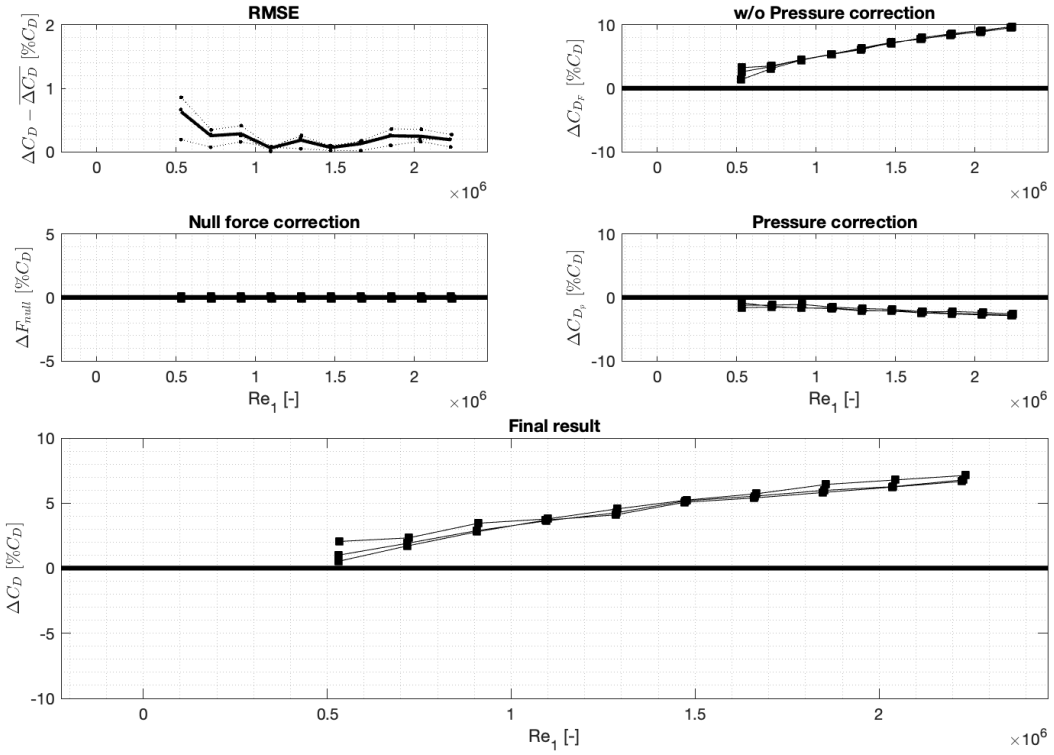

Figure C.25: Data for TP0098 in apex downstream configuration

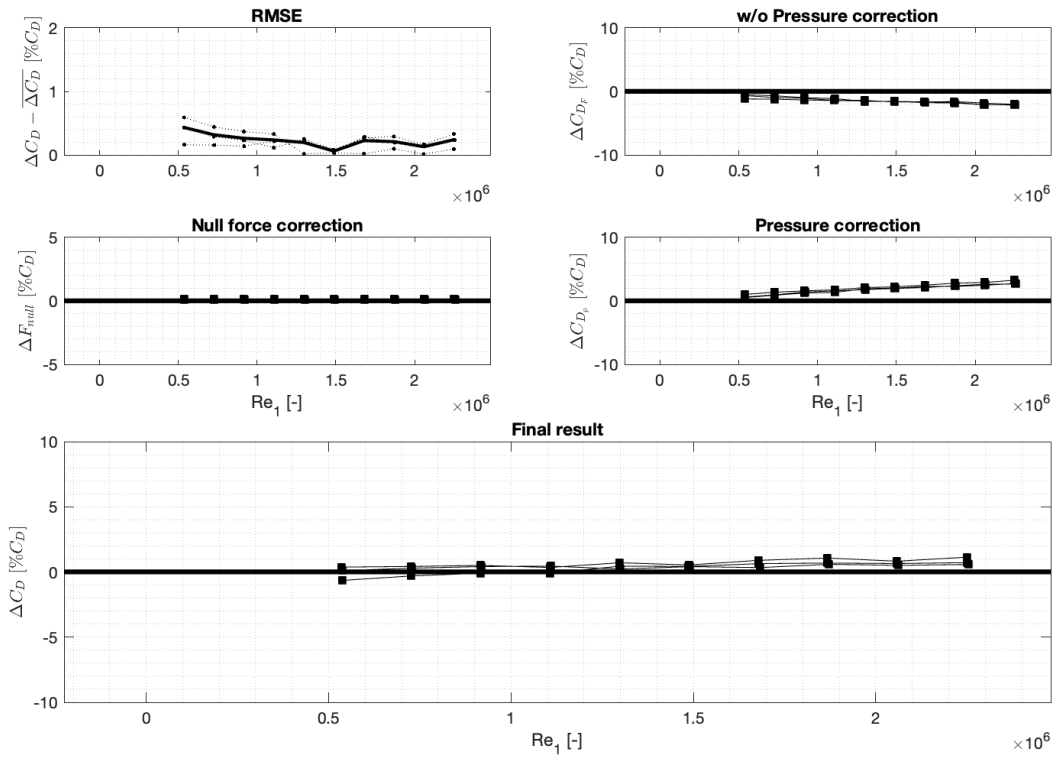

Figure C.26: Data for TP0098B as reference flat plate, before covering it with a vinyl array

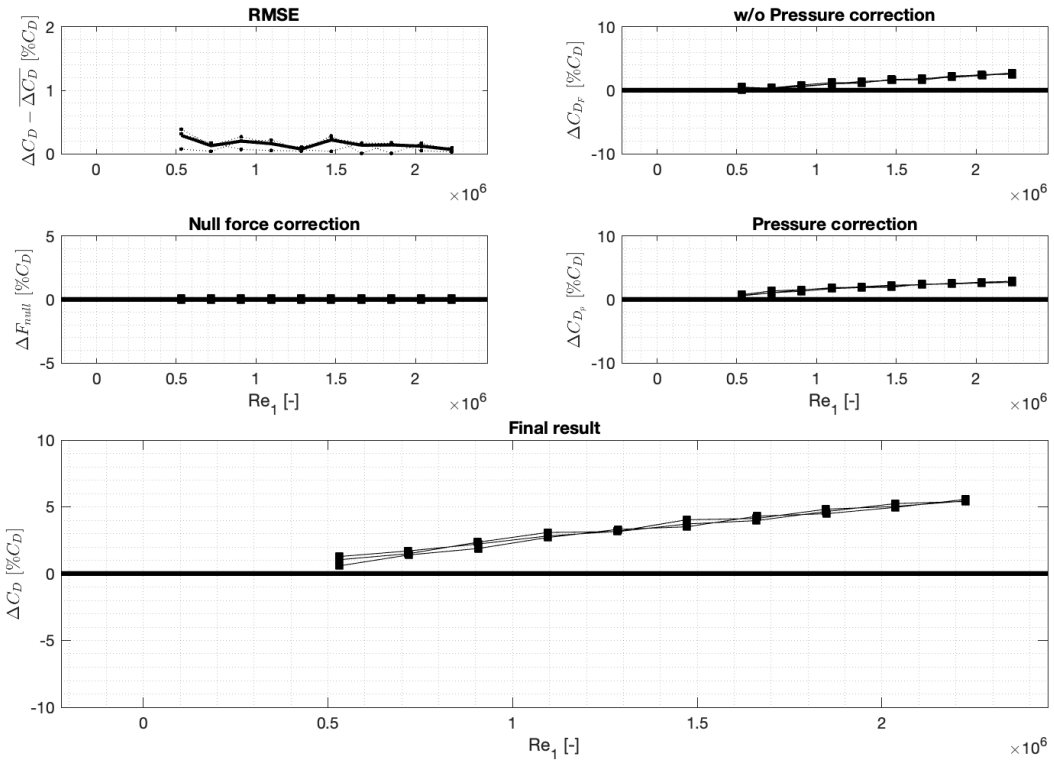

Figure C.27: Data for TP0098B in apex upstream configuration

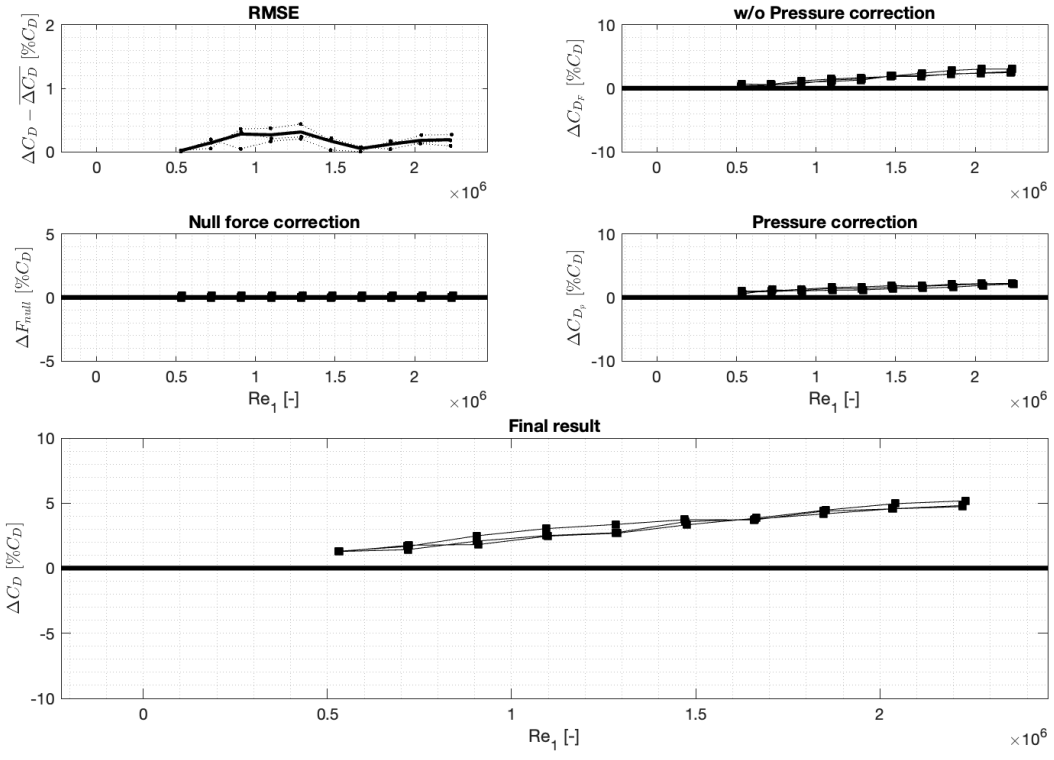

Figure C.28: Data for TP0098B in apex downstream configuration

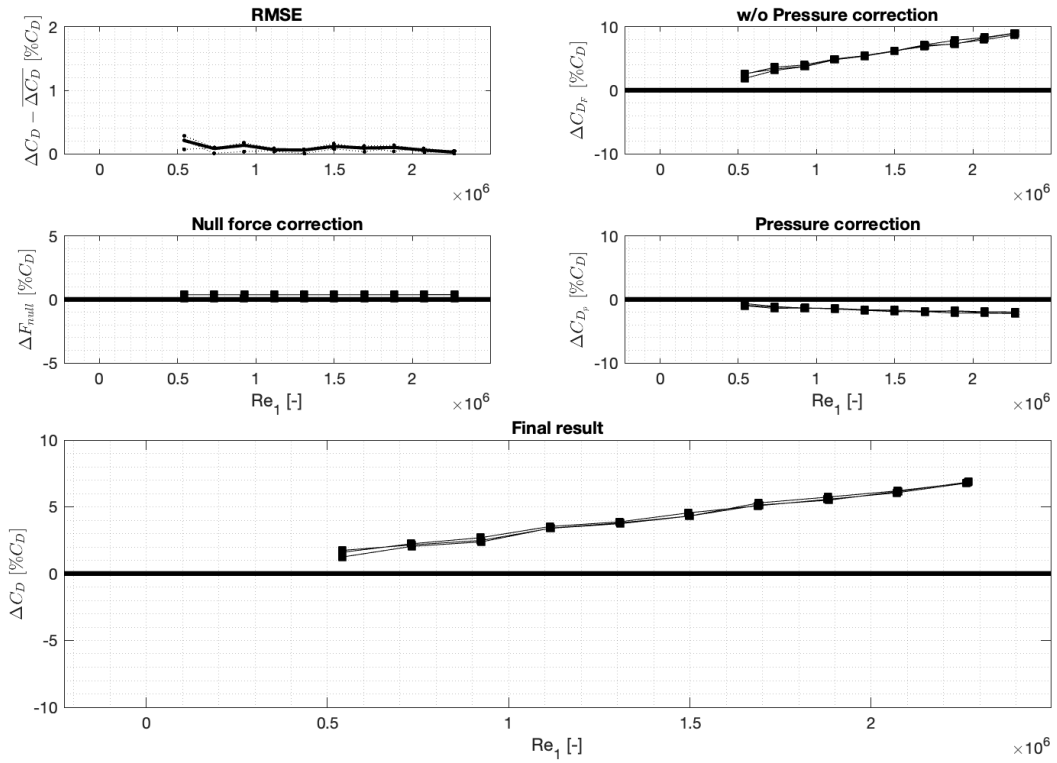

Figure C.29: Data for TP0099A in apex upstream configuration

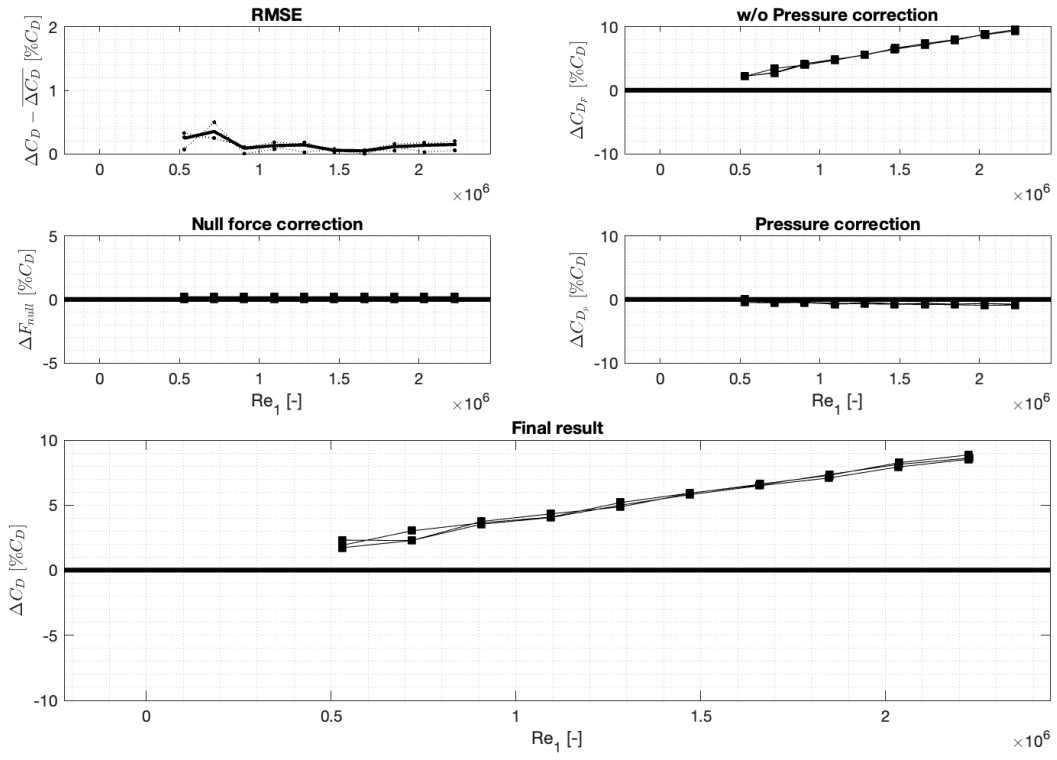

Figure C.30: Data for TP0099A in apex downstream configuration

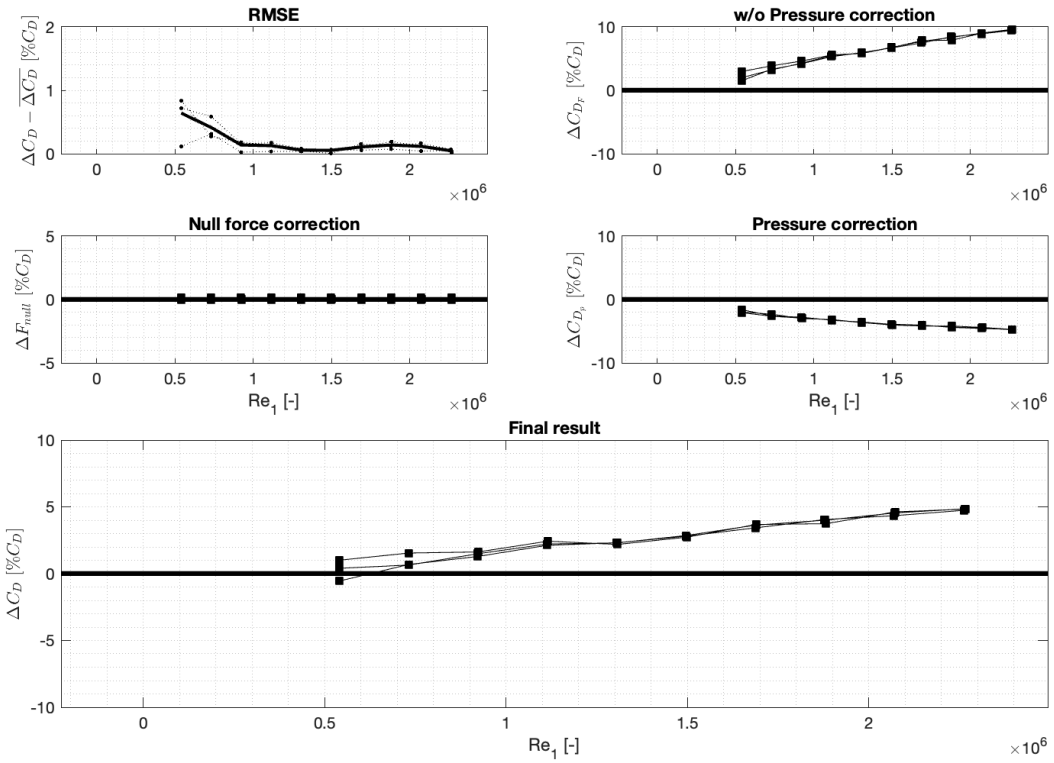

Figure C.31: Data for TP0099B in apex upstream configuration

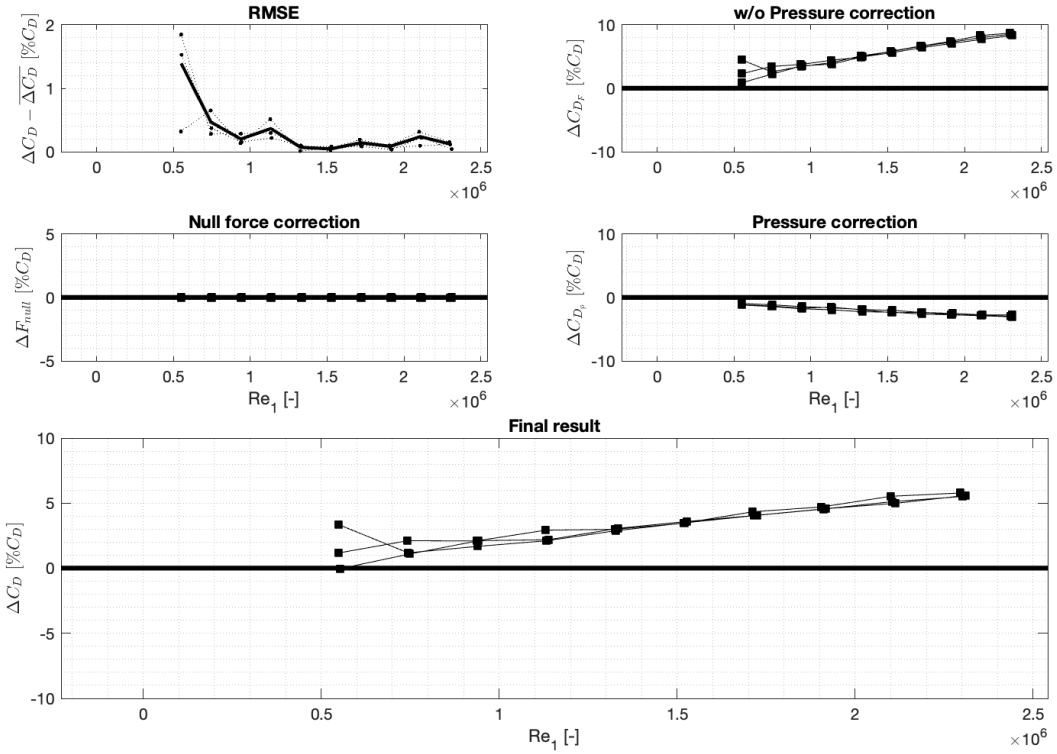

Figure C.32: Data for TP0099B in apex downstream configuration

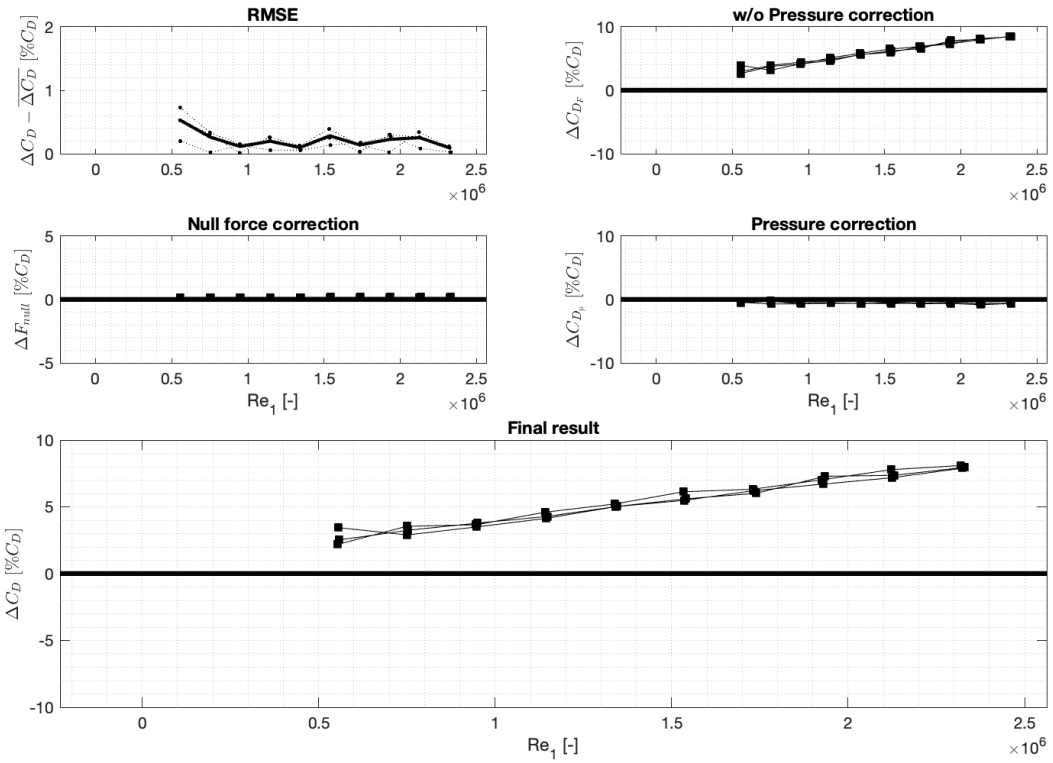

Figure C.33: Data for TP0100A in apex upstream configuration

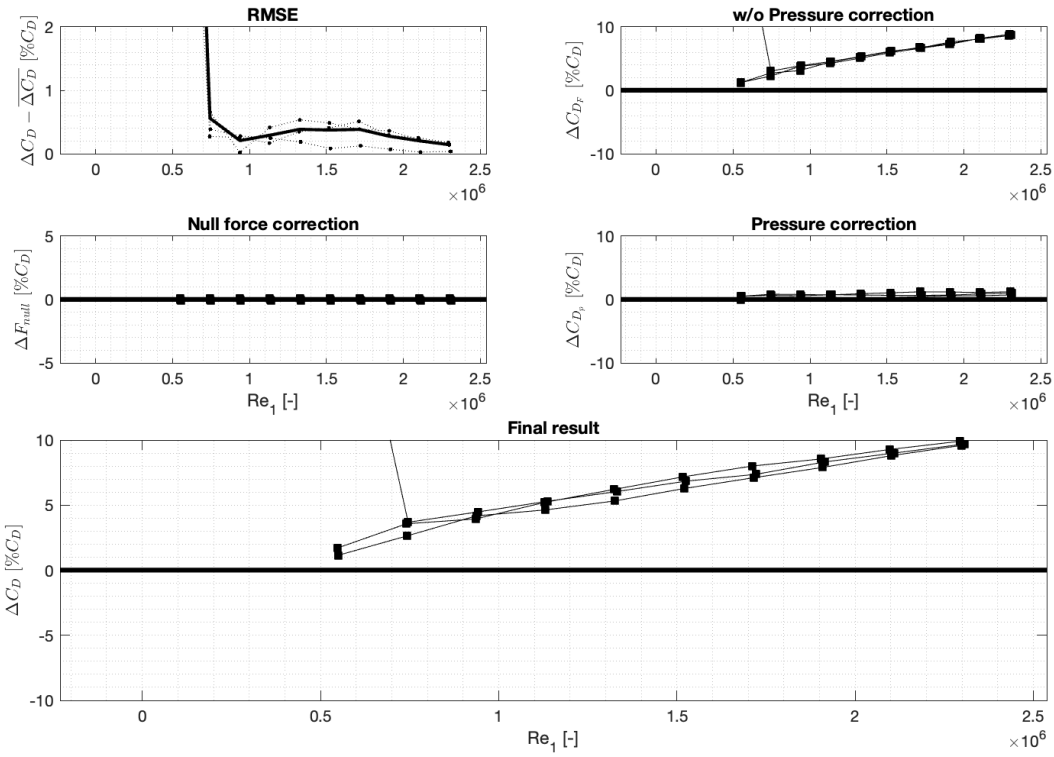

Figure C.34: Data for TP0100A in apex downstream configuration

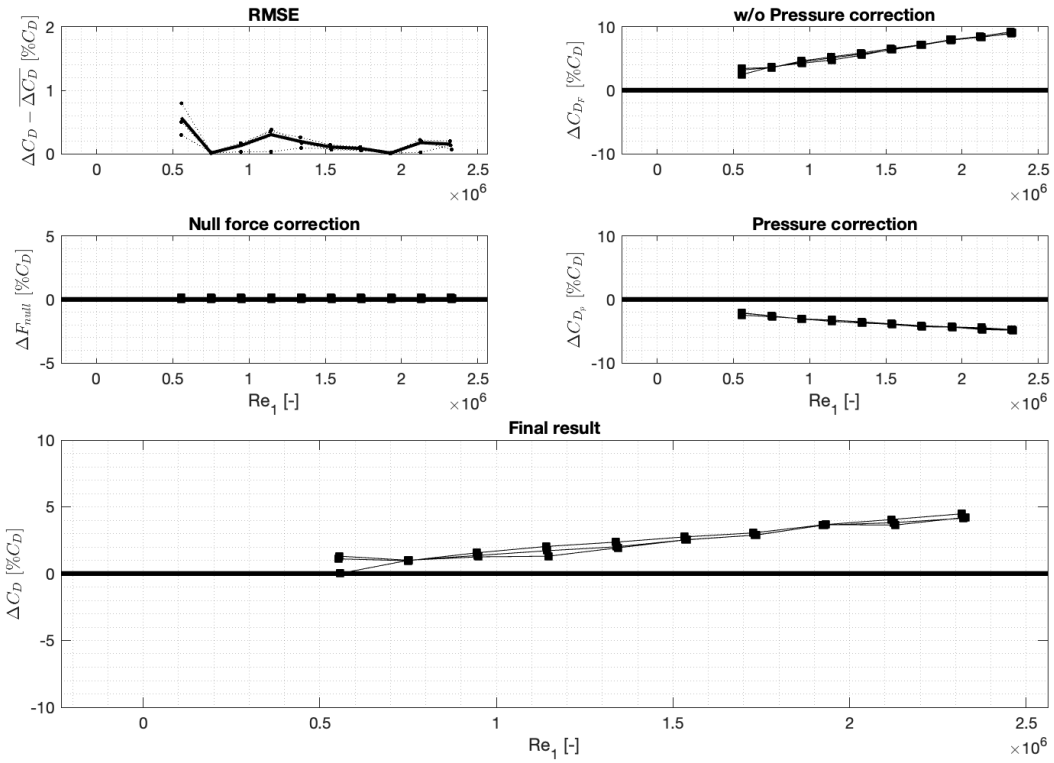

Figure C.35: Data for TP0100B in apex upstream configuration

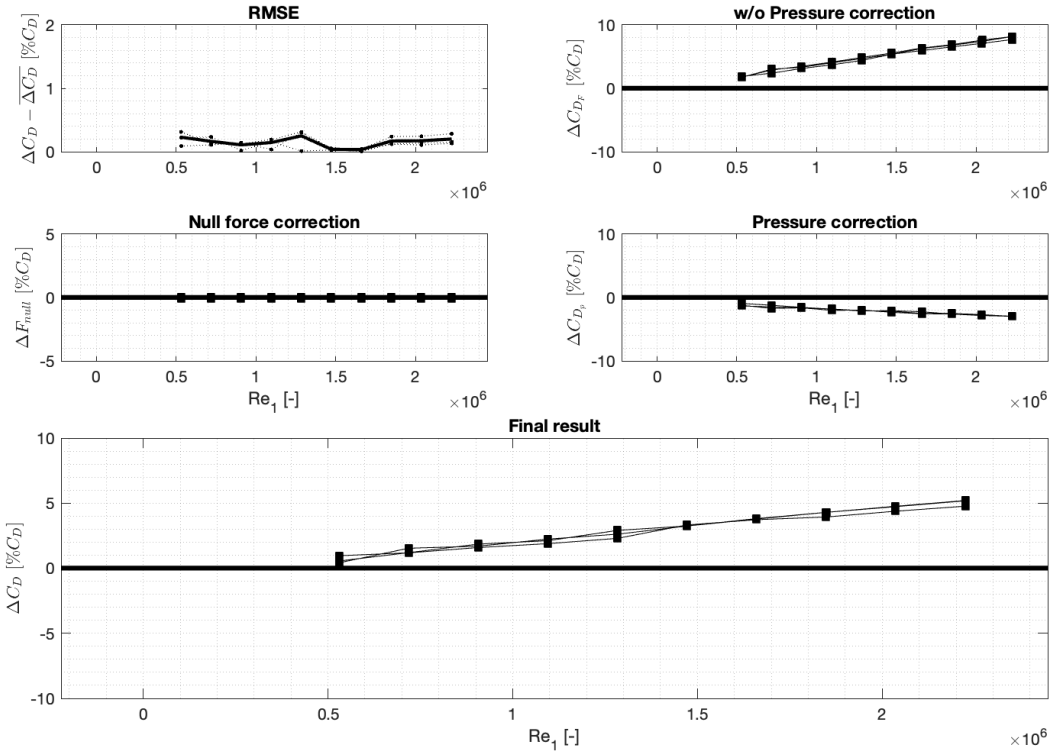

Figure C.36: Data for TP0100B in apex downstream configuration

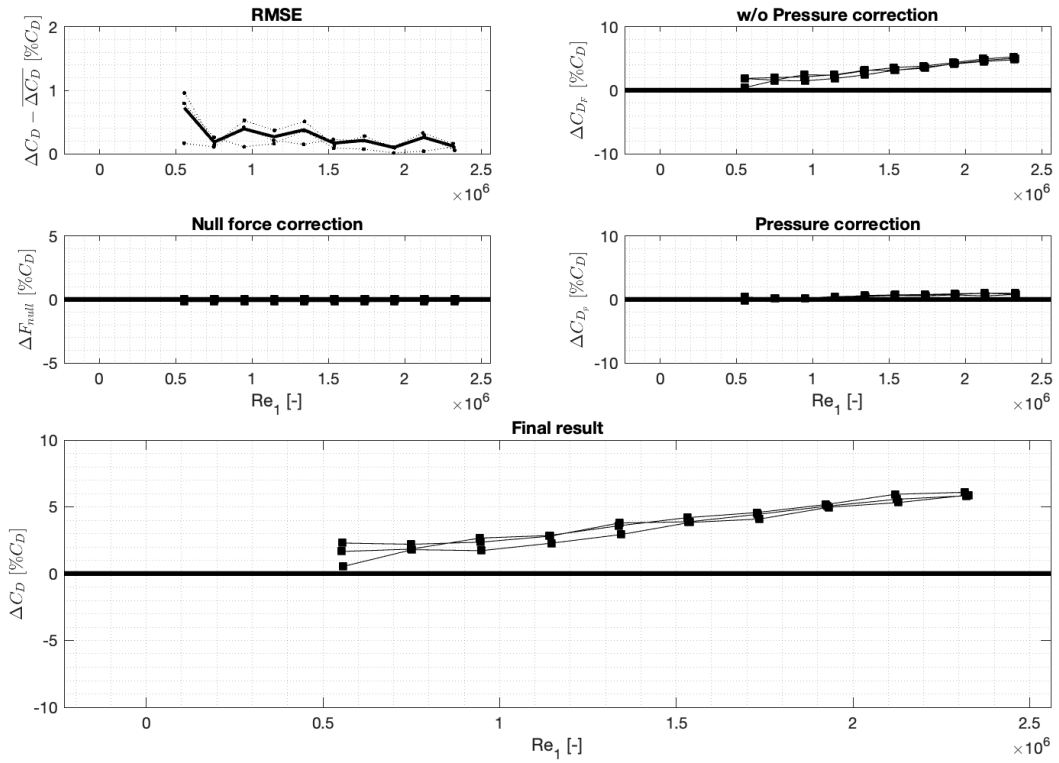

Figure C.37: Data for TP0101B in apex upstream configuration

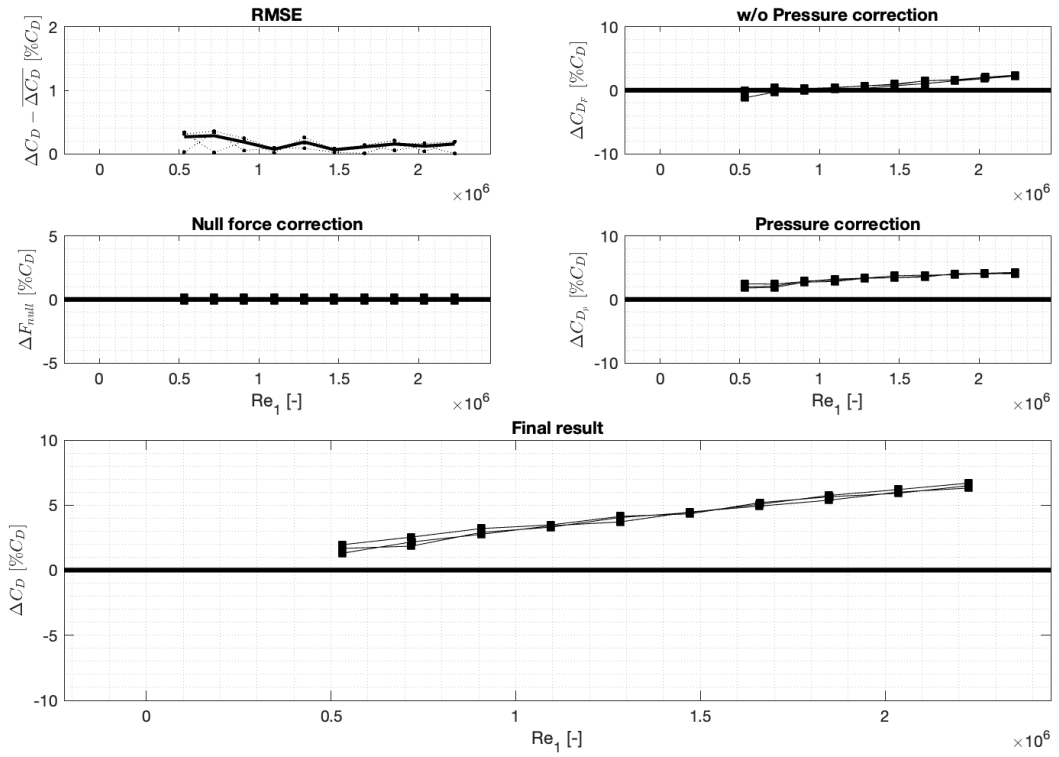

Figure C.38: Data for TP0101B in apex downstream configuration

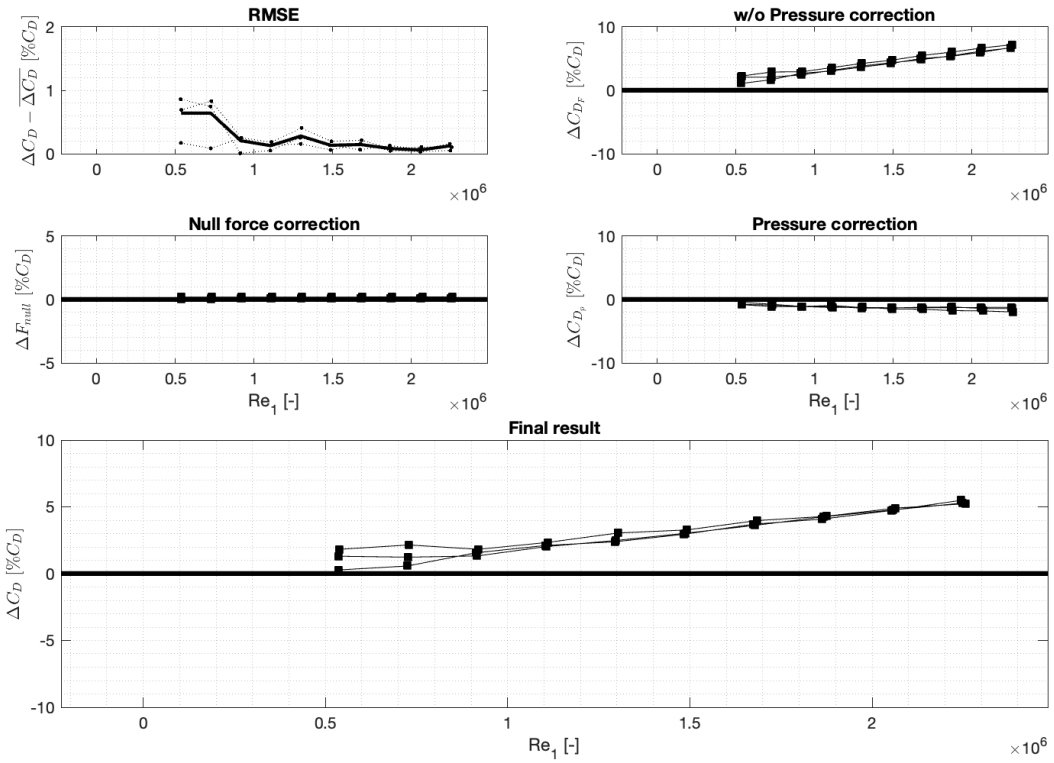

Figure C.39: Data for TP0102A in apex upstream configuration

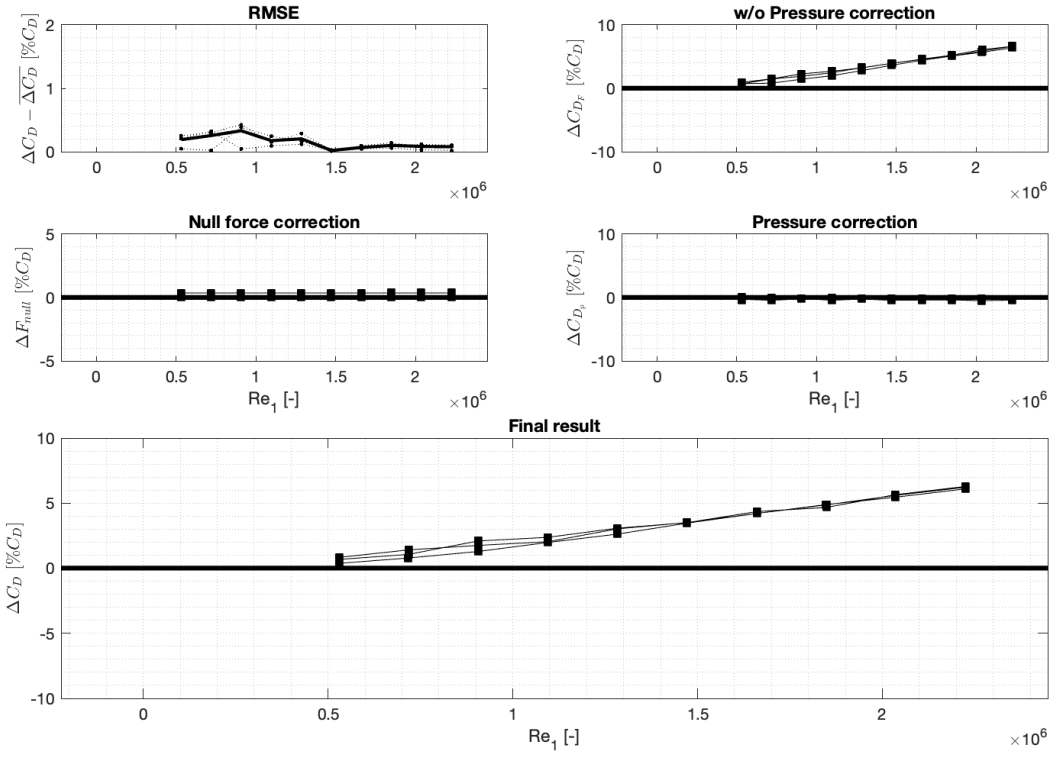

Figure C.40: Data for TP0102A in apex downstream configuration

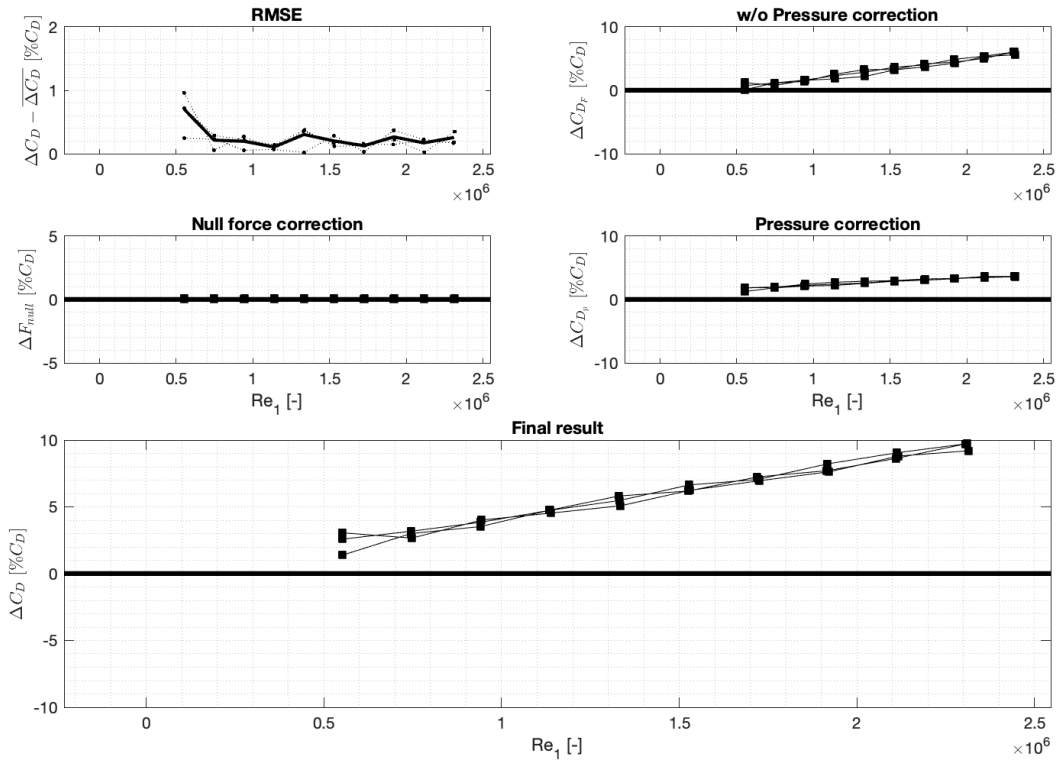

Figure C.41: Data for TP0103A in apex upstream configuration

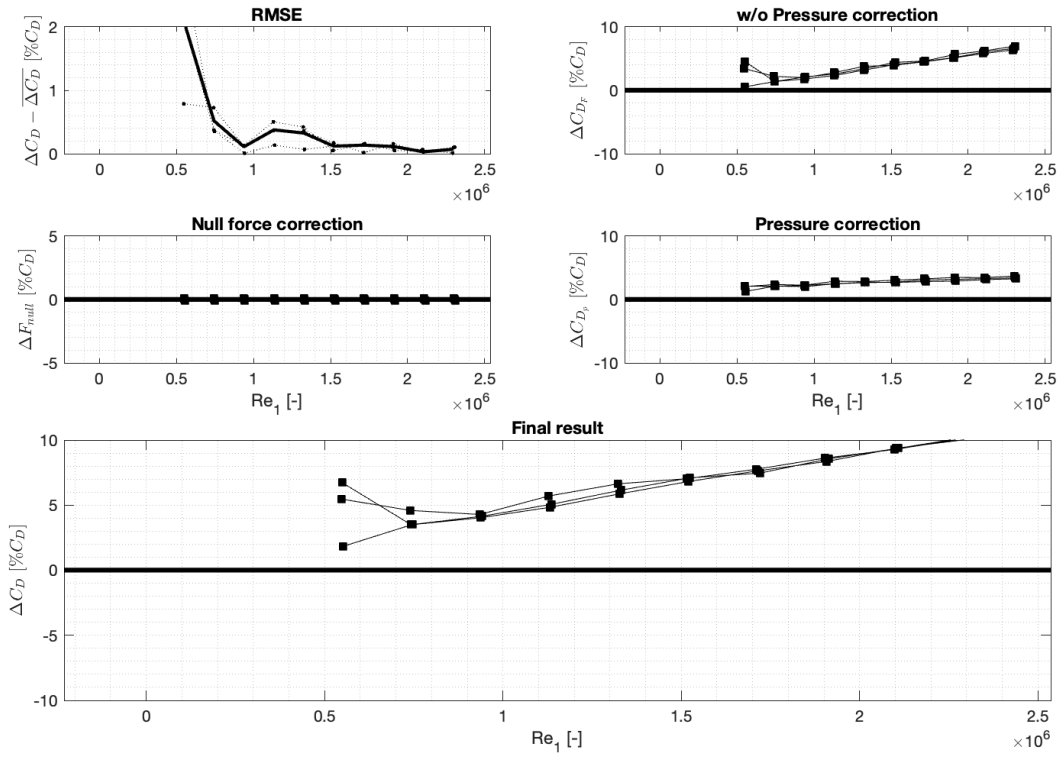

Figure C.42: Data for TP0103A in apex downstream configuration

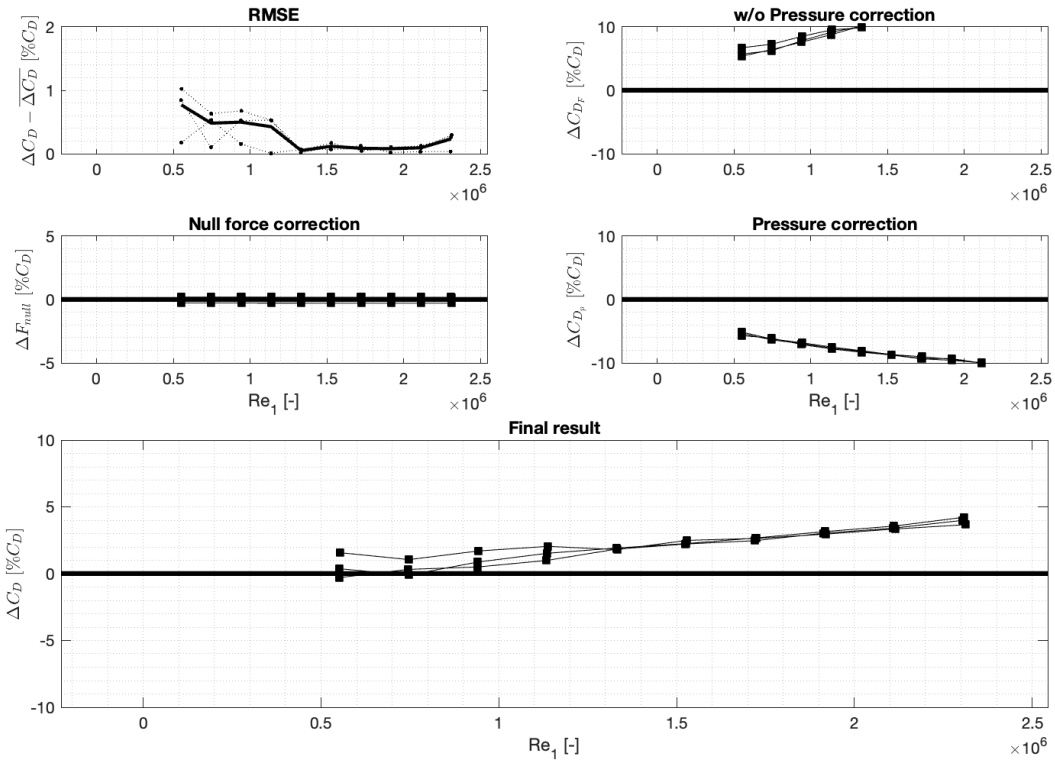

Figure C.43: Data for TP013B in apex upstream configuration

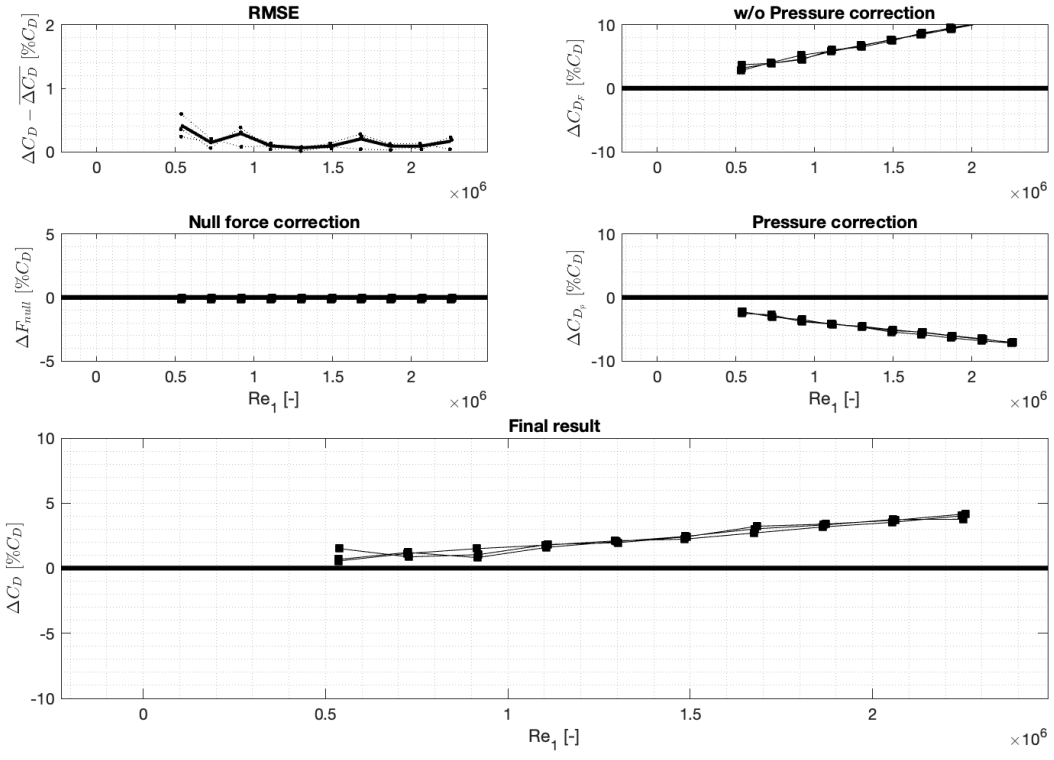

Figure C.44: Data for TP0103B in apex downstream configuration

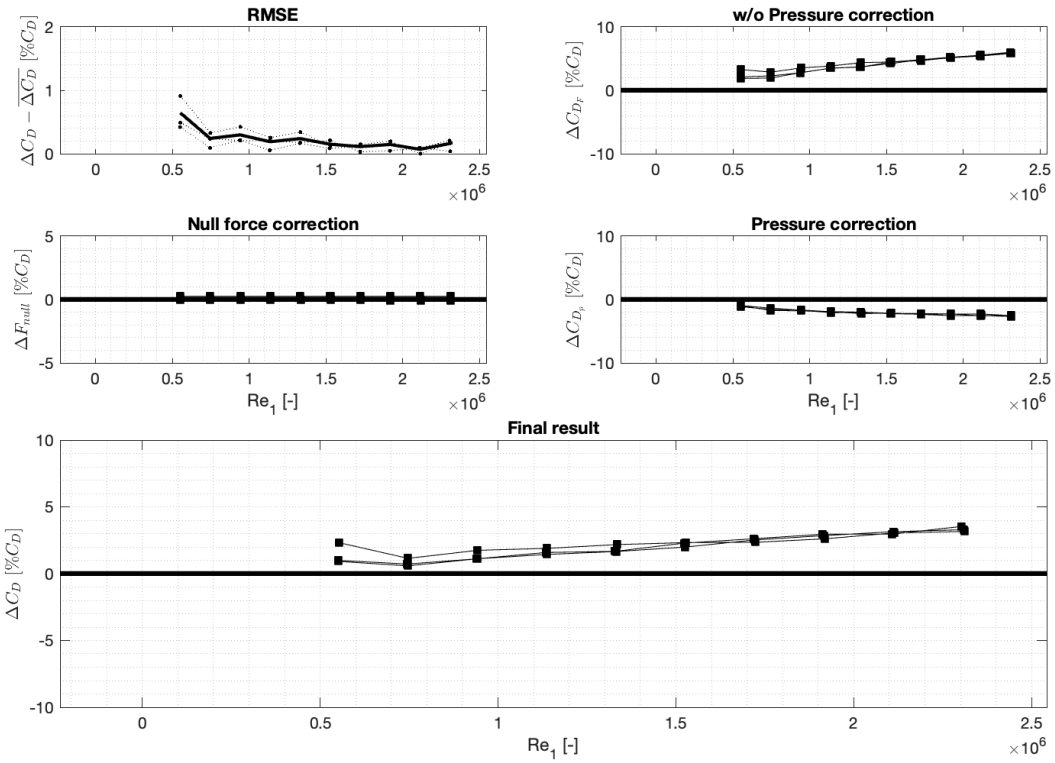

Figure C.45: Data for TP0104A in apex upstream configuration

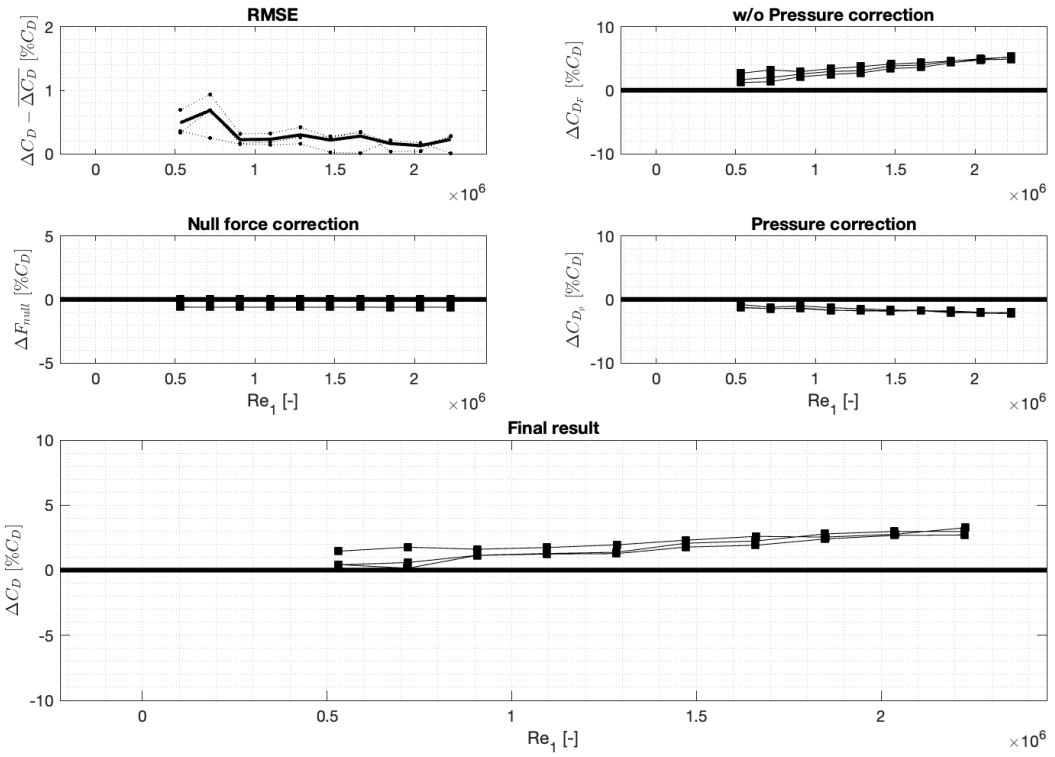

Figure C.46: Data for TP0104A in apex downstream configuration

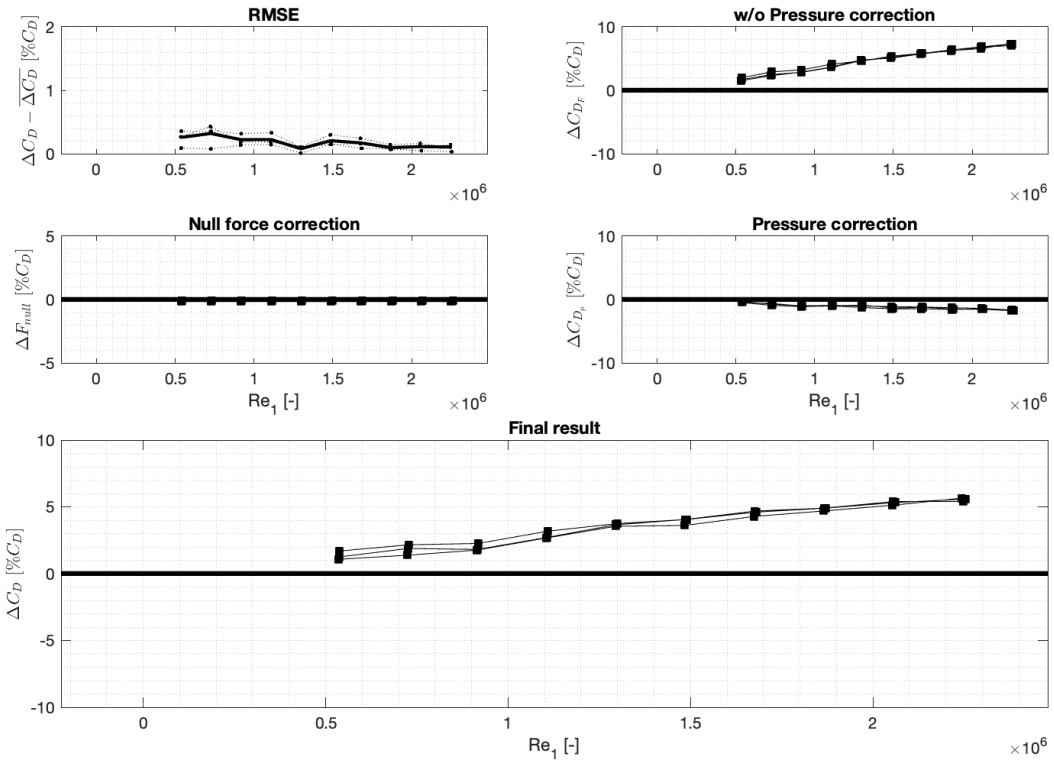

Figure C.47: Data for TP0104B in apex upstream configuration

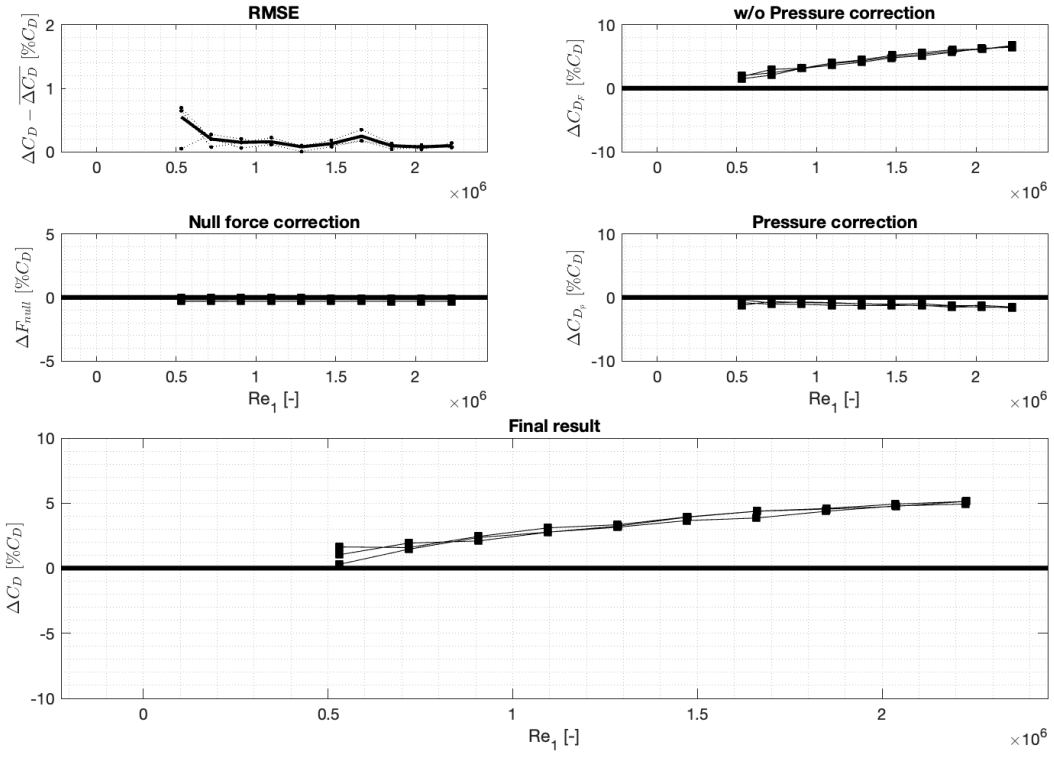

Figure C.48: Data for TP0104B in apex downstream configuration

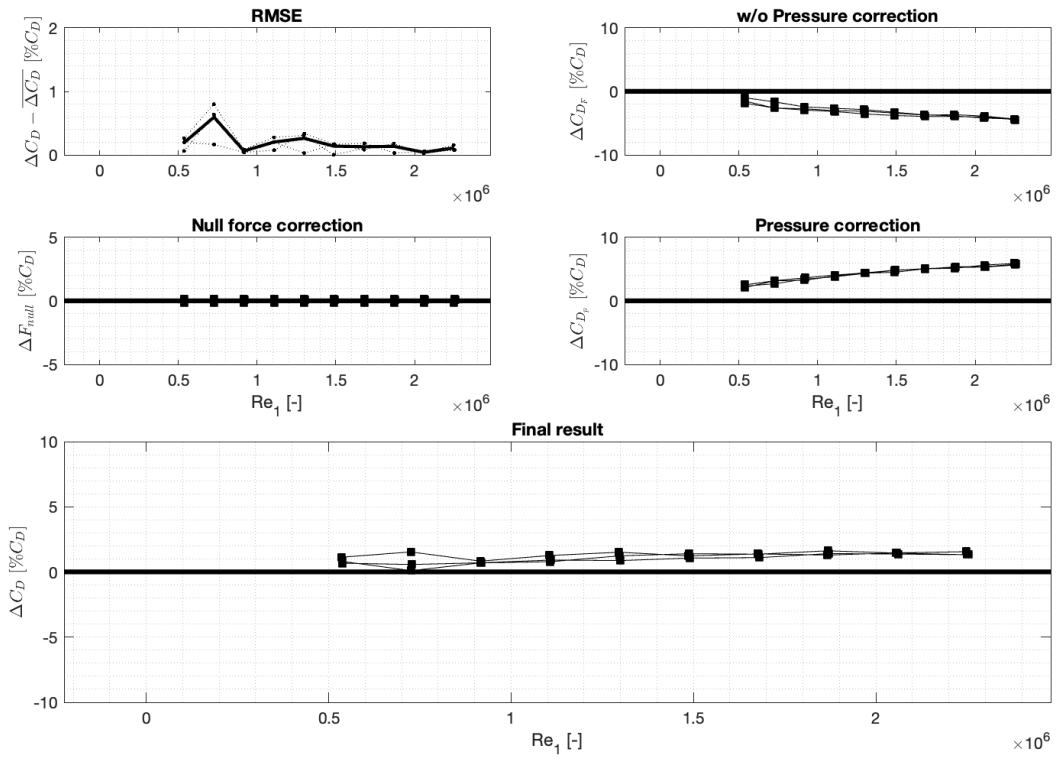

Figure C.49: Data for TP0105A as flat reference

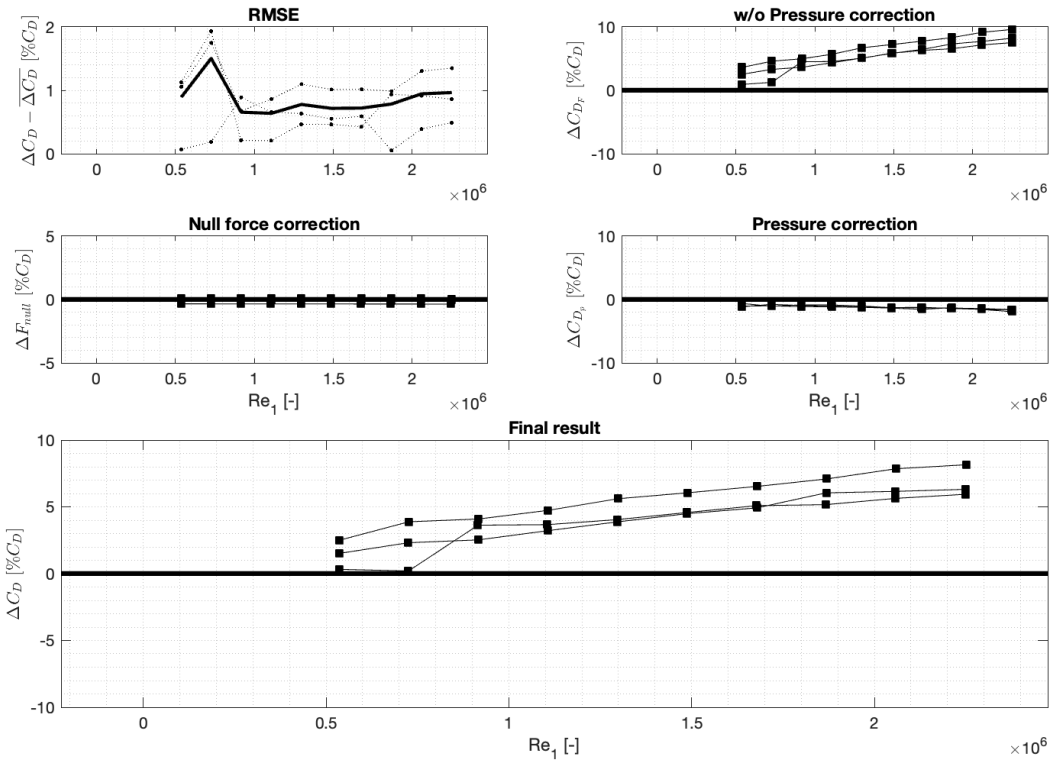

Figure C.50: Data for TP0106A in apex upstream configuration

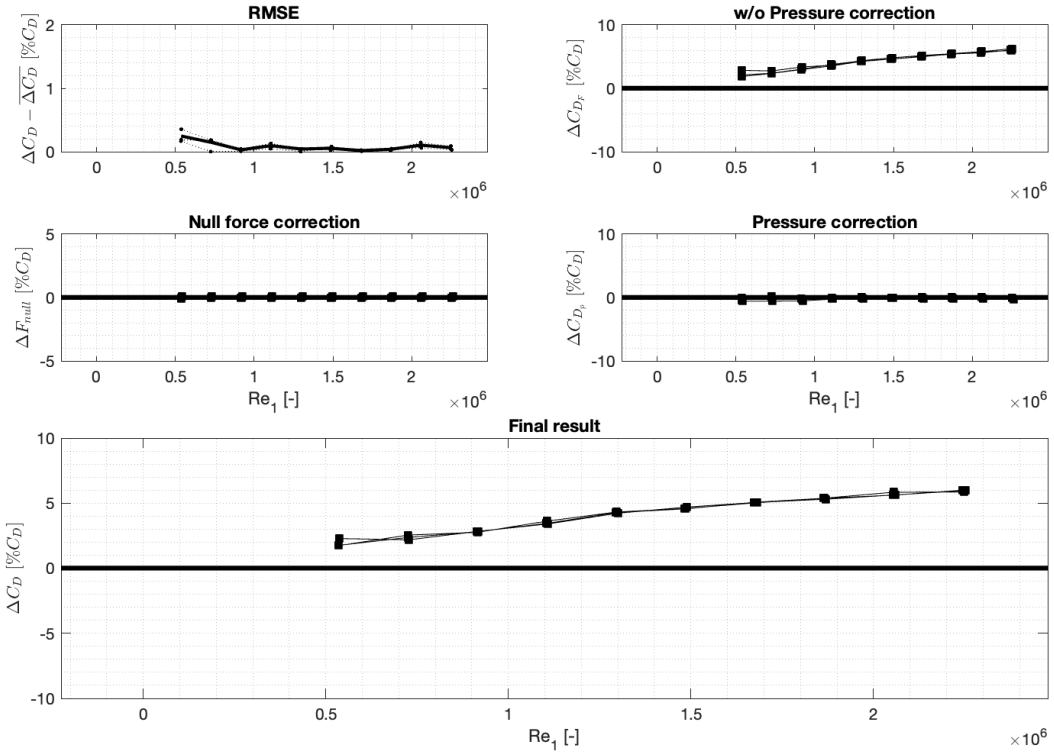

Figure C.51: Data for TP0106A in apex downstream configuration

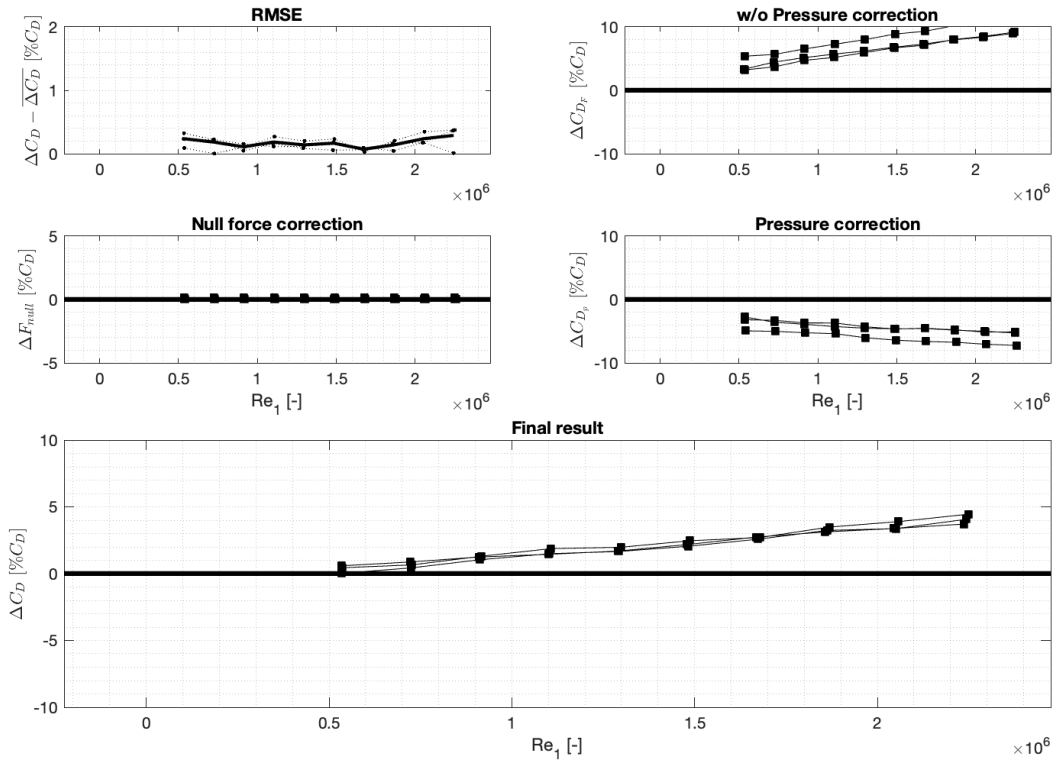

Figure C.52: Data for TP0106B in apex upstream configuration

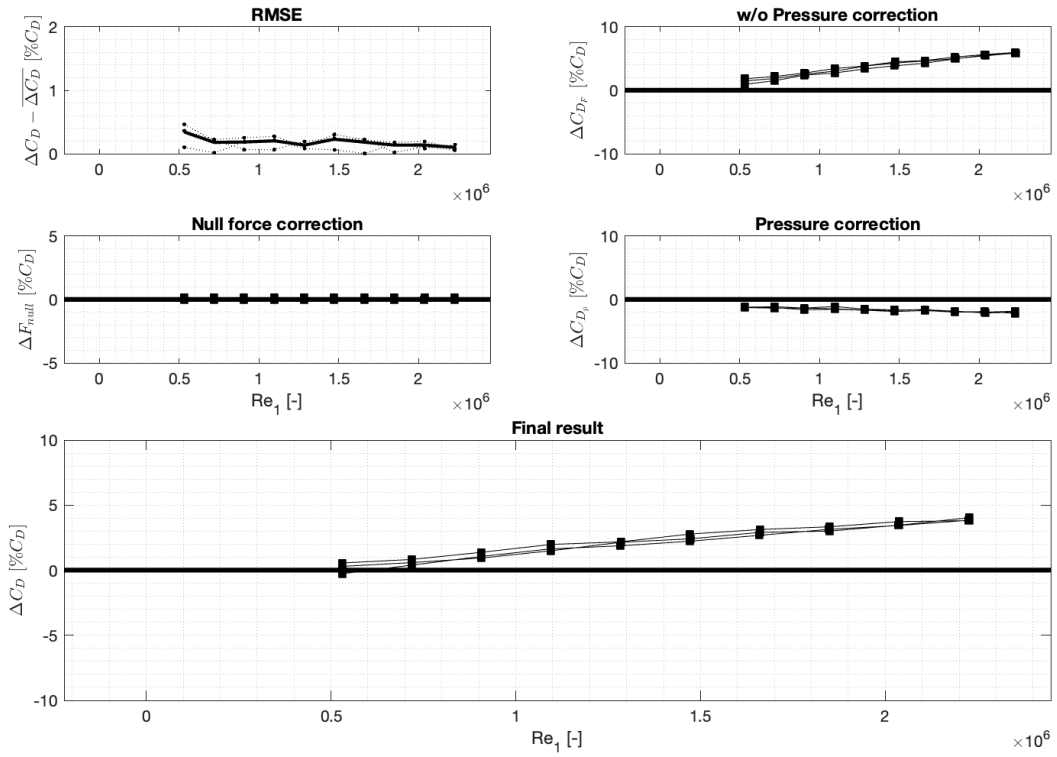

Figure C.53: Data for TP0106B in apex downstream configuration

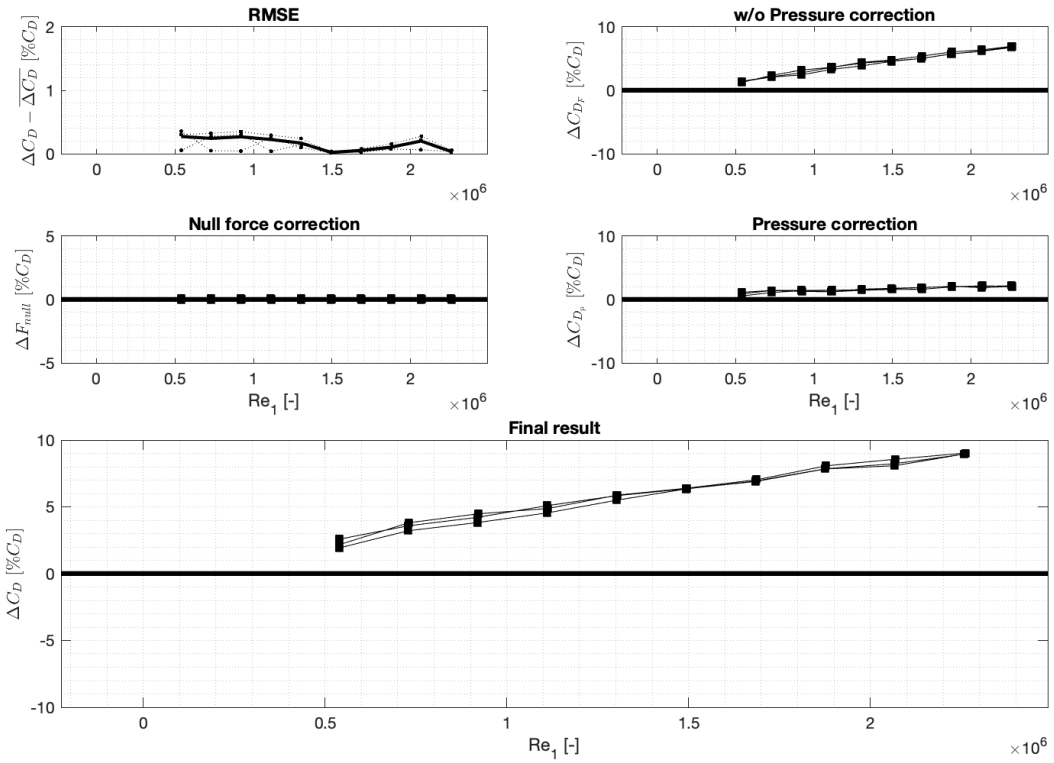

Figure C.54: Data for TP0109A in apex upstream configuration

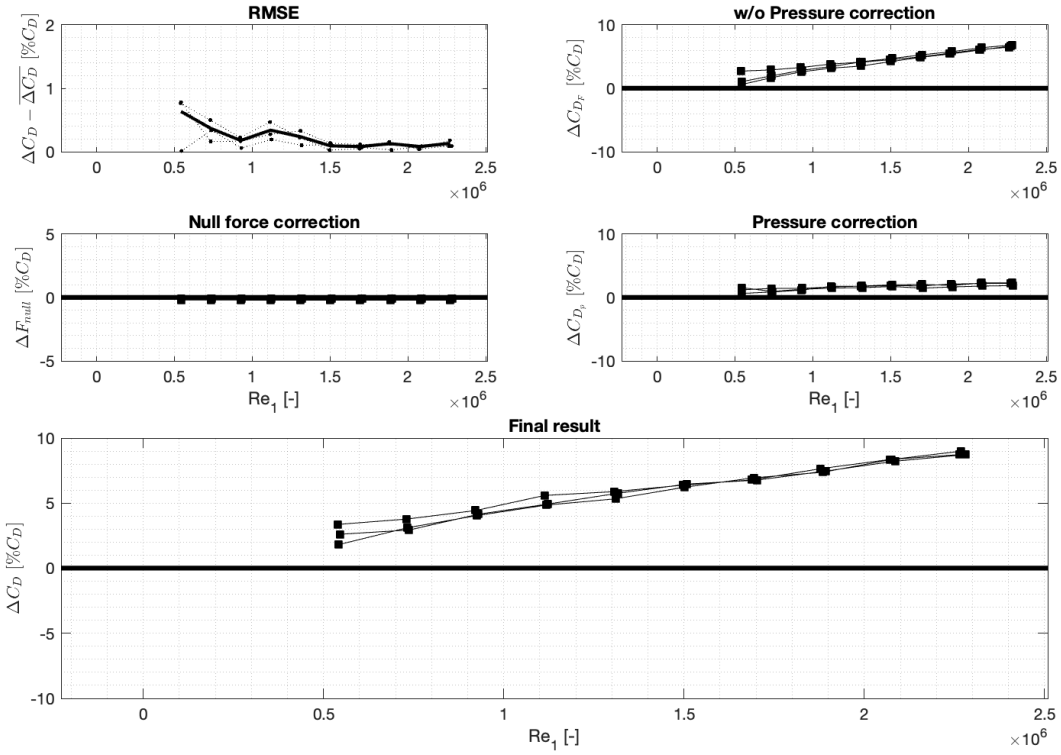

Figure C.55: Data for TP0109A in apex downstream configuration

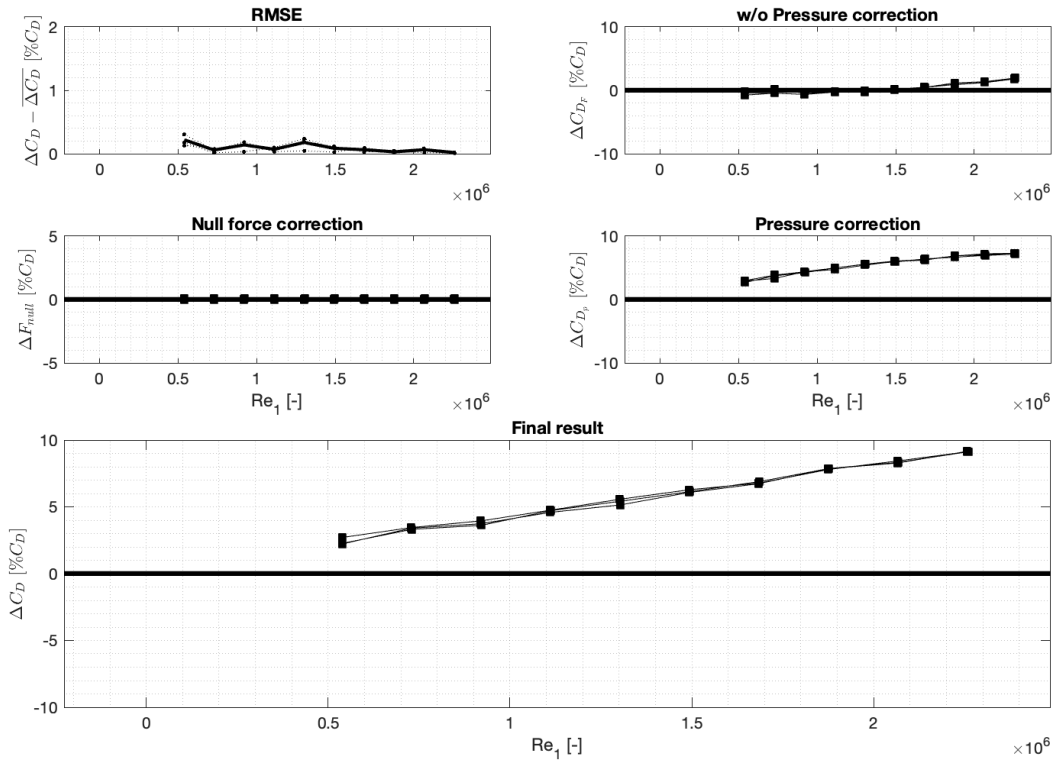

Figure C.56: Data for TP0110A in apex upstream configuration

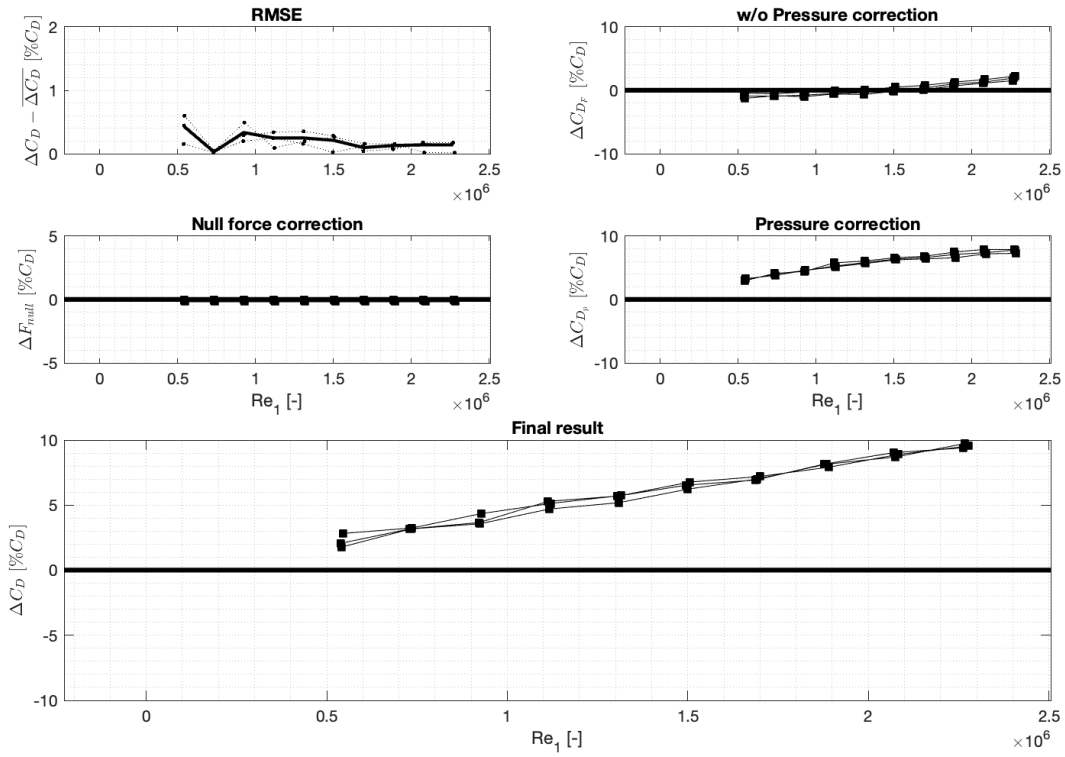

Figure C.57: Data for TP0110A in apex downstream configuration

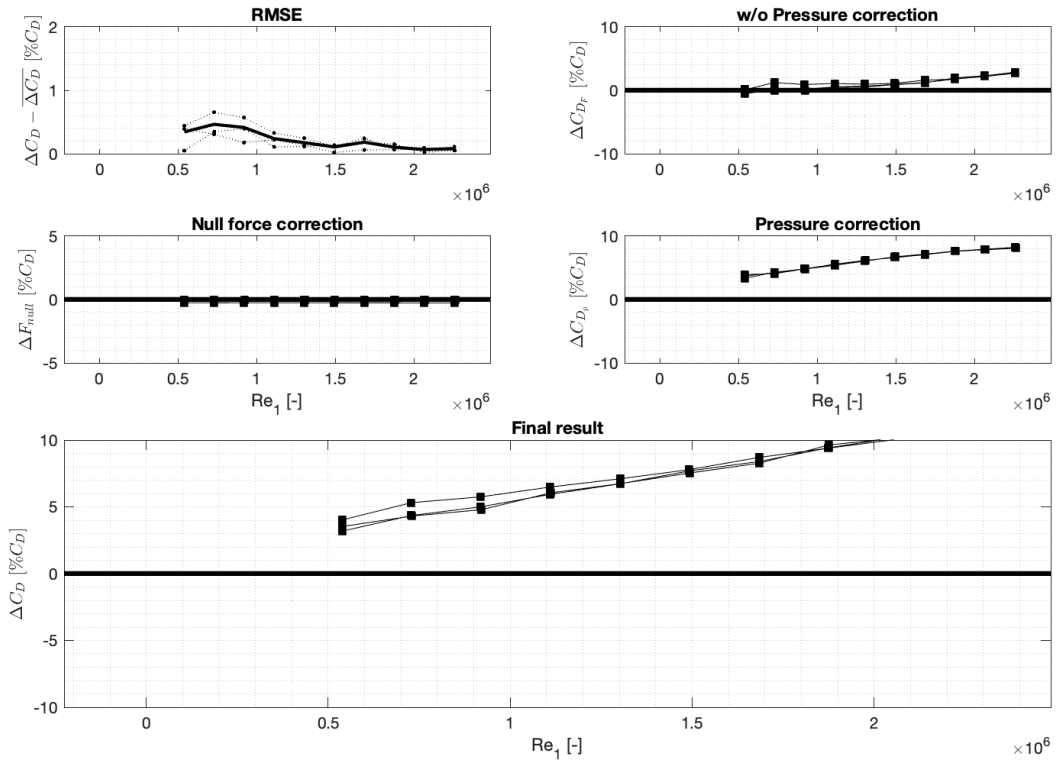

Figure C.58: Data for TP0111A in apex upstream configuration

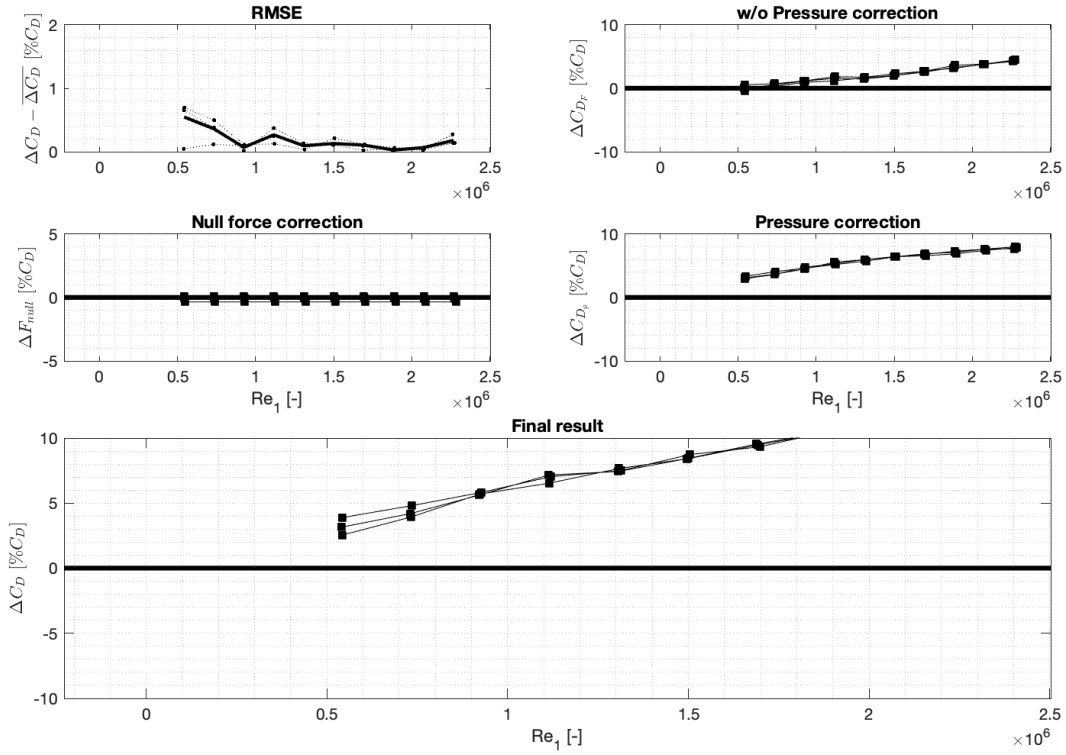

Figure C.59: Data for TP0111A in apex downstream configuration

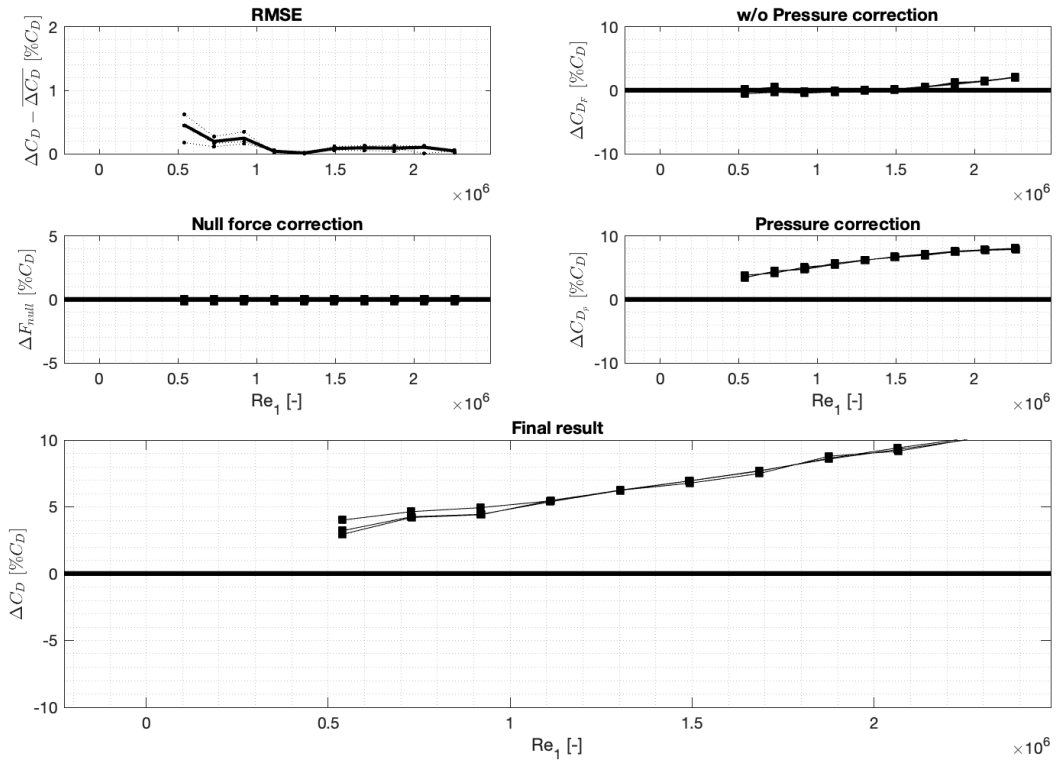

Figure C.60: Data for TP0112A in apex upstream configuration

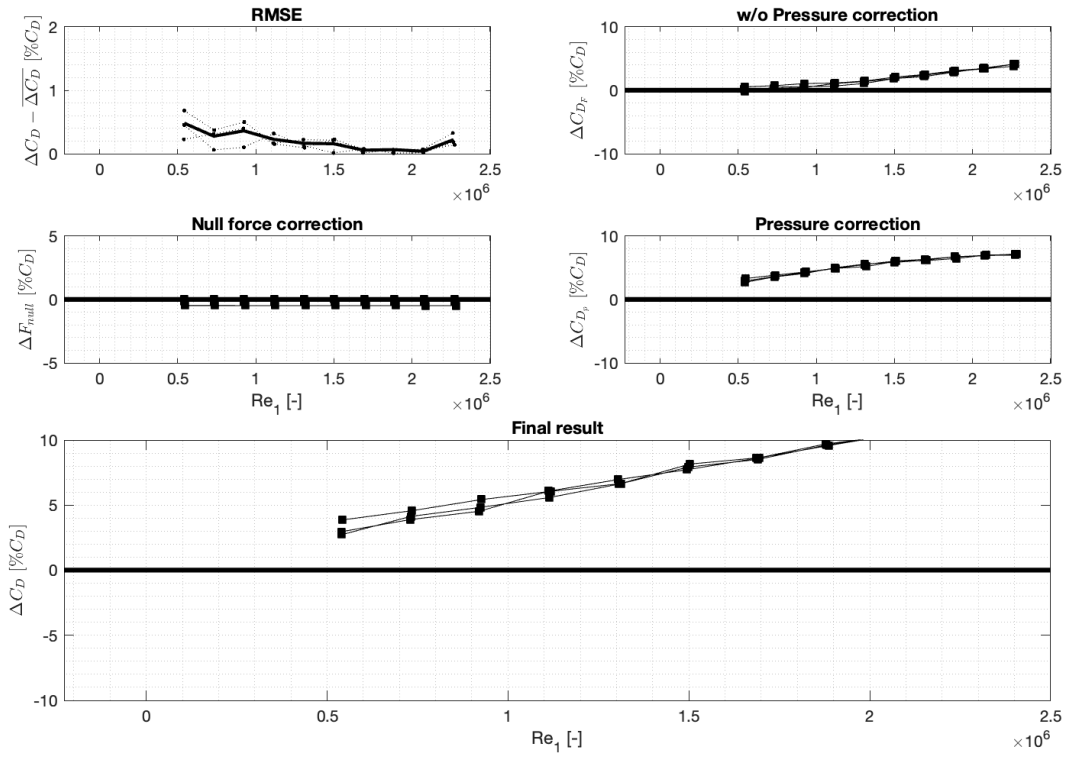

Figure C.61: Data for TP0112A in apex downstream configuration

D

Script for parameterised test plate design

This appendix includes the Matlab code used to generate the TikZ script for the test plate design. The code corresponds to the geometry for the random design by Sirovich and Karlsson (1997) (design 3 in this Master thesis).

```
%% Generation of protrusion arrays in 2D
%
% Master thesis project
% Author: Julio Carrasco Grau
% Date: 19/02/2022

close all; clear all; clc;

diary SaK_97_20ms_random.tex     % Save output to file

%% Geometry definitions (in mm)

origin = 0;
VU = 18*10^(-3); % [mm] MAYBE THIS CAN BE CONNECTED TO FRISOS SCRIPT

% Test plate

P_width = 366.3; % [mm]
P_length = 881.3; % [mm]
P_thickness = 5; % [mm] -- NOT USED
margin_top = 10; % margin between the top of the plate and the start of the design
margin_bottom = 10; % margin between the last element and the end of the plate

% Protrusion

a = 300*VU;      % Separation between rows (streamwise distance)
b = 200*VU;      % Length of an element (streamwise size)
c = 200*VU;      % Width of an element (transversal size)
d = 260*VU;      % Separation between elements in a row (transversal distance)
e = -130*VU;        % Offset between rows (can be random, aligned [zero] or staggered ...
    [constant])
e_how = 2 ; % Offset type: 0 for 'zero', 1 for 'constant', 2 for 'random'
e_std_dev = 50*VU;
f = 5*VU;        % Element height - NOT USED
alpha = 45;      % Apex angle [deg] - NOT USED
t = 40*VU;       % thickness of the chevron legs


%% Start building tikZ script
```

```
39
40  disp('\documentclass{article}')
41  disp('\usepackage{blindtext}')
42  disp('\usepackage[paperheight=90cm,paperwidth=40cm,margin=0cm]{geometry}')
43  disp('\usepackage{tikz}')
44  disp('\begin{document}')
45
46  disp('\begin{tikzpicture}')
47  disp('% Start defining the edges of the test plate')
48
49  % all in mm
50  x1 = 0;
51  x2 = 366.3;
52  x3 = 366.3;
53  x4 = 0;
54  y1 = 0;
55  y2 = 0;
56  y3 = - 881.3;
57  y4 = - 881.3;
58
59  disp(['\draw (', num2str(x1), 'mm,', num2str(y1), 'mm) -- (', num2str(x2), 'mm,', ...
        num2str(y2), 'mm) -- (', num2str(x3), 'mm,', num2str(y3), 'mm) -- (', num2str(x4), ...
        'mm,' num2str(y4), 'mm) -- cycle;'])
60  disp('% Define the patches to cover the attachment holes')
61
62  %
63  disp(['\draw (0mm, -10mm) -- (10mm, -10mm) -- (10mm, 0mm) -- (0mm, 0mm) -- cycle;'])
64  disp(['\draw (366.3mm, -10mm) -- (356.3mm, -10mm) -- (356.3mm, 0mm) -- (366.3mm, 0mm) ...
        -- cycle;'])
65  disp(['\draw (0mm, -871.3mm) -- (10mm, -871.3mm) -- (10mm, -881.3mm) -- (0mm, -881.3mm) ...
        -- cycle;'])
66  disp(['\draw (366.3mm, -871.3mm) -- (356.3mm, -871.3mm) -- (356.3mm, -881.3mm) -- ...
        (366.3mm, -881.3mm) -- cycle;'])
67  disp(['\draw (0mm, -445.65mm) -- (10mm, -445.65mm) -- (10mm, -435.65mm) -- (0mm, ...
        -435.65mm) -- cycle;'])
68  disp(['\draw (366.3mm, -445.65mm) -- (356.3mm, -445.65mm) -- (356.3mm, -435.65mm) -- ...
        (366.3mm, -435.65mm) -- cycle;'])
69  %
70
71  disp('% Define the protrusions')
72
73  rows = (P_length)/a;
74  columns = (P_width-2*d)/d;
75
76  e_vec = ones(1,int16(rows))';
77
78
79  if e_how == 0
80      for k = 1:rows
81      e_vec(k,1) = 0;
82      end
83  elseif e_how == 1
84      for k = 1:rows
85      e_vec(k,1) = e*k;
86      end
87  elseif e_how == 2
88      e_vec = e.*randn(int16(rows),1); %+ e_std_dev;
89  end
90
91  p1x = 2*d/3;
92  p2x = p1x + (t+c)/2;
93  p3x = p1x + t+c;
94  p4x = p1x + t/2 + c - t/2;
95  p5x = p1x + (t+c)/2;
96  p6x = p1x + t;
97
98  p1y = -a-10;
99  p2y = p1y + b;
100 p3y = p1y;
101 p4y = p1y;
102 p5y = p1y + tand(atand(b/(0.5*(t+c)))) * (0.5*(t+c)-t);
```

```
103 p6y = p1y;
104
105 for i = 1:rows-4 % loop over all rows
106
107     if p1x < 0
108         AAA = 'protrusions skipped';
109     else
110         disp(['\draw (', num2str(p1x), 'mm,', num2str(p1y), 'mm) -- (', num2str(p2x), ...
                'mm,', num2str(p2y), 'mm) -- (', num2str(p3x), 'mm,', num2str(p3y), 'mm) -- ...
                (', num2str(p4x), 'mm,' num2str(p4y), 'mm) -- (', num2str(p5x), 'mm,', ...
                num2str(p5y), 'mm) -- (', num2str(p6x), 'mm,' num2str(p6y), 'mm) -- cycle;'])
111     end
112
113     for j = 1:columns
114
115         p1x = p1x + d;
116         p2x = p1x + (t+c)/2;
117         p3x = p1x + t+c;
118         p4x = p1x + t/2 + c - t/2;
119         p5x = p1x + (t+c)/2;
120         p6x = p1x + t;
121
122
123         if p1x < 0
124             AAA = 'protrusions skipped';
125         else
126             disp(['\draw (', num2str(p1x), 'mm,', num2str(p1y), 'mm) -- (', ...
                    num2str(p2x), 'mm,', num2str(p2y), 'mm) -- (', num2str(p3x), 'mm,', ...
                    num2str(p3y), 'mm) -- (', num2str(p4x), 'mm,' num2str(p4y), 'mm) -- (', ...
                    num2str(p5x), 'mm,', num2str(p5y), 'mm) -- (', num2str(p6x), 'mm,' ...
                    num2str(p6y), 'mm) -- cycle;'])
127         end
128     end
129
130     columns = (P_width-2*d-e_vec(i,1))/d;
131
132     p1x = 2*d/3 + e_vec(i,1);
133     p2x = p1x + (t+c)/2;
134     p3x = p1x + t+c;
135     p4x = p1x + t/2 + c - t/2;
136     p5x = p1x + (t+c)/2;
137     p6x = p1x + t;
138
139     p1y = p1y-(a);
140     p2y = p1y + b;
141     p3y = p1y;
142     p4y = p1y;
143     p5y = p1y + tand(atand(b/(0.5*(t+c)))) * (0.5*(t+c)-t);
144     p6y = p1y;
145
146 end
147
148
149 disp(['% This grid has a total of ', num2str(i), ' rows and roughly ', num2str(j), ' ...
        columns'])
150 disp(['\end{tikzpicture}'])
151 disp('\end{document}')
```

E

PIV Additional data | x-z plane

This appendix provides additional PIV data for the x-z plane. In section E.1, velocity vector field information for all 27 test cases specified in table 6.4 is shown in the form of an average velocity field, the corresponding standard deviation, and one of the 600 instantaneous velocity fields. Section E.2 presents the values for the uncertainty quantification. Finally, in section E.3, the results of a two-point correlation analysis for the 27 test cases are included.

E.1. Velocity vector field

During the PIV campaign for the x-z plane, a total of 16,200 instantaneous velocity fields were captured for the 27 test cases. It is not possible to include all data in a reasonable manner in this thesis report; however, this section aims to provide an overview of the results by showing the average velocity field, the corresponding standard deviation, and a randomly selected instantaneous velocity field for each test case. The velocity corresponds to the total velocity, which is the combined velocity in the x and z directions. Furthermore, in the shown velocity fields, a margin of 5% from each side has been cropped to remove zero values and other artefacts.

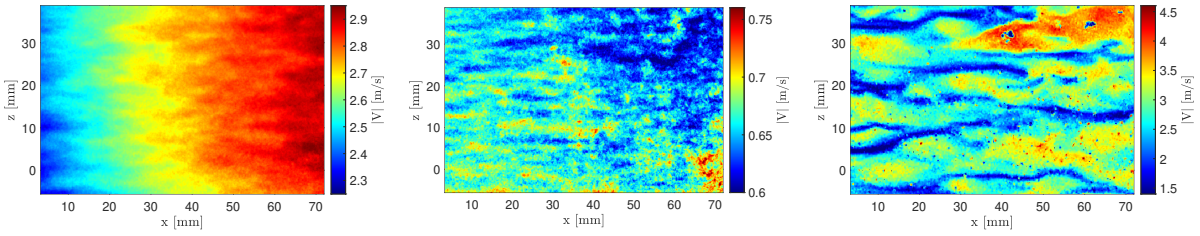

(a) Average velocity field (b) Standard deviation (c) Instantaneous velocity field

Figure E.1: PIV data for TP0000 at 5 m/s

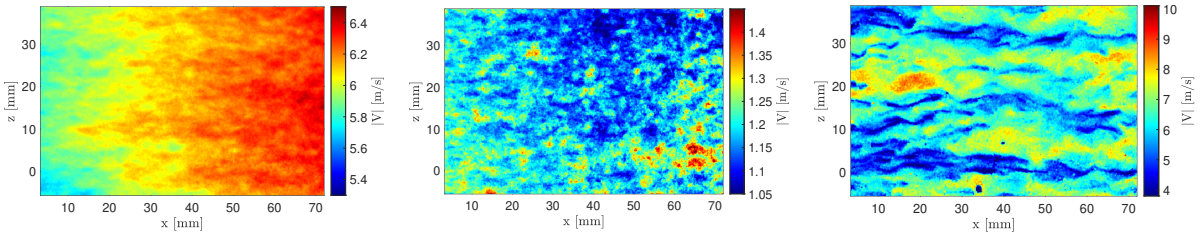

(a) Average velocity field (b) Standard deviation (c) Instantaneous velocity field

Figure E.2: PIV data for TP0000 at 10 m/s

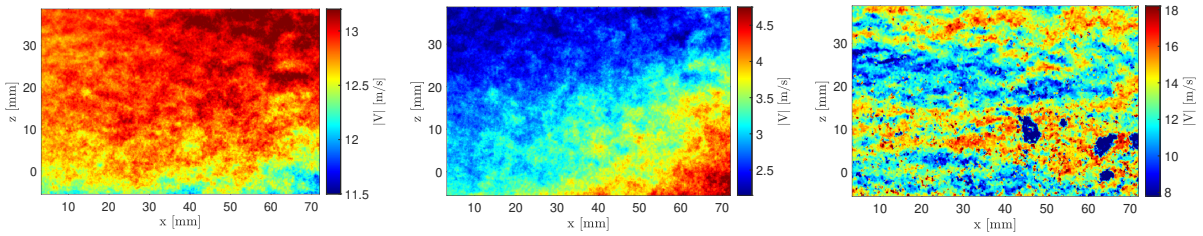

(a) Average velocity field (b) Standard deviation (c) Instantaneous velocity field

Figure E.3: PIV data for TP0000 at 20 m/s

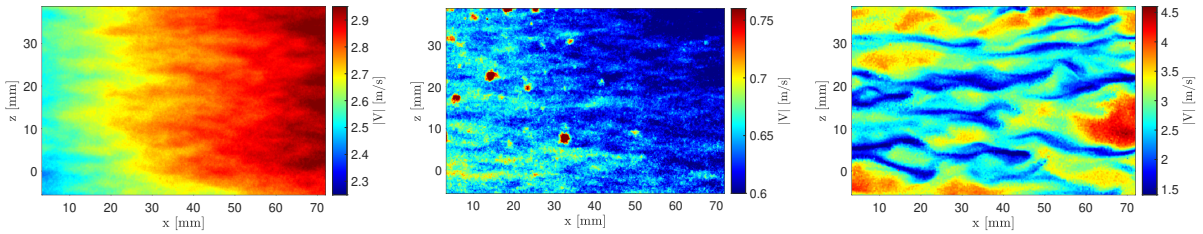

(a) Average velocity field (b) Standard deviation (c) Instantaneous velocity field

Figure E.4: PIV data for TP0109A [Sirovich (A)] at 5 m/s

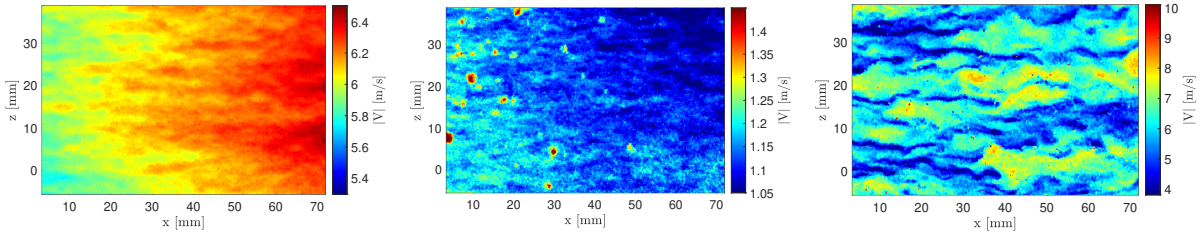

(a) Average velocity field (b) Standard deviation (c) Instantaneous velocity field

Figure E.5: PIV data for TP0109A [Sirovich (A)] at 10 m/s

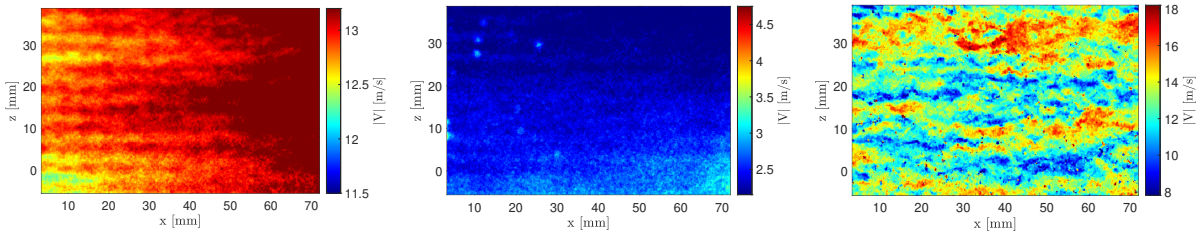

(a) Average velocity field (b) Standard deviation (c) Instantaneous velocity field

Figure E.6: PIV data for TP0109A [Sirovich (A)] at 20 m/s

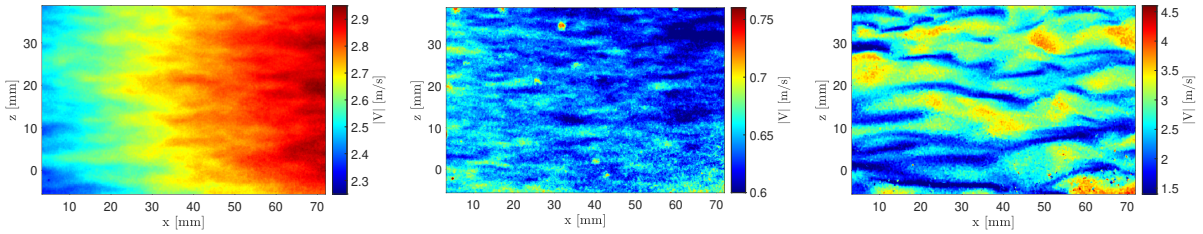

(a) Average velocity field (b) Standard deviation (c) Instantaneous velocity field

Figure E.7: PIV data for TP0109A [Sirovich (A)] reverse at 5 m/s

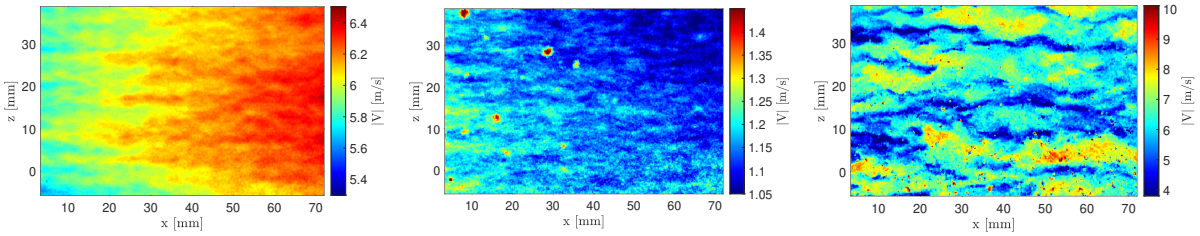

(a) Average velocity field (b) Standard deviation (c) Instantaneous velocity field

Figure E.8: PIV data for TP0109A [Sirovich (A)] reverse at 10 m/s

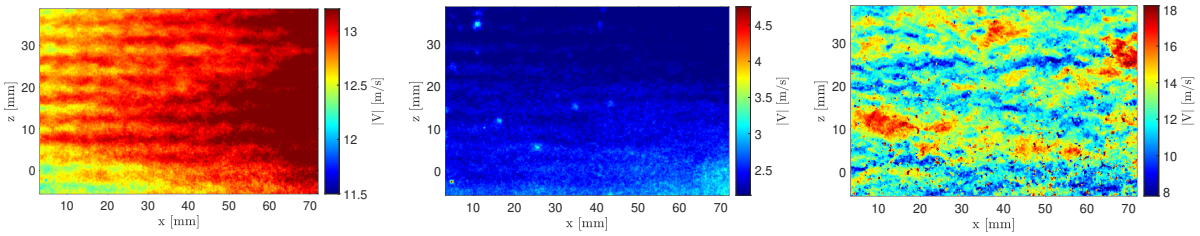

(a) Average velocity field (b) Standard deviation (c) Instantaneous velocity field

Figure E.9: PIV data for TP0109A [Sirovich (A)] reverse at 20 m/s

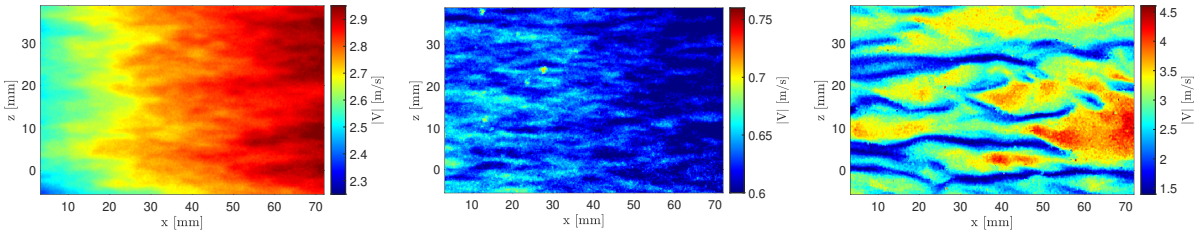

(a) Average velocity field (b) Standard deviation (c) Instantaneous velocity field

Figure E.10: PIV data for TP0110A [Sirovich (R)] at 5 m/s

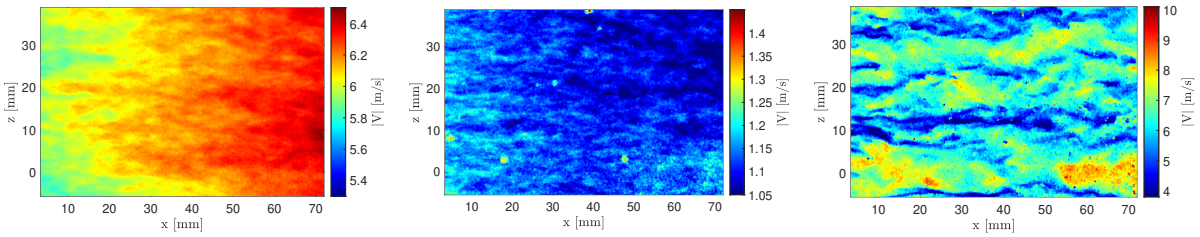

(a) Average velocity field (b) Standard deviation (c) Instantaneous velocity field

Figure E.11: PIV data for TP0110A [Sirovich (R)] at 10 m/s

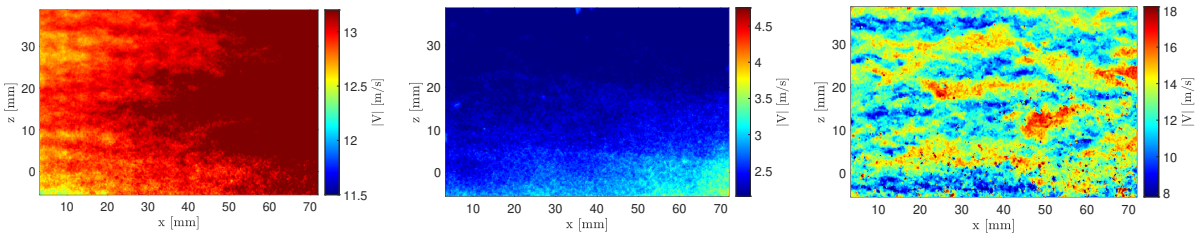

(a) Average velocity field (b) Standard deviation (c) Instantaneous velocity field

Figure E.12: PIV data for TP0110A [Sirovich (R)] at 20 m/s

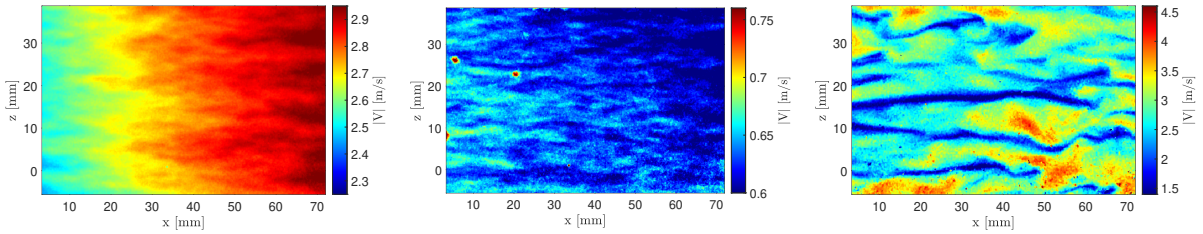

(a) Average velocity field (b) Standard deviation (c) Instantaneous velocity field

Figure E.13: PIV data for TP0110A [Sirovich (R)] reverse at 5 m/s

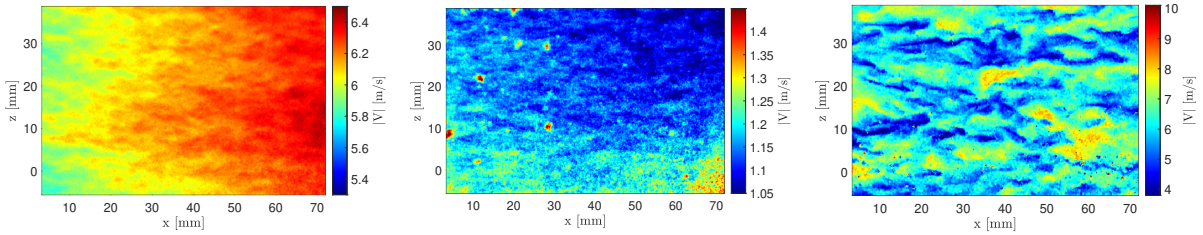

(a) Average velocity field (b) Standard deviation (c) Instantaneous velocity field

Figure E.14: PIV data for TP0110A [Sirovich (R)] reverse at 10 m/s

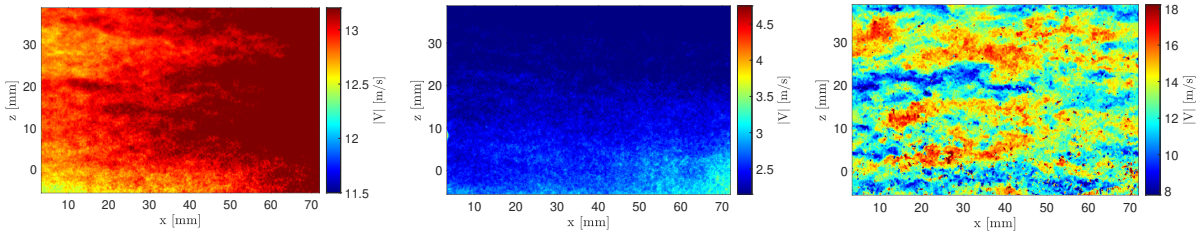

(a) Average velocity field (b) Standard deviation (c) Instantaneous velocity field

Figure E.15: PIV data for TP0110A [Sirovich (R)] reverse at 20 m/s

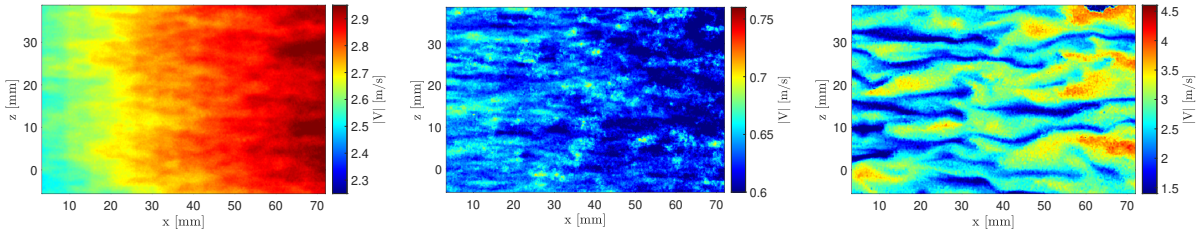

(a) Average velocity field (b) Standard deviation (c) Instantaneous velocity field

Figure E.16: PIV data for TP0111A [Deltas (A)] at 5 m/s

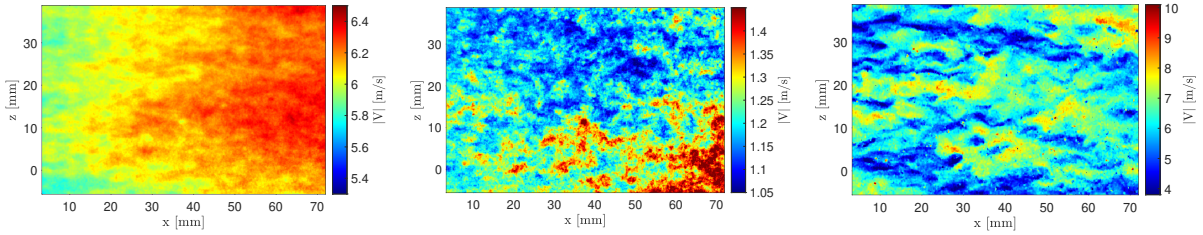

(a) Average velocity field (b) Standard deviation (c) Instantaneous velocity field

Figure E.17: PIV data for TP0111A [Deltas (A)] at 10 m/s

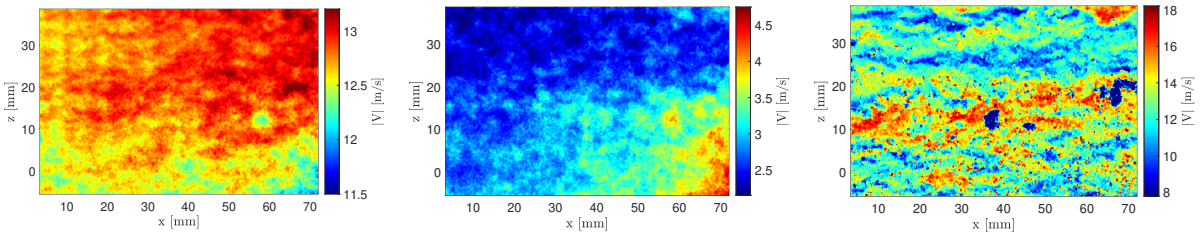

(a) Average velocity field (b) Standard deviation (c) Instantaneous velocity field

Figure E.18: PIV data for TP0111A [Deltas (A)] at 20 m/s

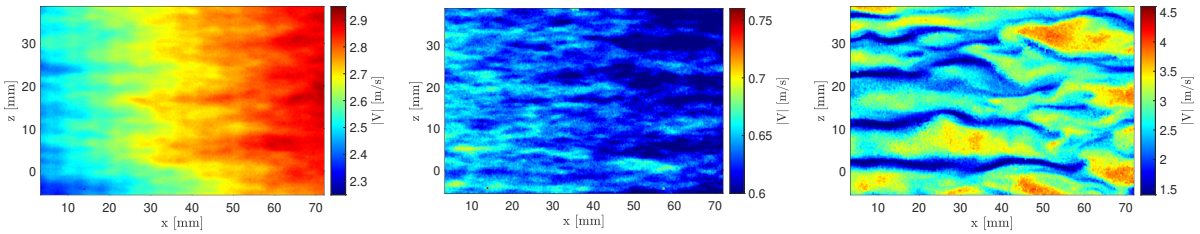

(a) Average velocity field (b) Standard deviation (c) Instantaneous velocity field

Figure E.19: PIV data for TP0111A [Deltas (A)] reverse at 5 m/s

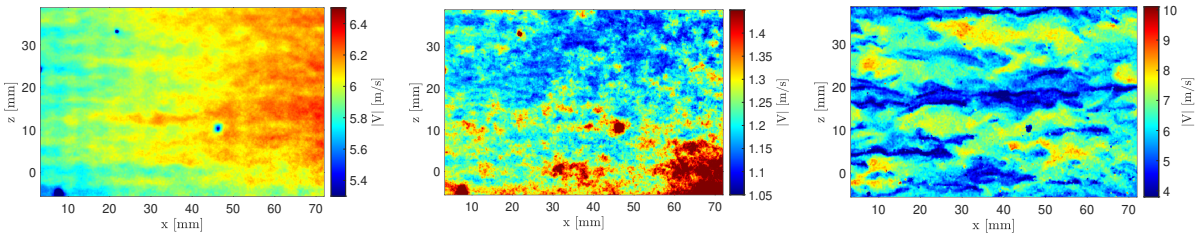

(a) Average velocity field (b) Standard deviation (c) Instantaneous velocity field

Figure E.20: PIV data for TP0111A [Deltas (A)] reverse at 10 m/s

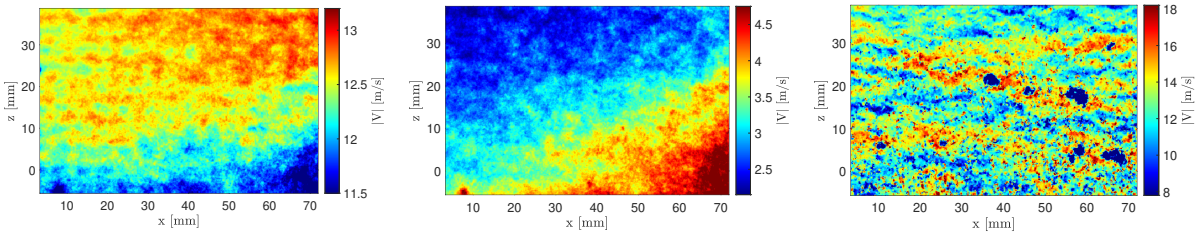

(a) Average velocity field (b) Standard deviation (c) Instantaneous velocity field

Figure E.21: PIV data for TP0111A [Deltas (A)] reverse at 20 m/s

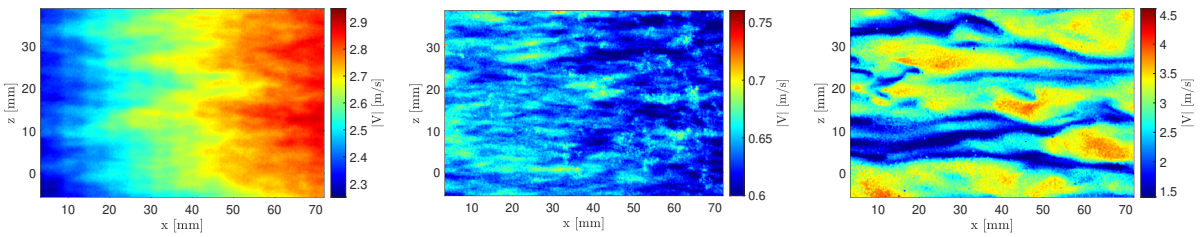

(a) Average velocity field (b) Standard deviation (c) Instantaneous velocity field

Figure E.22: PIV data for TP0112A [Deltas (R)] at 5 m/s

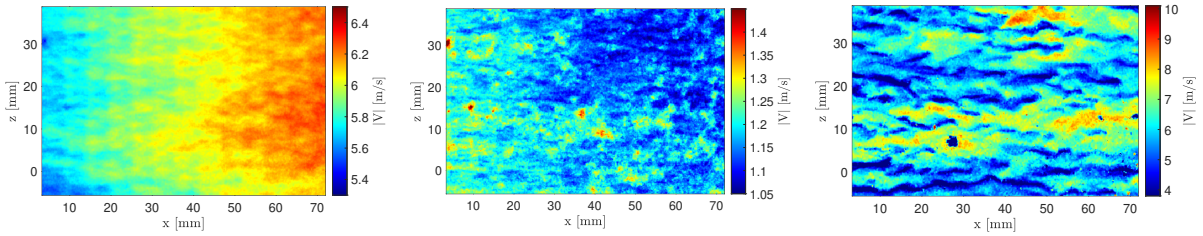

(a) Average velocity field (b) Standard deviation (c) Instantaneous velocity field

Figure E.23: PIV data for TP0112A [Deltas (R)] at 10 m/s

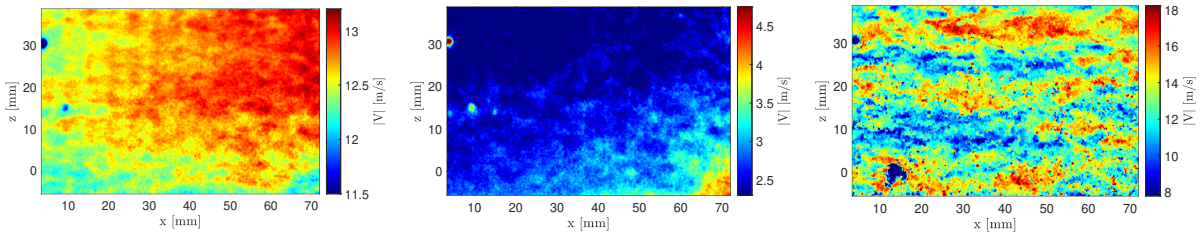

(a) Average velocity field (b) Standard deviation (c) Instantaneous velocity field

Figure E.24: PIV data for TP0112A [Deltas (R)] at 20 m/s

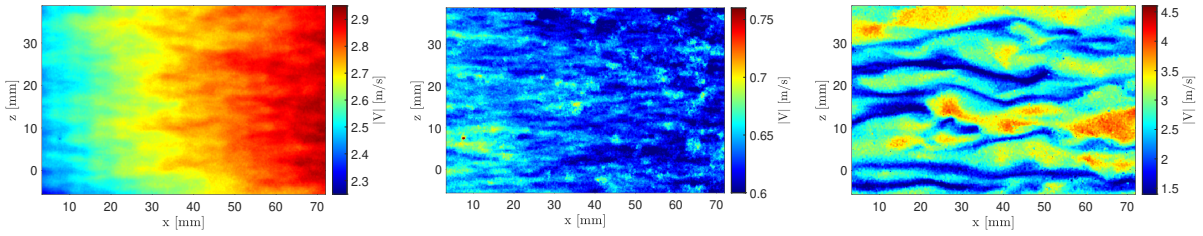

(a) Average velocity field (b) Standard deviation (c) Instantaneous velocity field

Figure E.25: PIV data for TP0112A [Deltas (R)] reverse at 5 m/s

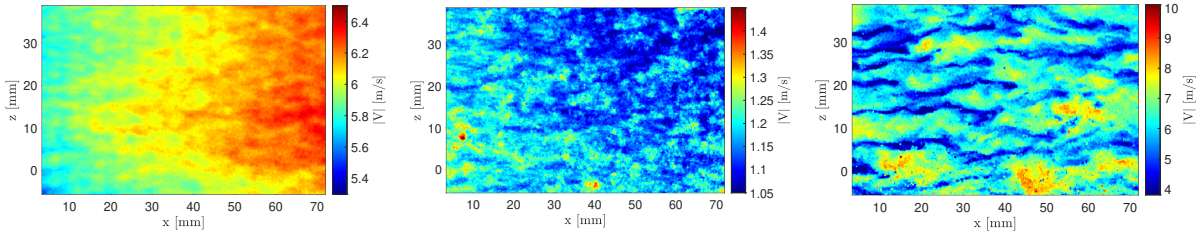

(a) Average velocity field (b) Standard deviation (c) Instantaneous velocity field

Figure E.26: PIV data for TP0112A [Deltas (R)] reverse at 10 m/s

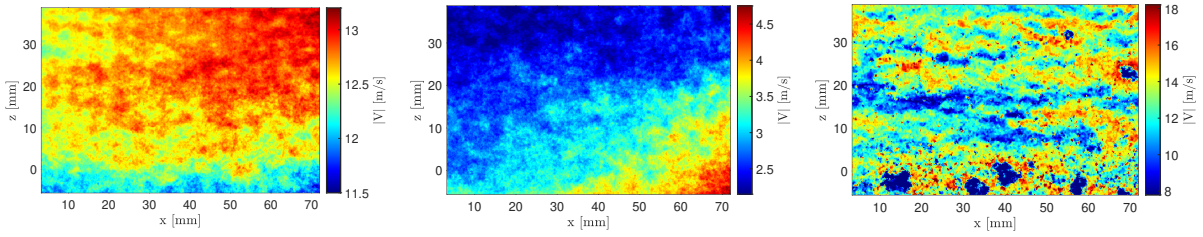

(a) Average velocity field (b) Standard deviation (c) Instantaneous velocity field

Figure E.27: PIV data for TP0112A [Deltas (R)] reverse at 20 m/s

E.2. Uncertainty quantification

This section presents the results for the uncertainty quantification in table E.1. The methodology used for this analysis has been presented in section 6.2.4. For the x-z plane, the uncertainty of the instantaneous velocity fields (ϵ_u, ϵ_w), of the mean velocity ($\epsilon_{\bar{u}}$, $\epsilon_{\bar{w}}$), of the standard deviation ($\epsilon_{\sigma(u)}$, $\epsilon_{\sigma(w)}$), and of the variance ($\epsilon_{\sigma(u)^2}$, $\epsilon_{\sigma(w)^2}$) are considered.

Test case [-]	U_∞ [m/s]	ϵ_u [%]	ϵ_w [%]	$\epsilon_{\bar{u}}$ [m/s]	$\epsilon_{\bar{w}}$ [m/s]	$\epsilon_{\sigma(u)}$ [m/s]	$\epsilon_{\sigma(w)}$ [m/s]	$\epsilon_{\sigma(u)^2}$ [m^2/s^2]	$\epsilon_{\sigma(w)^2}$ [m^2/s^2]
TP0000	5	1.38	359.5	0.0236	0.0127	0.0167	0.0090	0.0194	0.0056
TP0109A	5	1.35	393.2	0.0228	0.0123	0.0161	0.0087	0.0180	0.0053
TP0109A rev	5	1.38	469.2	0.0231	0.0120	0.0164	0.0085	0.0185	0.0050
TP0110A	5	1.35	384.2	0.0226	0.0118	0.0160	0.0083	0.0177	0.0048
TP0110A rev	5	1.35	353.3	0.0226	0.0120	0.0160	0.0085	0.0178	0.0050
TP0111A	5	1.35	317.5	0.0228	0.0119	0.0161	0.0084	0.0180	0.0049
TP0111A rev	5	1.39	738.3	0.0229	0.0116	0.0162	0.0082	0.0182	0.0046
TP0112A	5	1.42	357.9	0.0234	0.0114	0.0166	0.0081	0.0190	0.0045
TP0112A rev	5	1.38	820.6	0.0230	0.0118	0.0163	0.0083	0.0184	0.0048
TP0000	10	1.22	302.0	0.0406	0.0263	0.0287	0.0186	0.0573	0.0240
TP0109A	10	1.22	240.1	0.0383	0.0261	0.0271	0.0185	0.0509	0.0238
TP0109A rev	10	1.22	254.7	0.0389	0.0261	0.0275	0.0185	0.0526	0.0237
TP0110A	10	1.21	240.9	0.0379	0.0256	0.0268	0.0181	0.0498	0.0227
TP0110A rev	10	1.21	254.1	0.0386	0.0269	0.0273	0.0190	0.0518	0.0253
TP0111A	10	1.22	285.3	0.0416	0.0276	0.0294	0.0195	0.0602	0.0264
TP0111A rev	10	1.24	289.6	0.0421	0.0279	0.0298	0.0198	0.0619	0.0272
TP0112A	10	1.25	272.6	0.0403	0.0259	0.0285	0.0183	0.0566	0.0233
TP0112A rev	10	1.23	373.4	0.0396	0.0263	0.0280	0.0186	0.0546	0.0239
TP0000	20	1.16	172.7	0.1029	0.0704	0.0728	0.0498	0.3813	0.1767
TP0109A	20	1.14	163.1	0.0763	0.0600	0.0540	0.0424	0.2034	0.1269
TP0109A rev	20	1.15	182.1	0.0755	0.0581	0.0534	0.0411	0.1990	0.1190
TP0110A	20	1.14	148.4	0.0754	0.0591	0.0533	0.0418	0.1995	0.1246
TP0110A rev	20	1.14	164.9	0.0753	0.0591	0.0533	0.0418	0.1984	0.1237
TP0111A	20	1.17	173.4	0.0968	0.0645	0.0685	0.0456	0.3344	0.1470
TP0111A rev	20	1.20	196.7	0.1091	0.0728	0.0772	0.0515	0.4305	0.1893
TP0112A	20	1.18	163.0	0.0867	0.0597	0.0614	0.0423	0.2671	0.1258
TP0112A rev	20	1.18	231.1	0.0966	0.0676	0.0684	0.0479	0.3346	0.1627

Table E.1: PIV uncertainty values for the x-z plane; 'rev' indicates plates measured in the apex downstream orientation; plates without the annotation were tested in the apex upstream orientation

E.3. Two-point statistics results

This section contains the results of the two-point statistic analysis for 27 x-z planes corresponding to the 27 test cases specified in table 6.4. The results presented here are summarised and discussed in section 8.2. Each figure presented in this appendix consists of:

(a) A two-point correlation map for the two-dimensional flow field from an analysis of 600 velocity fields. Note that, for readability, the contours are shown in steps of $R_{uu} = 0.02$; the highest contour value is $R_{uu} = 1$; the zero contour ($R_{uu} = 0$) has been skipped; positive contours are represented by solid lines and negative contours, by dashed lines.

(b) A central spanwise cut which corresponds to a vertical cut through *(a)* at $\Delta x/\delta_v = 0$. The spanwise spacing of the streaks is interpreted as the peak-to-peak distance in this plot.

(c) A central streamwise cut which corresponds to a horizontal cut through *(a)* at $\Delta z/\delta_v = 0$. The streamwise length of the near-wall streaks is given by the integral length scale, interpreted as the $R_{uu} = 0.1$ crossing. In explanation, the streamwise length of the structures is given by the distance between the points where the correlation crosses $R_{uu} = 0.1$.

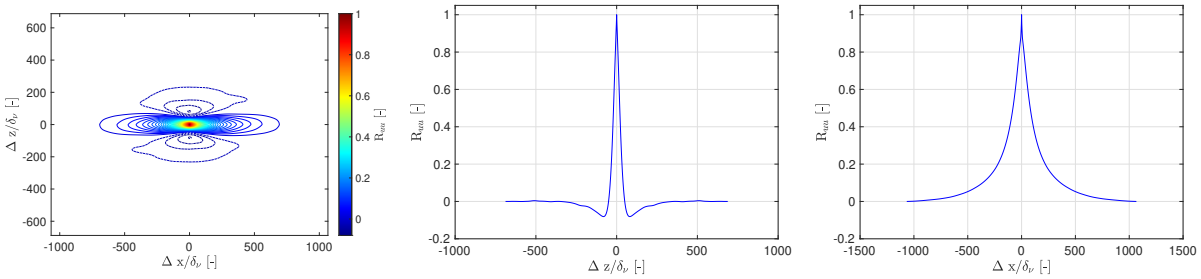

(a) Two-point correlation (b) Central spanwise cut ($\Delta x/\delta_v = 0$) (c) Central streamwise cut ($\Delta z/\delta_v = 0$)

Figure E.28: Two-point statistics for TP0000 at 5 m/s

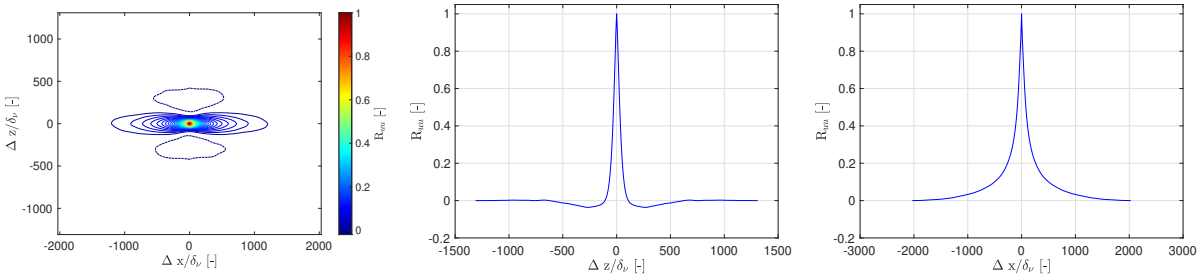

(a) Two-point correlation (b) Central spanwise cut ($\Delta x/\delta_v = 0$) (c) Central streamwise cut ($\Delta z/\delta_v = 0$)

Figure E.29: Two-point statistics for TP0000 at 10 m/s

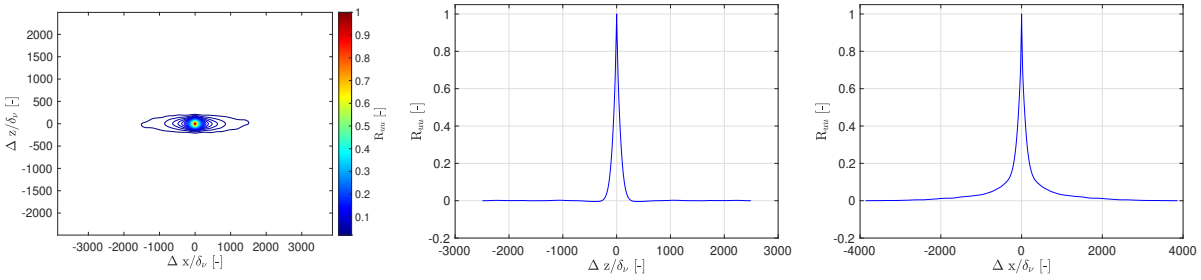

(a) Two-point correlation (b) Central spanwise cut ($\Delta x/\delta_v = 0$) (c) Central streamwise cut ($\Delta z/\delta_v = 0$)

Figure E.30: Two-point statistics for TP0000 at 20 m/s

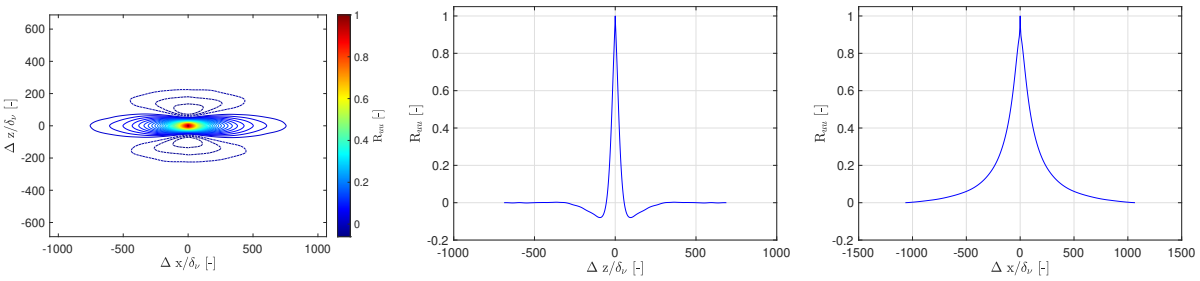

(a) Two-point correlation (b) Central spanwise cut ($\Delta x/\delta_\nu = 0$) (c) Central streamwise cut ($\Delta z/\delta_\nu = 0$)

Figure E.31: Two-point statistics for TP0109A [Sirovich (A)] at 5 m/s

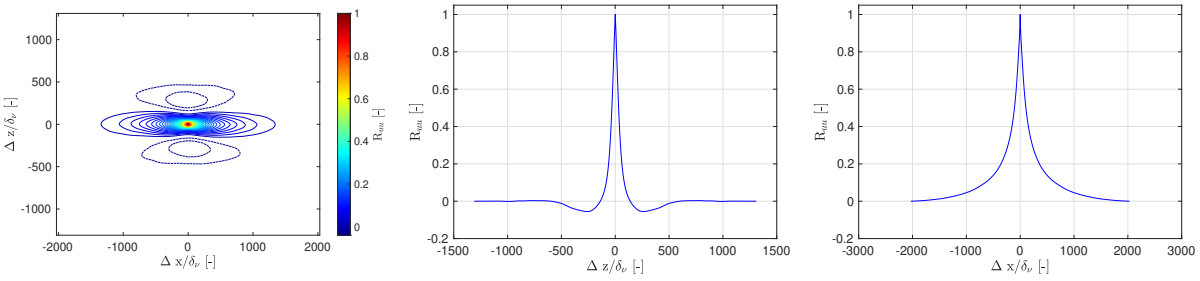

(a) Two-point correlation (b) Central spanwise cut ($\Delta x/\delta_\nu = 0$) (c) Central streamwise cut ($\Delta z/\delta_\nu = 0$)

Figure E.32: Two-point statistics for TP0109A [Sirovich (A)] at 10 m/s

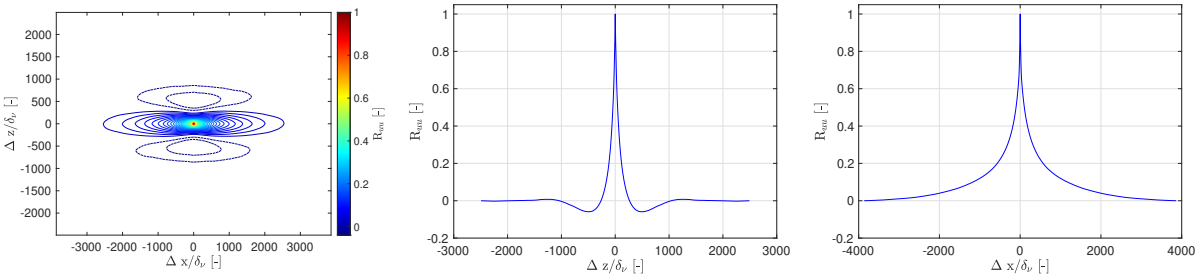

(a) Two-point correlation (b) Central spanwise cut ($\Delta x/\delta_\nu = 0$) (c) Central streamwise cut ($\Delta z/\delta_\nu = 0$)

Figure E.33: Two-point statistics for TP0109A [Sirovich (A)] at 20 m/s

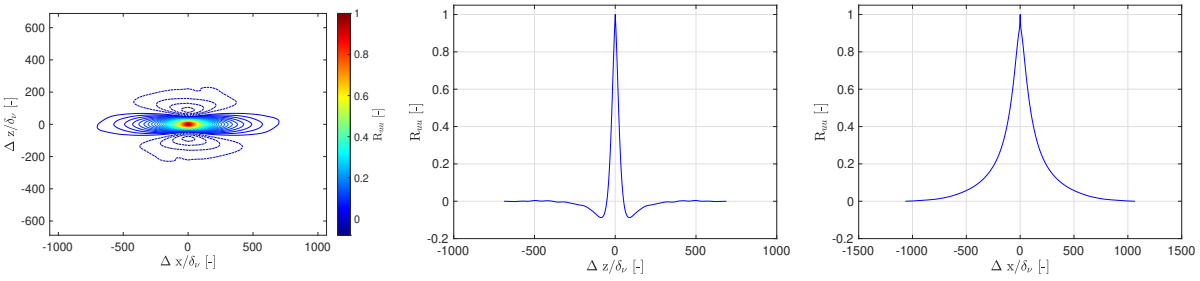

(a) Two-point correlation (b) Central spanwise cut ($\Delta x/\delta_\nu = 0$) (c) Central streamwise cut ($\Delta z/\delta_\nu = 0$)

Figure E.34: Two-point statistics for TP0109A [Sirovich (A)] reverse at 5 m/s

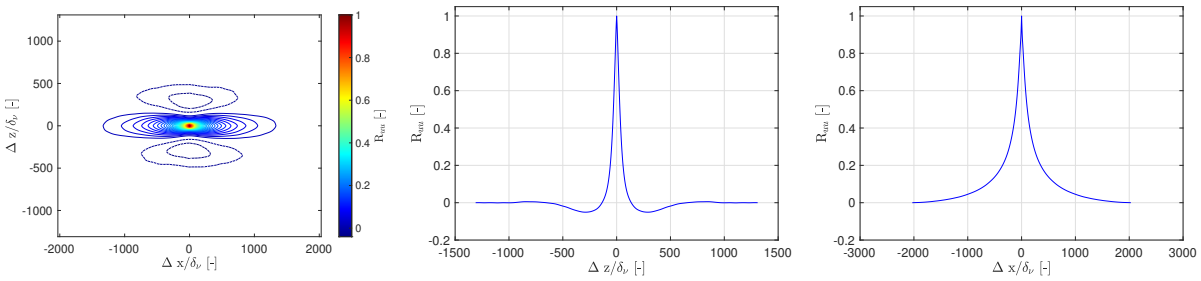

(a) Two-point correlation (b) Central spanwise cut ($\Delta x/\delta_\nu = 0$) (c) Central streamwise cut ($\Delta z/\delta_\nu = 0$)

Figure E.35: Two-point statistics for TP0109A [Sirovich (A)] reverse at 10 m/s

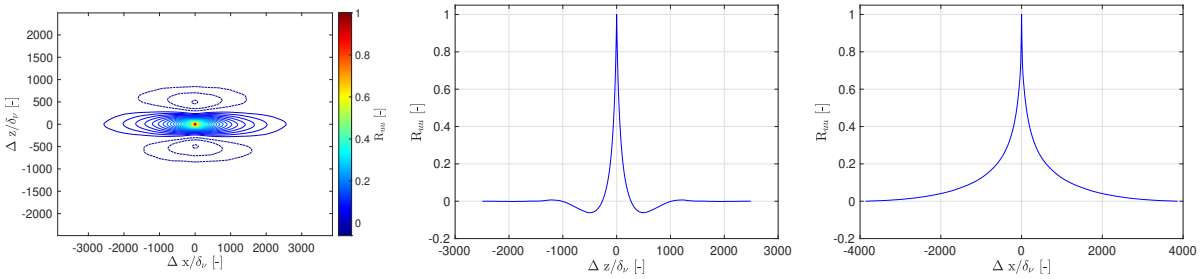

(a) Two-point correlation (b) Central spanwise cut ($\Delta x/\delta_\nu = 0$) (c) Central streamwise cut ($\Delta z/\delta_\nu = 0$)

Figure E.36: Two-point statistics for TP0109A [Sirovich (A)] reverse at 20 m/s

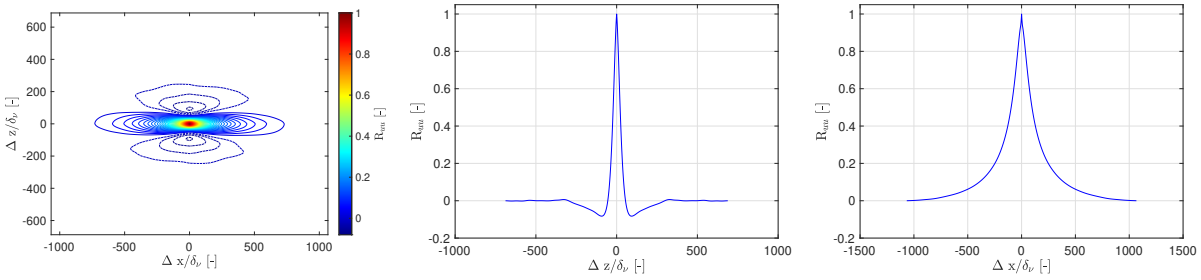

(a) Two-point correlation (b) Central spanwise cut ($\Delta x/\delta_\nu = 0$) (c) Central streamwise cut ($\Delta z/\delta_\nu = 0$)

Figure E.37: Two-point statistics for TP0110A [Sirovich (R)] at 5 m/s

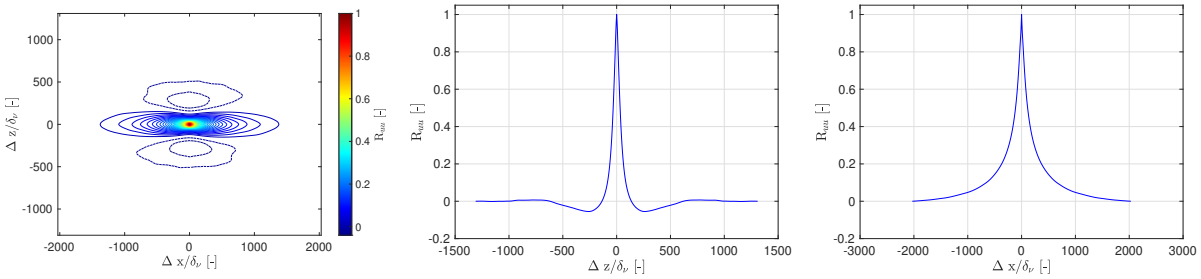

(a) Two-point correlation (b) Central spanwise cut ($\Delta x/\delta_\nu = 0$) (c) Central streamwise cut ($\Delta z/\delta_\nu = 0$)

Figure E.38: Two-point statistics for TP0110A [Sirovich (R)] at 10 m/s

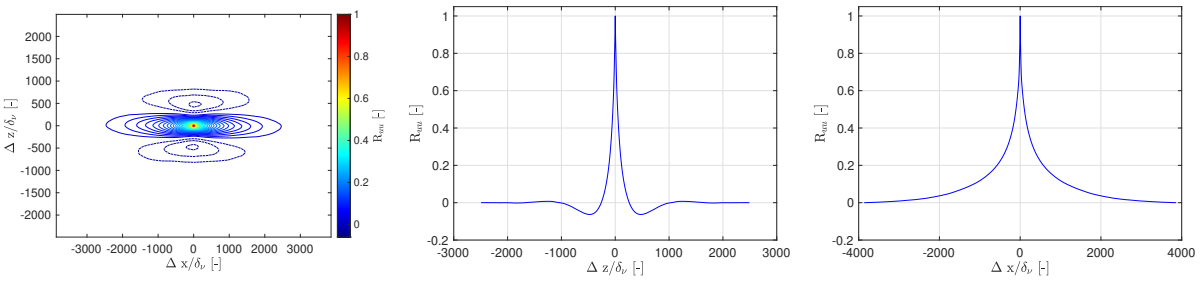

(a) Two-point correlation (b) Central spanwise cut ($\Delta x/\delta_\nu = 0$) (c) Central streamwise cut ($\Delta z/\delta_\nu = 0$)

Figure E.39: Two-point statistics for TP0110A [Sirovich (R)] at 20 m/s

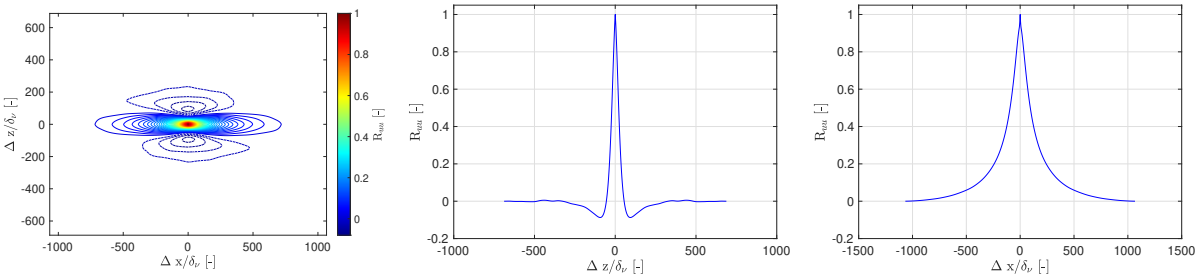

(a) Two-point correlation (b) Central spanwise cut ($\Delta x/\delta_\nu = 0$) (c) Central streamwise cut ($\Delta z/\delta_\nu = 0$)

Figure E.40: Two-point statistics for TP0110A [Sirovich (R)] reverse at 5 m/s

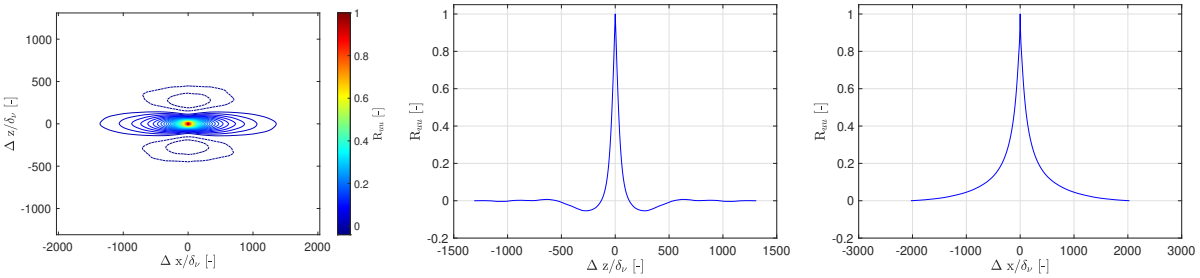

(a) Two-point correlation (b) Central spanwise cut ($\Delta x/\delta_\nu = 0$) (c) Central streamwise cut ($\Delta z/\delta_\nu = 0$)

Figure E.41: Two-point statistics for TP0110A [Sirovich (R)] reverse at 10 m/s

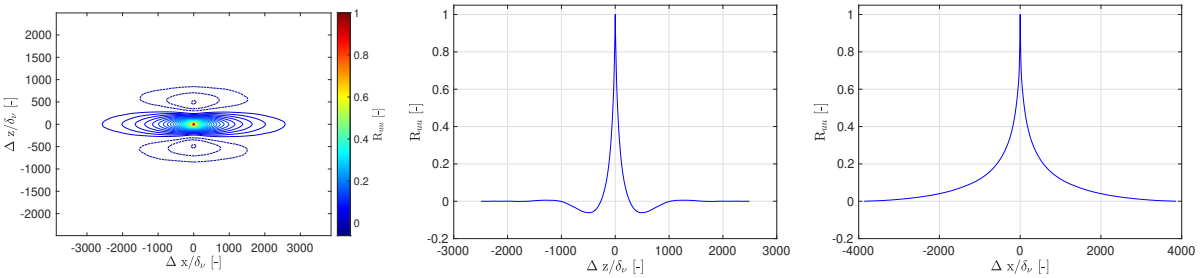

(a) Two-point correlation (b) Central spanwise cut ($\Delta x/\delta_\nu = 0$) (c) Central streamwise cut ($\Delta z/\delta_\nu = 0$)

Figure E.42: Two-point statistics for TP0110A [Sirovich (R)] reverse at 20 m/s

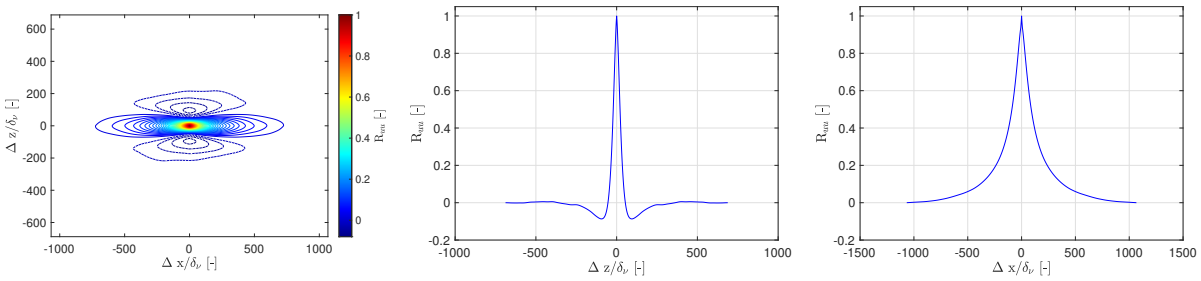

(a) Two-point correlation (b) Central spanwise cut ($\Delta x/\delta_\nu = 0$) (c) Central streamwise cut ($\Delta z/\delta_\nu = 0$)

Figure E.43: Two-point statistics for TP0111A [Deltas (A)] at 5 m/s

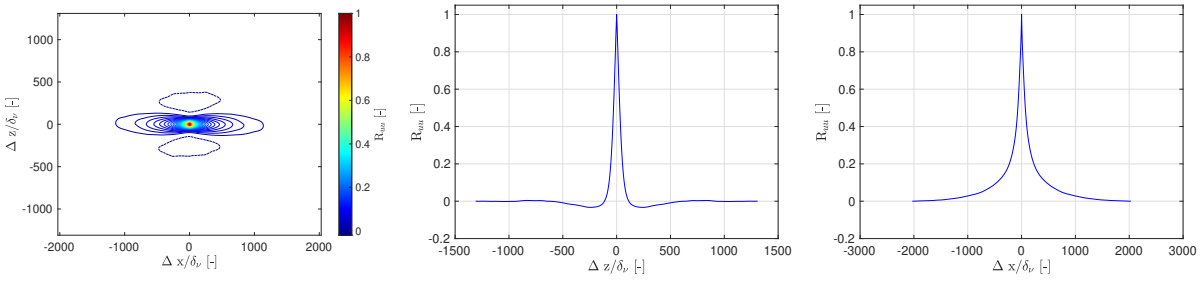

(a) Two-point correlation (b) Central spanwise cut ($\Delta x/\delta_\nu = 0$) (c) Central streamwise cut ($\Delta z/\delta_\nu = 0$)

Figure E.44: Two-point statistics for TP0111A [Deltas (A)] at 10 m/s

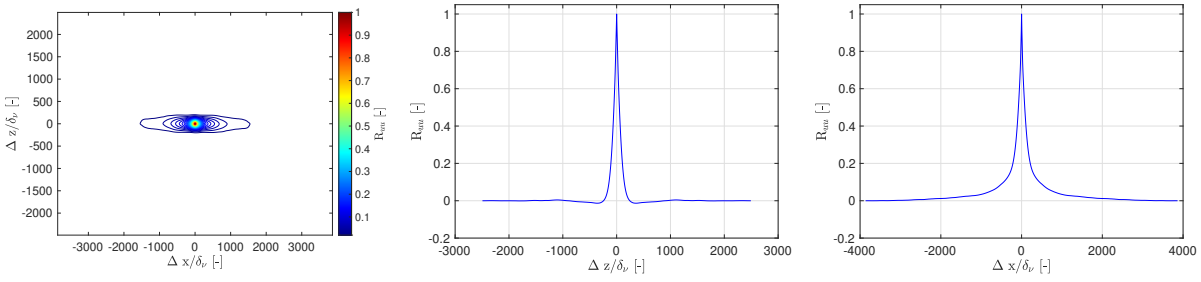

(a) Two-point correlation (b) Central spanwise cut ($\Delta x/\delta_\nu = 0$) (c) Central streamwise cut ($\Delta z/\delta_\nu = 0$)

Figure E.45: Two-point statistics for TP0111A [Deltas (A)] at 20 m/s

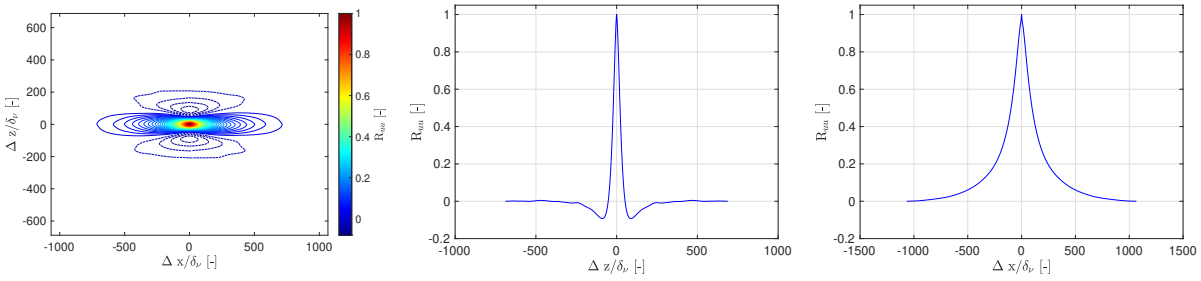

(a) Two-point correlation (b) Central spanwise cut ($\Delta x/\delta_\nu = 0$) (c) Central streamwise cut ($\Delta z/\delta_\nu = 0$)

Figure E.46: Two-point statistics for TP0111A [Deltas (A)] reverse at 5 m/s

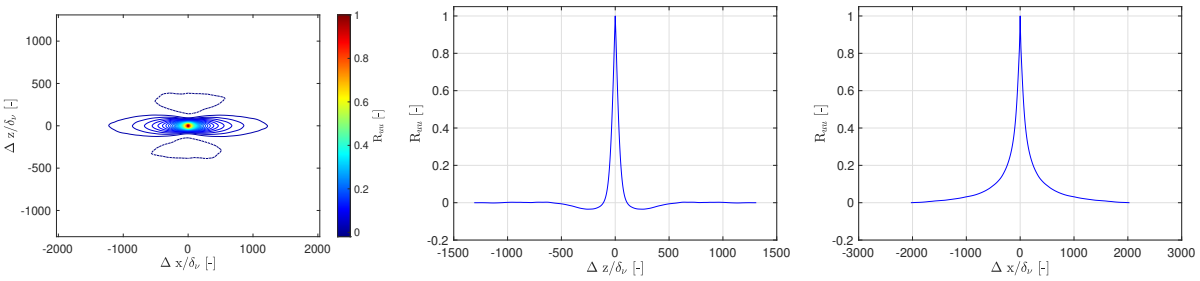

(a) Two-point correlation (b) Central spanwise cut ($\Delta x/\delta_\nu = 0$) (c) Central streamwise cut ($\Delta z/\delta_\nu = 0$)

Figure E.47: Two-point statistics for TP0111A [Deltas (A)] reverse at 10 m/s

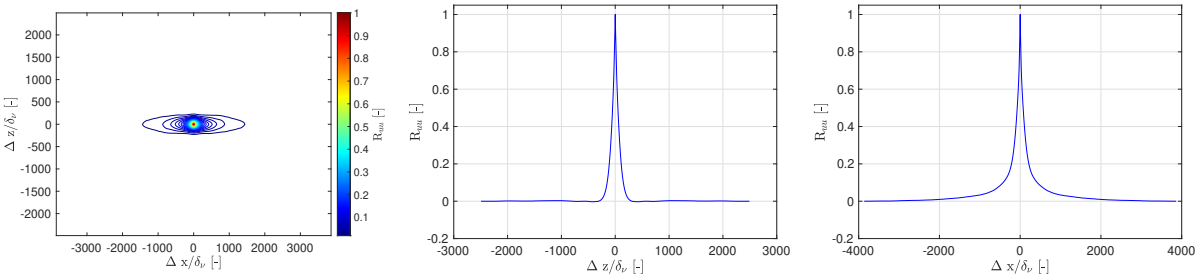

(a) Two-point correlation (b) Central spanwise cut ($\Delta x/\delta_\nu = 0$) (c) Central streamwise cut ($\Delta z/\delta_\nu = 0$)

Figure E.48: Two-point statistics for TP0111A [Deltas (A)] reverse at 20 m/s

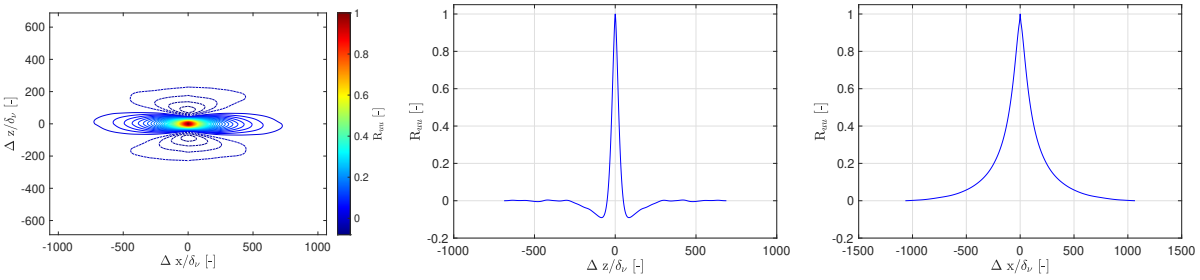

(a) Two-point correlation (b) Central spanwise cut ($\Delta x/\delta_\nu = 0$) (c) Central streamwise cut ($\Delta z/\delta_\nu = 0$)

Figure E.49: Two-point statistics for TP0112A [Deltas (R)] at 5 m/s

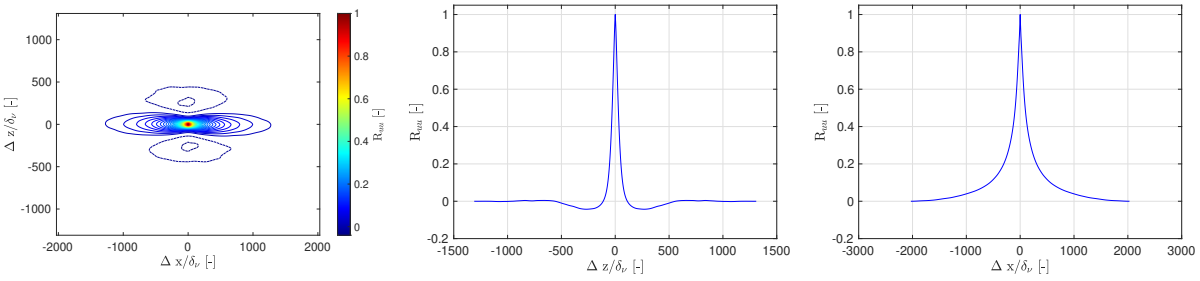

(a) Two-point correlation (b) Central spanwise cut ($\Delta x/\delta_\nu = 0$) (c) Central streamwise cut ($\Delta z/\delta_\nu = 0$)

Figure E.50: Two-point statistics for TP0112A [Deltas (R)] at 10 m/s

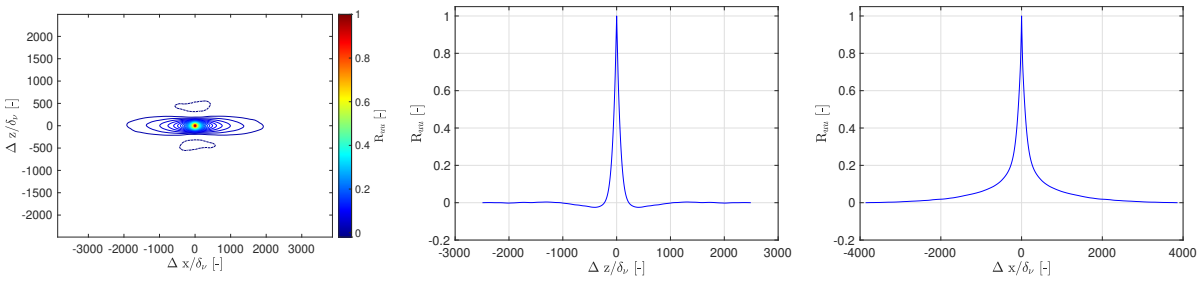

(a) Two-point correlation (b) Central spanwise cut ($\Delta x/\delta_\nu = 0$) (c) Central streamwise cut ($\Delta z/\delta_\nu = 0$)

Figure E.51: Two-point statistics for TP0112A [Deltas (R)] at 20 m/s

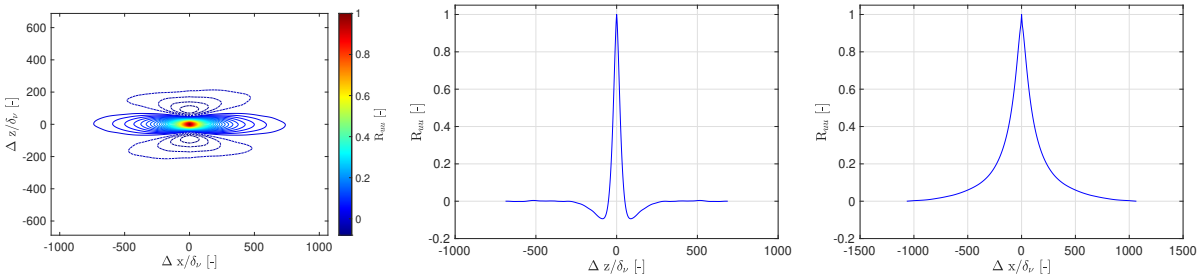

(a) Two-point correlation (b) Central spanwise cut ($\Delta x/\delta_\nu = 0$) (c) Central streamwise cut ($\Delta z/\delta_\nu = 0$)

Figure E.52: Two-point statistics for TP0112A [Deltas (R)] reverse at 5 m/s

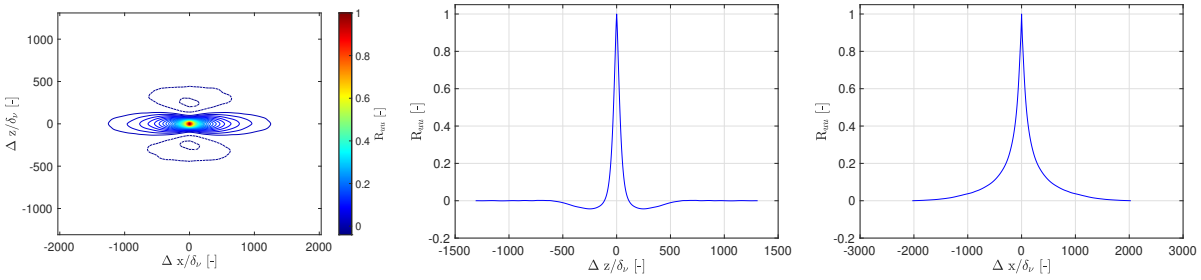

(a) Two-point correlation (b) Central spanwise cut ($\Delta x/\delta_\nu = 0$) (c) Central streamwise cut ($\Delta z/\delta_\nu = 0$)

Figure E.53: Two-point statistics for TP0112A [Deltas (R)] reverse at 10 m/s

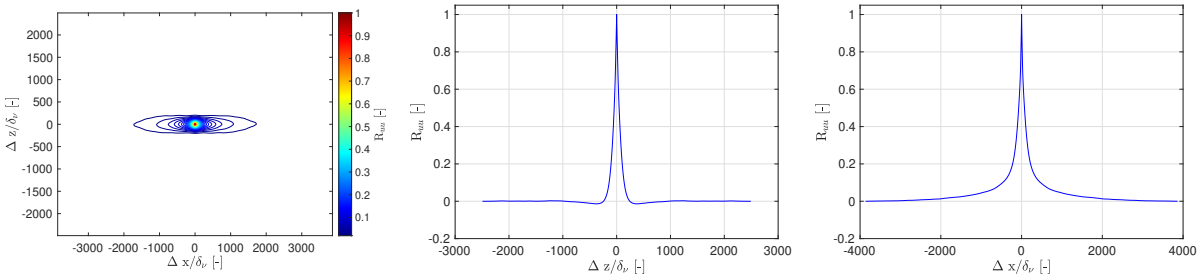

(a) Two-point correlation (b) Central spanwise cut ($\Delta x/\delta_\nu = 0$) (c) Central streamwise cut ($\Delta z/\delta_\nu = 0$)

Figure E.54: Two-point statistics for TP0112A [Deltas (R)] reverse at 20 m/s

F

PIV Additional data | y-z plane

This appendix provides additional PIV data for the y-z plane. In section F.1, the average velocity field and the corresponding standard deviation are presented for 12 test cases. The test cases are defined in table 6.4 and consist of a combination of different velocities (5 m/s, 10 m/s, and 20 m/s), different time intervals between frames in a pair, and two different fields of view. The sample size (i.e. the number of image pairs) is 1200 for each field.

F.1. Velocity vector field

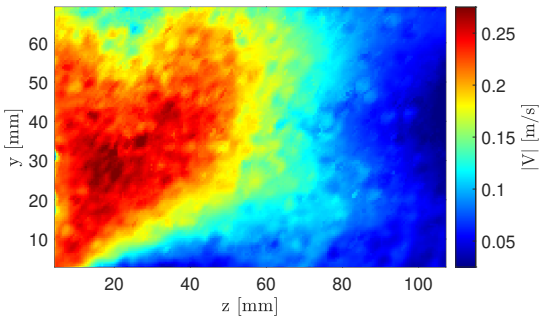

(a) Average velocity field

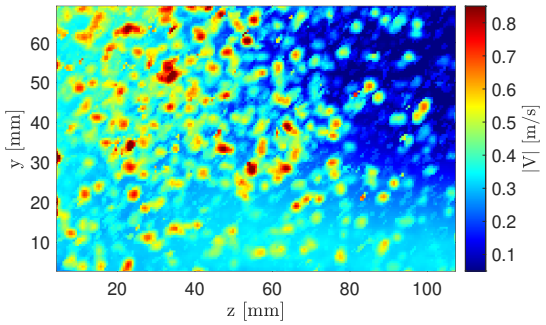

(b) Standard deviation

Figure F.1: Average and standard deviation for y-z plane at 5m/s and $\Delta t = 100$ μs; large FOV

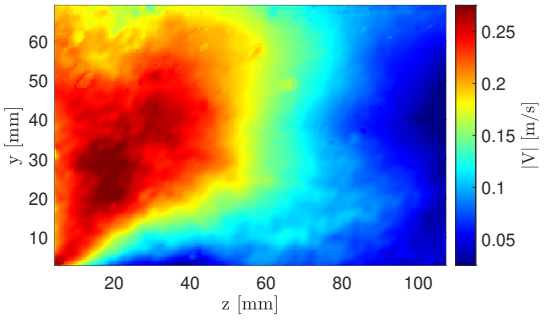

(a) Average velocity field

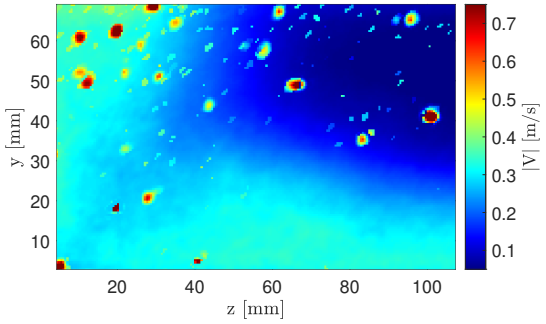

(b) Standard deviation

Figure F.2: Average and standard deviation for y-z plane at 5m/s and $\Delta t = 50$ μs; large FOV

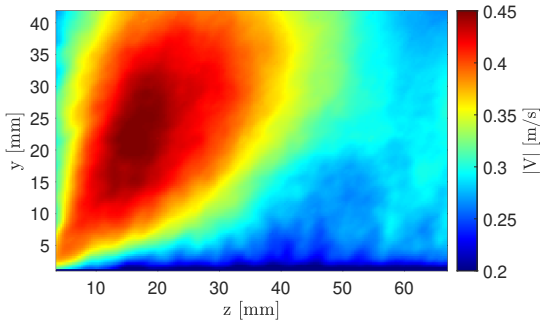

(a) Average velocity field

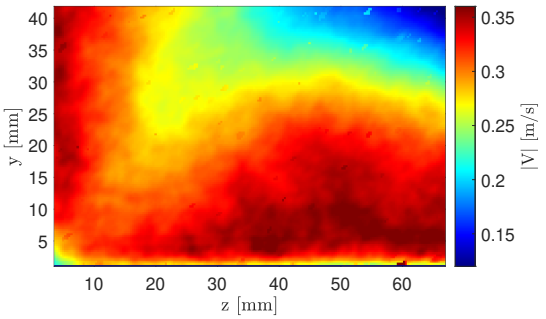

(b) Standard deviation

Figure F.3: Average and standard deviation for y-z plane at 5m/s and $\Delta t = 100$ μs; small FOV

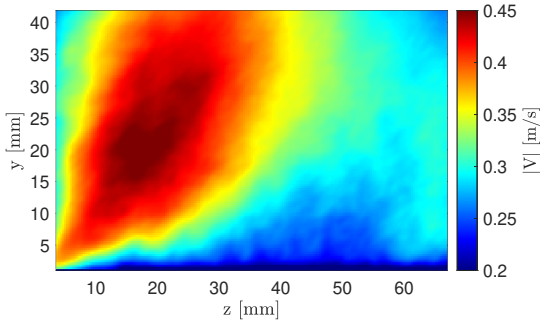

(a) Average velocity field

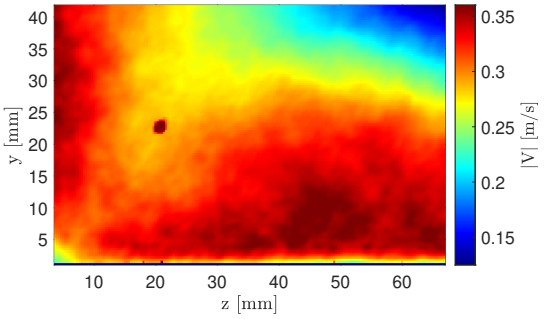

(b) Standard deviation

Figure F.4: Average and standard deviation for y-z plane at 5m/s and $\Delta t = 50$ μs; small FOV

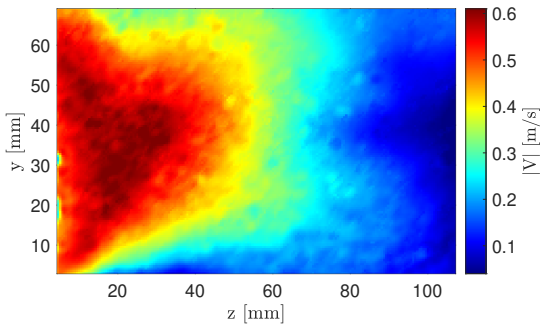

(a) Average velocity field

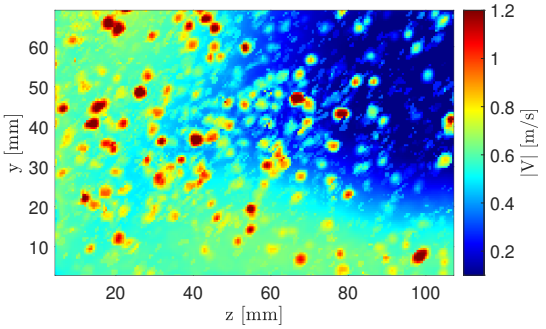

(b) Standard deviation

Figure F.5: Average and standard deviation for y-z plane at 10m/s and $\Delta t = 50$ μs; large FOV

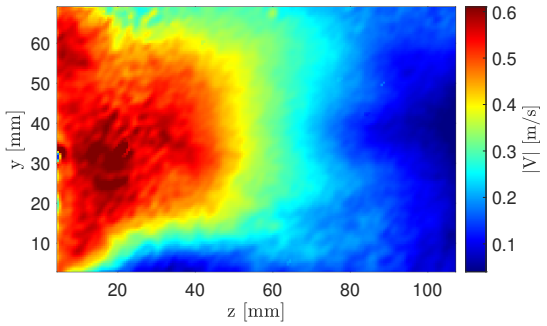

(a) Average velocity field

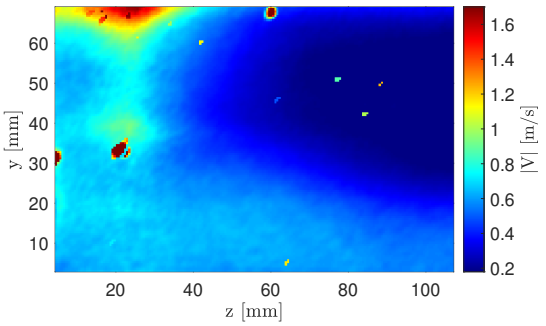

(b) Standard deviation

Figure F.6: Average and standard deviation for y-z plane at 10m/s and $\Delta t = 12$ μs; large FOV

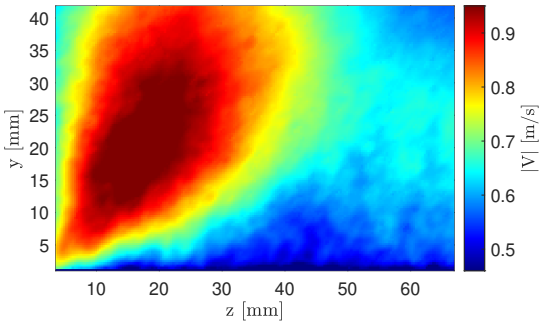

(a) Average velocity field

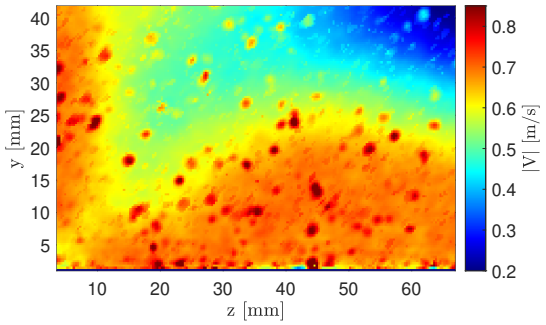

(b) Standard deviation

Figure F.7: Average and standard deviation for y-z plane at 10m/s and $\Delta t = 50$ μs; small FOV

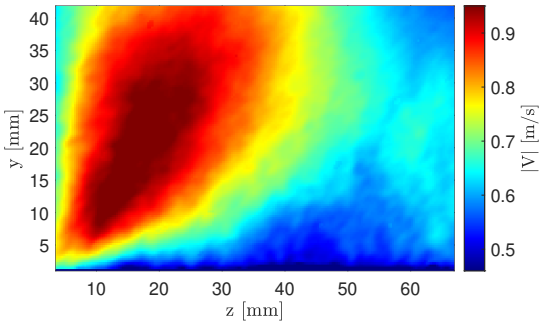

(a) Average velocity field

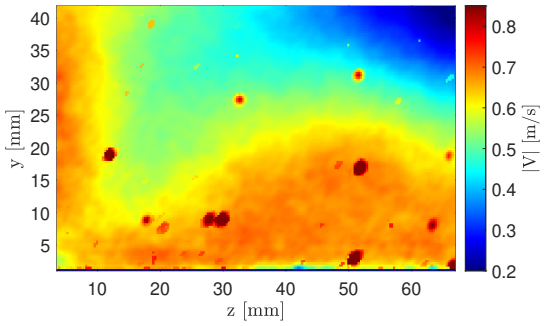

(b) Standard deviation

Figure F.8: Average and standard deviation for y-z plane at 10m/s and $\Delta t = 25$ μs; small FOV

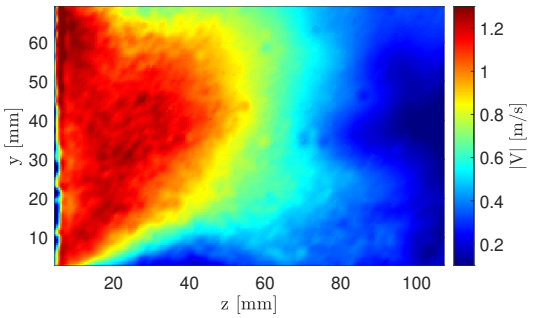

(a) Average velocity field

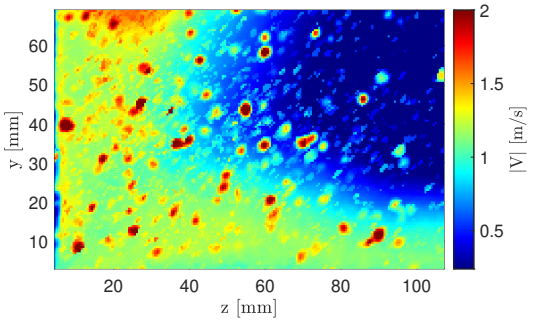

(b) Standard deviation

Figure F.9: Average and standard deviation for y-z plane at 20m/s and $\Delta t = 25$ μs; large FOV

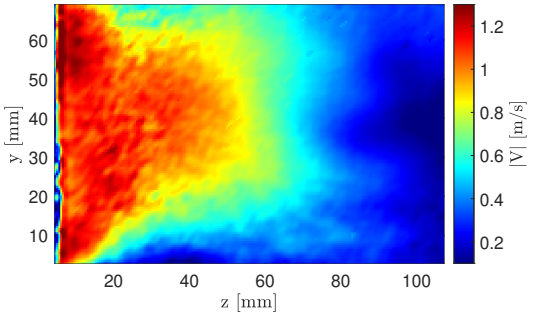

(a) Average velocity field

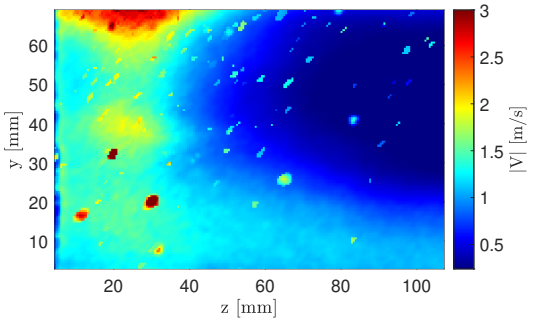

(b) Standard deviation

Figure F.10: Average and standard deviation for y-z plane at 20m/s and $\Delta t = 12$ μs; large FOV

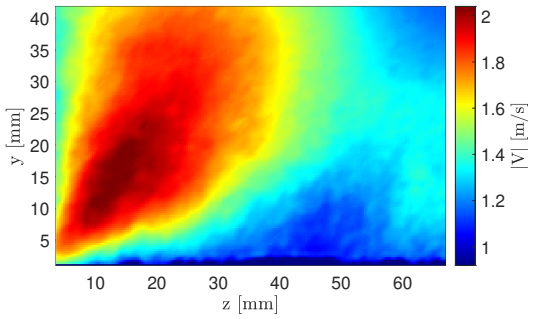

(a) Average velocity field

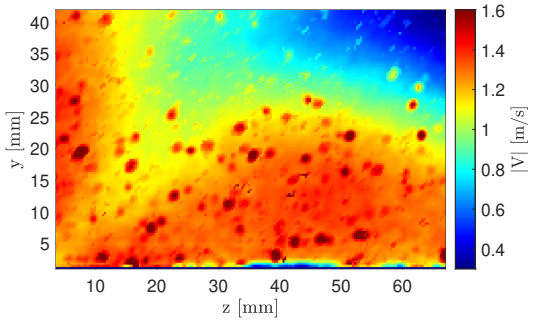

(b) Standard deviation

Figure F.11: Average and standard deviation for y-z plane at 20m/s and $\Delta t = 25\ \mu$s; small FOV

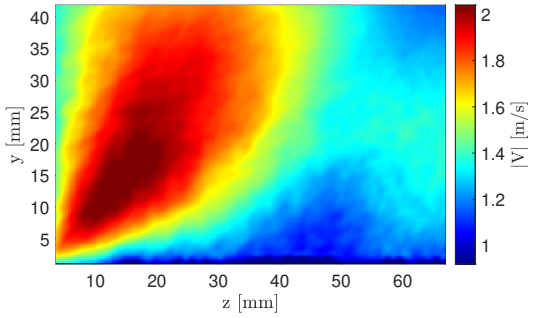

(a) Average velocity field

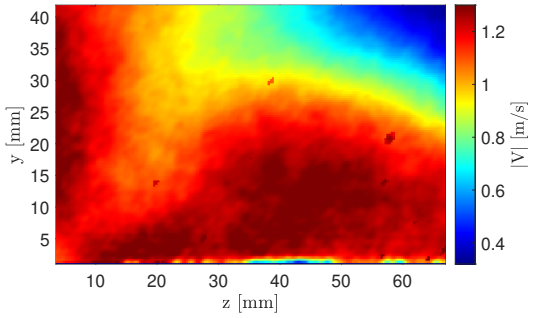

(b) Standard deviation

Figure F.12: Average and standard deviation for y-z plane at 20m/s and $\Delta t = 12\ \mu$s; small FOV

F.2. Uncertainty quantification

This section presents the results for the uncertainty quantification in table F.1. The methodology used for this analysis has been presented in section 6.2.4. For the y-z plane, the uncertainty of the instantaneous velocity fields (ϵ_v, ϵ_w), of the mean velocity ($\epsilon_{\bar{v}}$, $\epsilon_{\bar{w}}$), and of the standard deviation ($\epsilon_{\sigma(v)}$, $\epsilon_{\sigma(w)}$) are considered.

FOV [-]	U_∞ [m/s]	Δt [μ s]	ϵ_v [%]	ϵ_w [%]	$\epsilon_{\bar{v}}$ [m/s]	$\epsilon_{\bar{w}}$ [m/s]	$\epsilon_{\sigma(v)}$ [m/s]	$\epsilon_{\sigma(w)}$ [m/s]
large	5	100	906.5	32.62	0.0061	0.0074	0.0043	0.0052
large	5	50	2283.2	63.63	0.0045	0.0050	0.0032	0.0035
small	5	100	10.0	16.25	0.0058	0.0061	0.0041	0.0043
small	5	50	19.9	32.11	0.0059	0.0062	0.0041	0.0044
large	10	50	3290.1	29.10	0.0095	0.0107	0.0067	0.0076
large	10	12	4939.3	126.80	0.0091	0.0109	0.0065	0.0077
small	10	50	9.4	14.32	0.0115	0.0122	0.0082	0.0087
small	10	25	18.6	28.91	0.0112	0.0118	0.0079	0.0083
large	20	25	2474.3	28.20	0.0162	0.0191	0.0115	0.0135
large	20	12	1326.4	62.72	0.0166	0.0215	0.0118	0.0152
small	20	25	8.9	13.83	0.0217	0.0230	0.0154	0.0163
small	20	12	18.7	28.24	0.0211	0.0219	0.0149	0.0155

Table F.1: PIV uncertainty values for the y-z plane

G

Fluorescent oil visualisation

This appendix contains four sample images for the x-z wall visualised with fluorescent oil at four velocities: 0 m/s, 10 m/s, 20 m/s, and 30 m/s. This visualisation intends to identify the spanwise extent of the corner vortices. In the images, the 0 mm line coincides with the wind tunnel wall and the 200 mm line with the centre of the wind tunnel floor (in the spanwise direction). For the theoretical background of fluorescent oil visualisation, please refer to section 6.3

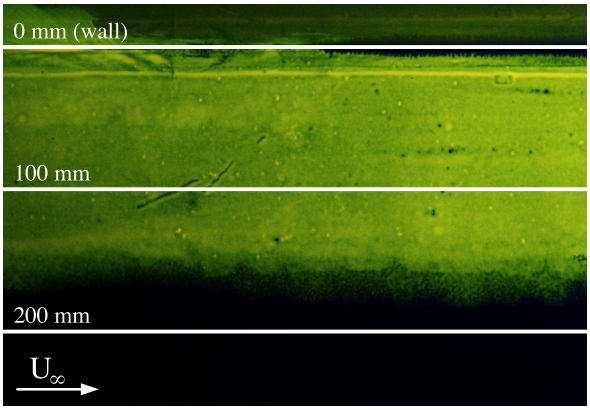

(a) Initial layer of oil on the test plate

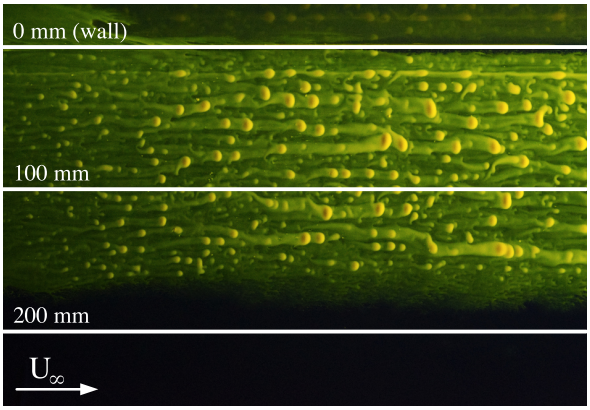

(b) Image of the oil layer after 12 minutes at 10 m/s

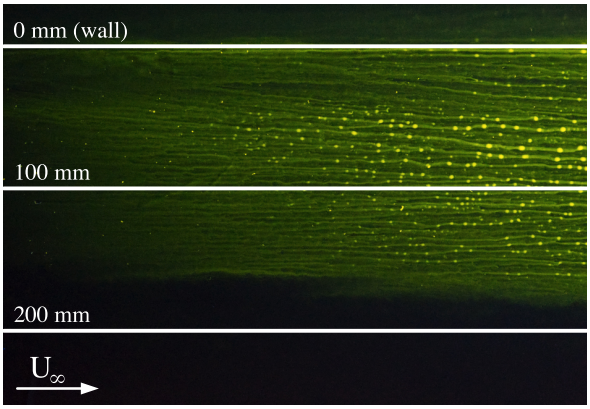

(c) Image of the oil layer after 30 minutes at 20 m/s

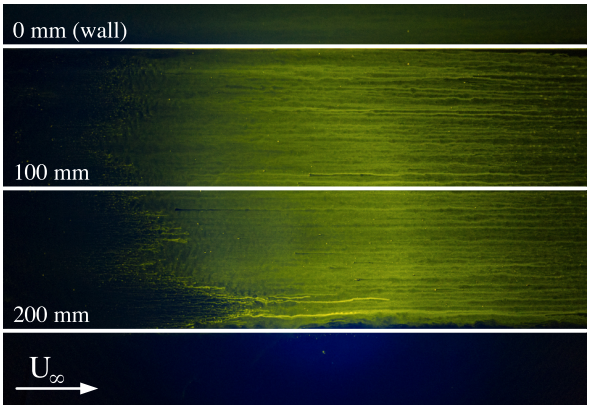

(d) Image of the oil layer after 38 minutes at 30 m/s

Figure G.1: Oil visualisation: top view on the test plate; 0 cm line coincides with the location of the side wall

Considering the images in figure G.1, no indication of a corner vortex can be seen, supporting the claim made in chapter 8: ‘no corner vortices could be identified using fluorescent oil visualisation for any of the tested velocities’.

H

Additional parametric study results

This appendix supplements chapter 7 by providing additional results for the discussion on the balance measurements results. First, the plots with the direct force measurements discussed in chapter 7 are presented here for a lower Reynolds number in section H.1. Next, an overview of the drag difference measured for all designs is given in section H.2.

H.1. Parametric study for $Re_1 = 10^6$

In this section, the results of the direct force measurements at $Re_1 = 10^6$ are presented. The results support the claim that was formulated in chapter 7: 'the Reynolds number of 2e6 was chosen for the discussion of the results; however, the same trends can be seen for other Reynolds numbers'

H.1.1. Parameter study

For the parameter study, the separation between rows (figure H.1a), the separation between elements in a row (figure H.1b), and the thickness of the chevron legs (figure H.1c) are considered.

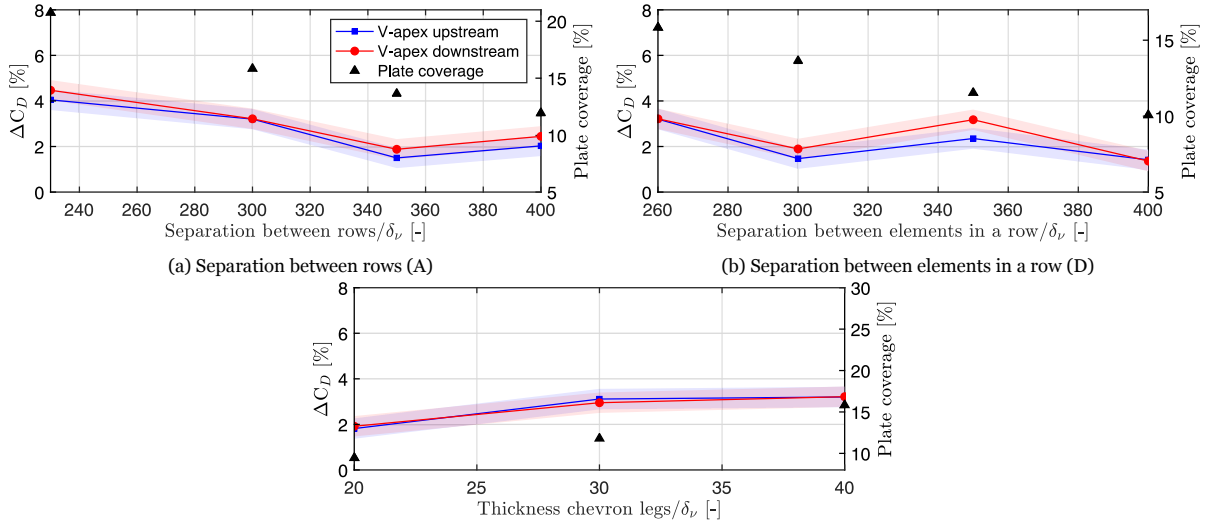

(a) Separation between rows (A)

(b) Separation between elements in a row (D)

(c) Thickness chevron legs (T)

Figure H.1: Parameter sweep; $Re_1 = 1 \times 10^6$

H.1.2. Hypotheses

Several hypotheses are discussed in this Master thesis. In this section, data at $Re_1 = 10^6$ is provided to address these. In particular, data to target the delta and cavity hypotheses is presented in figure H.2b.

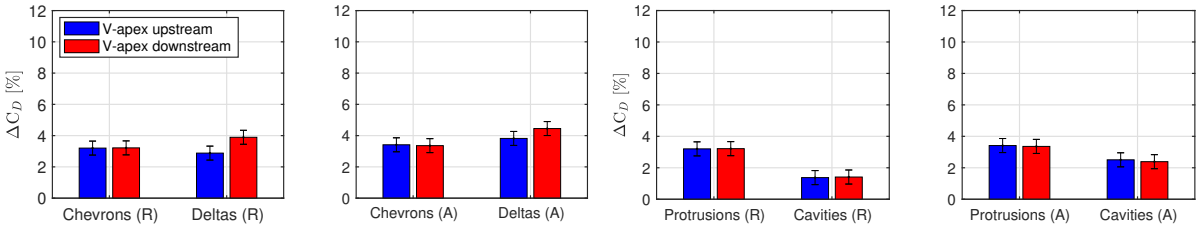

(a) Delta hypothesis (b) Cavity hypothesis

Figure H.2: Delta and Cavity hypotheses; $Re_1 = 1 \times 10^6$

The hypothesis regarding using different offsets (aligned, constant, and random) is covered in figure H.3.

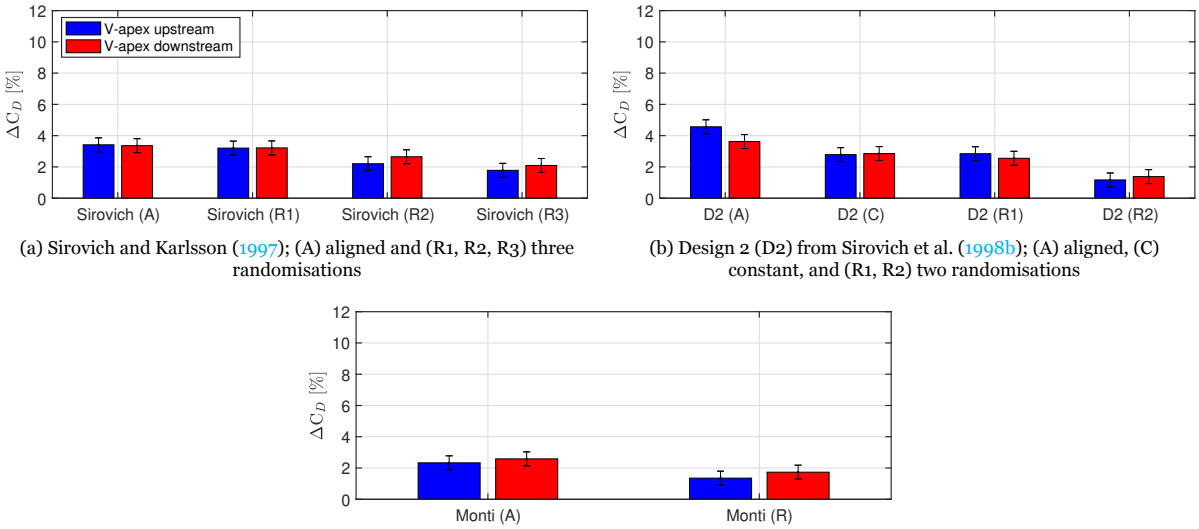

(a) Sirovich and Karlsson (1997); (A) aligned and (R1, R2, R3) three randomisations

(b) Design 2 (D2) from Sirovich et al. (1998b); (A) aligned, (C) constant, and (R1, R2) two randomisations

(c) Monti et al. (2001); (A) aligned and (R) random

Figure H.3: Effects of different offset types and values; $Re_1 = 1 \times 10^6$

To answer the apex orientation hypothesis, all figures presented in this section contain data for the apex upstream and downstream orientations. Finally, data showing the effect of anodising on the results are presented in figure H.4.

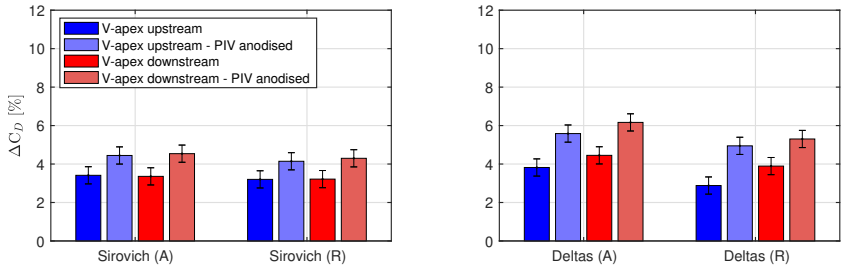

Figure H.4: Anodised plates for PIV; $Re_1 = 1 \times 10^6$

H.2. Overview of all test plates

For easier comparison of the results and to address the individual hypotheses more efficiently, the data has been presented clustered. This section gives an overview of the results for all tested designs in figure H.5. The results are expressed in terms of drag difference with respect to the reference smooth plate TP0000. This figure can serve as a reference to look up individual results and as a benchmark to see how the different designs compare. Note that the results have been ordered from highest to lowest drag increase in the apex upstream orientation.

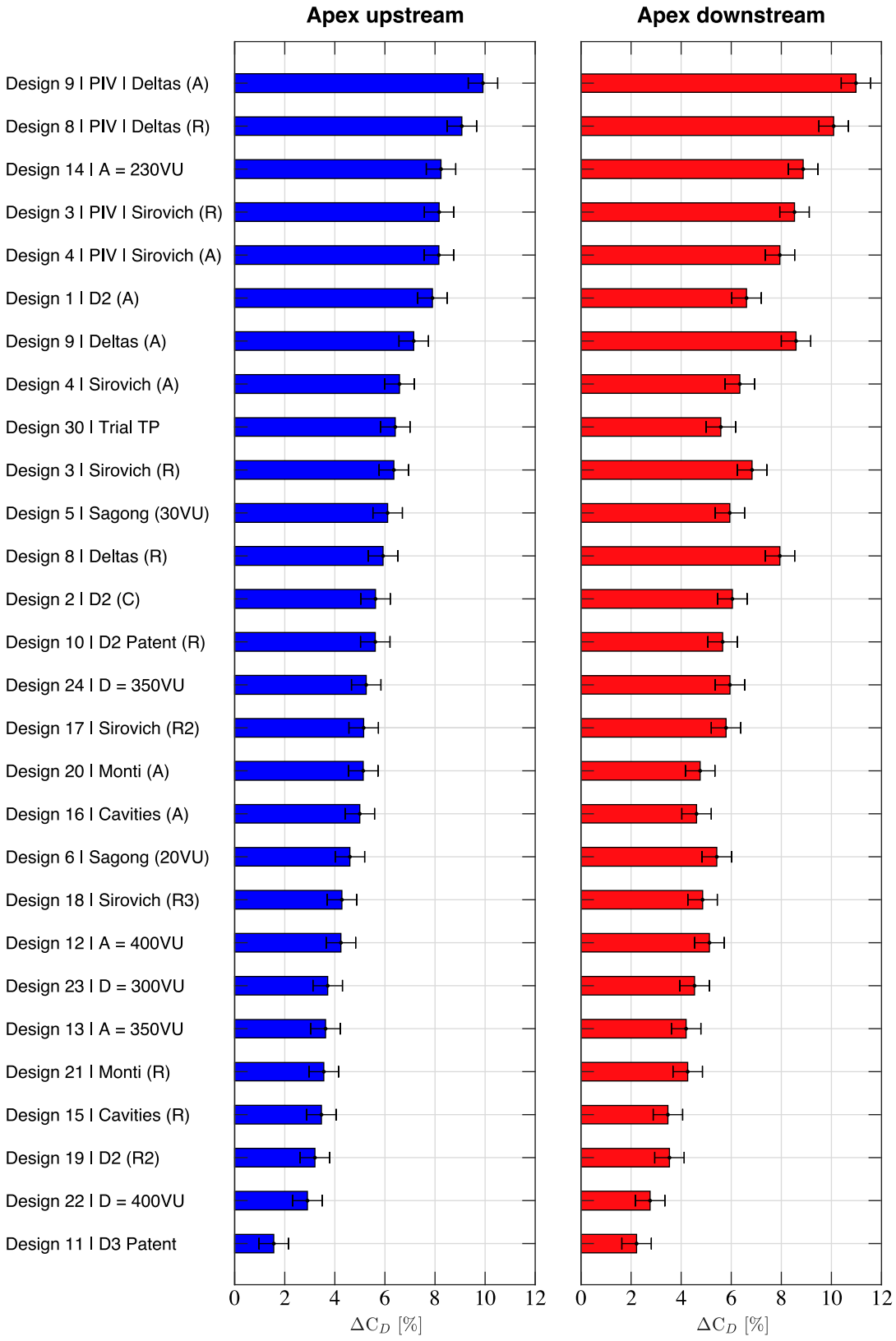

Figure H.5: Overview of drag difference for all measured designs at a $Re_1 = 2 \times 10^6$; order in descending drag increase (for apex upstream orientation)